'The Stress Analysis of Thin-Walled Screwed Tubular Joints'

by T.P. Broadbent, B.Sc.

Thesis submitted to the University of Nottingham
for the degree of Doctor of Philosophy, October, 1988.

ACKNOWLEDGMENT

The author wishes to thank all those colleagues who have assisted him with his work. Particular thanks are due to Professor Henry Fessler for his enthusiasm and guidance. Thanks are also due to the technicians of the Mechanical Engineering Department for their skilled assistance in casting and slicing the models, Mr. H. Rose for his skill in machining the early models and the threaded cores and moulds, Dr. R. E. Marston for the design of the Automatic Micropolariscope without which much of the work presented would not have been possible. Miss Kay Harwood for her care and patience in typing this script, Mr. G. Dearden formally of Hunting Oilfield Services, for his advice in the initial design stages of the work and finally and by no means least the author wishes to thank his wife Susan for her patience and understanding and for improving the authors written English.

Financial support for this project has been provided by the: Marine Technology Directorate of the SERC.

ABSTRACT

This report presents the findings of a project studying the stress analysis of screwed tubular joints using photoelastic and finite element techniques. The aim of the work was to optimise the thread form to be used in large diameter, thin walled, tubular screwed joints which may be used as connections in the tethers of Tension-Leg Platforms.

Frozen-stress, photoelastic techniques were used to measure the distributions of thread load and peak fillet stresses around the thread spirals of models with different thread shapes and loaded with different loading modes of axial tension, preload only, preload plus tension and eccentric tension.

From detailed photoelastic measurements of the distribution of stress around individual thread fillets it was found that the fillet stress at any position in the thread spiral is the sum of those due to the stresses in the model wall plus those due to the shear force carried by the thread.

Due to the time and cost involved in manufacturing and analysing a sufficient number of Araldite models to carry out a full analysis of the effect of thread parameters on fillet stresses it was decided to use axisymmetric, 8 noded, isoparametric, finite elements.

Fillet stress distributions obtained using finite elements and 3-dimensional photoelasticity were checked for agreement of results for threads of similar shapes before the range of shapes analysed was extended using finite elements.

It was found that simple trigonometric functions in terms of the position around the thread fillet accurately described the fillet stress distribution. The effect of changing thread shape on the fillet

stresses could also be described by using simple functions of the parameters concerned. Both the trigonometric and parametric functions were different for wall tension and shear force loading, but they could be combined to give the fillet stress distribution in a typical thread loaded with both shear force and wall tension.

The accuracy of the equations developed was investigated by comparing the predicted distributions of position and magnitude of peak fillet stresses with those measured in the 3-dimensional Araldite models. The pitch-average peak fillet stresses were generally within $\pm$10% of each other.

Finally, the effect of altering thread parameters was investigated using the equations developed.

TABLE OF CONTENTS

CHAPTER 5 ANALYSIS TECHNIQUES

CHAPTER 6 FINITE ELEMENT WORK

CHAPTER 7 ERROR ANALYSIS

CHAPTER 8 RESULTS

CHAPTER 9 DISCUSSION

CHAPTER 10 CONCLUSIONS

Definitions

Figures N1, N2 and N3 illustrate many of the terms used.

Coupling is used to describe the externally threaded part of the screwed connection. In the steel structure it would have two threaded parts and would be used to connect tube to tube.

Fillet the radius which blends the thread with the thread root.

Pitch numbers P are used to define the axial position of the loaded flank of both tube and coupling threads. As shown in Fig. N2 the datum, P=0, was the end of the loaded runout of the coupling, i.e. the end of the coupling thread nearest the tube undercut, see Fig. N1.

Fractional pitch numbers are also described in terms of the angle measured from the axial plane of P = 0 and increasing clockwise looking from the plain tube, e.g. the plane $\theta = 90^{\circ}$ contains P = 0.25, 1.25 etc. The same datum is also used for axial positions, z in the whole model. Hence

A value of θ refers to a plane through the axis

A value of z refers to a plane perpendicular to the axis

A value of P refers to a radial line through the axis at a point of thread contact.

Because the intersections of these radial lines with the outside of the tube formed a helix and their intersections with the conical threaded surfaces formed spirals, a value of P refers to a circumferential AND an axial position of thread contact. If a contact point is at $z = z_i$, the tube thread extended from z_i to $(z_i + w)$ and the coupling thread extended from z_i to $(z_i - w)$.

Preload If the joint was tightened beyond the 'hand-tight' position so that the tube nose was in compression and the coupling undercut was in tension, then the connection was preloaded.

Root was the region in the thread between the fillet radii of the loaded and trailing faces. For the photoelastic models it was parallel to the model axis, see Fig. N3.

Runout was the termination of the thread. For the photoelastic models the threads were usually terminated at a z=constant plane. If the runout was at the undercut end of the thread spiral, then the loaded face of the thread was removed and contact stopped abruptly. If the runout was at the other end of the thread spiral, then the unloaded flank of the thread was removed and contact extended over the 180^{o} degrees of the runout as the thread width w reduced from p/2 to 0. This runout is called loaded and has been truncated on several of the models, removing the region from w=0 to a specified position, eg. on Model 5, 120^{o} of loaded runout were removed from w=0 to w=p/3.

Seal was the region of the model or prototype which reacted the preload and for the steel structure prevented seawater ingress into the thread region.

Thread cross-section was the same for tube and coupling (see Fig. N3). Tip and root surfaces of both were cylindrical of varying radius to fit the cone angle. As the thread was single start, a z = constant section shows half a tube thread and half a coupling thread. The tube thread extended beyond the coupling at both ends.

Tube is used to describe the length of plain tube and its internally threaded end. In the steel structure these tubes would be the main parts of the tether with internal threads at both ends.

Undercut was the region between the thread spiral and the full tube model wall thickness and between the thread spiral and the coupling seal see Fig. N1. It was a plane portion of tube which enabled accurate calibrations of the applied loads and allowed the thread cutting tools to be located at a radially correct position before machining.

Notation

A_{ci}	cross-sectional area of coupling at section i
A_{ti}	cross-sectional area of tube at section i
$b_{t,c}$	tube or coupling wall thickness beneath thread, see Fig. N3
b_{max}	maximum tube or coupling wall thickness beneath thread,
b_{min}	minimum tube or coupling wall thickness beneath loaded thread
C_1, C_2, C_3, C_4	non-dimensional coefficients used to describe stresses in thread fillets
c	radial clearance between crest and root of mating threads, see Fig. N3
C_S	axial clearance between mating seal parts in the hand-tight, unloaded condition.
d	eccentricity of tensile load F from centre line of Araldite tubular model.
D_i	coupling model inside diameter, see Fig. N1
D_o	tube model outside diameter, see Fig. N1
D_m	mean diameter of thread contact
e	eccentricity of thread shear force from thread root, see Fig. N3
E	Young's Modulus of Elasticity
f_c	material fringe value of coupling model
f_t	material fringe value of tube model
F	tensile load applied to screwed connection
h	thread height, see Fig N3
g	normalised flexibility of screwed connection
G	Measured flexibility
G_{nom}	Calculated axial flexibility of plain tube
l	axial length of plane tube in finite element meshes
L	axial length of engagement of threads, see Fig N2
M_o	nominal bending moment applied to thread = V(e+b/2)

$F(M_o)_i$ calculated bending moment at any distance i from the thread considered, from beam on elastic foundations type equations using M_o

n isochromatic fringe order

N number of pitches of thread engagement = L/p

p thread pitch, see Fig. N3

P thread number, see Fig N2

R thread fillet radius, see Fig. N3

s photoelastic slice thickness

t full tube wall thickness, see Fig N1

T tension in torque loading cables

V shear force per unit spiral length of thread

V_F normalising shear force for models loaded with tension only or tension + preload

$$= \frac{F}{(L/p)(\pi^2 D_m^2 + p^2)^{\frac{1}{2}}}$$

V_Q normalising shear force for models loaded with preload only

$$= \frac{Q_o}{(L/p)(\pi^2 D_m^2 + p^2)^{\frac{1}{2}}}$$

$\bar{V}$ normalised shear force per unit spiral length of thread

w thread width, see Fig. N3

W Wall force

W_{ci} normalised coupling wall force at any section i

$$= \sum_{z=0}^{z=i} \bar{V} d\left(\frac{z}{L}\right)$$

W_{ti} normalised tube wall force at any section i

$$= 1 - \sum_{z=0}^{z=i} Vd\left(\frac{z}{L}\right)$$

$W_{CF,Q}$ normalised coupling wall force due to tension, preload

$W_{tF,Q}$ normalised tube wall force due to tension, preload

r,θ,Z threaded connection co-ordinate system, see Fig. N1

α thread loaded face angle, see Fig. N3

β thread unloaded face angle, see Fig. N3

γ thread taper, see Fig. N3

ε strain

Q_o preload applied to screwed connection

W_t preload remaining in seal region after application of preload

Q_o and tension $F = \frac{F A_t}{A_t + A_c} - Q_o$

μ coefficient of friction

ν Poissons ratio

σ stress

$\sigma_{1,2,3}$ principal stresses

σ_{nomF} nominal stress due to tension = $F/\pi t(D_o - t)$

σ_{nomQ} nominal stress due to preload = $Q_o/\pi t(D_o - t)$

σ_L surface stress anywhere in thread fillet

$\hat{\sigma}_L$ peak surface fillet stress at a particular section of thread

σ_a surface stress due to wall tension anywhere in thread fillet

σ_F surface stress due to shear force anywhere in thread fillet

σ_m maximum tube outside diameter stress due to eccentric tension

σ_{sb} wall surface stress due to wall bending

σ_{sa}	mean axial wall stress
σ_{sF}	calculated wall surface bending stress due to thread shear force
σ_{s}	surface stress in model wall adjacent to thread fillet
σ_{T}	mean axial stress at any section in model undercut
σ_{y}	prototype material yield stress
τ	shear stress
τ_{m}	maximum in-plane shear stress
Φ	isoclinic angle
θ_{c}	coupling seal angle, see Fig 3.4
θ_{t}	tube seal angle, see Fig. 3.4
ψ_{max}	position around thread fillet of peak surface fillet stress

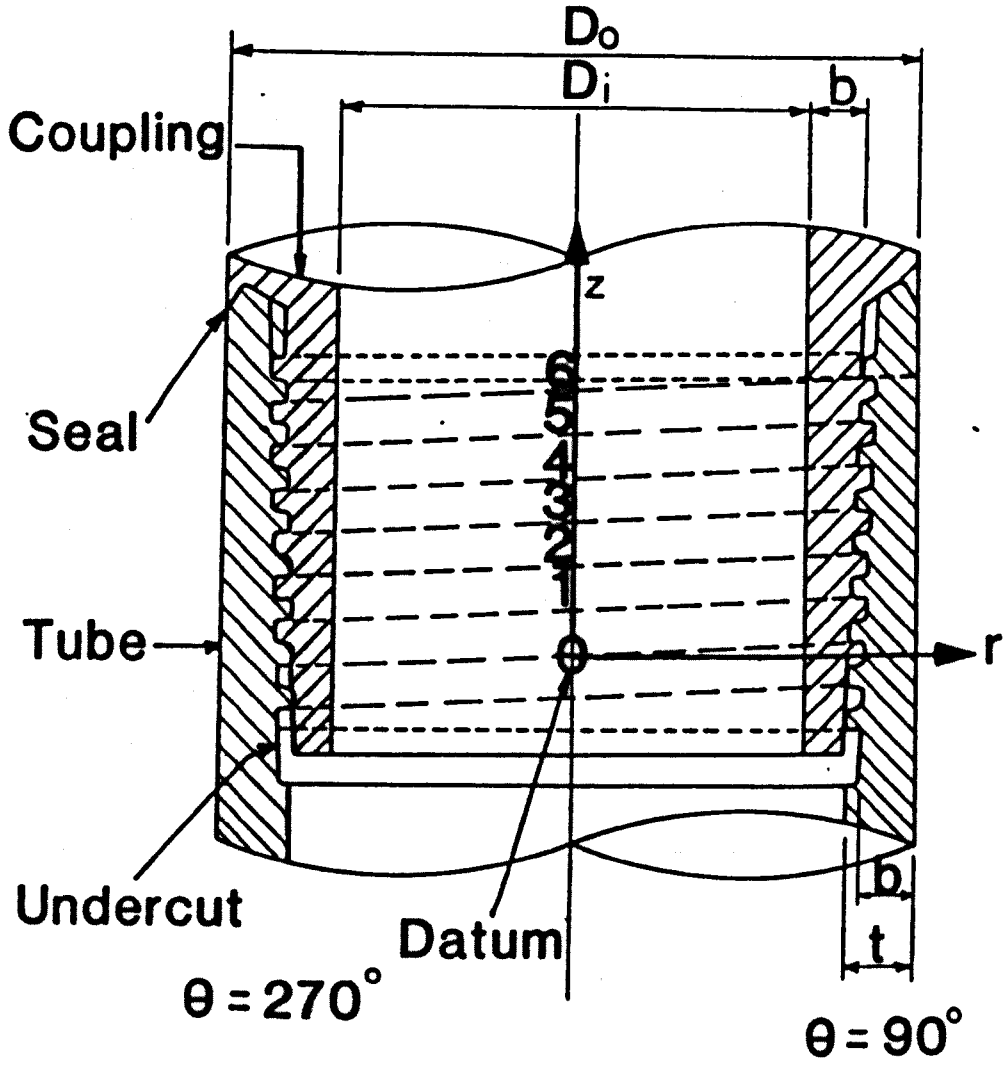

Fig. N1

Section Through Typical Connection

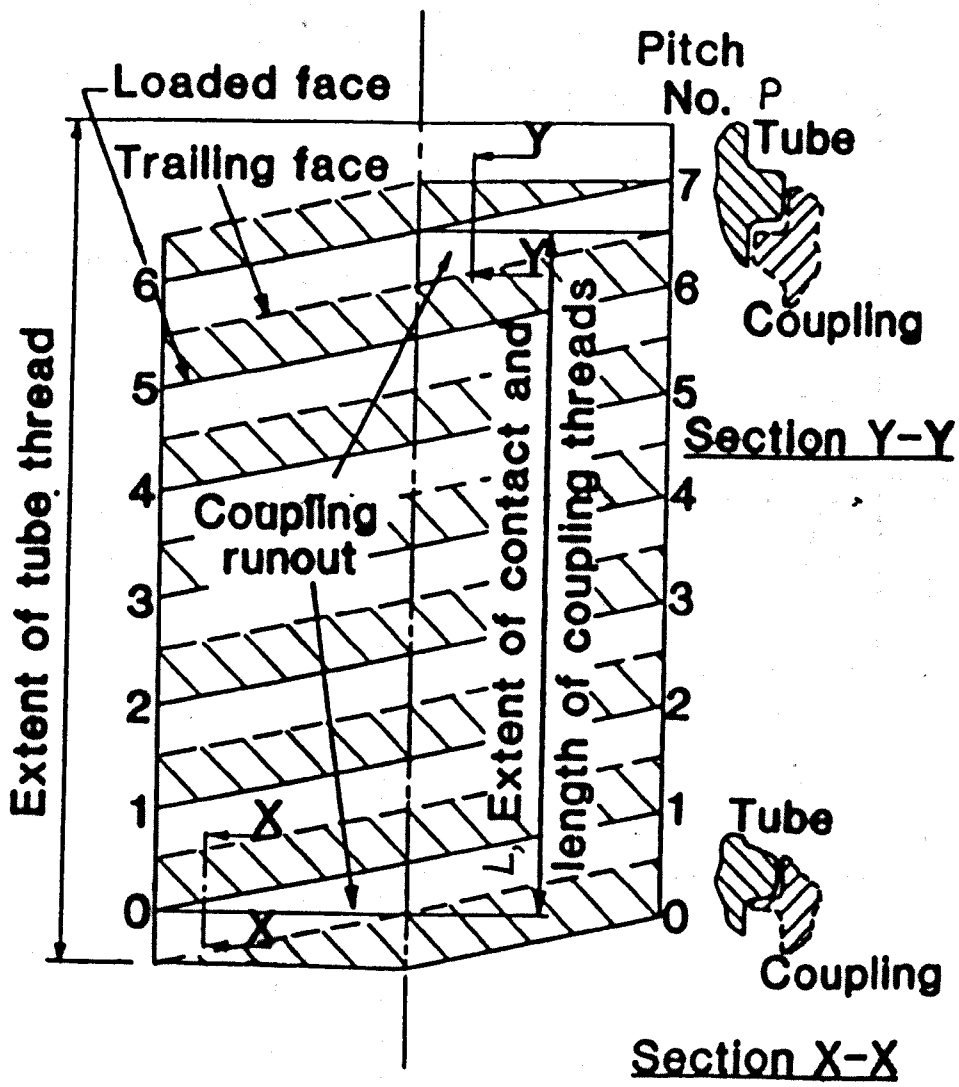

Fig. N2

Development of Threads

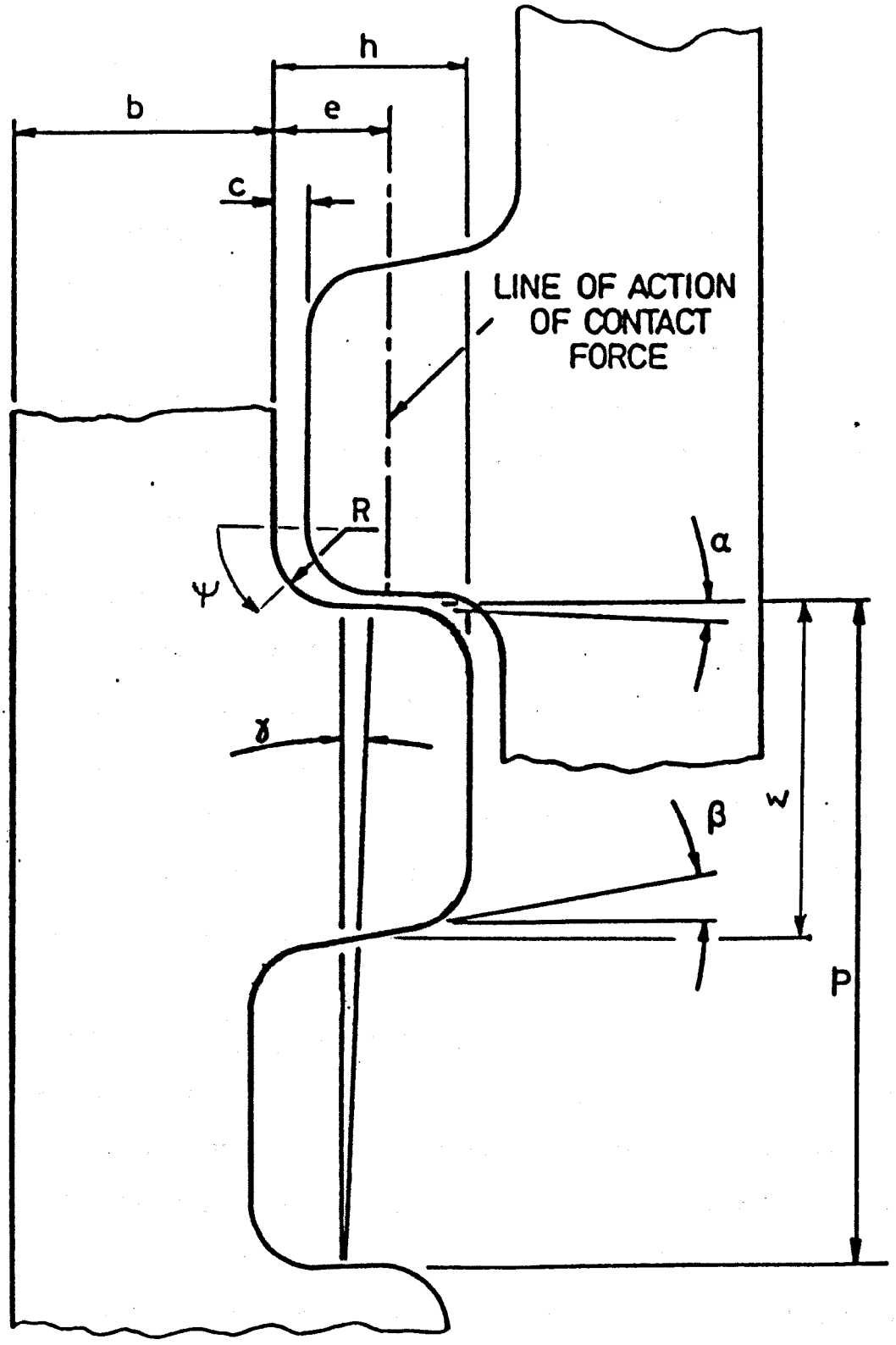

Fig. N3

Thread Parameters

CHAPTER ONE

INTRODUCTION

1.1 Objectives

The Tension Leg Platform (T.L.P.) is a novel design of oil producing platform for exploiting deep water and marginal offshore oil fields. The platform will be anchored to the sea bed, probably by large steel tubes, lengths of which will be connected together by screwed connections. In a thorough review of information on the fatigue of anchorage systems for the T.L.P, Webster (1) calls for either finite element or photoelastic testing of model connections to obtain data of which would be useful for determining fatigue initiation.

For this reason work has been carried out on the stress analysis of screwed connections for 'thin-walled' tubes. The results would be applicable to both thin-walled tether and riser connections. Using the linear elastic techniques of 3-dimensional 'frozen-stress' photoelasticity and some axisymmetric finite element analyses, the effect of thread parameters and loading modes on the stresses in the threads of tubular screwed connections were analysed.

1.2 General Introduction to the T.L.P.

The cost of fixed concrete or steel structures increases exponentially with water depth and severity of weather conditions. In general 150-220 m (2) water depth may be the practical limit for fixed structures in a harsh environment such as the North Sea. Several novel designs have been proposed to meet the requirements of deep water and marginal oil field production, for example articulated column, guyed tower, semi-submersible, tension leg platform (T.L.P). Several of these designs,

including semi-submersibles and T.L.P.'s, have the advantage that they can be moved from oil field to oil field as the oil reserves become exhausted.

The T.L.P concept was introduced in the 1960's (3). It is a positively buoyant, compliant, floating structure attached to the sea-bed by tethers. As a compliant structure it exhibits motion under loading and therefore experiences reduced loadings.

A prototype T.L.P. weighing 635 tonnes was installed in 200 ft of water off California by Deep Oil Technology in 1975 (4). This 1/3 scale model provided much information on responses of loads, motions and stresses due to wind and waves.

Fig. 1.1 shows a typical design of T.L.P. The structure can be considered to be made up of 3 major parts:-

i) the decks, including accommodation, drilling equipment, etc.

ii) the hull, consisting of columns and pontoons which provides the platform's buoyancy and rigid support for the decks.

iii) the mooring system, made up of the tension leg elements which connect the hull to the anchor template and piles via flexible joints.

The tension legs hold the platform down beneath its natural buoyancy in all weather and loading conditions, hence the tension legs effectively eliminate the vertical plane motions of heave, pitch and roll, while the lateral movements of surge, sway and yaw are compliantly restrained.

1.3 Types of Tether

The function of the tether is to anchor the floating hull of the T.L.P. to the seabed beneath its natural buoyancy level in order to provide the stability required to produce oil in the worst weather conditions.

Three main types of tether have been proposed:-

a) wire ropes (spiral or parallel stranded)

b) 'thin-walled' tubulars

c) 'thick-walled' tubulars

The large diameter wire ropes, which can be either parallel or spiral wound, would be made up of individual strands of typically 5-7 mm diameter 0.7% carbon steel rod. The ropes would be cold drawn with a tensile strength of 1500 N/mm^2.

In theory wire ropes can be made in any length but in practise the length and diameter are limited by the capacity of the manufacturing equipment, the rope weight for handling and transportation and the ability of the rope to be coiled.

Parallel stranded wire ropes are lighter than spiral stranded wire ropes for the same load carrying capacity, for example, 127 mm spiral stranded rope weighs 80 kg/m whilst parallel stranded rope of similar load carrying capacity weighs 50 kg/m. But the increased stiffness associated with large parallel stranded rope causes problems in coiling and transportation difficulties may limit their use. Spiral stranded rope has a relatively low Young's Modulus which would allow the T.L.P. both greater heave and limit its stability in deeper waters.

Both parallel and spiral wire ropes require end termination which are much stiffer than the rope itself and are likely to cause problems particularly if the ropes are subjected to bending.

It has been concluded (1) that wire rope tethering systems would not survive a 20 year design life. Improved detection systems would be required to measure individual strand breakages so that the ropes could be replaced before they are seriously weakened.

'Thin-walled' tubulars (wall thickness less than 60 mm) are based on drill pipes and casings which have been used for many years. Seamless tubes can be manufactured over a large range of diameters and strengths and would have outside diameter/wall thickness ratios in the range 5-14, in lengths of up to 10 m, however the length is reduced as the diameter/thickness ratio reduces.

'Thin-walled' tubulars can be chosen which are self-buoyant, this would be a distinct advantage in deep water application but the relatively low cross-sectional areas means low load carrying capacity hence more tethers therefore increased assembly time.

'Thick-walled' tubulars can be produced as either shaped forgings or parallel walled tubulars. The parallel walled tubulars can be produced by extrusion processes with almost any internal diameter greater than 150 mm and up to 10 m long for 80 mm wall thickness. Centrifugal casting could also be used but the maximum length is likely to be not more than 7m (1). Shaped forgings can be produced with very thick walls and have been used in Conoco's Hutton T.L.P. They have the advantage of greater load carrying capacity and fewer tethers are necessary. But they are heavier and self weight could be a problem especially for deeper water applications.

Because of the afore mentioned problems associated with wire ropes, it is likely that tubulars will be favoured for use as tethers.

1.4 Types of Connection for Tubular Tethers

Several different forms of tubular screwed connections have been proposed as well as welded and flanged connections. This work is concerned with screwed connections for tubulars.

Joining the tubular members by welding would probably have to be done on site. This would require specially designed equipment and the quality of weld would be difficult to achieve at sea. Post weld heat treatment would be impractical, hence the stress levels in and around the welds would be unknown. If the rig was required to be moved to a new site or if a leg was damaged it would be very difficult to unmake the connections. Hence it is unlikely that welded connections would be used.

Using flanged and bolted assemblies has advantages over welded connections. The flanges could be welded on to the tubes on-shore and the bolting up off-shore would be a relatively quick process. The main problem lies in the protection of the bolts which would have to be made of a high strength steel due to high tensile loads applied and hence would be prone to stress corrosion cracking.

The main advantages of screwed connections are that the assembly time is short and that the highly stressed regions, i.e. the threads, can be relatively easily protected from the sea. Although the thread manufacture will be to tight tolerances and of a complex nature, experience has been gained in the production of drill pipe and casing connections such as the VAM (5) joint.

There are several possible designs of screwed connection which relate primarily to the tube thickness, axial flexibility and buoyancy of the tether. Shaped forgings with 'upset' ends are likely to be screwed together via a 'pin and box' arrangement, see Fig 1.2. The large wall thickness allows male and female threads to be cut at opposite ends of the tube. Thinner tubes could also use this type of connection but would require the 'pins and boxes' to be welded onto the ends of the tubes.

Thin tubes could be connected using 'couplings', i.e. the tubes would have male or female threads at both ends and would be connected by short lengths of threaded coupling, see Fig. 1.3. This type of connection is similar to the VAM joint.

The thread roots may be rolled but due to the size of the threads and the small flank angles it is unlikely that the full shape would be rolled. The remainder or all of the thread would be machined by either a single point tool or by the quicker thread milling process.

1.5 Stress Analysis Techniques

To accurately measure the position and magnitudes of the peak stresses in a complicated 3-dimensional structure such as a screwed tubular joint, a technique is required which represents the true structure as faithfully as possible. Strain gauging is impractical since the peak stresses occur at inaccessible positions on the thread spiral. Using 3-dimensional finite element techniques it would be very costly to generate a mesh which would be sufficiently fine to give accurate stresses around the thread spiral. Axisymmetric finite elements are less costly and useful results can be obtained as to the relative merits of different thread shapes subjected to similar loads,

but accurate distributions of loads along the thread spiral requires a fine mesh for the complete structure in order to accurately model the stiffnesses. Using axisymmetric finite element techniques alone would not show the effects due to the thread spiral terminations. 3-dimensional photoelasticity allows accurate measurements of the distributions of loads and stresses to be made and has been used to analyse threaded connections with several different thread forms subjected to the different loads of preload only, tension only and preload plus tension.

Ten Araldite models were designed, manufactured, loaded and analysed photoelastically. Chapter 3 describes the design of each model. Briefly, the thread pitch p was kept constant throughout and the parameters R/p, b/p and L/p were varied. Also similar models were subjected separately to preload only, tension only or tension plus preload. The manufacture, loading and mechanical measurements of the models is described in Chapter 4 and the analysis techniques are described in Chapter 5.

Only a limited number of changes to the important parameters could be made using 3-dimensional photoelastic techniques. In order to extend the range of the parameters investigated, axisymmetric finite elements were used to analyse many different individual thread shapes. It is well understood that the stresses in a thread fillet are made up of those due to the tension carried beneath the thread plus those due to the shear forces applied directly to the thread. These two loading modes were investigated separately using finite elements and Chapter 6 describes the meshes and techniques used in the finite element analyses.

Chapter 7 describes the error analyses performed for the photoelastic and finite element techniques.

1.6 Results, Discussion and Conclusions

Chapter 8 gives the photoelastic and finite element results. These include the distributions of shear forces which were measured photoelastically around the thread spirals of several models. From these distributions equations for the distributions of shear force, wall forces, and wall stresses have been obtained for the loading modes of tension only, preload only and tension plus preload. Chapter 8 gives parametric equations for the stress distributions around the thread fillet for threads loaded with either wall forces, directly applied shear forces or both. The equations for the distributions of forces and the distribution of stresses have been used to calculate the distribution of peak fillet stresses for threaded connections with similar shapes and loads to the photoelastic models. These calculated stresses have been compared with the photoelastically measured peak fillet stresses.

The equations developed in Chapter 8 have been used to examine the effect on peak fillet stresses of varying individual thread parameters in Chapter 9.

The effect of likely maximum and minimum axial tensions on the peak fillet stresses in a preloaded connection and hence the maximum stress ranges in any fatigue cycle have been calculated and their effect on the fatigue analysis has also been discussed in Chapter 9. Other design considerations and limitations and their effect on thread design and stresses are considered.

Chapter 10, the Conclusions, reviews the most important results and makes recommendations for the design of screwed tubular connections.

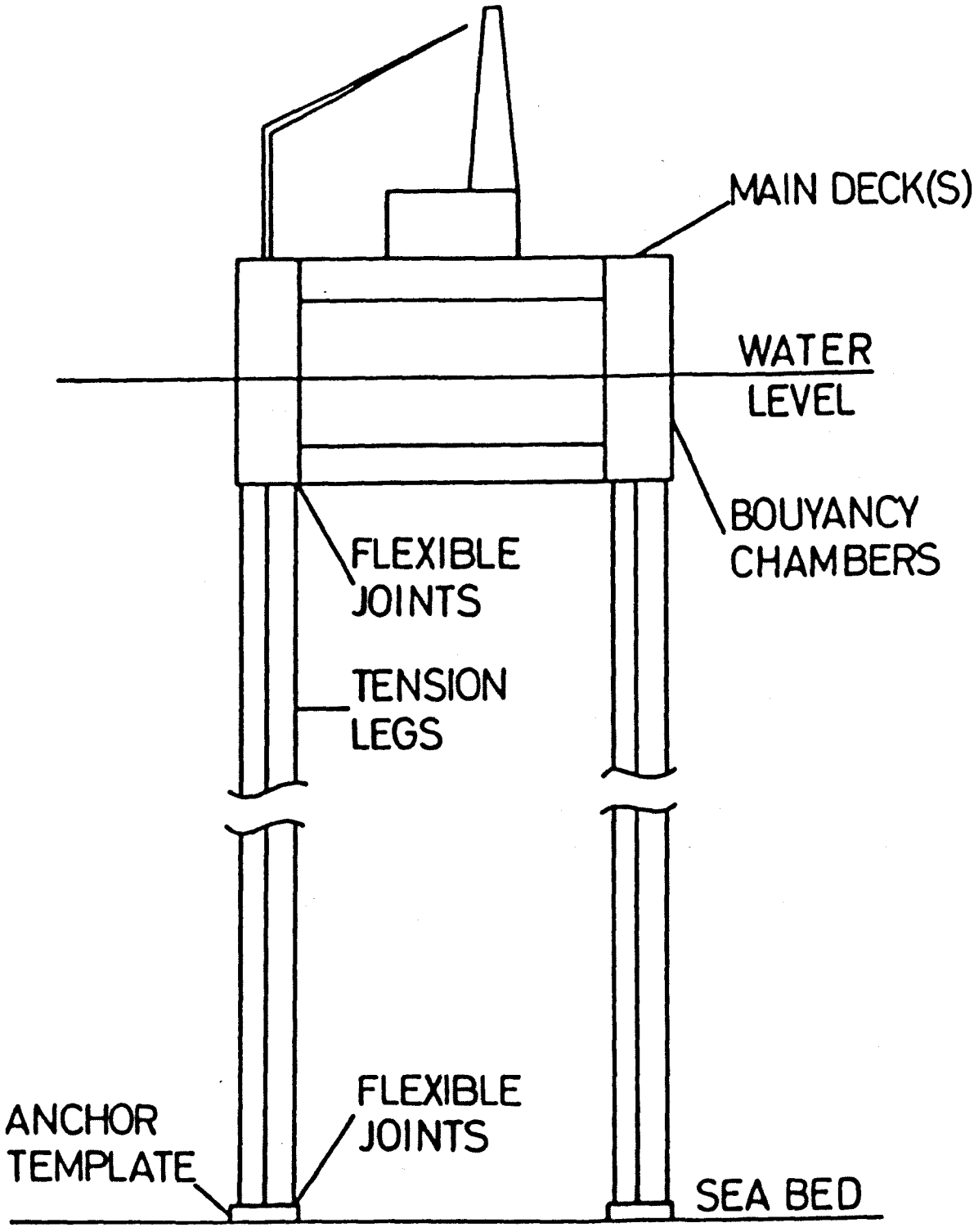

Fig. 1.1

Main Features of a Typical Tension Leg Platform

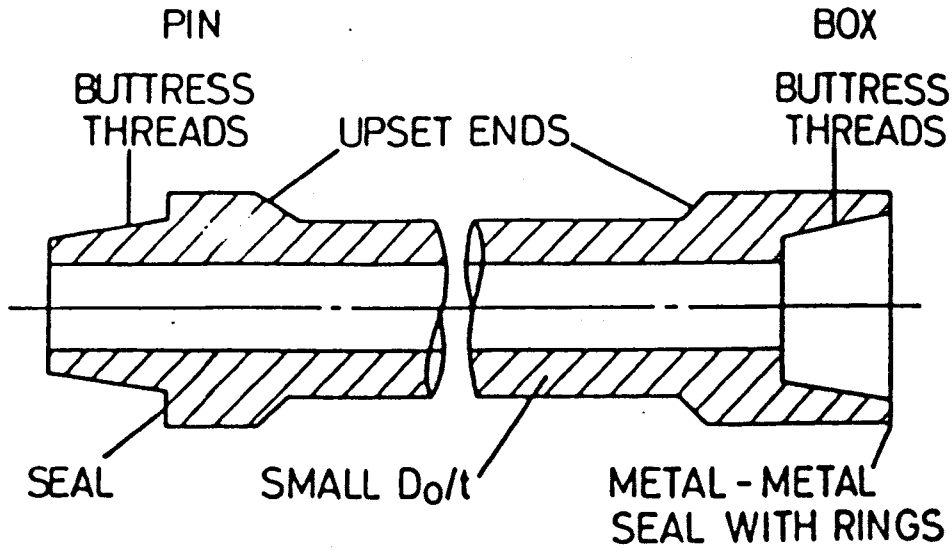

Fig. 1.2 Typical Pin And Box Screwed Connection

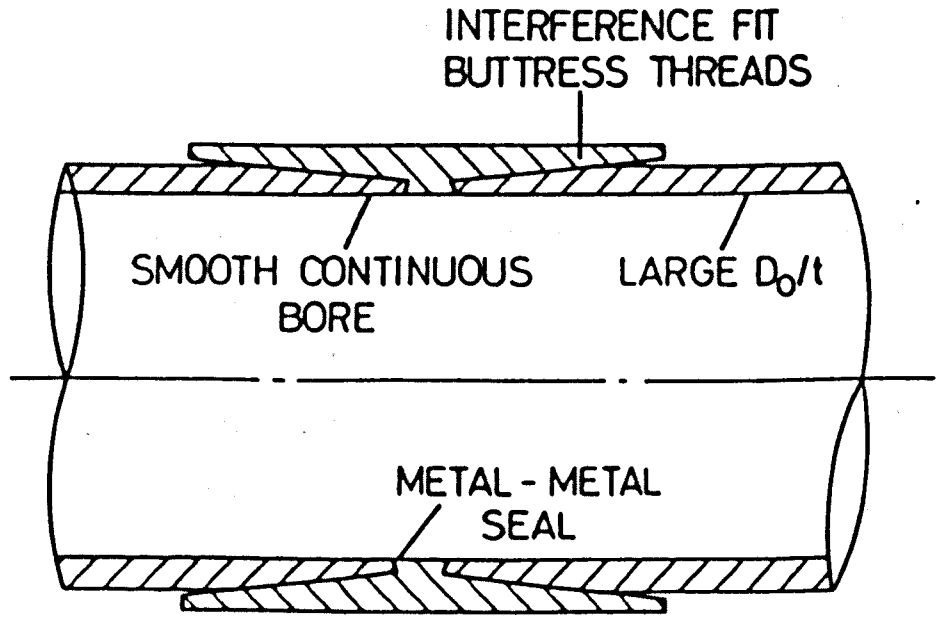

Fig. 1.3 Typical Pipeline Screwed Connection

CHAPTER TWO

LITERATURE REVIEW

2.1 Introduction

The concept of the T.L.P. has evolved from semi-submersible floating vessels which are used to drill exploratory wells. Much of the technology employed in the T.L.P. is based on existing experience gained from semi-submersibles and conventional rig design. But one of the novel parts of the T.L.P. is the tether system proposed and the screwed connections which are likely to be used to connect the lengths of tubes which will be used as tethers.

Prior to about 1980 there was a lack of data useful to the designer of a tubular screwed connection. However, research on screw threads, bolted connections, gear teeth and other loaded projections as well as experience gained in-service with well-riser screwed connections did provide qualitative information. This lack of data was highlighted by Webster et. al. (1). In response to the introduction by Conoco of the Hutton Field T.L.P. work has been carried out into the design of tubular screwed connections, the majority of which are axisymmetric Finite Element Analyses of design similar to the 'pin and box' used in the Hutton T.L.P. (6,7,8,9). Although such results are useful they are generally only for individual thread shapes or a limited number of shape changes and no thorough parametric investigation of the thread form has been carried out.

The research reported on in this work (and that carried out by Glinka and others (10)) is a parametric analysis of the thread shape and tether loads on the peak stresses found in these screwed connections.

2.2 Techniques for the Stress Analysis of Screwed Tubular Connections

Skilbeck et. al. (6) in their paper describing the design and manufacture of the only operating T.L.P. refer to a hybrid design process incorporating finite element analysis and 3-d photoelastic modelling of the prototype screwed connections. Although no results are presented, the paper does give an indication of the processes required for a thorough analysis of a given design.

Most stress analyses of screwed connections for T.L.P's have used axisymmetric finite elements. Dutta and Wendler (7) analysed thin-walled seamless tubular screwed connections using axisymmetric 8-noded-ring elements. The rotationally symmetrical loadings of tension and preload could be applied and bending could also be applied by the use of a Fourier series. Although a section of the complete connection was modelled, it could be seen that the mesh was coarse which may have led to underestimates of the peak stresses (see Ref 8).

Crose et. al. (12) have used axisymmetric finite elements to model the elastic and elastic-plastic stresses in buttress threaded casing connections loaded with preloaded plus compression and preload plus tension.

Sakaguchi, et. al. (8) analysed a similar type of joint to Dutta and Wendler (7) initially with a similar mesh density,however by increasing the mesh density in the vicinity of the thread fillet they measured increases in fillet stresses of the order of 25%.

In order to get around the problem of coarse meshes, Glinka, Dover and Topp (10) have used a mixed Finite Element- Analogue method. Finite Elements were used to calculate the local stress concentration factor and stiffness of each thread in the connection. The measured

stiffnesses were then used in an electrical analogue to determine the load distributions. From the load distributions and the local stress concentrations, the peak fillet stress distributions have been calculated.

The only practical alternative to Finite Elements is photoelasticity. The only photoelastic analysis of tether screwed connections which has been carried out to the authors' knowledge is that reported by Skilbeck et. al. (6) but no details were given in the paper. The techniques employed in the photoelastic analysis of complicated structures are well reported, (13,14). Several types of screwed connections have been analysed using 3-dimensional photoelasticity. Marino and Riley (15) used both 3 and 2 dimensional photoelastic techniques to study the stresses in the fillets and roots of sectored buttress threads which were used to connect the tubular components of pressure vessels. There have been several analyses of bolted connections using 3-dimensional photoelasticity (16,17). Kenny and Patterson (16) analysed full scale machined Araldite models of 30 mm I.S.O. nuts and bolts using a fringe multiplying polariscope. The load distribution in the thread was found by measuring and integrating the shear stresses parallel to the bolt axis along a line joining the roots of the threads. Fessler and Wang (17) analysed the stresses in bolts and tapped holes in axisymmetric blocks. The thread types analysed were 1 in. BSW and M36.

Fessler, Marston and Ollerton (18) have developed an Automatic Micropolariscope (A.M.P.). which has been used to take many of the photoelastic readings required for the thorough analysis of the screwed tubular connections. The A.M.P. has been designed to take photoelastic measurements of sufficient accuracy so that the Frocht shear difference method (19) could be used to analyse three-dimensional stress fields.

The accuracy of the measurements of fractional fringe orders to ± 0.0001 fringes, isoclinic angle to ± 0.08° and positional accuracy of the measurements of ± 0.002 mm, also allowed the measurements to be made of stresses around thread fillets.

2.3 Screwed Tubular Connections

The majority of screwed connections analysed have buttress threads which are based upon the API buttress thread (20). Although many of the thread parameters were changed, the important parameter, α (i.e. loaded face angle) was generally small so as to minimise tube wall bending and hence reduce the tendency of the threads to disengage under high axial loads. The most obvious aspect of the API buttress thread is the small fillet radii, only 0.008 in. With a pitch of 0.200 in. and a thread height of 0.062 in., the fatigue performance of the thread could be most easily improved by increasing the radii.

No published work has developed parametric equations for the thread fillet stresses found in screwed tubular joints. Generally the published work has dealt with screwed tubular joints with upset ends similar to Conoco's Hutton T.L.P. (6). The peak fillet stress values presented have usually been normalised by the stress in the wall beneath the thread. This normalising stress may be due to both tension and preload. So that comparisons can be made with the author's results presented in Chapter 8 the published fillet stresses have been presented here as normalised by the mean tensile stress due to tension only which would have occurred in a tube with wall thickness = $b_{max}+h$ (i.e. the same wall thickness as the author's tube models).

Dutta and Wendler (7) analysed one design of thin walled seamless tubular screwed connections with upset ends using axisymmetric finite elements. They also dealt with the development of suitable high strength steels. The connection design consisted of 20 inches diameter, 1 inch wall thickness tubes which were upset at the ends to a wall thickness of 1.65 inches in order to accommodate male threads with a large cone angle which were cut at each end. Short couplings with female threads and wall thicknesses in the threaded regions similar to the tubes were used to connect tube to tube. The important thread parameters in the region of the most highly loaded tube thread were b_{max} = 1.25 in., p/b_{max} = 0.263, h/b_{max} = 0.069, $\alpha = 0^{o}, \beta = 30^{o}, \gamma = 7.6^{o}$. The thread fillet radius was not given and from a private communication (11) Mr Dutta stated 'The radii of the threads were very small and for the F.E. analysis were taken to be zero'.

From the above communication (11) mesh details were also given which indicated that the mesh could be considered coarse. Similar coarse meshes were used by Sakaguchi et. al. (8) and gave peak stresses which were 25% lower than fine meshes. Two preload magnitudes were considered by Dutta and Wendler for the same axial tension. The smaller preload was considered insufficient to adequately seal the joint. This effectively tension only loading led to peak fillet stresses of 4 while the tension plus preload loading led to a peak normalised fillet stress of 8.2. These stresses were normalised by the stress due to tension only in a tube of wall thickness $b_{max} + h$. Both of these stress values seem low considering the size and shape of the threads.

Sakaguchi et. al. (8) analysed pin and box-type connections using axisymmetric finite elements. V threads were analysed and the parameters p, γ and $\alpha = \beta$ were altered and the fillet stresses found for the tension

only loading case. The results presented showed that changing $\alpha = \beta$ had a negligible effect on peak fillet stresses, also large increases in peak fillet stresses were observed for $p/b < 0.25$ while for $p/b \geq 0.25$ peak fillet stresses were little altered and increasing the thread taper γ from 4.8° to 14.0° increased the peak fillet stresses.

The 'best' thread form was then loaded with preload only and preload plus tension. This 'best' thread form had $\alpha = \beta = 30^{\circ}$, $\gamma = 9.5^{\circ}$, $p/b_{max} = 0.25$ and $R/b_{max} = 0.04$. When normalised by the mean stress due to tension only in the pin undercut, the peak normalised fillet stresses were 7.4 due to tension only and 11.2 due to tension plus preload. The pin was the half of the connection where the preload gave tensile wall stresses. Sakaguchi et al also showed that fine meshes are required around thread fillets in order to accurately obtain the peak fillet stress. A fatigue life assessment was then carried out for the 'best' design of thread using the class B D.N.V. S-N curve (21). The predicted life was found to exceed the 20 year design life.

Glinka et. al. (10) presented thread shear force, wall force and peak fillet stress distributions for buttress threads with different thread radii in a connection loaded with axial tension only which was similar in shape to those in the Hutton T.L.P. The important thread parameters were $p/b_{max} \sim 0.133$, $h/b_{max} \sim 0.0411$, $\alpha \sim 3^{\circ}, \alpha \sim 0^{\circ}, \beta \sim 10^{\circ}$ and the three radii considered $R/b_{max} = 0.021$, 0.010 and 0.005. These different radii gave maximum peak normalisd fillet stresses of 4.0, 5.2 and 7.0 respectively. For all three thread shapes the distribution of peak normalised fillet stresses were symmetrical about $z/L=0.5$. The shear force distributions were similar for the three thread shapes and concentrated near the end of the male threaded component (the pin) with

the thicker wall and $V_{max}/V_{mean} \sim 4$. The male component had a taper on the unthreaded surface which also reduced the wall thickness in the same way as the thread taper.

Glinka (22) has proposed the equation

$$\sigma_y = \frac{\hat{\sigma}_y}{2\sqrt{2}} \left[\left(\frac{R}{r_f - R/2} \right)^{1/2} + \frac{1}{2} \left(\frac{R}{r_f - R/2} \right)^{3/2} \right] \quad \ldots\ldots 2.1$$

for the stress σ_y at a distance $r_f - R$ from the position on the thread fillet surface where the peak fillet stress $\hat{\sigma}_y$ occurs (see Fig. 2.1.) Distributions of stress obtained using Finite Elements in Ref. 10 show good agreement with Equation 2.1 up to 2 radii from the fillet surface.

Marino and Riley (15) analysed photoelastically 3/8 inch pitch buttress threads with different radii used in closed ended pressure vessels loaded with interval pressure. The important features of the threads analysed were $p/b \sim 0.55$, $h/b \sim 0.3$, $\alpha \sim 5^\circ$, $\beta \sim 45^\circ$, $\gamma = 0^\circ$ and R/b was varied from 0.04 to 0.07. As a result a reduction of approximately 20% in the peak fillet stresses was observed. Marino and Riley also observed that decreases in peak fillet stresses in the most highly stressed first thread could be obtained by having large radii ($R/b = 0.175$) between the first thread and the undercut, despite the reductions in cross-sectional area of the undercut.

2.4 Experimental and Theoretical Analyses of Threads and other Thread-Like Projections

Heywood (23) made use of Neuber's work on stress concentrations in grooves (24), Sopwith's analysis of the load distribution along the thread helix (25) and his own work (26,27) in order to calculate the peak fillet stresses in nut and bolt connections. This method considers the effect of wall tension and thread load separately and shows that the positions of the peak fillet stresses are different for the two loading

positions of the peak fillet stresses are different for the two loading modes. He proposes the empirical relationship

$$\hat{\sigma}_L = \hat{\sigma}_a + \frac{\hat{\sigma}_F}{1 + C\frac{\hat{\sigma}_a}{\hat{\sigma}_F}} \quad \ldots\ldots \quad 2.2$$

where $\hat{\sigma}_L$, $\hat{\sigma}_a$ and $\hat{\sigma}_F$ are the peak fillet stresses due to combined loading, wall tension only and shear force only and C is a constant which depends on the thread shape. Equation 2.2 is similar to empirical equations developed by the author and presented in Chapter 8 in the fact that the peak fillet stress due to combined loading is less than the sum of the peak fillet stresses due to wall tension only and shear force only.

The Sopwith analysis (25) primarily deals with the distribution of load in nuts and bolts (i.e. where the tension in the bolt is reacted by compression in the nut, this situation is similar to preload of the screwed tubular connections considered in this work). The thread form considered by Sopwith was the symmetrical V thread and although the buttress thread was considered by Sopwith, in the interest of paper saving during the immediate post-war period it was necessary to omit the work on buttress threads. The elastic analysis considered the different strains in the nut and bolt threads due to the loads applied to them and the axial separation of the threads caused by these strains. Since contact is maintained in the threads the separation is equal to the strains. Sopwith shows that for nuts and bolts the load concentration factor H is a function of p/D_m, L/D_m, size of nut D_o/D_m, the size of any hole in the bolt D_i/D_m, the thread angle $\alpha = \beta$, the depth factor and the coefficient of friction. Kenny and Patterson (16) showed photoelastically measured shear force distributions in V threads which agreed closely with Sopwith's analysis.

Heywood (26) proposed the empirical equation based on 2-dimensional photoelastic work.

$$\hat{\sigma}_L = \left[1 + 0.26\left(\frac{g}{R}\right)^{0.7}\right]\left[\frac{1.5u}{g^2} + \sqrt{\frac{0.36}{jg}\left(1 + \frac{1}{4}\sin\rho\right)}\right]\frac{V}{s} \quad \ldots \quad 2.3$$

The dimensions $\alpha, g, j,$ u and R are defined in Fig. 2.2 and V/s is the shear force per unit length of engagement. For the special case of the buttress threads examined by the author where $\alpha = \beta$, $\rho = 0$ and the symbols used by the author are substituted into Equation 2.3, then the Equation

$$\hat{\sigma}_L = a(b + c)d \quad \ldots\ldots \quad 2.4$$

where

$$a = 1 + 0.26\left(\frac{\frac{w}{2} + 0.293R}{R}\right)^{0.7}$$

$$b = 1.5\,\frac{\left(\frac{h}{2} - 0.293R\right)}{\left(\frac{w}{2} + 0.293R\right)^2}$$

$$c = \sqrt{\frac{0.36}{\left(\frac{h}{2} - 0.293R\right)\left(\frac{w}{2} + 0.293R\right)}}$$

$$d = \frac{1}{\pi\left(D_i + 2b + 2e\right)}$$

is developed.

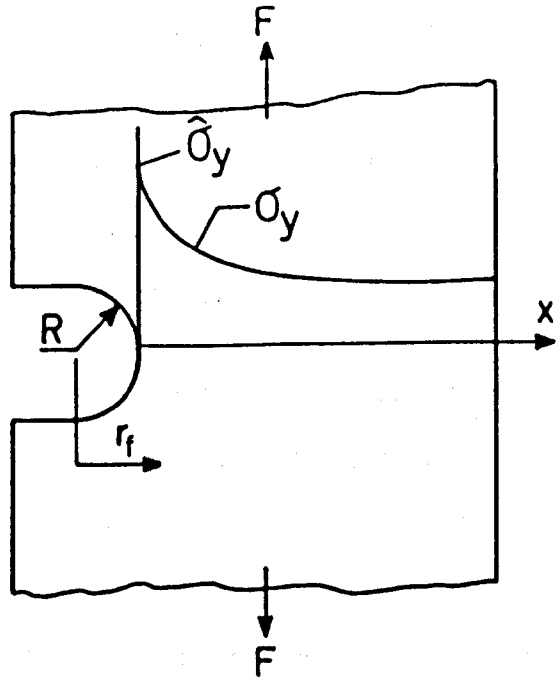

Fig. 2.1 - Stress Distribution Ahead of a Notch Tip, From Glinka (22)

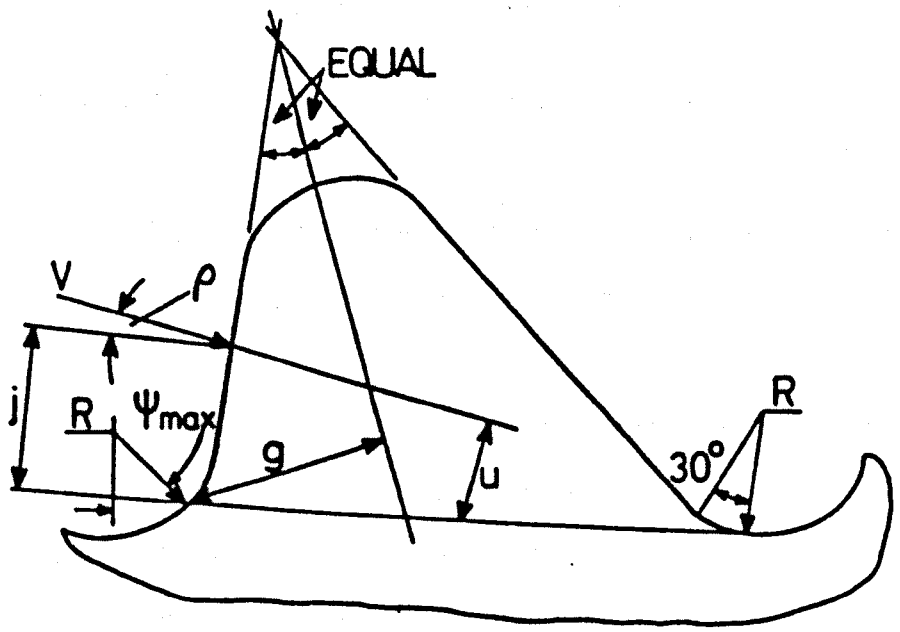

Fig. 2.2 - Dimensions Used for Calculating Fillet Stress Using Heywood's Formula

CHAPTER THREE

SCREWED CONNECTION SHAPES, THREAD SHAPES AND LOADING

3.1 Introduction

The main application of the work is for the tubular screwed connections of tension legs of offshore platforms, but it may also be relevant to drill pipes and risers.

'Thin' walled tubular screwed connections with Do/t ratios in the range 10 to 12 have been analysed. The 3-d photoelastic connections model 'thin' walled tubes with female threads cut at both ends. These tubes would be connected by short thicker-walled and smaller-inside-diameter couplings which have male threads cut at each end (see Fig. 3.1).

The couplings had the same outside diameter as the tubes which allowed the seals to be simply machined into the connection.

This type of arrangement has several advantages:-

i) the more easily protected female threads are the more expensive and less easily transportable main tubular members,

ii) the tubular members do not need thicker sections at the ends since male and female threads do not need to be cut at opposite ends, hence they would not need to be forged or to have forgings welded on to plain tubes,

iii) there are no external protrusions on the tension leg.

The likely prototype tube sizes and the largest practicable model sizes are:-

Dimension or ratio	D_o	t	D_o/t
Prototype, in.	48	2.5	20
Model, in.	10	1	10
Scale ratio	1/5	2/5	-

Because prototype and model are thin-walled tubes, the stress concentrations at the threads depend much more on the ratio of thread size to wall thickness than thread size to diameter. The model wall thickness was the smallest which gives conveniently large thread fillet radii. The difference in D_o/t ratios between model and prototype was not important and the results are applicable to a wide range of prototype D_o/t ratios. To make the analysis simpler it was decided to make the tube and coupling p/b_{max} ratios equal.

3.2 Photoelastic Model Sizes and Shapes

A 3-d model arrangement is shown in Fig. 3.1. Because the prototype coupling was symmetrical and to save time and cost, the model contained only one threaded connection; the other connection was replaced by a solid 'dummy'. The 'dummy' had the same internal diameter, external diameter and axial length as the threaded part of the connection. The 'dummy' also modelled the groove formed by the coupling undercut. This 'dummy' groove was vented to the outside by a small hole which prevented gas pressure building up during the heating cycle required for model loading. The threaded tube and 'dummy' coupling were joined to re-usable extension tubes. The extension tubes were long enough to be effectively infinite and the same dimensions as the unthreaded tubes. The ends of the extension tubes were closed by

end plates (approximately 2t thick) through which loads were applied. Changes in section of the unthreaded parts were accomplished by large radii which minimised any stress concentrations. The complete model length and the size of available ovens determined D_o, the outside diameter of the tubes. The wall thickness t was the greatest which could be considered as 'thin'. The thread size was determined by the fillet radius R = 1/16in; this was the smallest photoelastically convenient value.

Previous work (25) has shown load concentrations at the ends of screwed connections. The lengths of engagement was made long enough to ensure that these load concentrations did not influence each other. Due to the time and cost involved in manufacture the minimum number of threads was used. It was decided that a minimum of 6 fully engaged pitches would be required. Having few pitches also has the advantage, in service, of reducing assembly time.

3.3 Thread Shapes

Thin-walled tubes, joined by screwed connections, have been used for many years for drill pipes or casing applications. They usually have tapered API (20) or similar buttress threads with an interference fit between the male and female components to help sealing when fully tightened. The threads are 'tapered' (i.e. constant thread profile cut into conical blanks) because this shape is easier to assemble and considered stronger than 'parallel' threads.

The API buttress thread has different profiles for the male and female components. But to simplify manufacture and the analysis of the results, both tube and coupling models have the same thread profile in any joint.

The thread form, shown in Fig. N3 may be defined by the pitch p, thread height h, fillet radii R, distance of resultant contact force from root e, the thickness of the tube at the root of the 1st thread b_{max}, the loaded flank angle α and the unloaded flank angle β. The tip and root surfaces of the threads were cylindrical of varying radius to fit the cone angle. This also simplified machining and measurements.

From general considerations of stresses in cantilevers and from published information (28) it was concluded that the pitch p should be as large as possible. It was chosen as the basic thread dimension and was kept constant at 5/8 in. for all 3-d models. Imperial units have often been used since the best screw cutting lathe was imperial.

For Models 1 to 4 the loaded flank angle was reduced from the API value of 3° to 0° to eliminate the component of contact force pushing the threads out of engagement. These models were machined from rough castings but Models 5 to 10 were all cast precisely, and no machining was performed on the thread. In order to ease extraction of the precision cast models from the moulds and cores a 3° loaded face angle was introduced.

The unloaded flank angle β may have affected the flexibility of the thread to some extent. The API value $\beta = 10^{\circ}$ was used throughout. The cone angle γ was limited by the minimum wall thickness at the thin end of the tubes and couplings. In the absence of any knowledge of the effect of cone angle on the stress distribution, the same radial cone angle $\gamma = 2.38^{\circ}$ as used for the API thread form was specified for all the models.

The API thread and the most widely used design of drill casing screwed connection (5) have interference fit threads in order to seal

the joint. T.L.P. screwed connections are likely to use other means of sealing. The screwed connections may be assembled and disassembled several times during their life and galling may occur if interference-fit threads are used. For the above reasons and to minimise friction the photoelastic models were all designed to have clearance between the unloaded flanks and a radial clearance when fully tightened. Since there was a clearance between the unloaded flanks of the thread, the thread width w, measured at mid thread height, was slightly less than p/2.

The thread height h was minimised to reduce the nominal 'cantilever' bending stresses in the threads. It was determined by the root and crest radii and the minimum width of flat nominal contact. For identical threads in contact, with crest radius equal to the root radius, the minimum width of contact is (h - 2R - c), where c is the radial clearance of the threads. A small width of flat surface is essential for practicable machining, accurate measurement of pitch extension and to minimise contact stresses. The nominal distance of the centre of contact from the root of thread, e = (h+c)/2 for identical threads in contact with each other.

The thickness b of the tube and coupling at the thread root varies for taper threads. The maximum value within the thread contact b_{max} has been used to characterise the thread shape. For tube models, at a distance z from the start of thread contact, the wall thickness $b = b_{max} - z \tan\gamma$. For coupling models, if the total axial length of contact = L, then at a distance z from the start of contact $b = b_{max} - (L-z) \tan\gamma$.

The fillet radii of the threads have been greatly increased over the API value and several different values of R have been analysed. To

minimise machining of the tubes, the diameter of the crest of the first tube thread is the largest bore which can be 'cleaned up' (machined to a complete conical surface) and equals $D_o - 2t$. As shown in Fig. 3.2 an undercut is bored at the start of the thread for the screw cutting tool to 'run into'. This should be cheaper than the gradual run-out of many increasingly more shallow threads specified by API, but either could be used.

At the other end of the tube, the threads continue beyond the extent of contact and are machined off at a z = constant plane. The tube threads extend beyond the coupling threads at both ends of contact, hence the length of coupling threads L, defines the axial length of contact.

To simplify and minimise machining, the coupling threads were machined off at the planes z = 0 and z = L. At the z = L plane, the loaded flank of the thread was machined away from w = p/2 to w = 0, over 180^o which meant that thread contact stopped abruptly when w became $< p/2$. Having this type of runout at z = L allowed the seal region to be machined close to the threads. At the z = 0 plane, the unloaded flank of the thread was machined away over 180^o which meant that the runout thread was in contact until w = 0. This loaded runout was shown to give high fillet stresses as $w \rightarrow 0$ and the thread bending stiffness reduced. The extent of the loaded runout was reduced to varying degrees for Models 5 to 10 by milling away the end of the runout.

It should be noted that the datums of z = 0 and P = 0 were always at the start of contact.

The thread parameters likely to have the biggest influence on the peak fillet stresses in the connection are R/b, w/b and e/b. b has been

chosen as the normalising parameter, so that comparisons with other published work (7, 8, 10) can be easily made. It also seemed likely that the length of contact L would influence the load distribution. Table 3.1 shows the important thread parameters of the models investigated.

Table 3.1 Photoelastic Model Parameters (defined in Fig. N3)

MODEL NUMBER	b_{max} (mm)	$\frac{R}{b_{max}}$	$\frac{p}{b_{max}}$	$\frac{h}{b_{max}}$	$\frac{L}{p}$	EXTENT OF LOADED RUNOUT, ^{o}	LOADING
1 TUBE	20.85	0.076	0.76	0.228	6.5	-	TENSION
1 COUPLING	20.05	0.079	0.79	0.238		180	"
2 TUBE	20.85	0.076	0.76	0.228	"	-	ECCENTRIC
2 COUPLING	20.15	0.079	0.79	0.237		180	TENSION
3 TUBE	15.7	0.101	1.01	0.303	"	-	TENSION
3 COUPLING	15.3	0.103	1.04	0.311		180	
4 TUBE	20.2	0.096	0.79	0.294	"	-	TENSION
4 COUPLING	20.4	0.095	0.78	"		180	
5 TUBE	14.7	0.162	1.08	0.390	6.17	-	TENSION
5 COUPLING	"	"	"	"		60	
6 TUBE	14.45	0.165	1.10	0.405	"	-	TENSION
6 COUPLING	14.8	0.161	1.07	0.395		60	
7 TUBE	14.7	0.162	1.08	0.390	"	-	PRELOAD
7 COUPLING	14.8	0.161	1.07	0.395		60	
8 TUBE	14.32	0.166	1.11	0.408	7.75	-	TENSION
8 COUPLING	15.05	0.158	1.06	0.388		60	+PRELOAD
9 TUBE	19.55	0.122	0.81	0.299	7.54	-	TENSION
9 COUPLING	20.7	0.115	0.77	0.283		120	+PRELOAD
10 TUBE	20.8	0.114	0.76	0.281	7.75	-	PRELOAD
10 COUPLING	20.9	"	"	0.280		120	

$\beta = 10^{o}$, $\gamma = 2.38^{o}$, Models 1 to 4 $\alpha = 0^{o}$, Model 5 to 10 $\alpha = 3^{o}$.

Taking Model 4 as the basic design the effect of decreasing R/b_{max} was investigated with Model 1. The effect of increasing p/b_{max} was investigated with Model 3. The effect of increasing R/b_{max} and p/b_{max} was investigated with Model 5. The effect of increasing R/b_{max} and L/p was investigated with Models 8, 9 and 10. The thread runouts of Models 6 to 8 were similar to Model 5. Thread fillet stresses in Models 1 to 4 showed that peak model stresses occurred in the loaded coupling runout as $w \to 0$. To remove this, the coupling thread runout near P = 0 was removed between w = 0 and w = p/6 for Models 5 to 8.

The fillet stresses and thread load distributions of Models 1 to 5 showed concentrations of both load and fillet stresses at the ends of contact. Model 6 was intended to reduce these concentrations. It was identical to Model 5 except for annular grooves as shown in Fig 3.3. The grooves were intended to reduce the axial stiffness of the regions which were in contact with the most highly loaded threads. It was hoped that increased axial strains in these grooved regions would reduce the thread load. The model was loaded in axial tension.

Models 7 and 10, which were identical to Models 6 and 9 were loaded with tightening torque only to investigate the effect of pre-load. Thread friction tests were also carried out on Model 7.

3.4 Prototype and Model Loading Modes

The environmental loads on the TLP tethers will be tension, bending and pressure. All can be modelled, but pressure is least important because it is unlikely to cause stress concentrations (its effect can be estimated using Lamé theory). External pressure will be due to the sea and internal pressure may be needed for a tether release mechanism.

If flexible joints are used at the ends of the legs, bending stresses are expected to be no more than 1/7 of the tensile stresses (1) and are mainly caused by wind, waves and currents acting in different directions. Although the magnitude of the bending stresses are likely to be relatively small, the effect will be important since peak fillet stresses, peak thread loads and loss of seal integrity are likely to occur in the plane of highest tensile stresses due to the bending.

Tension will be the major environmental load. In a dead calm sea, the naturally bouyant platforms would be held beneath its natural bouyancy level. Hence the tension per leg

$$= \frac{\text{excess platform bouyancy}}{\text{no of legs}} - \text{leg weight}$$

and the legs will be vertical.

Under the action of wind, waves and currents, the platform will drift from the vertical. As it does so, the hull will be dragged deeper, hence increasing the excess bouyancy and the tether tension. In addition to this slow variation the tether tension will also vary with the rise and fall of each wave. Hence the relevance of fatigue analysis. The loads on the connection will be the above and the applied tightening (or loosening) torque. This would preload the joint to ensure sealing under all service conditions. The majority of proposed designs rely on a precompressed metal to metal seal as the primary method of keeping sea water from the thread region. Hence contact must be maintained in this seal under the most severe loading conditions. The compression in the seal will be applied in the prototype legs and has been applied in the photoelastic models by screwing the 2 halves of

the connection together until there was initial contact in the seal, then the connection was screwed a further set relative angular displacement. This tightening torque caused initial tension in the coupling and compression in the tube end. Axial tension of the tether increased the tension in the coupling and reduced the initial compression of the tube.

The photoelastic model test program was designed to investigate the effect on fillet stress distributions and thread shear force distribution of both thread shape and loading modes. Table 3.1 defines both the shapes and the loading modes applied to each model analysed. An exaggerated bending was applied to Model 2, which in all other respects was identical to Model 1. It was assumed that the distribution of thread load and wall stresses due to preload could be superimposed upon those due to axial tension.

In order to obtain the distributions of thread load and wall stresses due to preload, Model 7 and Model 10 were loaded with preload only. Models 6 and 9 which were identical to Models 7 and 10 were loaded with tension and preload.

3.5 Sealing of Models

Unlike the modified VAM joints (29) it was decided to model a metal-to-metal seal at the OUTSIDE of the tubes, because

a) this does not rely on an 'O' ring or other radial seal to prevent seawater attack of the threads

b) a reliable, metal-to-metal, external seal removes the need for interference of the threads to act as a secondary seal. Such interference could lead to damage of threads which may have to be tightened many times if the leg is moved.

c) the absence of a gap or soft filling at the outside gives the stiffest possible connection

d) threads on the inside of the large components are less likely to be damaged in transit and assembly.

e) a smooth cylindrical outside assists underwater inspection.

As shown in Fig. 3.4 Models 1 to 4 the main external seal was formed by a conical lip or projection on the coupling (the smaller, more easily protected and replaced part) which was forced outwards by the mismatch of cone angles. The expansion of this lip was limited by the initial clearance. When the coupling was fully tightened, this clearance was taken up and a second seal was formed on the inner, 60^{o} cone. Using this type of seal lower values of torque would be required to produce the preload necessary. The angle of relative twist would be set by the initial seal clearance c_s. The tube 'belling out' under load would also increase the contact stresses in the lip and the effectiveness of the seal. A further advantage of this type of seal is that the coupling lip would tend to centre the tube hence preventing variations in thread radial clearance which could lead to greater than expected fillet stresses due to increased thread couples in the plane of greatest thread clearance.

It has been shown (30) that the conical seals of the type made in Models 1, 2, 3 and 4 are likely to fail due to fretting, because of the relative movement of mating parts during a fatigue cycle. Since the seal design does not affect the fillet stresses, it was decided that the seal regions of Models 5 to 10 would be as simple as possible but still model a realistic prototype structure; both the tube and coupling seal surfaces were made perpendicular to the model axes (see Fig. 3.4)

Table 3.2 shows the important features of the seals of the models analysed.

Table 3.2 Model Seal Features

	Model				
Seal Features	1	2	3	4	5 to 10
TUBE SEAL ANGLE θ_t ($^\circ$)	31	31	20	30	90
COUPLING SEAL ANGLE θ_c ($^\circ$)	30	30	17.7	27.0	90
INITIAL CLEARANCE C_s (mm)	0.25	0.25	1.0	1.0	0

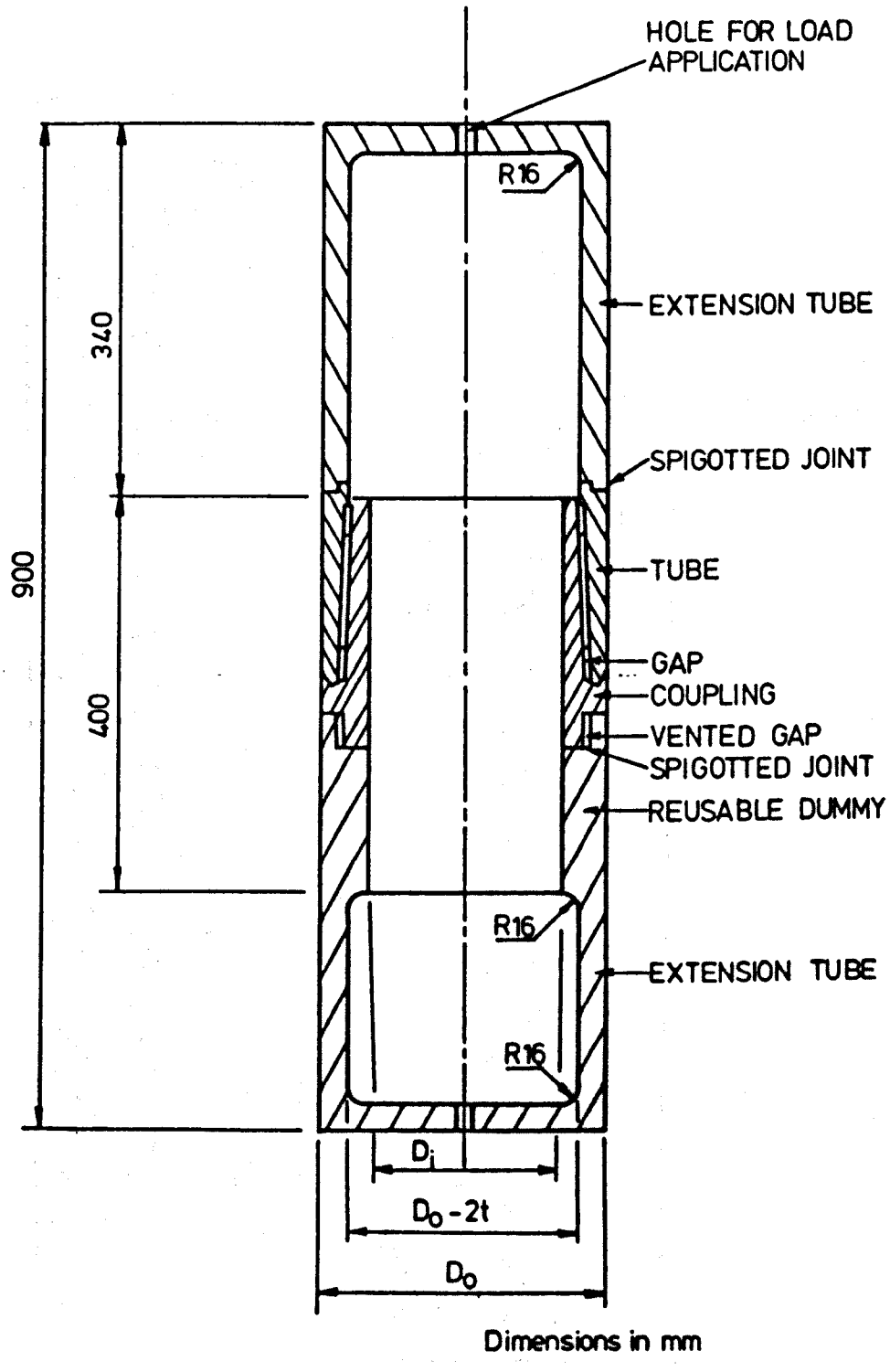

Fig. 3.1 - 3D Model Arrangement

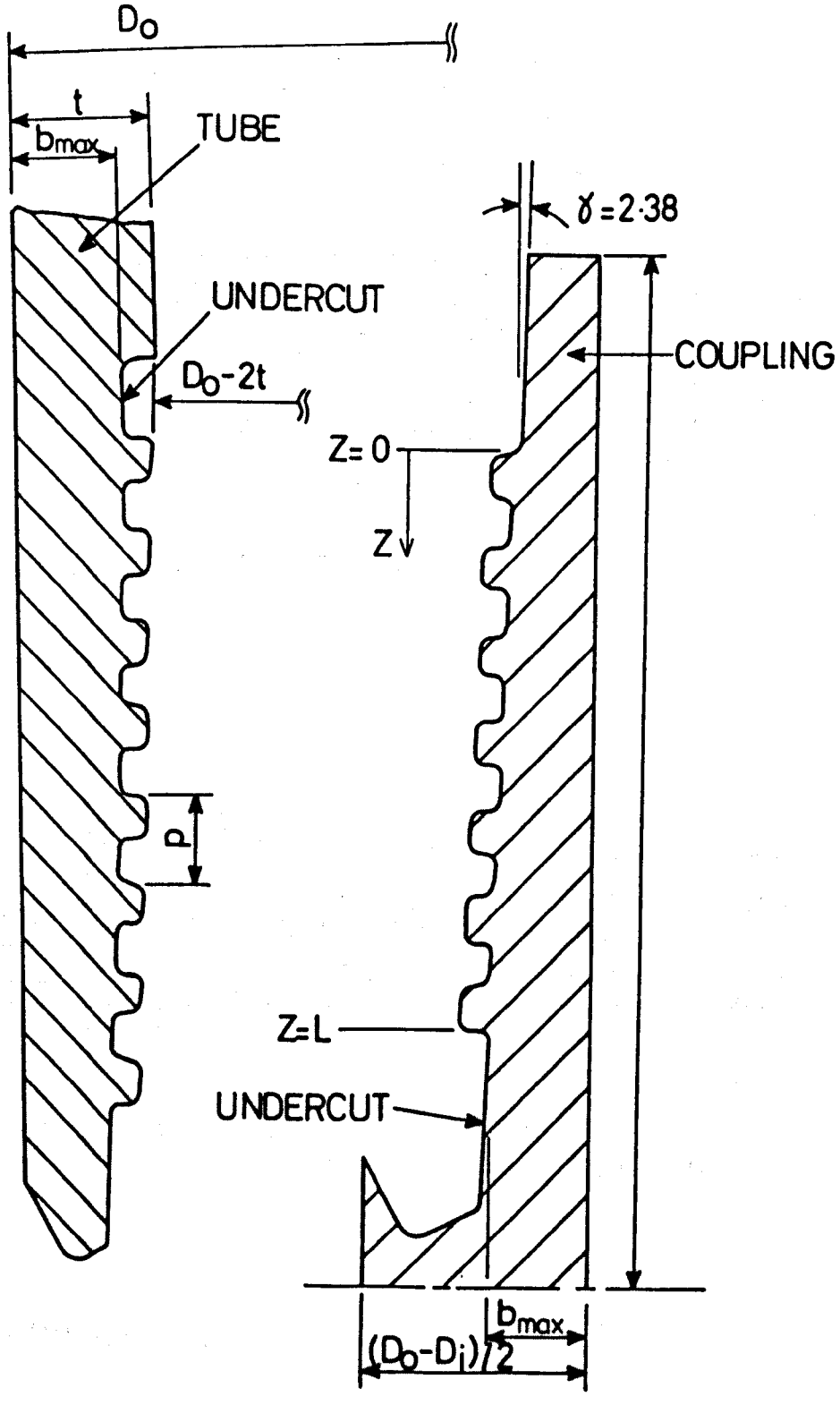

Fig. 3.2 - Screwed Model Details

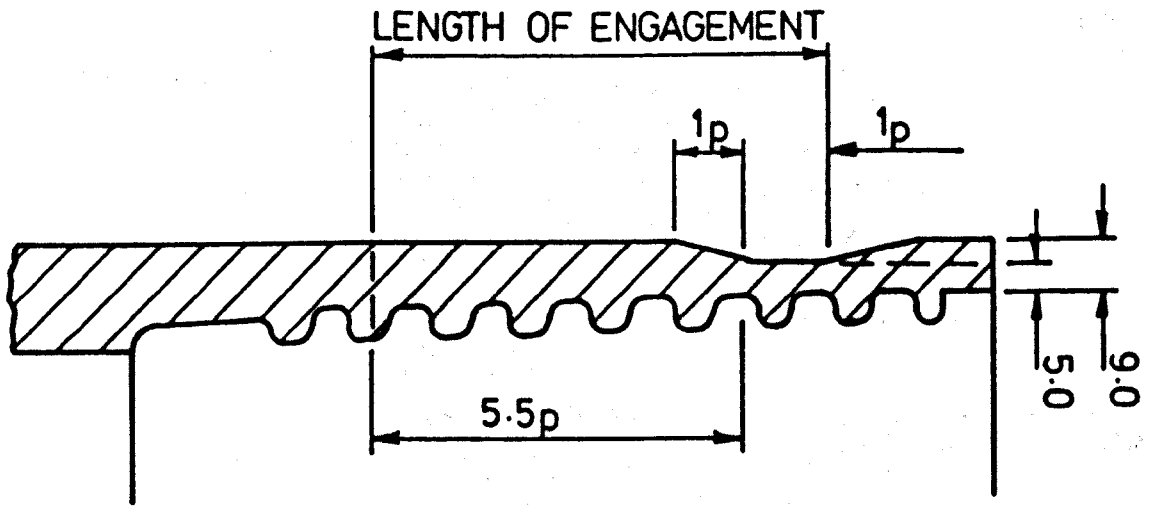

SECTION OF TUBE MODEL 6 AND 7

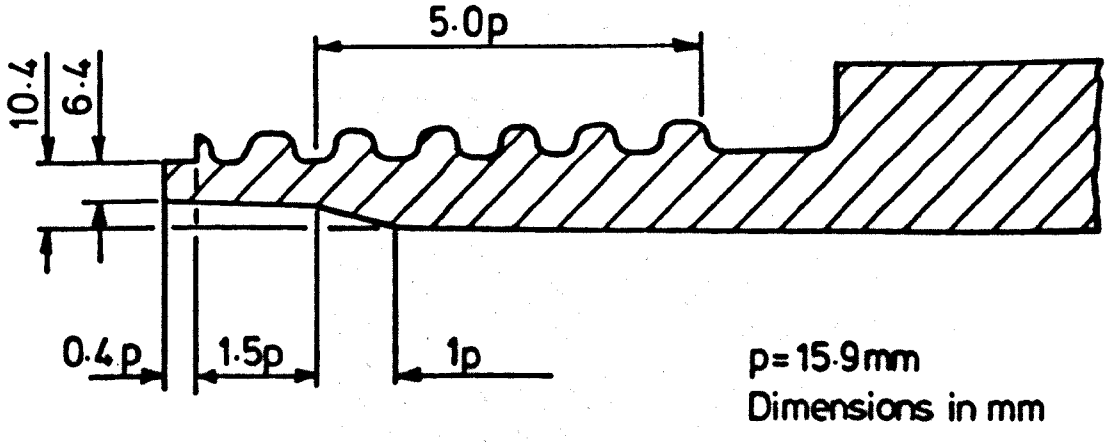

SECTION OF COUPLING MODEL 6 AND 7

Fig. 3.3 - Grooved Models 6 and 7

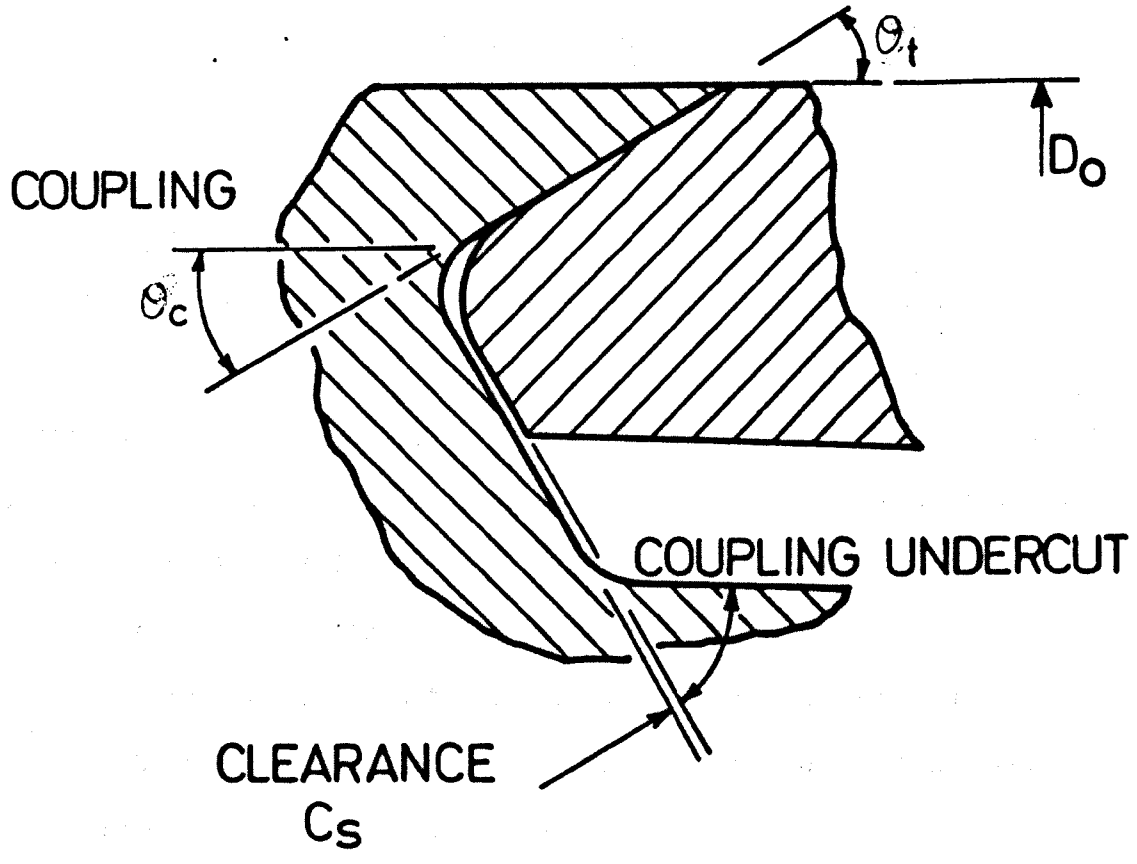

DETAIL OF CONICAL SEAL - MODELS 1 TO 4

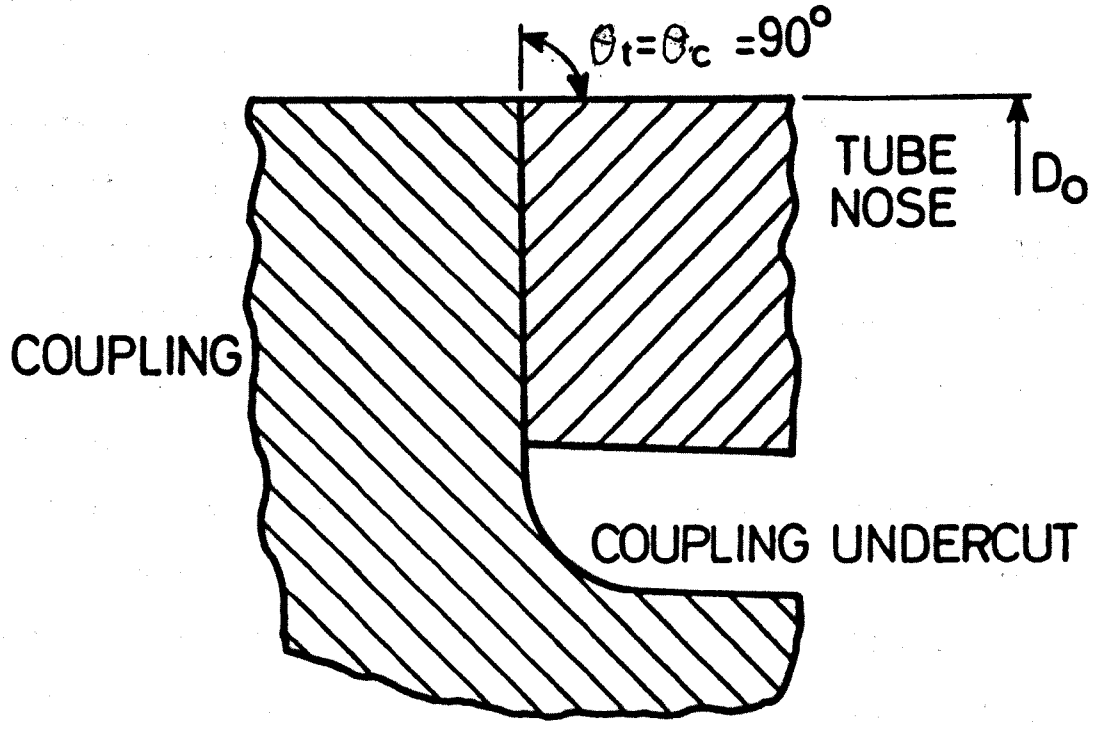

DETAIL OF PLANE SEAL - MODELS 5 TO 10

Fig. 3.4 Araldite Model Seal Regions

CHAPTER FOUR

EXPERIMENTAL TECHNIQUES

4.1 Photoelastic Model Manufacture

4.1.1 Introduction

The objective of the manufacturing process was to produce dimensionally accurate, homogeneous and reproducible models. The accuracy was particularly important for the thread region where errors in pitch could affect the thread load distributions and errors in the shape of the thread form would affect the stress distributions.

Three manufacturing processes were considered:-

i casting large, plain tubes from which the models would be machined,

ii casting partially finished models, onto which the final thread form and other details could be machined,

iii precision castings of the models so that the threads did not need to be machined.

Of the processes, precision casting would have been cheapest and quickest once the moulds and cores had been made, but it would have limited the investigation to the thread form of the moulds and cores.

Casting plain tubes and completely machining the models would have been most expensive and have taken the longest to produce but had the advantage that any shape of thread could have been machined in any shape of connection.

Casting partially finished models reduced machining time and still allowed some freedom to alter the thread form, but required the moulds and cores either to be cast from patterns or machined.

Taking into account the above considerations the models were manufactured using the following processes.

Model 1 was fully machined from plain tubes, but, before it was fully machined, the tube and coupling models were used as patterns to

produce moulds and cores, from which Models 2, 3 and 4 were cast as partially finished models. Models 5 to 10 were all cast precisely with the same finished thread form (from machined moulds and cores).

Many of the dimensions are in Imperial units, because the best screw cutting lathe was Imperial and this set the thread pitch. Also many of the measurement techniques used, employed Imperial measuring devices.

4.1.2 Rough and Precision Casting and Machining Final Shape

Model 1 was machined from 2 plain tubular castings. The castings were approximately 10 mm oversize in wall thickness and 20 mm oversize in length to allow for casting shrinkage (Ref 13) and misalignment of the tubes which were used as moulds and cores.

The castings for tube and coupling were cast at the same time, using the same mix of Araldite CT200 and hardener HT907 to minimise mechanical and optical property differences between the tube and coupling castings.

The casting procedure used for all the castings required the Araldite to be melted and thoroughly mixed with the hardener at 100° C in an Araldite:Hardener ratio of 100:60 by weight. The mix was then poured into the mould and left for 4 days at 105°C until the Araldite had solidified. The castings were then removed from their moulds and cores and cured at 135°C for 4 days.

Rough Casting

As was stated in Section 3.3, the pitch and taper of all the models were kept constant. This allowed different thread forms to be machined out of the same rough castings. Model 1 was partially machined to within 2 mm of the final shape. At this stage the partially machined models were used as patterns, from which slate filled epoxy resin moulds

and cores were cast; a detailed description of the development and use of slate filled epoxy resins as moulds and cores is given in REF 14.

For the rough tube model castings, 4 piece, collapsible, slate-resin, threaded cores were used to facilitate extraction from the casting. The partially machined tube model was heavily greased prior to the casting of the cores. The cores were cast with the tube model horizontal. The open ends of the tube model were blocked off with 2 slate epoxy end plates. Referring to Fig 4.1, each core had 2 threaded steel studs cast into it, to aid extraction of the cores from the castings. Each end plate had heavily greased location pins set into it, around which the cores were cast. These location pins, 2 at each end of each core, accurately located the cores for each model casting.

Core number 1 was cast first. After the slate resin had fully solidified and with it still in position, the assembly was rotated approximately 85° and core number 2 cast. The thickness of core 2 was large enough to ensure overlap between cores 1 and 2. After core 2 had solidified and with both cores 1 and 2 in place, the assembly was rotated 105° and core number 3 cast. This core was thick enough to ensure overlap between cores 2 and 3. Finally, after core 3 had solidified, and with cores 1, 2 and 3 in place, the assembly was rotated through 85° and core number 4 cast.

The angles between the cores allowed easy removal of the cores from the models in the order 4,3,2,1, after a model had been cast and solidified. For model casting, the assembly was put together as shown in Fig 4.1.The slate epoxy plates provide location for both the threaded cores and the outer slate epoxy mould. The boundaries between the cores and between the cores and plates were sealed with Silicon rubber to minimise any Araldite casting flashes and leaks. The liquid Araldite was poured through the top slate epoxy plate.

For the rough coupling model castings, a 2 part slate-epoxy resin thread mould was cast around the thread region only of the heavily greased, partially machined coupling of model 1. Care was taken to ensure that each thread mould extended only 180^{o} around the model. For casting of Models 2 to 4 breakable inner cores and outer moulds were used, see Fig 4.2. These were paper tubes supported with a relatively thin layer (approximately 5 mm) of brittle epoxy resin, which were broken in order to remove the casting and new ones made for each casting.

Precision Casting

Models 1, 2, 3 and 4 were all machined from rough castings. This was time consuming and costly. Thread cutting contributed approximately 85% of the total time of machining.

Ideally we would have liked to have produced precision castings to the final shape of the whole of both tube and coupling models. Practical problems of removing the castings from the moulds made this impossible, but machining time of the models was reduced from about 15 man-days per model to 2 man-days per model.

The objective of the casting process was to obtain dimensionally accurate and reproducible precision castings. The moulds and cores needed to be durable (as several castings would be required), dimensionally stable, accurately produced, and have a smooth, high quality surface finish to prevent adhesion between the cast model and the mould and core surfaces.

Two different processes were considered for the manufacture of the moulds and cores. The first was to machine patterns, probably in Araldite, from which moulds and cores could be cast in slate powder filled epoxy resin. This is a tried and tested method of manufacture for modelling welded tubular joints. The second process was to machine

the moulds and cores directly. This required aluminium thread cores and moulds due to the very abrasive nature of slate-epoxy, which would have rapidly blunted carbide tools.

Machining the moulds and cores directly was likely to be more accurate in the thread regions; any machining errors of the pattern or excess of lubricant or separator would be reproduced in the cast moulds and also bubbles introduced during the mould and core casting would show up and possibly be exaggerated in the final model castings. Hence, the second process was used.

The aluminium tubes used for the coupling thread mould and coupling core as well as the aluminium billet used for the tube thread core were all annealed after the external surfaces had been skimmed off and prior to machining. This minimised distortion due to the release of any residual stresses during machining.

Carbide tip form tools, of a similar design to those used to machine the models directly, were used to machine the thread forms in aluminium to avoid changes in thread profile due to the blunting of the tools.

The slate epoxy tube and coupling casting moulds were cast using the machined Araldite extension tubes as patterns. After curing and the associated shrinkage, both parts were machined to the required size.

During solidification of liquid Araldite in the casting process, polymerisation causes shrinkage both radially onto internal diameters and also axially which causes model pitch reductions. Careful design of the method of extracting the models from the moulds and cores was required due to this shrinkage and potential interfacial adhesion which could have required large forces to extract the castings from the moulds and cores during unscrewing.

Having a collapsible core made of 4 pieces similar in principle to that used for Models 2 to 4 would have provided a sure method of extraction, but difficulties in machining a pre-split aluminium core, the likelihood of casting flashes and the errors, however small, in the assembly of this complicated core, ruled this method out. Hence 1 piece cores were machined (see Fig 4.3 and 4.4) and it was expected that large torques would be required to overcome friction. The cone angle γ of 2.38° was helpful since, once the model was initially turned, it would get progressively easier to unscrew the models. It was decided to introduce a loaded face angle α of 3° (as in the API buttress thread) also to help extraction. The tube model's slate-epoxy outer mould and the coupling model's aluminium core had slight radial tapers of 1 in 1000 also to help with extraction.

The method chosen to apply large, evenly distributed torques during the extraction stage was to form splines with minimum stress concentration shapes. This was achieved by casting the models around round, ball-ended annealed pins shown in Figures 4.3 and 4.4. The pins were glued into the aluminium top plates prior to final machining to provide location of the pins on the tube aluminium core and on the coupling slate-epoxy outer mould. A long bar was provided to apply large torques to the aluminium top plates while the lower parts were held firmly by bolting to the floor. After extraction of the models from the moulds and cores, the pin and top plate assemblies had to be withdrawn from the models. To facilitate this, the pins were machined with a radial taper of 1 in 100 and heavily greased. The pins were designed with large radii to minimise the stresses in both the pins and the models during extraction.

Locations for both tube and coupling moulds and cores were provided in the 12.5 mm thick Aluminium top and bottom plates by 6 mm deep spiggots with nominally 0.1 mm radial clearance between the two mating parts. To prevent leaks of Araldite during casting, silicon rubber was used to seal where the mating parts fitted, excepting the interfaces between the pins and their mating parts. Prior to assembly of the moulds and cores, each part was thoroughly cleaned and a light, even coat of lubricator and separator was applied to all surfaces.

After assembly, the casting assemblies were placed in the oven and heated to $100^{o}C$.

The coupling model was cast with the coupling axis vertical , see Fig 4.4. To prevent air bubbles remaining on the thread surfaces, the filled assembly was spun manually to fling the liquid Araldite to the outside. The tube model was cast with the tube axis inclined about 10^{o} to the horizontal, the inlets and outlets are shown in Fig 4.3. Funnels indicated when the moulds were full. The holes required to apply torque had to be stoppered to prevent the liquid Araldite leaking. Bubbles were dislodged from the thread surfaces of the tube model by rocking the assembly.

After 4 days at 105^{0} the assemblies were cooled to 90^{o} prior to removal from the oven. The tube model filler and riser had to be drilled out. The assembly bottom plates were bolted to the floor and the torque applied to unscrew the castings from the casting assemblies.

After polymerisation the material had to be cured at 135°C for 4 days. During curing Araldite shrinks by approximately 0.5%. To ensure that the models did not distort and remained perfectly round, they were vertically mounted in oil on Araldite mandrils made to the final cured model dimensions. The oil minimised self weight effects.

TABLE 4.1 Cast and Cured Model Sizes.

Dimension	Model	Cast size ,mm	Cured size ,mm	% shrinkage
Thread pitch	6	15.88	15.80	0.50
Coupling inside Diameter	5	186.00	185.09	0.49
	6	186.00	185.12	0.48
	9	175.60	174.78	0.49
Tube outside Diameter	5	250.01	249.00	0.40
	6	250.01	249.09	0.37
	9	260.60	259.44	0.46

Table 4.1 shows the curing shrinkages in several regions of different precision cast models.

It can be seen from Table 3.1 that the wall thicknesses of Models 9 and 10 were increased. This was achieved by removing material from the inside diameter of the tube slate epoxy mould and from the outside diameter of the coupling Aluminium core.

4.1.3 Machining Of Models To Their Final Shape

Model 1, which had been used as patterns for the rough castings, was then machined to its final shape. The machining technique was the same as that used on the rough castings of Models 2, 3 and 4. Cutting

the large, complicated threads was difficult due to tool wear and thermal distortion. Due to the large size of the threads, cutting the whole thread form with one tool could have required large cutting forces which may have caused additional polymerisation due to overheating, leaving machining stresses, chatter and damage. Hence 2 tools were used, one extended $\frac{1}{4}$ pitch on both sides of the loaded face of the thread, the other $\frac{1}{4}$ pitch on both sides of the unloaded face. Araldite is a very abrasive material and carbide tipped form tools were used to minimise tool wear. Fig 4.5 shows the design of a typical pair of tools used. The tools were manufactured by specialist tool grinders. Before use, the form tools profiles were all checked optically in a 100x magnification shadowgraph and so any errors in the manufacture of the form tools were found.

Prior to the final machining of the thread form the undercut region of both tubes and couplings were accurately machined and the undercut surface was used as a datum for the thread root. In machining the undercuts, the threads were truncated using a radiused tool at the required z = constant plane. In order for the tools to cut smoothly, only very small increments in tool feed were made between each cut. These were never more than 0.006" and only 0.0005" as the thread form neared its final shape.

As was previously stated in Section 3.3 the length of coupling thread set the length of thread contact. Hence, the threads had to be removed at both the coupling undercut, $z = L$ plane, and in region of $z < 0$. At the $z = 0$ plane a radius form tool was used to remove the unloaded flank of the thread and after the machining the thread width varied from $w = p/2$ to $w = 0$ over 180°.

Prior to loading and slicing the dimensions D_i, D_o, L and t of all the machined models were measured and found to be correct to ± 0.001 " and the cone angle to $\pm$ 0.3 ^{o}. After loading and slicing, the tube and coupling thread form of each model was measured in selected θ = constant planes using the 100 x magnification shadowgraph. Tracings of the thread forms at this magnifacation are shown in Fig 4.6. It can be seen that there were machining errors in both the coupling threads of Model 1 and Model 2. The coupling root fillet of Model 1 extended 2.39 mm into the loaded face, while the coupling crest fillet was truncated 1.02 mm into the loaded face. The coupling root fillet of Model 2 extended 1.73 mm while the coupling crest fillet was truncated 1.37 mm into the loaded face. These errors caused contacts to occur at the fillets. The fillet radii were nominally 1.59 mm.

Machining errors were only present on the loaded face. The coupling threads of Models 1 and 2 were machined by machining the threads to depth by feeding the tool in small increments in the radial direction. The thread width was measured using a gauge made accurately to the thread form. If the thread width was too large, it was reduced by feeding the tool in the axial direction until the desired width was achieved. The machining errors were due to the thread width being reduced by the loaded face form tool which had not been moved to the full thread depth, see Fig 4.7. The problem was overcome by making adjustments only to the trailing face, and it can be seen from Fig 4.6 that the loaded flanks of the threads of Models 3 and 4 were accurately machined. Any errors that were present in the unloaded thread flanks would have had a negligible effect of the stress distributions..

In addition to the thread cutting, other regions of the rough cast models also required machining; the seal regions, the plane unthreaded

surfaces and the spiggots required for glueing the models to the extension tubes. These were all machined with single point tools, which could easily be sharpened when they became blunt.

Fig 4.8 and 4.9 show the precision cast models and the machining which had to be done to produce the spiggots so that they could be glued to the extension tubes and also the model undercuts which could not be cast but were required for load calibrations and to keep cast models as similar as possible to machined models. The coupling threads beyond $0 < z < L$ and the tube threads in the tube undercut were removed in a similar manner to the machined models.

Visual examination of slices from the cast models in the polariscope showed no photoelastic differences between these and the machined models.

4.1.4 Manufacture of Extension Tubes

The coupling and tube, reusable extension tubes were each manufactured in 2 parts:- the tubular members and the end plates, and then glued together before the threaded members were glued to them.

Each part of each extension tube was cast roughly to size in the same material as the threaded models. After curing in oil, they were machined to final size, see Fig 3.1. The join between the end plate and the tubular section was made as far away from the end plate as possible in order to minimise the stress concentration across the potentially weaker glued connection, see Fig. 4.10. The end plates both had 4 equi-spaced and equi-sized radial slots milled into them using a ball-ended milling tool. Torque load was applied through these slots in the tube model end cap. The slots were longer than the steel pins which fitted into them to allow for the differential thermal expansions of steel and Araldite.

Models 1 to 8 used the same extension tubes, and between the loadings of Models 4 and 3, the outside diameters of both extension tubes were reduced. The inside diameter of the dummy coupling was also increased to accomodate the reduced wall thicknesses of Models 3,5,6,7, and 8. New extension tubes with thicker walls for Models 9 and 10 were made in the same manner as described earlier.

After each loading, the loaded models were cut from the extension tubes and the steel end plates were removed from the extension tubes which were immersed in oil and heated to 130^{o} in order to anneal them. After annealing, new spiggots were machined on the extension tubes by removing all traces of the previously loaded model and glue. The minimum amount of extension tube was removed so as not to reduce the length of plain tube or dummy coupling. The extension tubes were then ready for glueing to the next model.

4.2 Model Preparation, Loading and Slicing

After the model and extension tubes were manufactured they were thoroughly dried out by leaving in a hot air oven at 70^{o} for 48 hours. After cooling, the model and extension tube spiggot surfaces were cleaned and degreased with Inhibisol and glued together with heat resistant Araldite glue 2004.

The extension tube end caps were sandwiched between steel plates with silicon rubber sheets between the Araldite and steel to prevent damage due to differential thermal expansion. This arrangement allowed tension to be applied evenly to the models. The external steel plates had radially flat pins screwed into them, which were used to apply torque to the tube model and to restrain the coupling model from turning.

For stress-freezing, the model and loading rig were placed in a hot air oven. The models were arranged with their axes vertical because the largest oven was higher than it was wide and because this position eliminated bending of the models due to their own weight. (This effect may have been significant due to the very low Young's modulus of Araldite at the stress-freezing temperature). The alternative of eliminating self-weight effects by immersion in a dense liquid would have complicated the rig and loading procedures.

The loading rig had to be capable of applying torque (to tighten the joint), tension and bending. Fig 4.11 shows the attachments which were designed to load the models.

The torque was applied by wire cables passing over pulleys and tensioned by freely hanging weights. Axial tension was applied by a lever and freely hanging weights. Bending was superimposed on axial tension by moving the model along slots in the load positioning plates to make the tensile force eccentric to the axis of the model. Differential thermal expansion and extension of the model were taken up by vertical adjustment of the upper pivot.

As the magnitude of the tension to give approximately 1% nominal strain was too large (2kN) to apply directly, a lever of ratio of 8:1 was employed. To allow for deflections of the lever due to thermal expansion and model strain, the position of the lever could be adjusted to keep it horizontal during loading.

After the threads and seals were cleaned, degreased and lubricated the models were screwed down hand tight in the rig and their relative position marked so that the ralative twist could be measured after torque loading. A thermocouple was placed inside the model (by pushing through the top hollow loading bolt) so that the model temperature could be accurately monitored. The model was then heated to the loading

temperature of 130°C.

If preload was applied to the models, it was applied prior to any tension loading. The torque was applied simultaneously through two cables and loading bolts exactly 180° apart; care was taken to set up correctly to prevent bending of the model. The two torque loads were applied at the same time by levers, pulleys and cables to the top external steel plate. The cables were attached to the top external plate by looping them around bolts which were screwed into the plate. The bolt holes were diametrically opposite. To ensure that the cables were horizontal as the models screwed together during the application of torque, the vertical position of the pulleys could be adjusted, See Fig 4.11. The radially flat pins transferred the torque to the tube extension. The models were left at 130° for at least 1 hour to ensure that full deformation had taken place. The torque loads were removed before the tension was applied. The relative twist of the tube model was measured to ensure that the models had been preloaded. The torque loads were removed, to release the shear stresses in the models and extension tubes caused by the torque. For Models 7 and 10, which were loaded with preload only, a small axial tension was applied which was equal to the self weight of the model and rig above the threads.

With the tensile loads still applied, the models were slow cooled at 2°C/hour until the model inside temperature was below 90°C. The tensile loads were then removed and the relative positions of the models marked in the seal region. The models were removed from the loading rig and with the models at room temperature, measurements of outside diameter taken.

Generally, loading was sucessful at the first attempt. But after the loading of Model 6, it was noticed that the tube outside diameter

had 'belled out' in the thread region. Initially, it was thought that the model had been loaded non-uniformly. The model was rotated through 180° and repositioned in the rig. It was reheated to 130° to ensure that the stresses due to the first loading were annealed and the model was reloaded. On the second loading, similar deflections occured in the same region of the model, and it was concluded that they were a feature of the models response to the loads and not non-uniformity of loading. Hence, the model was removed from the rig and analysed as the other models. Similar, but less marked deflections were noticed in the preloaded Model 7.

The screwed connection was then cut using a band saw from the extension tubes in the regions of the spiggoted glued joints, see Fig 3.1. The models were then glued to 12 mm thick Araldite plates and glued together in the seal region to prevent movement during slicing, see Fig 4.12. Prior to slicing, the angular position measured from the start of contact of the required slices was marked off using a dividing head. The slices cut were all axial over the whole length of models and generally every 22½° or 30°. Generally the slice thickness s ≃ 2 mm, which at the mean-pitch circle diameter of the model threads was approximately equivalent to 1° in the hoop direction. In regions of particular interest, such as near the ends of contacts, further slices were cut. The positions of the centre of each slice were lightly scribed onto the outside of the model, and across the full diameter of one of the end plates. The models were then mounted on an angle plate on the slicing machine with their axes horizontal.

The model was rotated until the centre of the slice to be cut was top dead centre. The top dead centre position was found when the scribed line on the end plate was parallel to a set square on the machine table. A diamond cutting wheel would be traversed s/2 + half

the width of the cut from the centre of the slice, the cutting wheel thickness = 1.65 mm, but the thickness of the cut ≈ 1.73 mm.

The cut would then be made by feeding the model horizontally onto the cutting wheel. The depth of each cut was greater than the combined tube and coupling wall thicknesses. After each cut the model was returned to its original position. The wheel would then be traversed by the slice thickness s, + the cut width, to the other side of the slice. After each slice had been cut, the model was rotated so the next slice centre was top dead centre, and the process repeated. During slicing copious amounts of water soluble cutting oil (mixed in the ratio of oil to water used for grinding) were applied to the cutting edge of the wheel. This prevented overheating of the Araldite, which may have caused local annealing of the model.

After all the cuts had been made the slices were removed from the Araldite plates. The model number and angular position were scribed on each slice at a region where no fringe readings would be taken. The remaining unsliced wedges of model, which were still glued to the end plates and hence in 1 piece, were stored for possible future use. The slices were washed to remove dry Araldite powder and suds. They were then placed in an oven at 70°C for at least 48 hours to dry out prior to analysis.

4.3 Mechanical Measurements

4.3.1 Diametral Strains

Having found the planes of maximum and minimum outside diameter at the tube model side of the seal the outside diameters of these planes were measured using vernier micrometers at different axial positions along the extension tubes and threaded connections of Models 1, 2 and 4. In these same planes and axial positions, the inside diameters of the

coupling models were also measured.

These measurements were converted into strains by dividing by the unloaded outside diameter of the models and are plotted against z in Fig 4.13. Also plotted are the nominal calculated diametral strains due to Poissons ratio.

$$\varepsilon_{nom} = -\frac{\nu W}{EA} \qquad \ldots\ldots 4.1$$

Where A is the cross sectional area.

To calculate the diametral strains in the thread region, it was assumed that the wall tension W reduced linearly from F to 0 over the length of thread contact L.

The measurements for Model 1 showed that the extension tubes and dummy coupling ovalised slightly, but the mean strains in these regions agree closely with the calculated strain due to Poisson's ratio. In the threaded region the strains were controlled by local bending caused by the positions of load transfer in the threads being offset from the middle of the tube wall thickness. This local bending was restrained by the hoop stiffness. It caused the nose end of the tube to 'bellout' and the free end of the coupling to contract. The corresponding results for Model 2 show that the eccentric tension loading caused greater ovalisation than in Model 1 but the mean deformations were similar to those in Model 1. The measurements of diameter in the thread region of Models 2 and 4 show similar strains to those of Model 1.

4.3.2 Thread Radial Clearances

Values of the thread radial clearance, c, were obtained from the measurements of tube outside diameter and coupling inside diameter, since at each section the local wall thickness of the tube, b_t and the coupling b_c were known as well as the thread height h, see Fig 4.14 hence,

$$2c = Do - Di - 2b_t - 2b_c - 2h \qquad \ldots\ldots 4.2$$

Thread clearance has been plotted against z, the distance from the origin, for Models 1, 2 and 4 in Fig 4.14 a, b and c for the planes of maximum and minimum outside tube diameter at the seal. It can be seen from Equation 4.2 that the values of c obtained are the averages of the clearances at diametrically opposite positions.

For Model 6, the thread clearances were measured at selected positions for pairs of mating threads. This was done by placing mating slices in the polariscope in their loaded positions by lining up the thread contact fringes. The slices were clamped in this position and the radial clearances measured using a travelling microscope.

Fig 4.14d and 4.15 show the variation of thread radial clearance in the hoop and axial directions in Model 6. Between $60^{\circ}<\theta<240^{\circ}$ the clearances in all pitches were approximately 0.2 mm. The clearances increased from $\theta = 240^{\circ}$ and reach a peak at $\theta = 315^{\circ}$ before reducing again. For clearances less than 1.4 mm, the centre of contact was on the loaded flank, while for 1.4 mm $< c < h$, the centre of contact would be in the top radii. It can also be seen from Fig 4.14d that clearance along a plane of constant θ increased with z in a similar manner to Models 2 and 4.

4.3.3 Measurements of Loaded Pitch

For the selected positions in Models 1 and 2 shown in Table 4.2, the pitch p was measured for each thread in the loaded conditions. Pitches were measured at mid thread height position in the 100x magnification shadowgraph. Each slice was set up with its sliced surfaces normal to the light path and the unthreaded surface of the slice horizontal. The slice could be positioned with an accuracy of $\pm$

0.0001" in both the axial and radial directions (relative to the slice). The viewing screen of the shadowgraph was 450 mm in diameter, which at 100x magnification allowed most of the thread loaded face to be viewed. The slice was positioned so that the mid-thread-height position of the loaded flank was coincident with cross-hairs on the viewing screen, this position was read from a vernier scale. The slice was then traversed until the next thread came into view. This thread was positioned in a similar manner and the new reading on the vernier scale read off. The difference between the two readings was equal to the loaded pitch p'. From Fig 4.16 it can be seen that

$$p' = p + X + (\delta_2 - \delta_1) \qquad \text{.....4.3}$$

where p' is the loaded pitch, p is the unloaded pitch, X is the wall extension and $\delta_2 - \delta_1$ is the difference in the thread bending.

It can be seen from Table 4.2 that pitch strains vary little along the length of the models. This is not surprising since the sums of the tube and coupling cross-sectional-areas and the sum of the wall tensions are similar along the joint. But, since the tube wall tension varies from a maximum at z = 0 to 0 at z = L, the wall extension, x, must similarly reduce and the pitch extension must be made up from the differences in thread and wall bending deflections. The same will apply to the coupling but from z = L to z = 0. This is supported by the coupling inside diameter and tube outside diameter measurements shown in Fig 4.13 which show increasing curvature as the wall tension reduces.

4.3.4 Flexibility

The axial flexibilities of each model were measured at several locations around the model. To measure model flexibilities, the axial lengths of wedges from each model, left after the slices had been cut, were measured in their fully loaded state. These wedges were then annealed in mesh and remeasured to obtain the change in length Δl (due

TABLE 4.2 - Loaded Pitch Measurements

MODEL	θ	PITCH NUMBER											
		0-1 TUBE	0-1 COUPLING	1-2 TUBE	1-2 C	2-3 T	2-3 C	3-4 T	3-4 C	4-5 T	4-5 C	5-6 T	5-6 C
1	57½	0.6288	6287	6300	6293	6285	6288	6299	6289	6288	6288	6292	6288
% STRAIN		0.61	0.59	0.80	0.69	0.56	0.61	0.78	0.62	0.61	0.61	0.67	0.61
2	0			6291	6289	6292	6294	6291	6289	6292	6290	6290	6283
% STRAIN				0.66	0.62	0.67	0.70	0.66	0.62	0.67	0.64	0.64	0.53
2	180	6292	6287	6292	6285	6290	6291	6296	6297	6291	6289	6294	6297
% STRAIN		0.67	0.59	0.67	0.56	0.64	0.66	0.74	0.75	0.66	0.62	0.70	0.75

NOTE Models 1 and 2 nominal (unloaded) pitch taken as 0.625".

to the tensile force F). Wedges were typically 25° wide. The length l was measured from the middle of the coupling (about 10 mm from the tip of the tube seal) to a position in the plain tube, about 10 mm from the end of the undercut. This was the length of the slices cut for photoelastic analysis. The latter position is obviously arbitrary but was very similar from model to model and for comparing flexibilities from model to model, the exact value of l is unimportant.

If preload had been applied to a model, the tube nose was put into compression and the coupling undercut into tension as the tube was forced into the "wedge" formed by the coupling seal and the thread spiral. The model wedges were annealed (heated to the stress-freezing temperature and then cooled at 2°C/hour without any applied loads) with the tube and coupling wedges in mesh, and the externally applied tension was removed, leaving the preload only. For Model 7, loaded with preload only, the wedges were annealed out of meash, hence, the extension measured was due to preload Q only.

The measured flexibilities G, were normalised by the calculated flexibilities G_{nom} of a tube with an inside diameter equal to that of the coupling, an outside diameter equal to that of the tube and a length l.

$$\underline{ie} \quad G_{nom} = \frac{\Delta l_{nom}}{F} \quad \text{where} \quad F = A \epsilon E \qquad \ldots\ldots 4.3$$

$$\text{hence } G_{nom} = \frac{4l}{\pi(D_o^2 - D_i^2) E} \qquad \ldots\ldots 4.4$$

The normalised flexibility g,

$$= \frac{G}{G_{nom}} \qquad \ldots\ldots 4.5$$

For models loaded with tension

$$g = \frac{\Delta l}{F} \frac{E}{l} \frac{\pi(D_o^2 - D_i^2)}{4} \quad \ldots\ldots 4.6$$

For models loaded with preload only

$$g = \frac{\Delta l \quad E \quad \pi(D_o^2 - D_i^2)}{Q \quad l \quad 4} \quad \ldots\ldots 4.7$$

For Model 2, loaded with eccentric tension, the local wall tension was used.

Results for Models 1 to 5 are the average of 3 measurements taken at different positions around the model while the results for Models 6 and 7 are for 8 different positions. The results are shown below.

Model	Flexibility g
1	$1.00 \pm \begin{matrix} 0.03 \\ 0.04 \end{matrix}$
2	$0.95 \pm \begin{matrix} 0.29 \\ 0.28 \end{matrix}$
3	1.11 ± 0.05
4	1.00 ± 0.03
5	1.00 ± 0.02
6	$1.09 \pm \begin{matrix} 0.49 \\ 0.23 \end{matrix}$
7	$1.25 \pm \begin{matrix} 0.51 \\ 0.36 \end{matrix}$

There is a large scatter of results for Models 2, 6 and 7. Model 2 was subjected to a large bending moment. Models 6 and 7 had circumferential grooves in the models; these grooves were intended to reduce the peak fillet stresses by locally increasing the flexibility of the tube, but they caused significant local wall bending.

The other four models, which had ungrooved, unthreaded surfaces and were subjected to axial loads only, show very small circumferential variations of model extension, indicating good experimental accuracy. The normalised flexibilities are suprisingly low. This shows that the threads were very stiff, contributing 11% or less to the flexibility of the joint. From the definition of flexibility it is seen that these joints were significantly stiffer than the plain tube.

4.4 Photoelastic Measurements

Manual photoelastic techniques have been used to measure the peak fillet stress distributions. Also, stress distributions have been measured manually around the surfaces of complicated shapes, such as a full thread and also when many widely spaced measurements were required, such as across the tube and coupling undercuts in order to photoelastically measure the applied loads.

Manual measurements of fringe order and isoclinic angle have been made in a diffused light transmission polariscope using Tardy compensation for fractional fringe orders. The equipment and techniques have been used for many years in the Department and are reported in Ref 31.

Photoelastic measurements using on Automatic Micropolariscope (AMP), see Ref 18, have been made in regions where the high precision, both positionally and in the accuracy of the measurements, was required. This accuracy was required in the measurements of shear stress distributions across the roots of threads, which were required to determine thread loads, measurements of through thickness cartesian stress distributions, detailed distributions of stresses around the thread fillets and contact regions. Ref 34 serves as an instruction

manual for the use of AMP.

Briefly, the AMP is a diffused light transmission polariscope which is built around a Vickers M17 microscope. The AMP uses Tardy compensation for measuring fractional fringe orders. The functions of slice positioning, analyser rotation, quarter wave plate movement and rotation of the slice relative to the polariser and analyser (rotation of the polariser would have required too much modification to the microscope) were all microprocessor controlled and motorised using stepper motors for all but the quarter wave plate movements. The quarter wave plates were moved by d.c. motors.

A photomultiplier measured the average light intensity over a 0.04 mm diameter of slice. The light was emitted by a 100 W tungsten halogen light, which was filtered to give monochromatic green light.

The angular positions of the stage (for isoclinics) and the analyser (for fractional fringe orders), which gave a minimum intensity of light transmitted through the slice, were determined by fitting 3rd order polynominals to the measurements of light intensity at about 10 widely-spaced positions and calculated the position of the minimum value of light intensity using the polynomial. To achieve accuracies in isoclinic angle of $\pm 0.05^{\circ}$ and ± 0.001 fringes, this process was repeated for positions near the previous minimum. The automatic reading of one point took about 1.2 minutes. Integral Fringes were measured separately and 'edited' into the automatically obtained data. Software developed by Marston (34), (the program is called READAGRID), controlled the movements and recorded the co-ordinates, isoclinics and fractional fringe orders on a floppy disc and produced a hard copy of all the measurements for points in a grid of up to 3 straight lines with up to 50 points in each line.

A program has been developed from READAGRID which will read and record the isoclinics, fractional fringe orders and co-ordinates of any number of points of equal angular displacements around a segment (of any size) of a radius of any size (READARAD). Both READAGRID and READARAD require the accurate initial positioning of the slice.

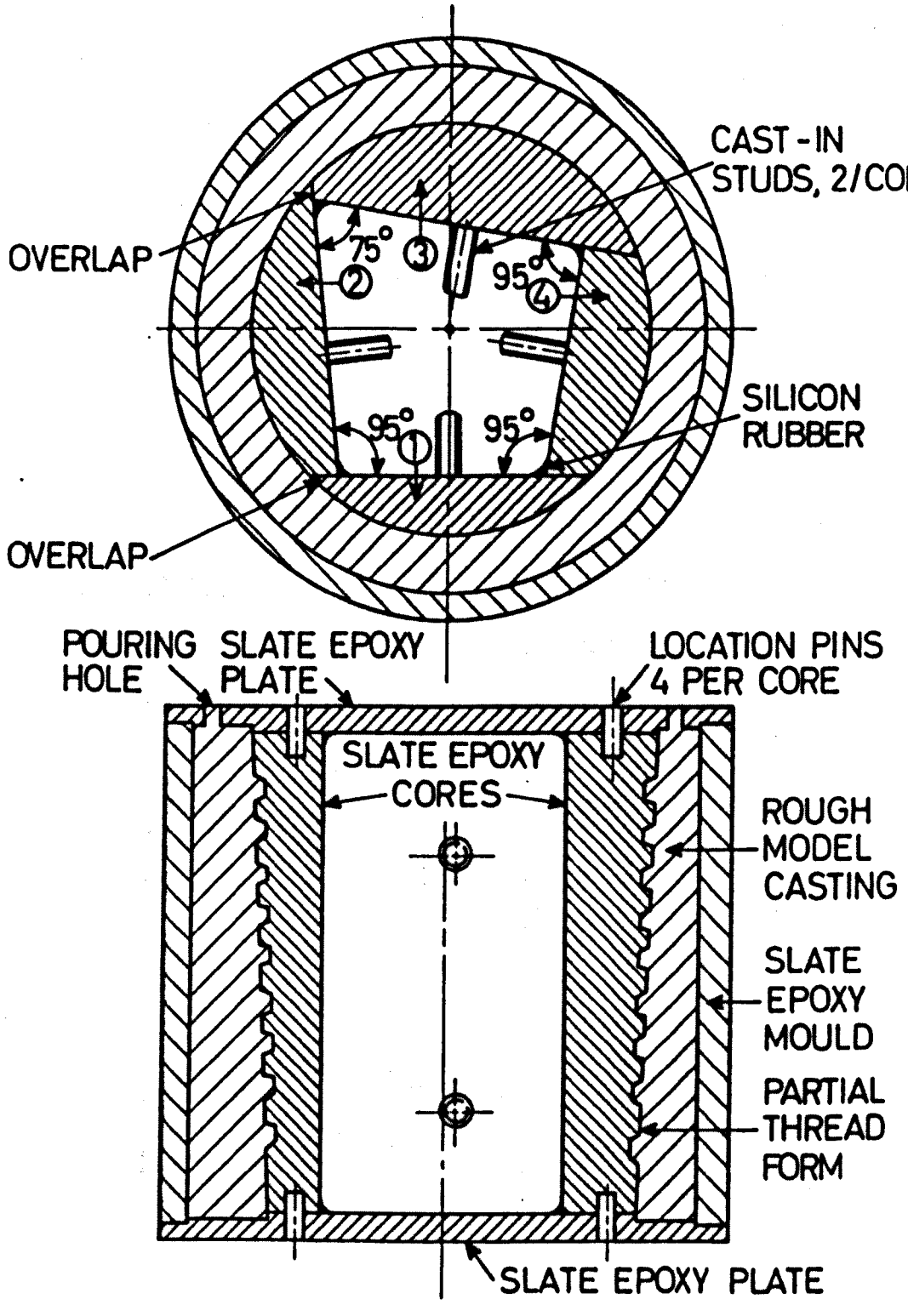

Fig 4.1

Tube Models 2 To 4 Casting Assembly

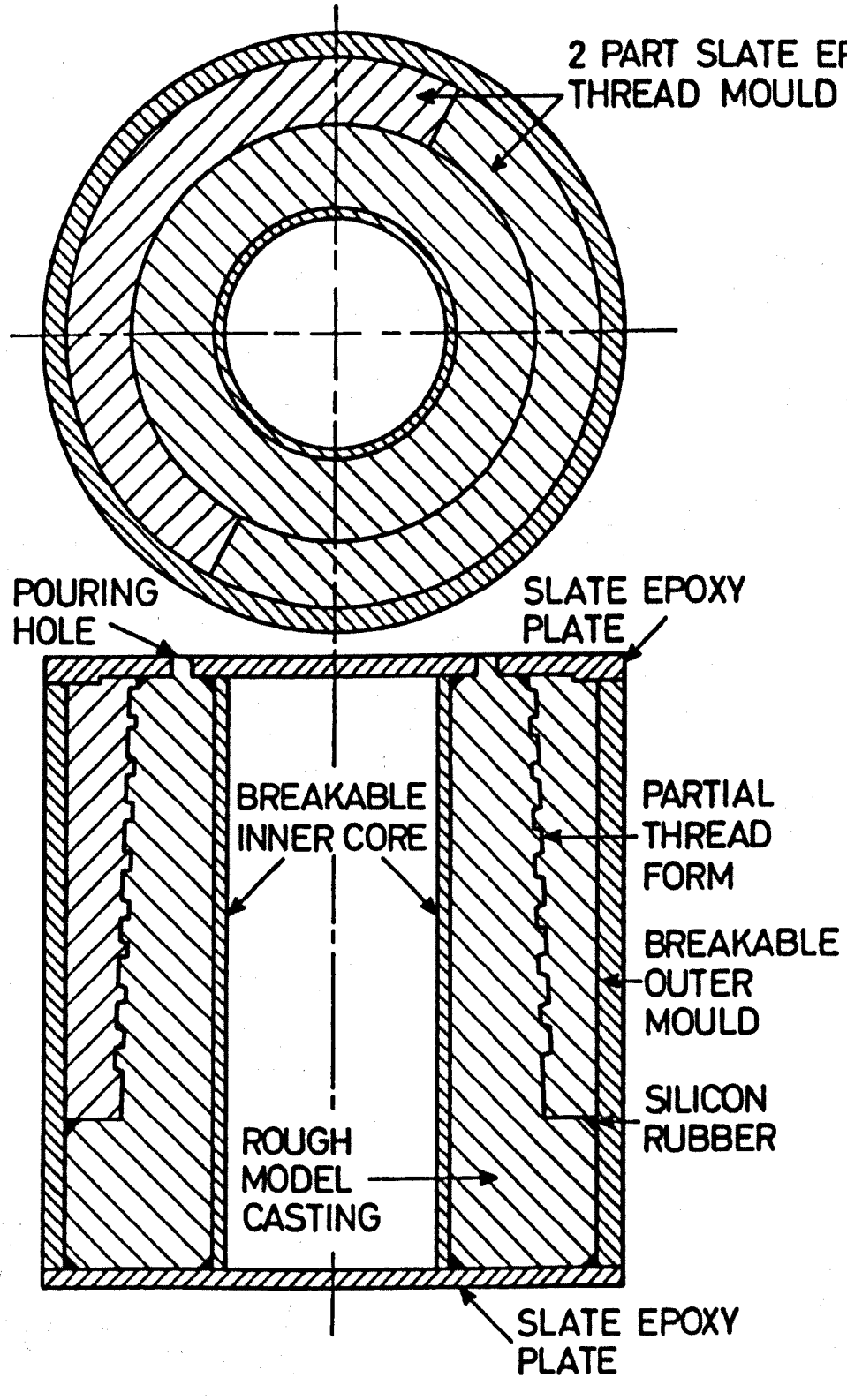

Fig 4.2

Coupling Models 2 To 4 Casting Assembly

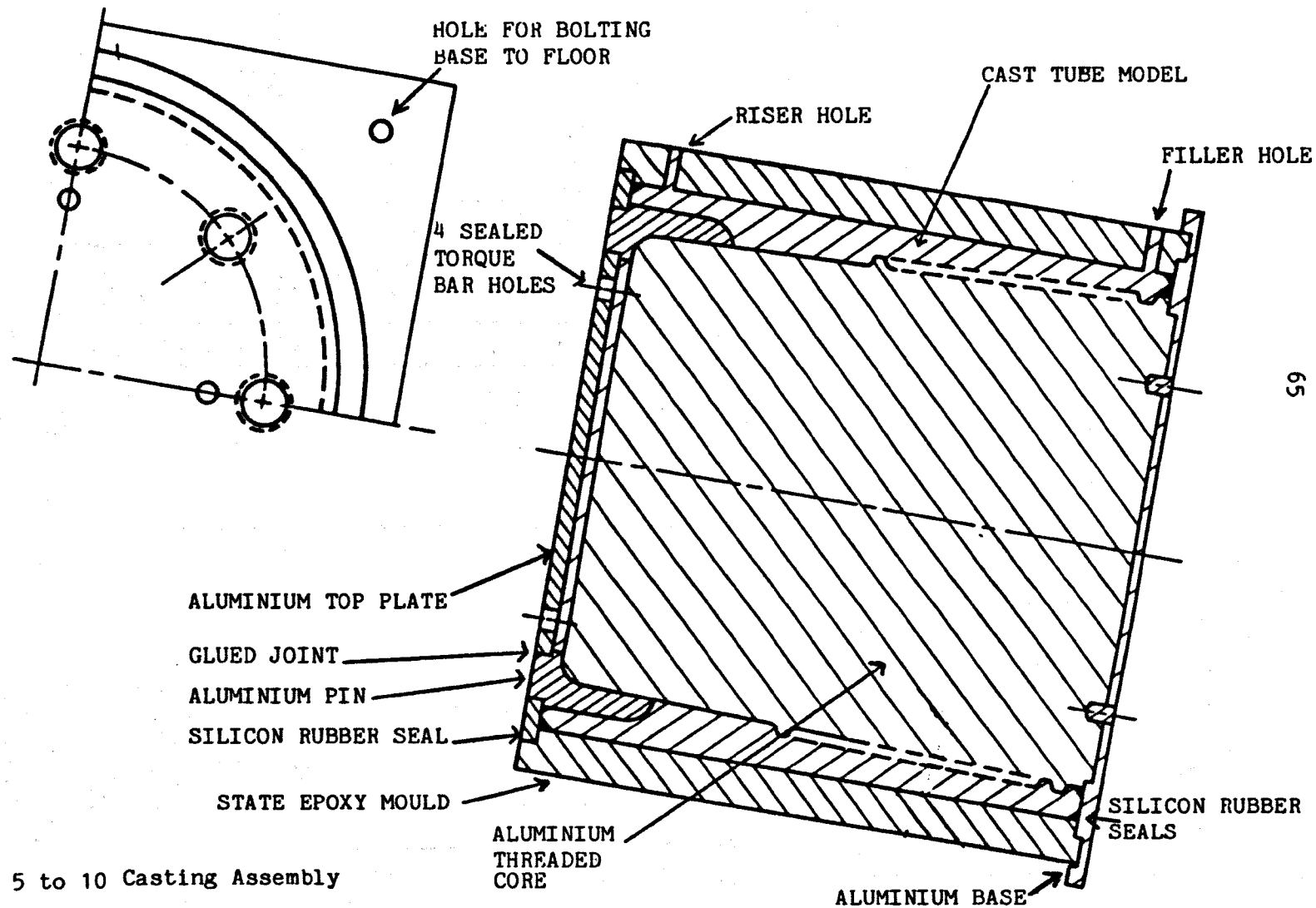

Fig 4.3 Tube Models 5 to 10 Casting Assembly

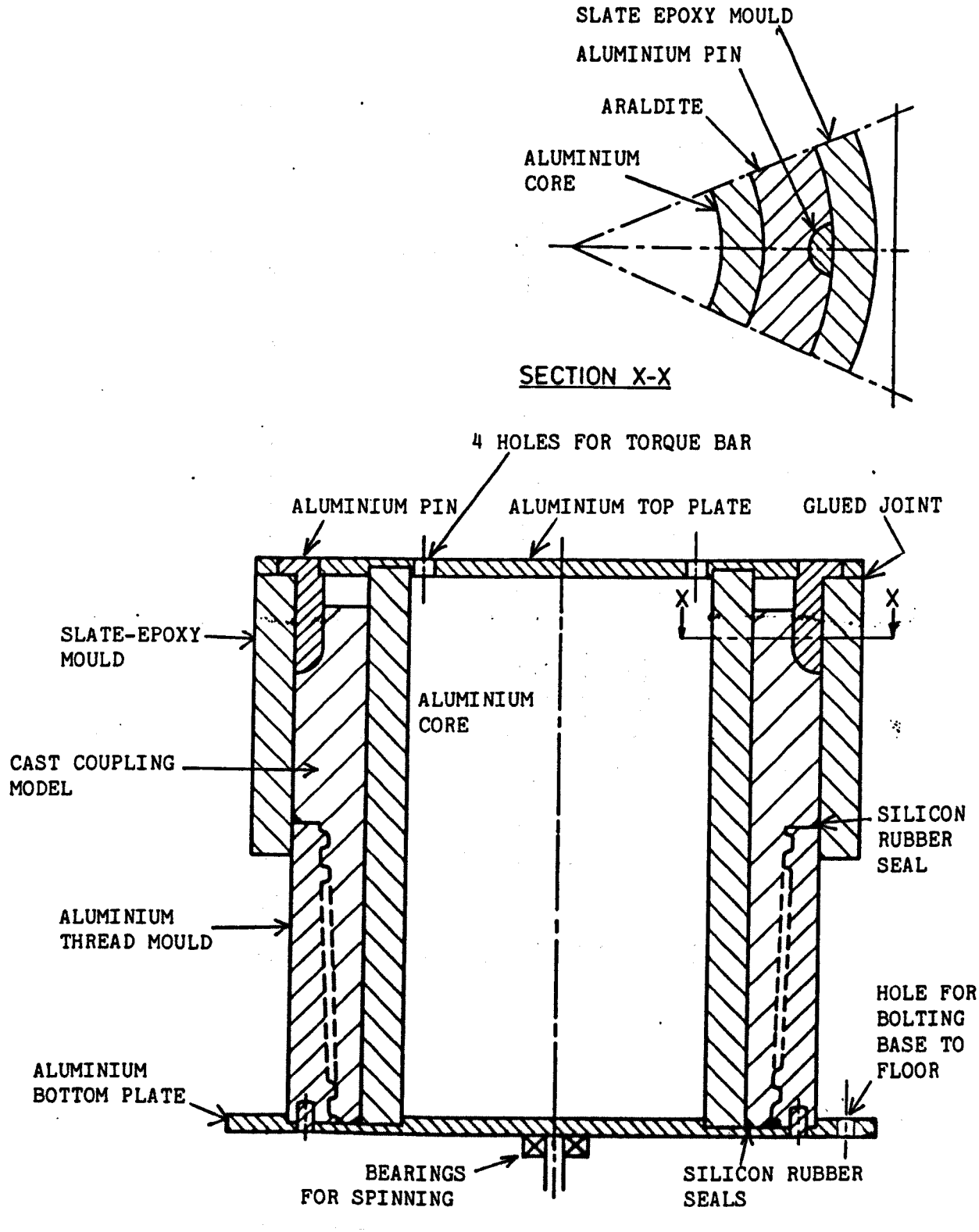

Fig 4.4 Coupling Models 5 to 10 Casting Assembly

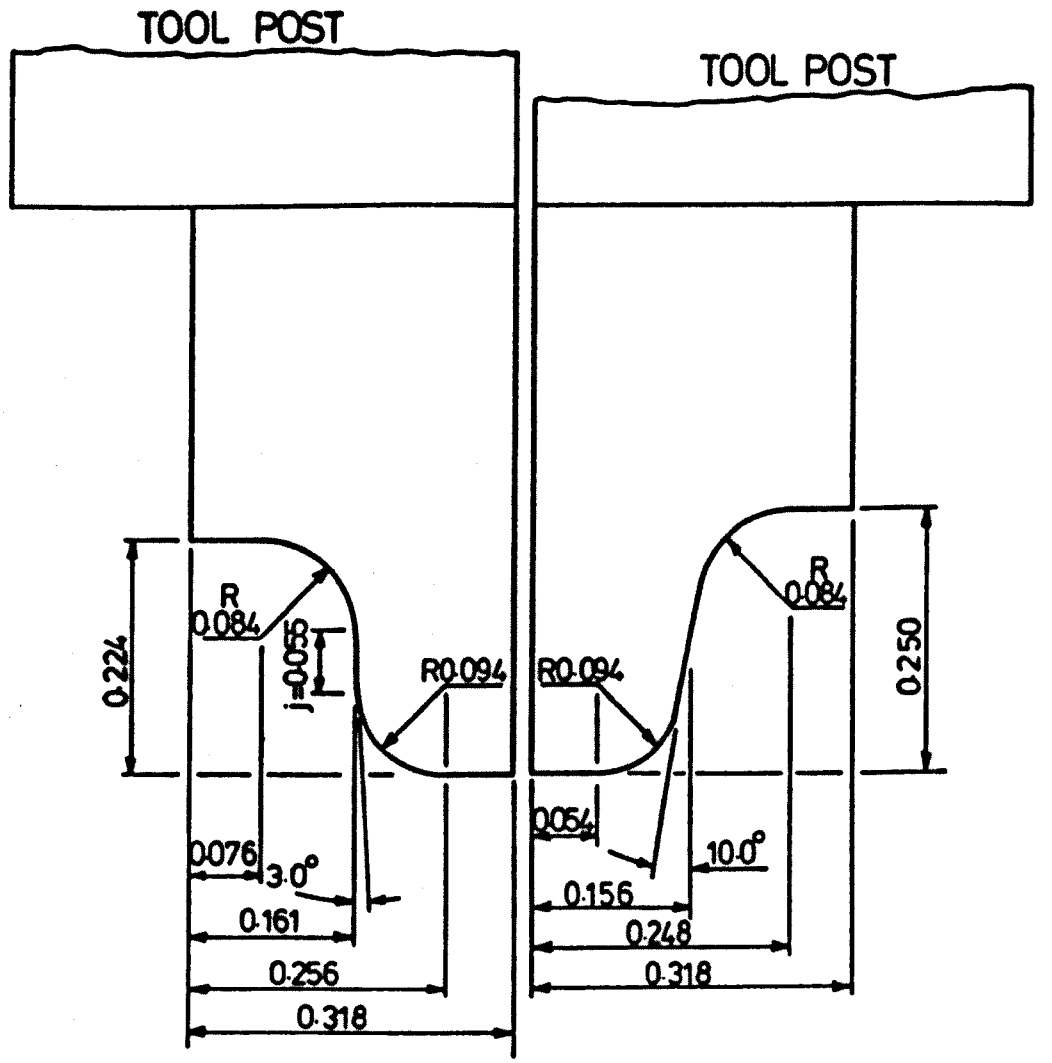

DIMENSIONS IN INCHES

Fig 4.5

Thread Form Tools - Used for Machining Moulds
And Cores for Models 5 to 10

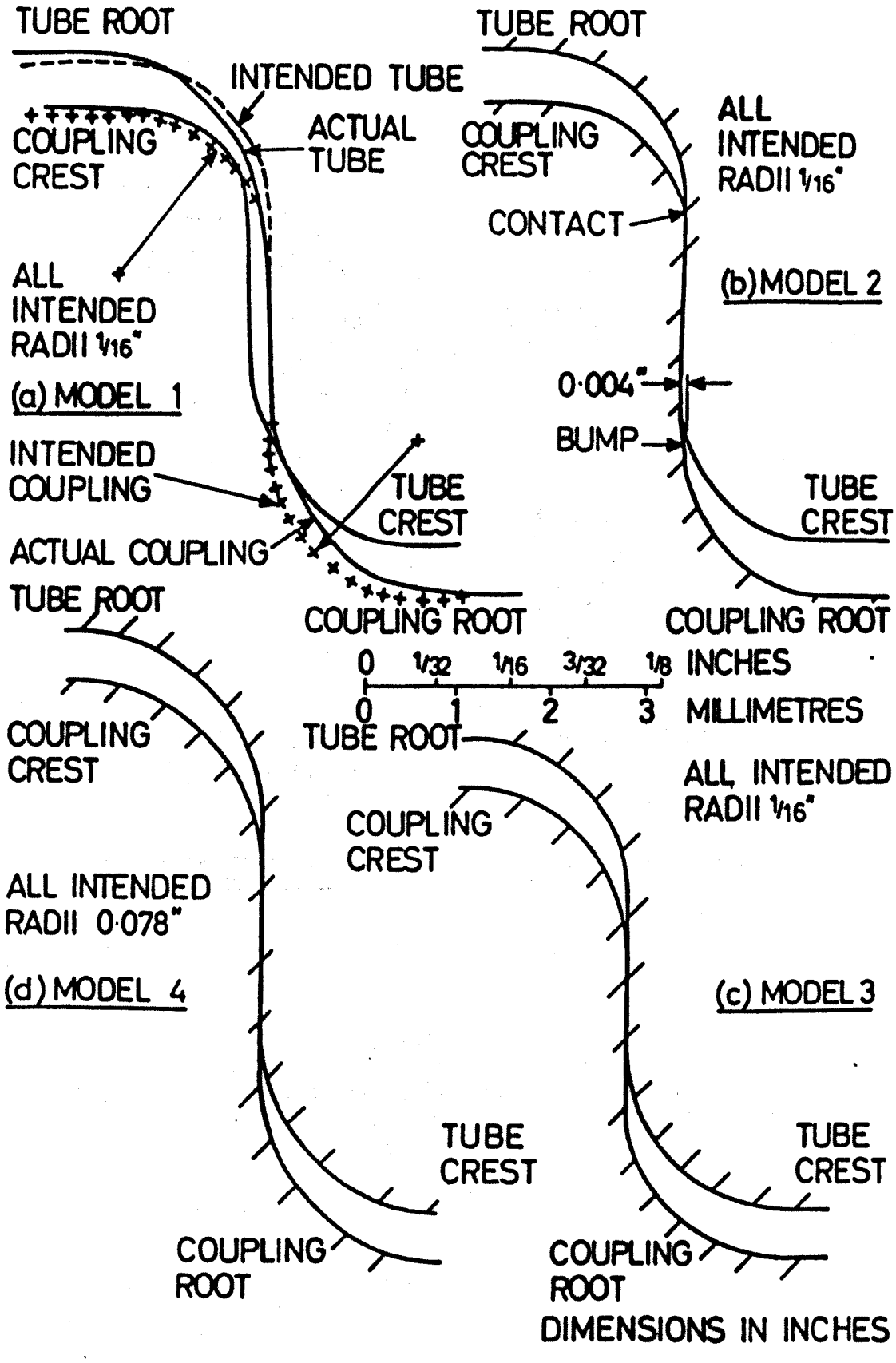

Fig 4.6

Actual And Intended Thread Profiles

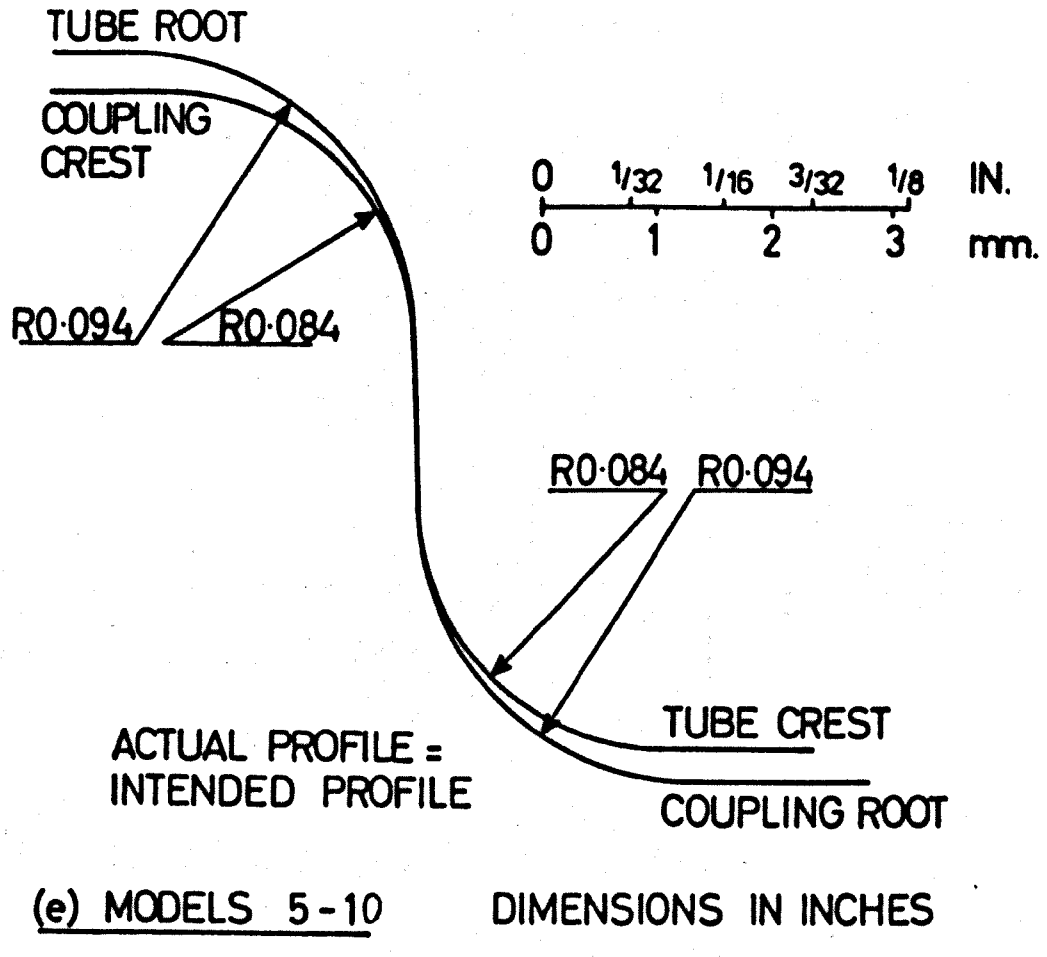

Fig 4.6 (cont)

Actual And Intended Thread Profiles

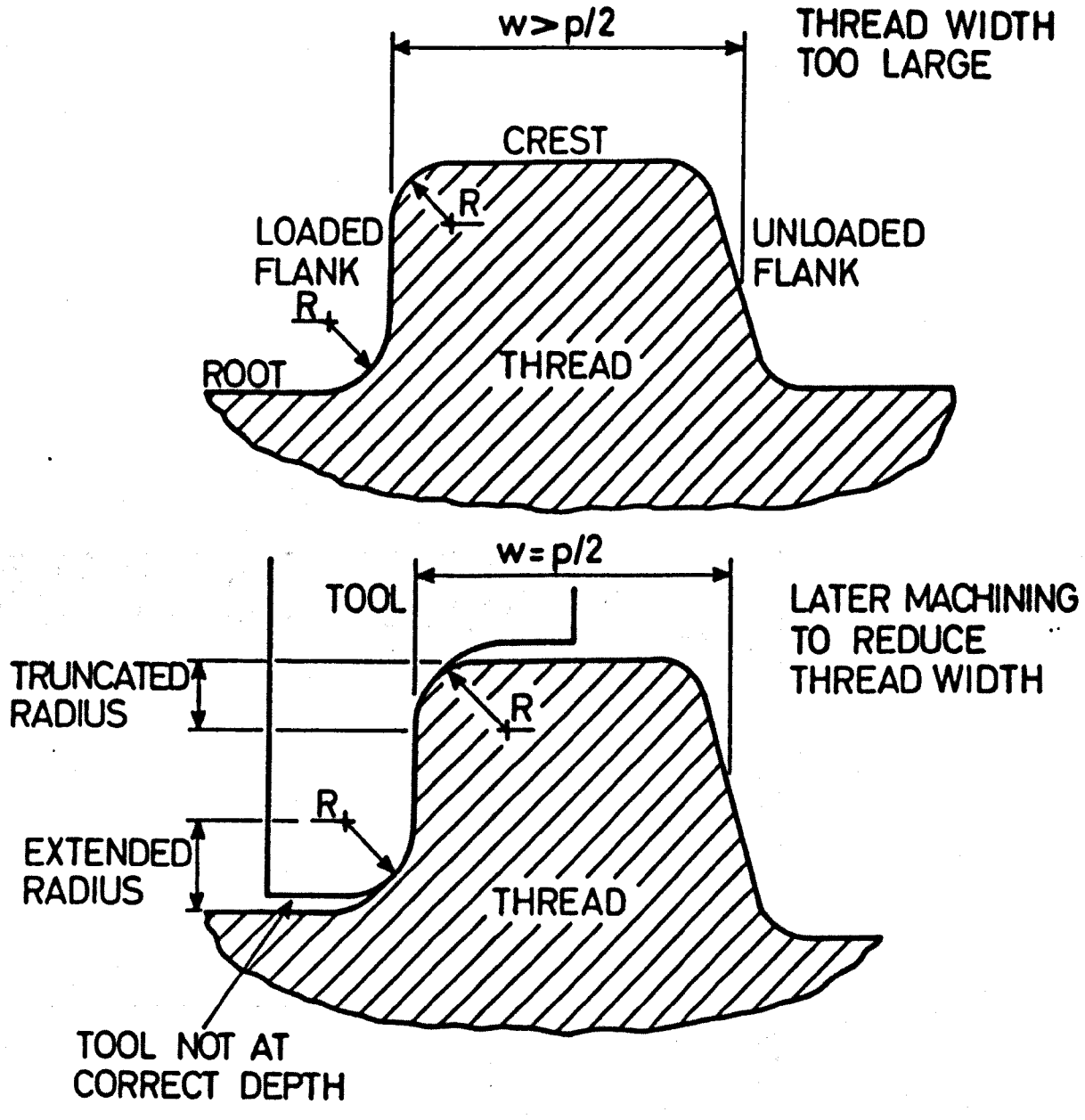

Fig. 4.7

Models 1 and 2 Thread Form Machining Errors

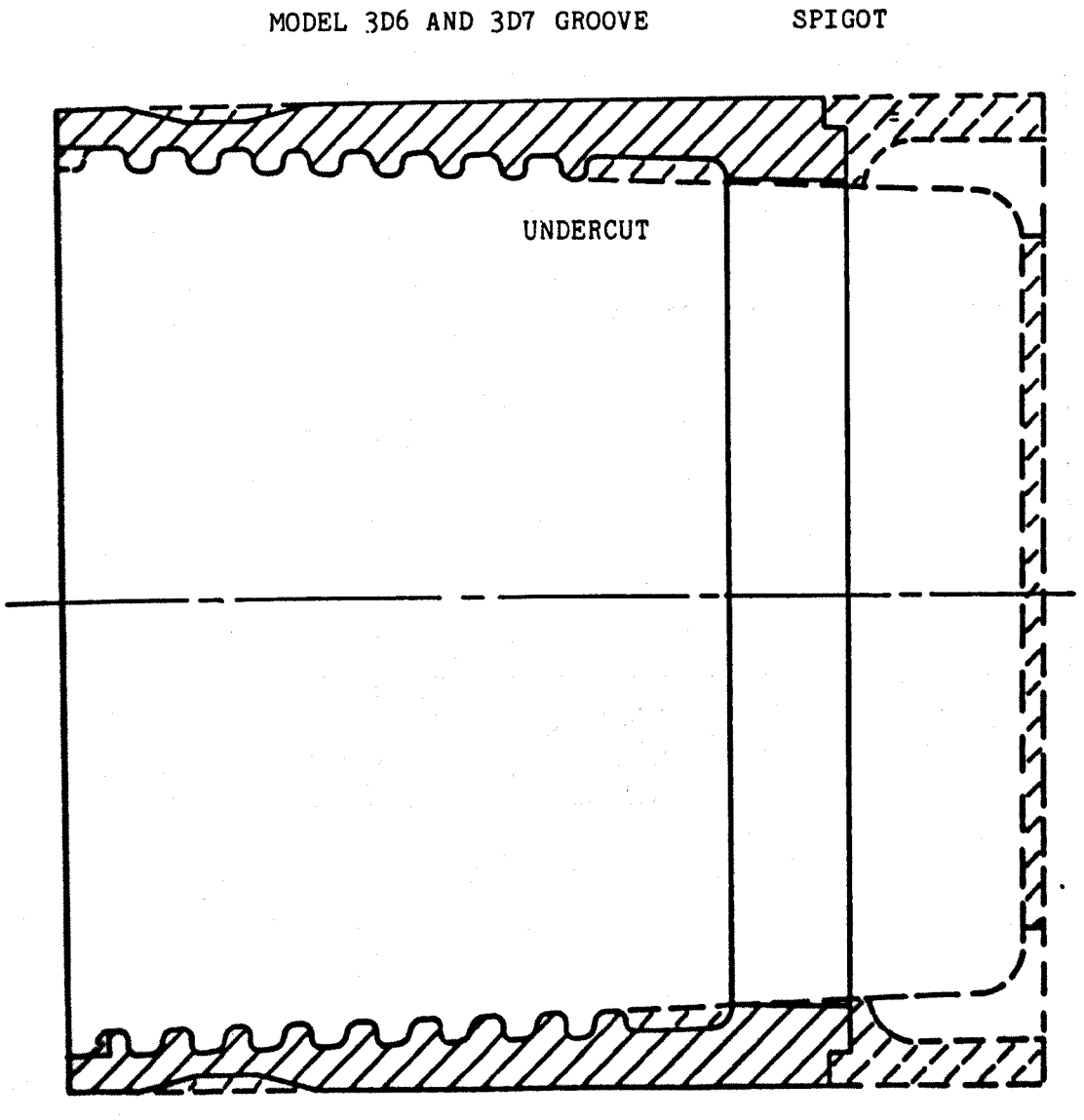

Fig 4.8 Machining of Precision Cast Tube Models

dotted lines show model as cast

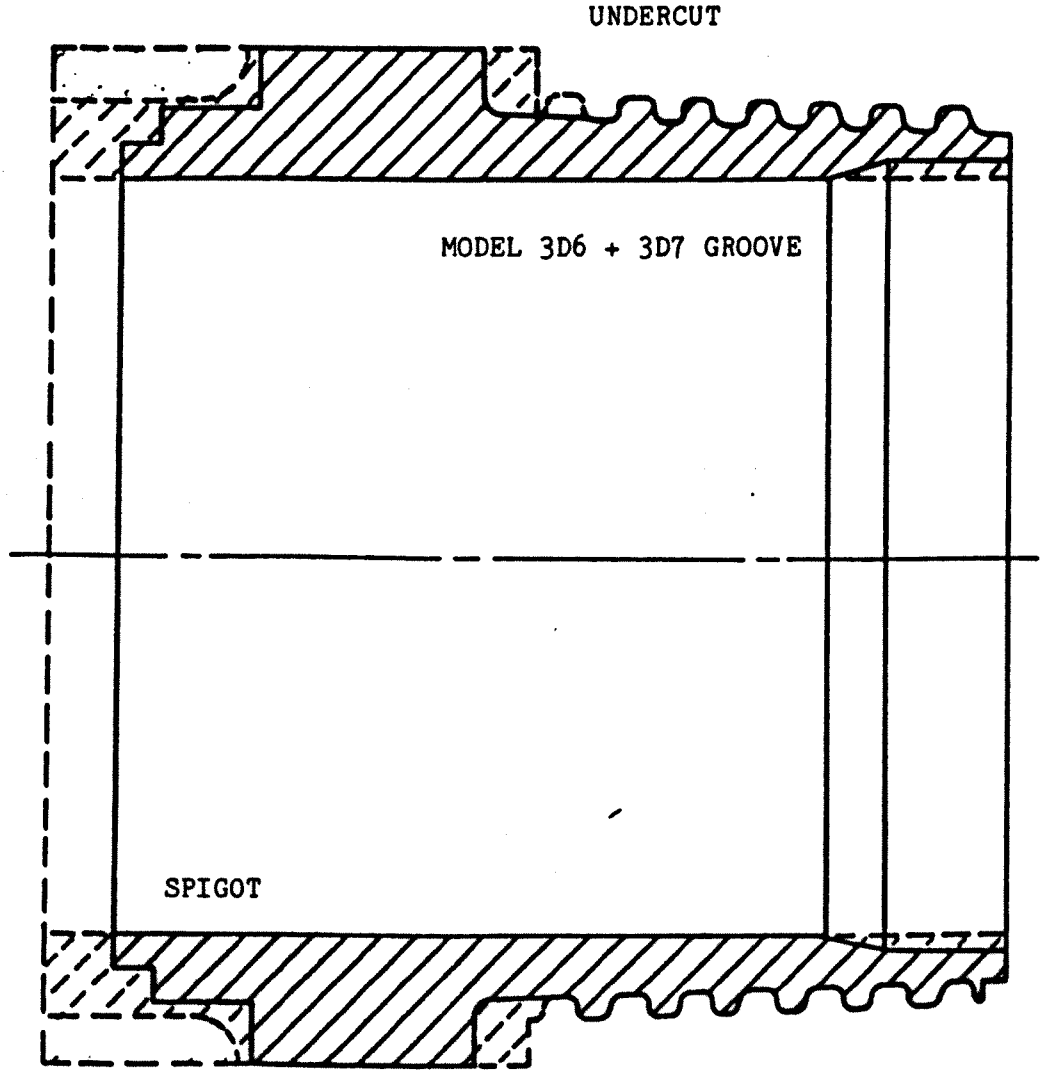

Fig 4.9

Machining of Precision Cast Coupling Models

dotted lines show model as cast

Precision Cast Model

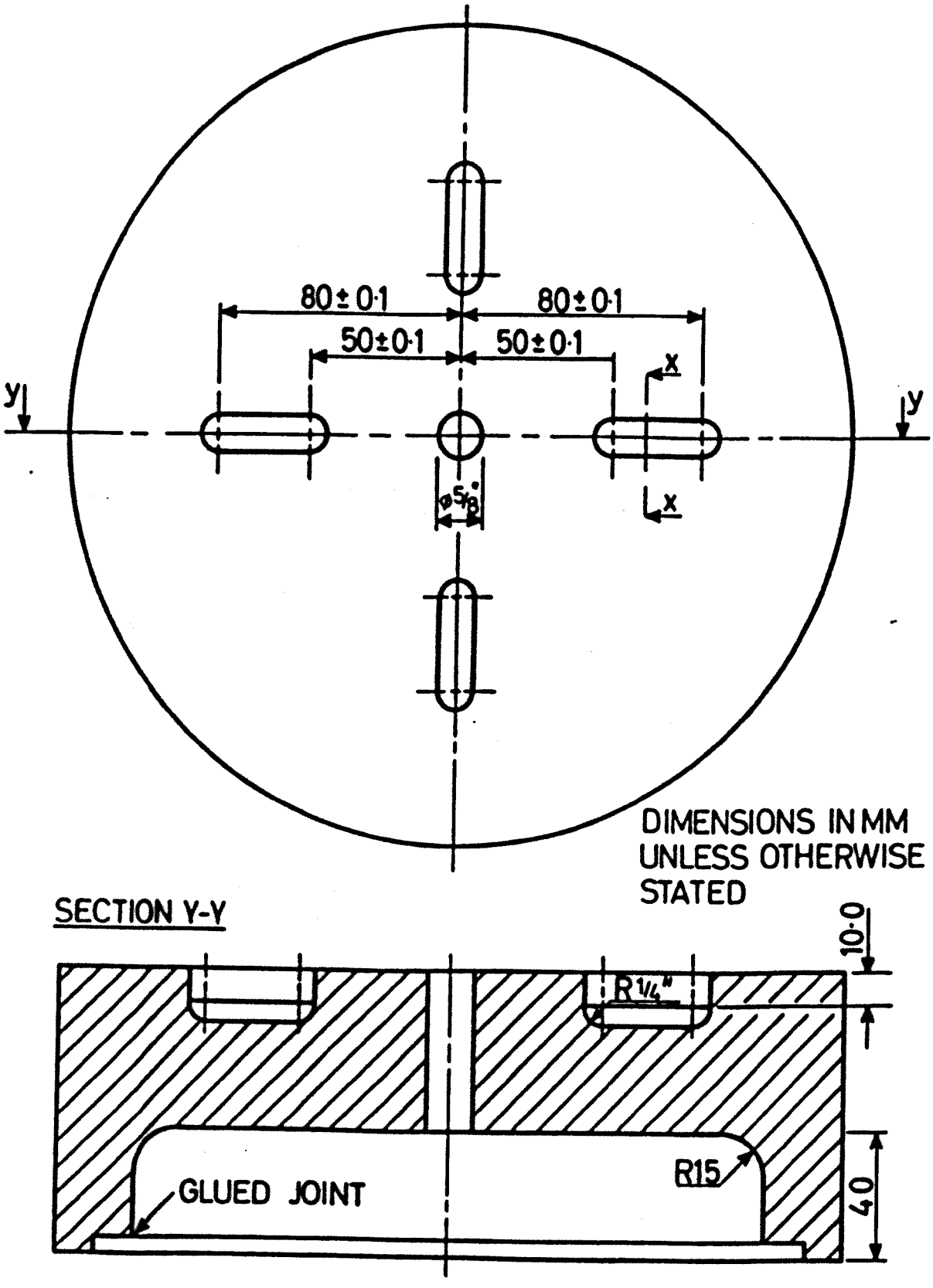

Fig 4.10

Extension Tube End Caps

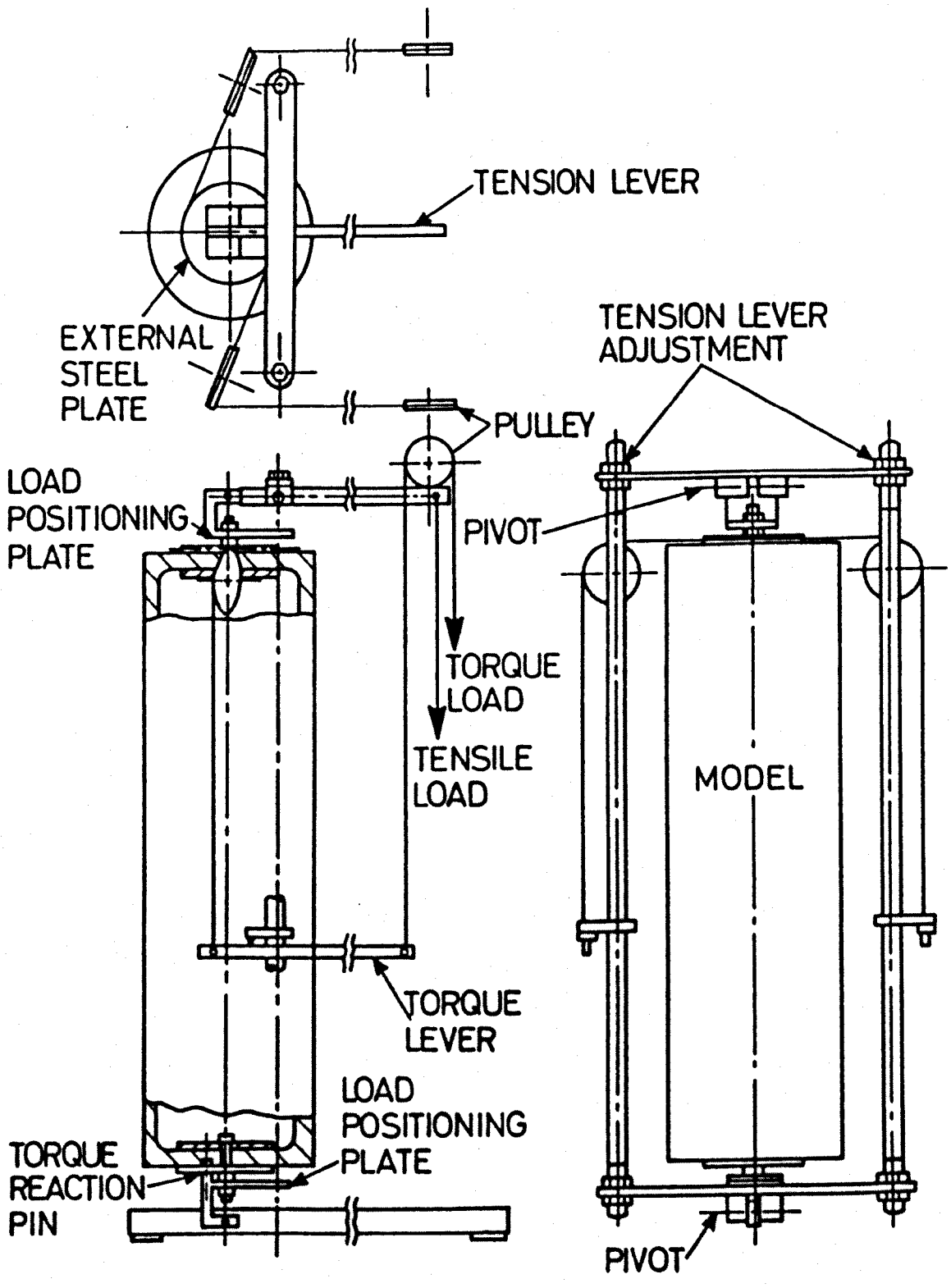

Fig 4.11

Model Loading Rig


Assembled Model in Loading Rig

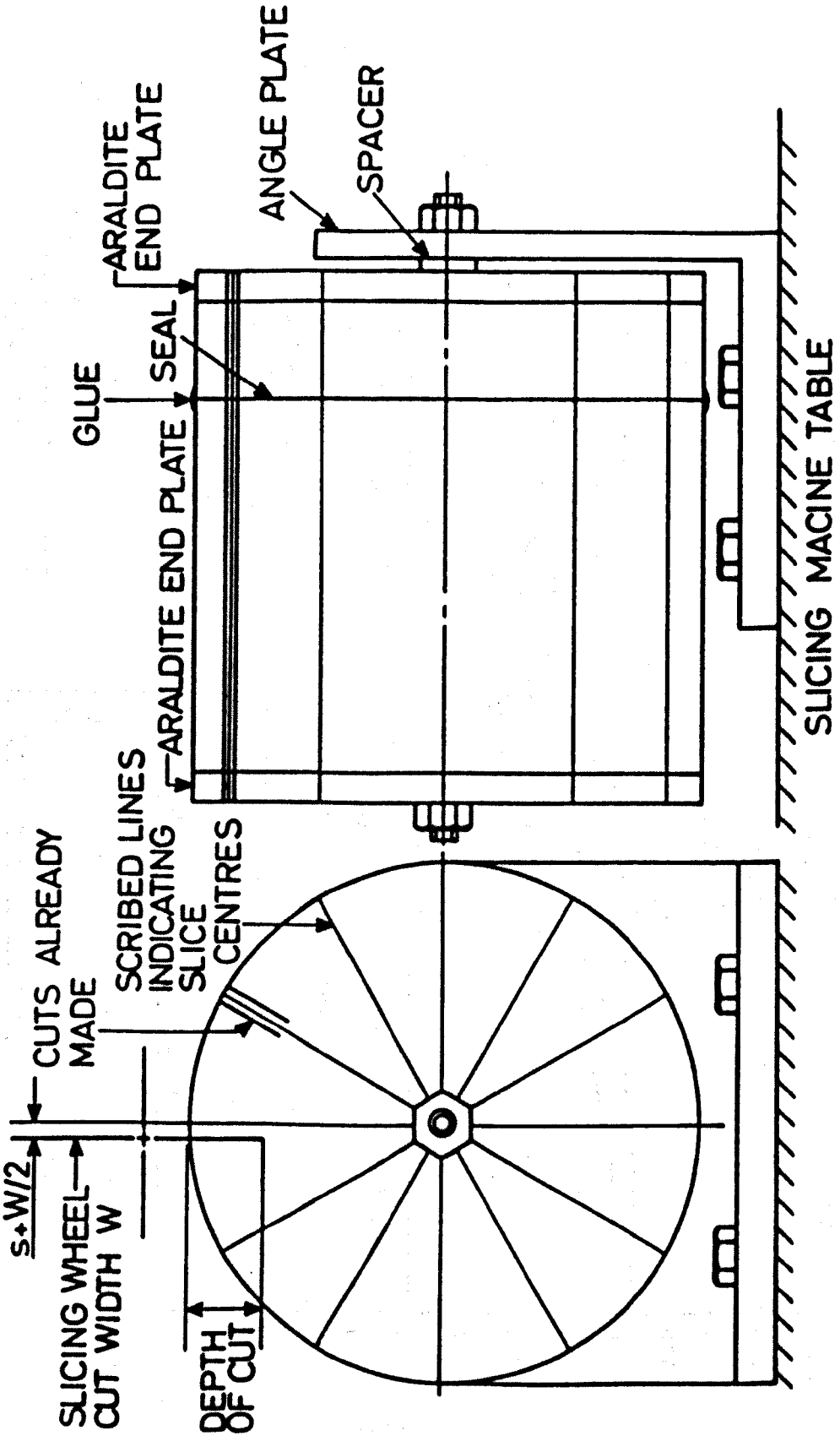

Fig 4.12

Model Slicing Arrangement

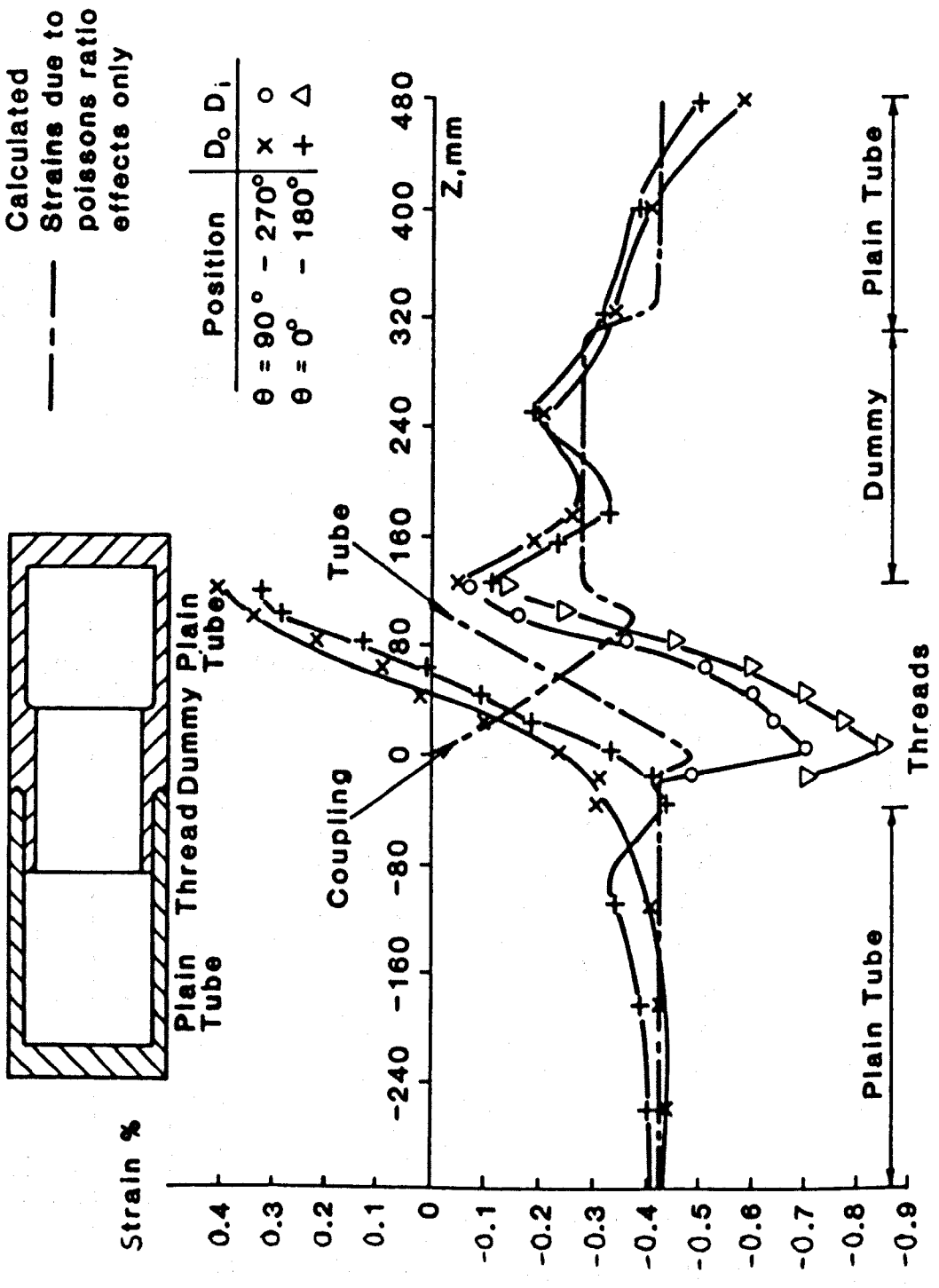

Fig4.13a

Diametral Strains in Model 1

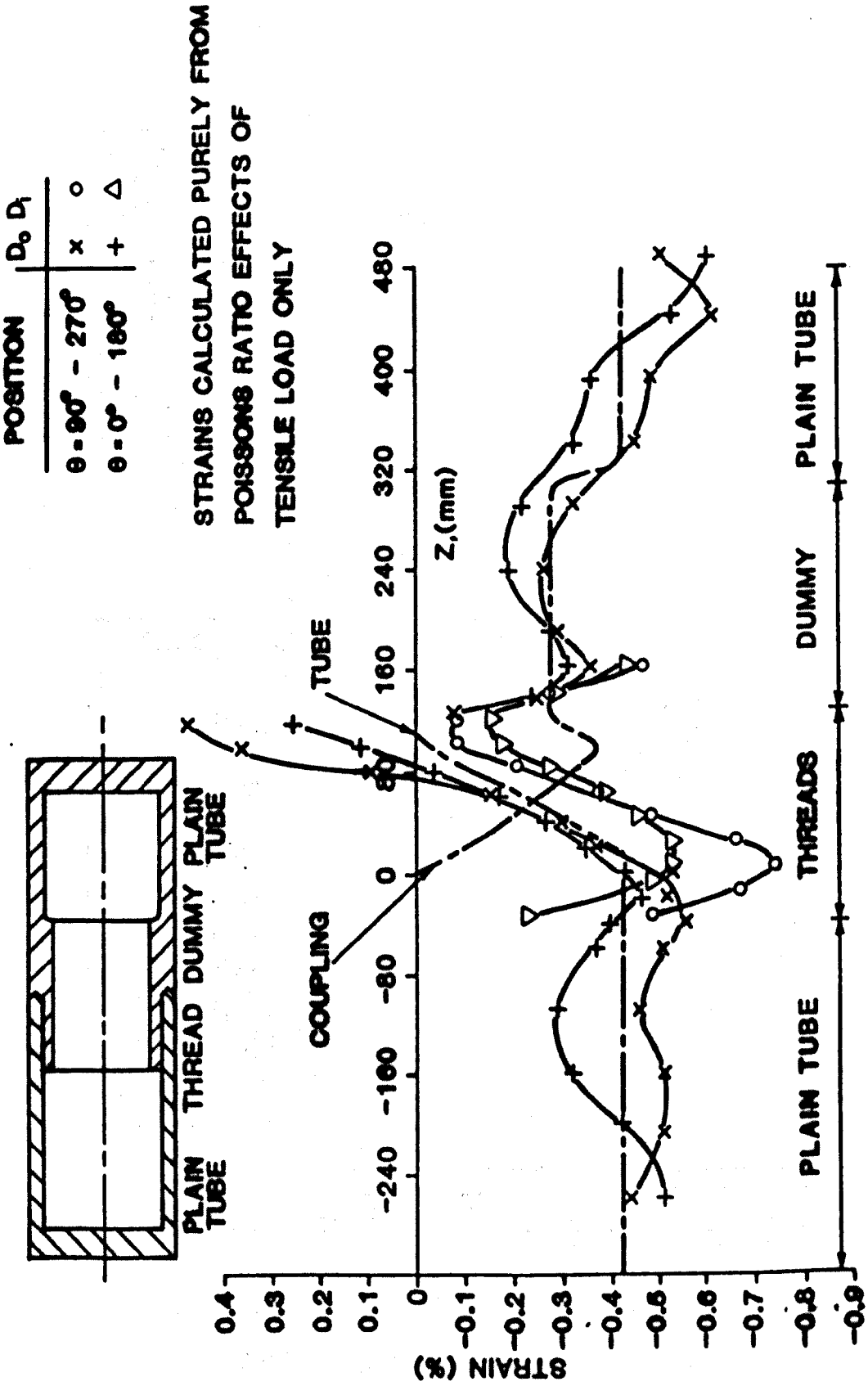

Fig 4.13b

Diametral Strains in Model 2

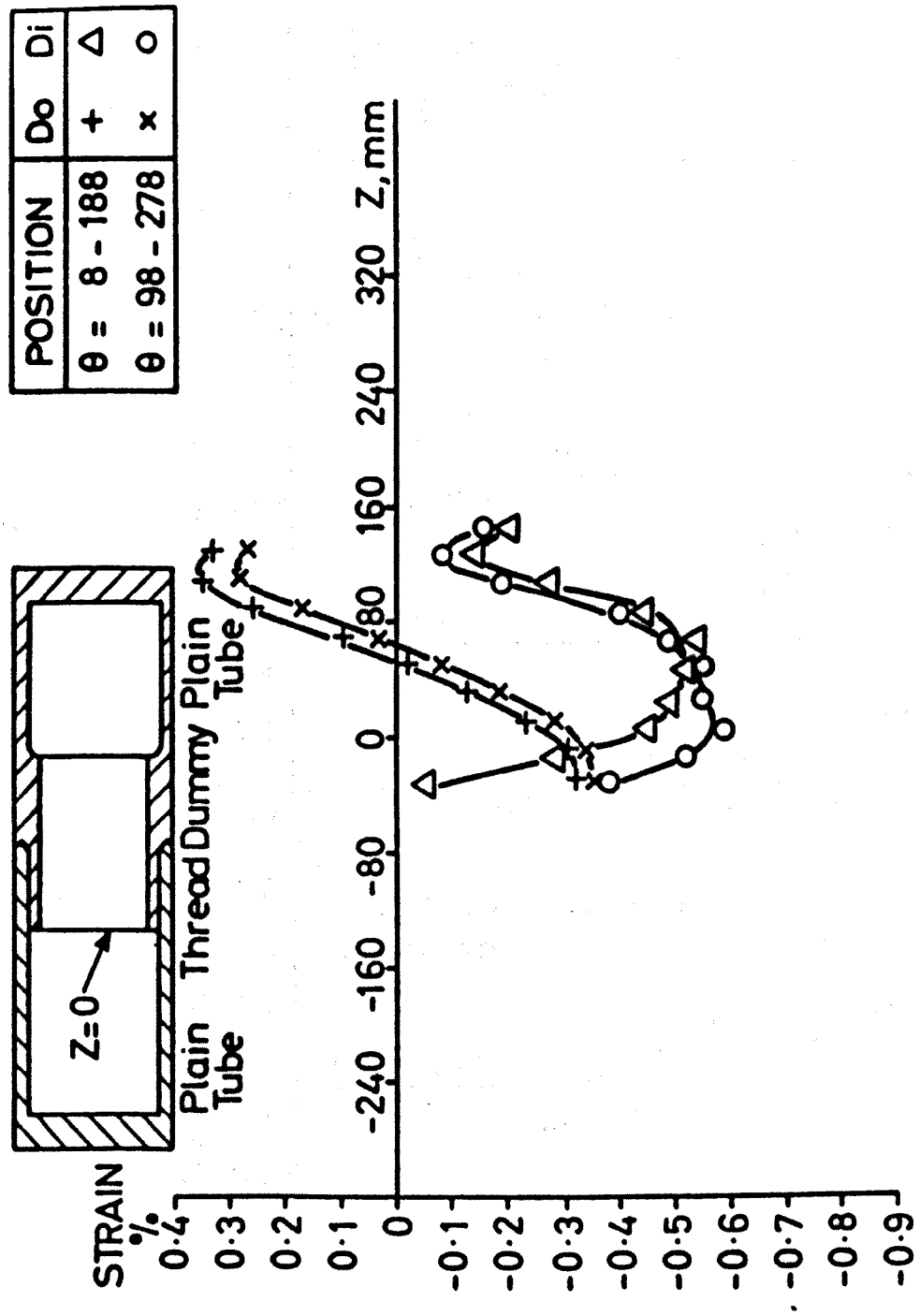

Fig 4.13c

Diametral Strains in Model 4

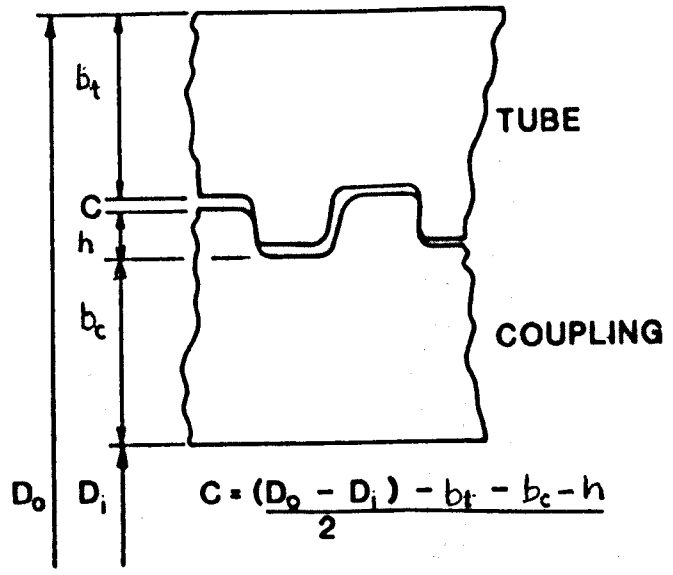

a) Model 1

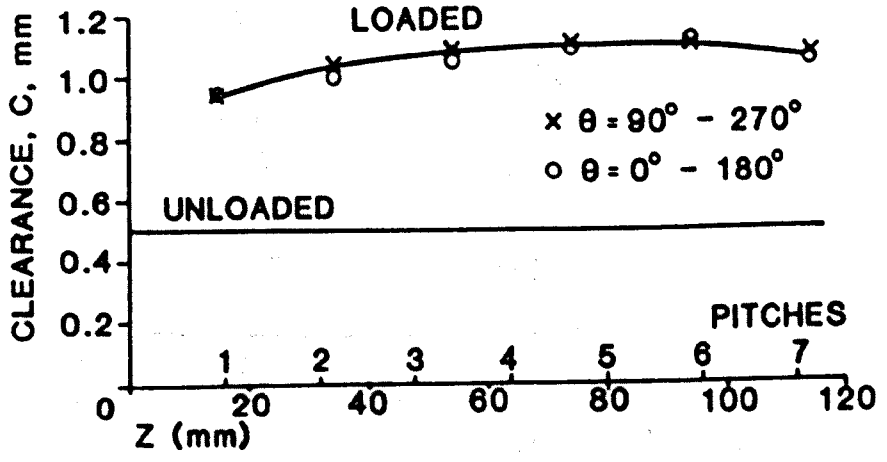

b) Model 2

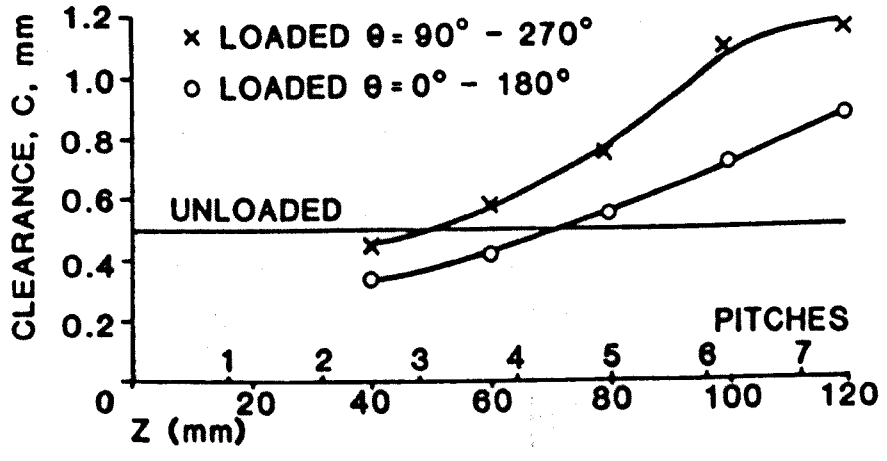

Fig 4.14a & b

Thread Root-Crest Radial Clearances of Models 1 and 2

c) Model 4

X θ = 8° - 188°

0 θ =98° - 278°

IF C > 1.98 mm contact occurs in fillets

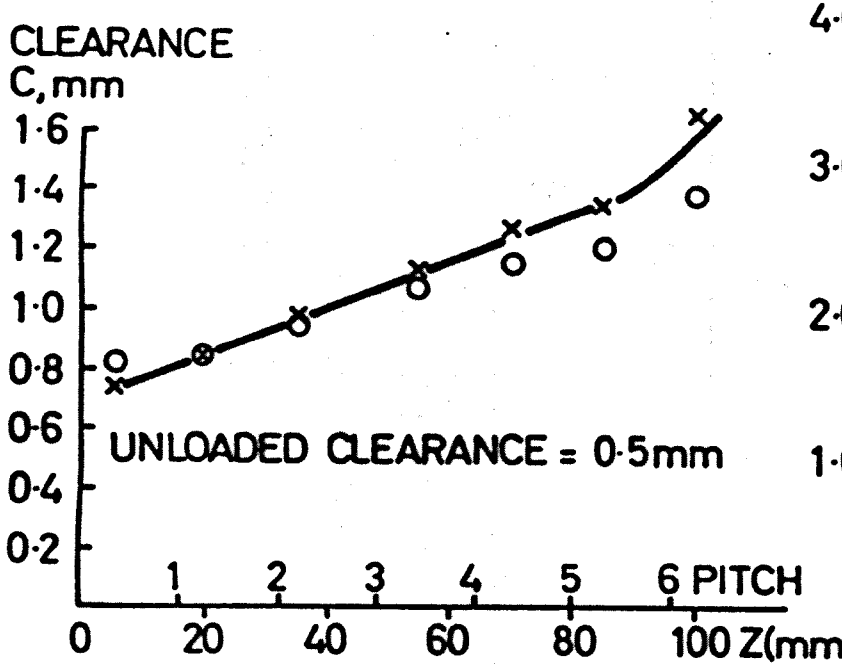

d) Model 6

θ

0 215

X 260

\+ 300

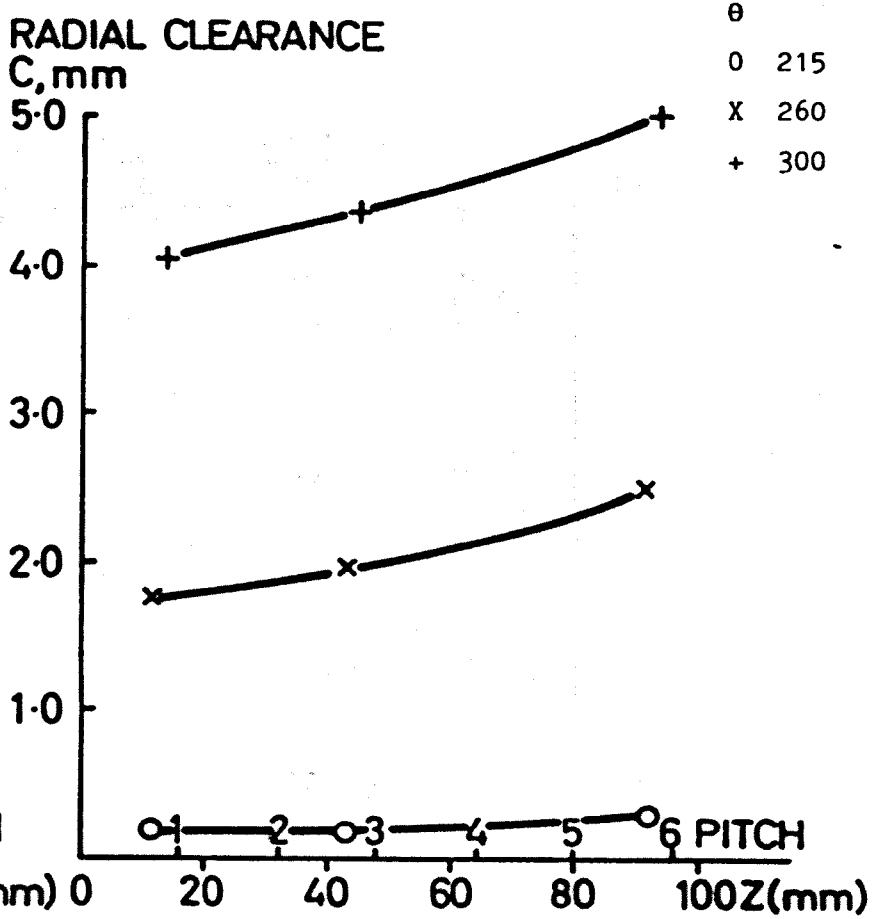

Fig 4.14c & d

Thread Root-Crest Radial Clearances of Models 4 and 6

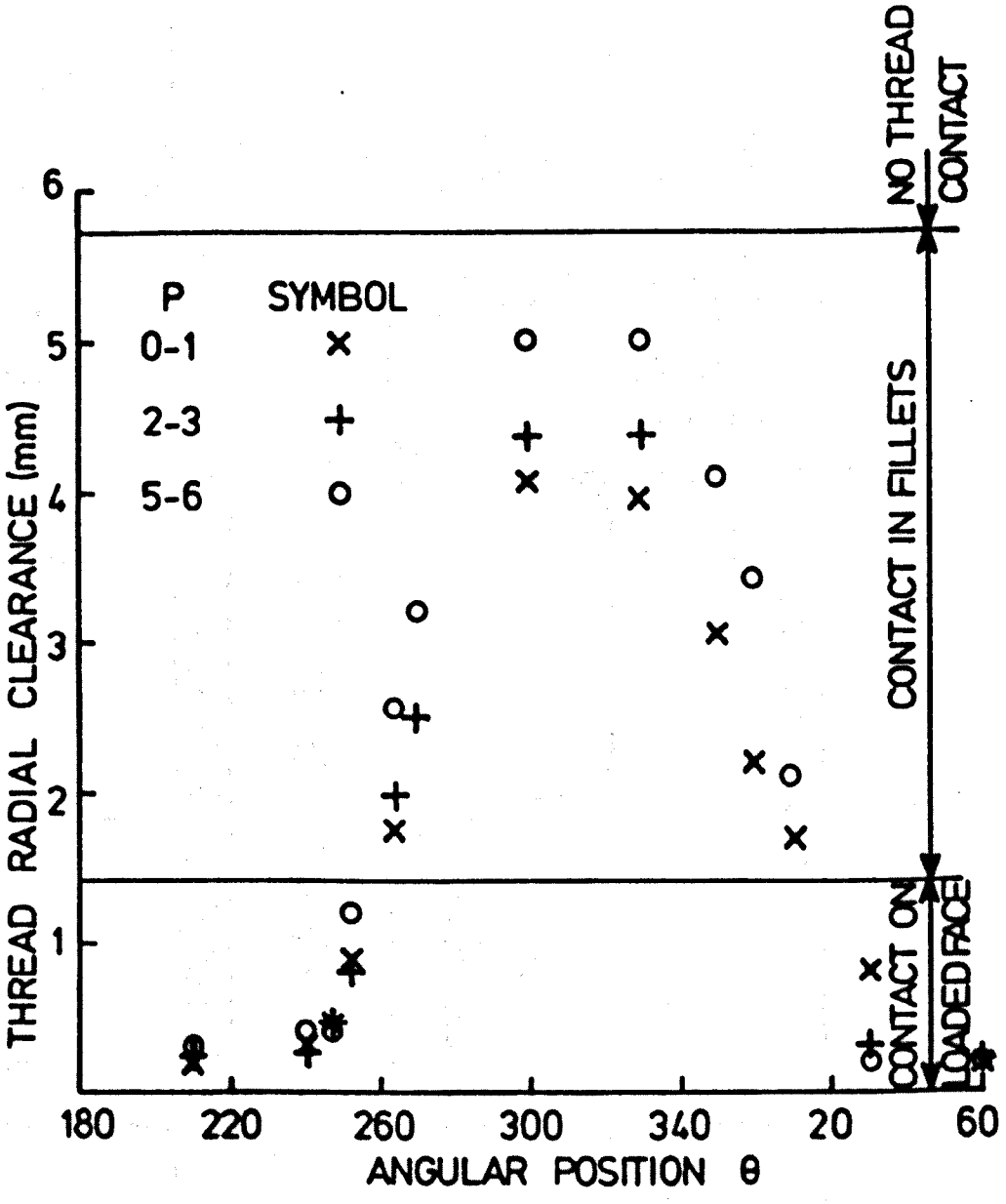

Fig 4.15

Variation of Thread Radial Clearances with Pitch and Angular Position In Thread 6

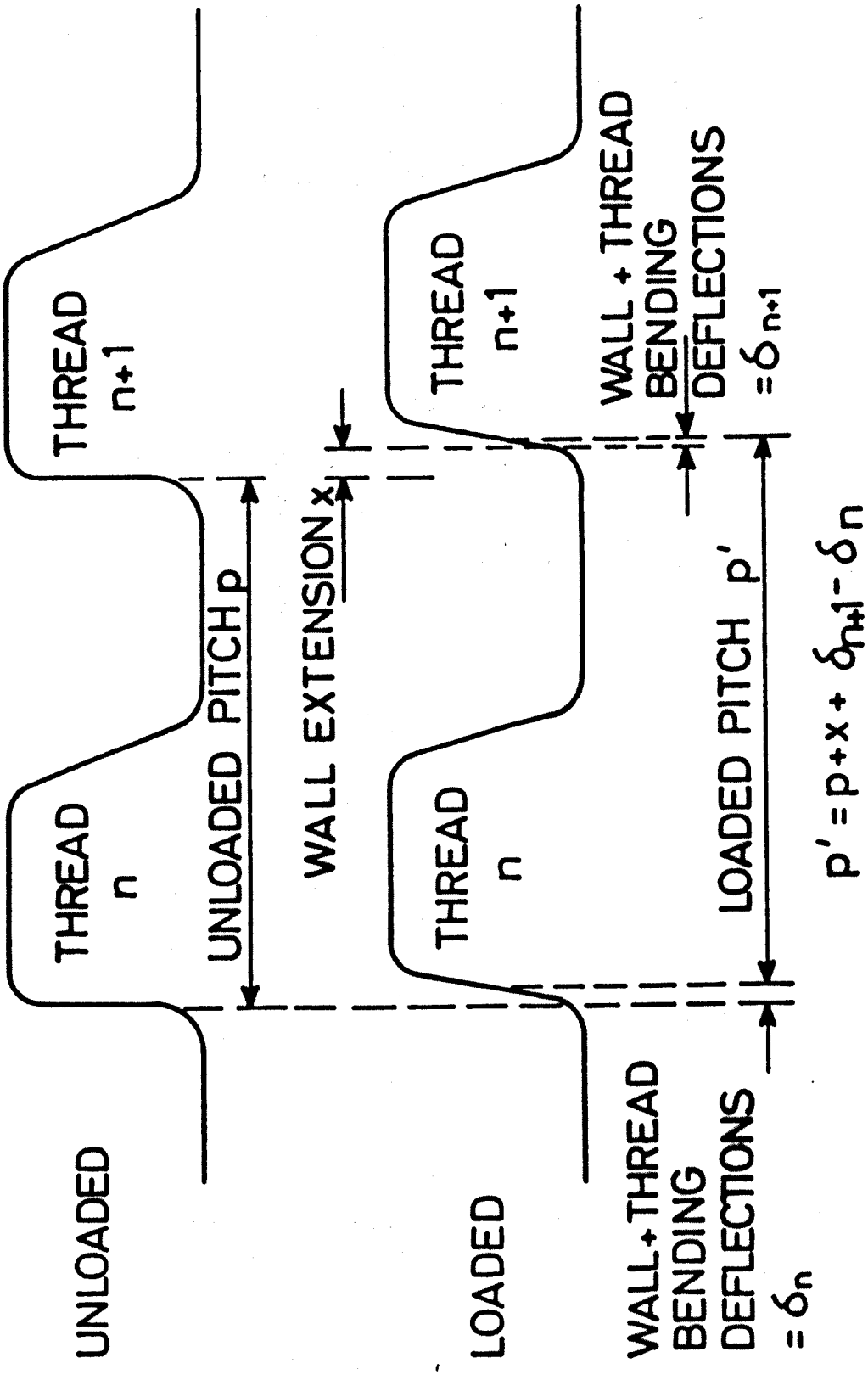

Fig. 4.16

Loaded Thread Deformations

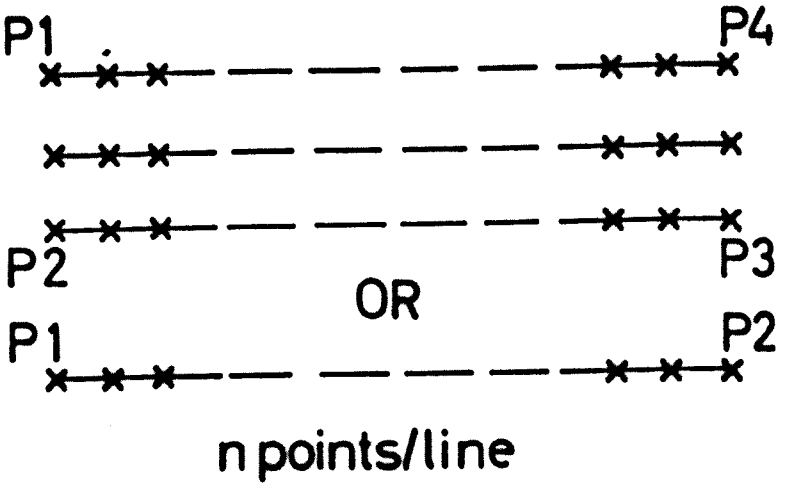

READADGRID

3 LINES, UP TO 50 EQUISPACED POINTS IN EACH

1 LINE UP TO 50 EQUISPACED POINTS

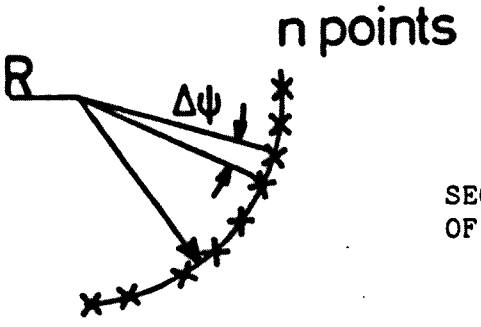

READARAD

SEGMENT OF RADIUS, ANY NUMBER OF POINTS, $\Delta\psi$ APART

Fig 4.17

Grids Showing Positions at which Photoelastic Measurements Made using the A.M.P.

CHAPTER FIVE

ANALYSIS TECHNIQUES

5.1 Photoelastic Measurements of Loads

The loads which have been applied to the models are axial tension F, preload Q and tension F eccentric from the model centre line by a distance d, which gives a bending moment = F.d

The axial tension is considered the primary load and is defined by σ_{nom}, the mean axial stress in the unthreaded tube

$$\sigma_{nom} = F/\pi t(D_o - t) \qquad \ldots\ldots 5.1$$

The eccentric tension is defined by the maximum bending stress at the outside diameter of the unthreaded tube σ_M where

$$\sigma_M = 32F.d\ D_o\ /\pi(D_o^4 - (D_o - 2t)^4) \qquad \ldots\ldots 5.2$$

and the normalised maximum bending stress

$$= \sigma_M/\sigma_{nom}$$

The preload is defined by the increased wall tension in the coupling undercut which equals the tube nose compression. The increased coupling undercut tensile stress

$$\sigma_{QC} = Q_o/\pi b_{max}\ (D_i + b_{max}) \qquad \ldots\ldots 5.3$$

and the tube nose compressive stress

$$\sigma_{Qt} = Q_o/\pi\ (b_{max} - L\tan\gamma)[D_o - (b_{max} - L\tan\gamma)] \qquad \ldots\ldots 5.4$$

For combined tension and preload, stresses are normalised by σ_{nom}. While for preload only, stresses are normalised by

$$Q_o/\pi t\,(D_o - t) \qquad \ldots\ldots 5.5$$

For models loaded with both preload and tension the measured preload is less than the applied preload because the release of contact in the seal by the tension.

Referring to a section between the threads and the seal (see Fig. 5.1) tightening the screwed connection causes a tensile force + Q_o in the coupling and an equal compressive force - Q_o in the tube.

Because the extensions of these parts of tube and coupling must be equal when an external tensile force F is applied to the joint and because the tube and coupling are made of the same material

$$\frac{F_c}{A_c} = \frac{E}{\varepsilon} = \frac{F_t}{A_t}$$

where F_c and F_t are the tensions in the coupling and tube due to the external force F (i.e. $F_t + F_c = F$)
and A_c, A_t are the corresponding cross-sectional areas.
Hence the total forces under both loads are in the tube

$$W_t = F_t - Q_o = F\,\frac{A_t}{A_c + A_t} - Q_o \qquad \ldots\ldots 5.6$$

and in the coupling $W_c = F_c + Q_o = F\,\dfrac{A_c}{A_c + A_t} + Q_o$ 5.7

If $F_t = Q_o$ then $W_t = 0$ and $W_c = \dfrac{FA_c}{A_c+A_t} + \dfrac{FA_t}{A_c+A_t} = F$

Because all the quantities except Q_o can be measured for the stress-frozen model, Q_o can be readily evaluated. From Equation 5.7.

For each model it was important to know accurately the applied load F and any remaining preload W_t so that σ_{nom} could be evaluated. Accurate measurements of F and W_c were also required to normalise the measured thread shear forces, see Section 5.2.

The applied tension and eccentric tension were determined by weighing the applied loads and measuring the distance of the loading from the model centre line. They were also determined from photoelastic measurements. Any remaining preload in the models manifests itself as tube nose compression and an increased coupling undercut tension and could only be measured accurately by photoelastic methods.

For each model the through-thickness distributions of fringe order and isoclinic angle were measured in the undercuts of both the tube and coupling at regular intervals around the models, generally 30^o. Typical distributions are shown in Fig. 5.2 for measurements taken using the AMP and taken manually. Close agreement was achieved between manual and automatic measurements and generally measurements were made manually.

It can be seen from Fig. 5.2 that the isoclinic angle was less than $\pm 4^o$, and this was general for all the slices analysed. Hence, the greater principal stress was axial, σ_z and the smaller, σ_r, insignificant. From each distribution of σ_z, the mean through-thickness axial stress was found, σ_T. Fig. 5.3 shows the distribution of σ_T and both surface values of σ_z for both the tube and coupling of Model 4. The distributions of σ_T and surface stresses for each of the other models are shown in Appendix 1.

From the distribution of q_T, the mean undercut axial stress $\bar{\sigma}_T$ was found and hence measurements of the applied load.

For the tube models,

$$F = \bar{\sigma}_T f \frac{\pi}{4} (D_o^2 - (D_o - 2 b_{max})^2) \qquad \ldots\ldots 5.8$$

and for the coupling models

$$F_c + Q_o = \bar{\sigma}_T f \frac{\pi}{4} ((D_i + 2 b_{max})^2 - D_i^2) \qquad \ldots\ldots 5.9$$

where f is the material fringe value which was determined from calibration strips cut from annealed tube and coupling slices, loading them in another stress freezing cycle and measuring the fringe orders. The Youngs Modulus of elasticity, E, for each model was also found from these calibration strips by measuring the strain and from knowledge of the applied load and cross sectional area.

The measured shear force distribution of Model 4, see Section 8.1, showed that the threads carried 86% of the applied tension. It was noticed that there was contact in the conical seal and some stress in the tube nose. Manual photoelastic measurements in the tube nose showed compressive axial stresses at the threaded surface and tensile axial stresses at the unthreaded outside diameter and large variations in isoclinic angle through the thickness. Accurate meaurements of σ_z could not be made manually, hence stress separations in the tube nose in the $\theta=0^o$ and $\theta=180^o$ planes were carried out. Measurements of maximum shear stresses in the r-z and r-θ planes were obtained with the A.M.P. and the Frocht shear difference (19) method was used to calculate the sub-surface distributions of cartesian stresses, σ_r, σ_z and σ_θ and shear stresses $\tau_{r\theta}$ and τ_{rz}. A typical example is shown in Fig 5.4 for the $\theta=180^o$ position. The measurements of Fringe orders, isoclinic angles,

shear stresses, shear stress gradients and cartesian stresses are shown in Appendix 2. From the through thickness distribution of σ_z, the remaining wall tensions were found and are shown below. The method and theory are explained thoroughly in Ref. 18.

θ^o	Mean σ_z N/mm^2	Average σ_z N/mm^2	Average Wall Tension ,N
0	0.114	0.245	206
180	0.375		

The average remaining wall tension in the tube nose ≃ 15% of the applied tension. It is assumed that friction between the tube nose and coupling lip prevented the coupling undercut from straining fully. Also the contact in the seal region was due to a radial force caused by tube model wall bending. The equilibrium of forces is explained more fully in Appendix 3.

For all the other models, the remaining preload was obtained by taking the tube undercut tension from the coupling undercut tension i.e. $F - W_c$.

Table 5.1 gives the material properties, photoelastically measured loads, the weighed axial loads and full tube mean stresses and strains.

5.2 Measurements of Thread Shear Forces

Each thread analysed was set up in the AMP such that the thread root was parallel with the x-axis of the AMP (it is assumed that the thread root remained parallel to the model centre line during loading).

The AMP was then used to measure the fringe order n and isoclinic angle Φ along a line parallel to the thread root starting from between

TABLE 5.1 - MATERIAL AND MODEL PROPERTIES AND LOADS

Model Reference:	1	2	3	4	5	6	7	8	9	10
Frozen Stress MATERIAL										
Tube material fringe value, N/mm fr	0.258	0.270	0.268	0.265	0.255	0.249	0.250	0.254	0.252	0.250
Coupling material fringe value, N/mm fr	0.258	0.266	0.271	0.265	0.263	0.245	0.250	0.250	0.254	0.249
Tube Young's modulus, N/mm^2	12.3	13.2	13.1	13.1	10.4	10.8	10.8	11.5	11.0	11.3
Couplings Young's modulus, N/mm^2	12.3	13.0	13.0	13.1	11.6	10.4	10.6	11.0	11.2	11.2
LOADS										
P.E. Measured tube nose load, N	-	-	-	-206	-	-	-	-	-	-
Calculated preload, from Equation 5.7, N	0	0	0	-630	0	0	580	333	420	652
Applied Tension, from weights, N	1987	1987	1133	1490	1180	1050	0	690	764	0
P.E. Measured tube undercut tension, F, N	1893	2030	1198	1510	1213	1051	0	690	764	0
P.E. Measured coupling undercut tension F+Q N	1990	1955	1151	1384	1164	953	580	1023	1184	652
Bending moment at tube undercut, Nm	0	126	0	0	0	0	0	0	0	0
NORMALISED										
Mean axial stress in tube due to tension N/mm^2	0.104	0.104	0.072	0.078	0.080	0.071	0	0.046	0.051	0
Mean axial strain in tube due to tension %	0.85	0.79	0.55	0.59	0.77	0.66	0	0.40	0.47	0
σ_M/σ_{nom} from fringe measurements	0	1.19	0	0	0	0	0	0	0	0

the root and the thread contacts. The data was stored on floppy discs and analysed at a later time using the program 'EDPLOTNCRUNCH' (34). This program can be used to 'edit in' the integral fringe value, convert the data into fr/mm by dividing by the slice thickness s, and calculate the shear stresses parallel to the x axis of the AMP (equivalent to the z axis of the model) in N/mm^2 by multiplying by f

i.e. $\tau_{rz} = \frac{nf}{2s} \sin 2\Phi$, N/mm^2 ..... 5.10

Generally τ_{rz} was obtained at 30 equi-spaced position (i.e. $\delta z \simeq 0.25mm$) across the thread. The first and last measurements were taken 0.1 mm from the free surfaces so that edge and moisture effects did not influence the readings. A typical distribution of shear stress is shown in Fig 5.5 and further distributions are shown in Appendix 4. In order to determine the thread load V, the shear stresses were integrated with respect to z using Simpsons Rule. Extrapolated values of τ_{rz} were used at the free surfaces and included in the numerical integrations

Table 5.2 snows the positions in each model where the shear forces, V, were measured. Measurements were not taken in the couplings of most models because measurements in the $\theta=60^{o}$ and 300^{o} planes of Model 4 snowed that coupling shear force $\simeq$ tube shear force for mating threads (this was expected from equilibrium).

Measurements were taken in the loaded runout of Models 3 and 4 at different values of w in order to investigate the effect of this type of runout on the shear force distribution.

The planes of measurements of Models 4 and 5 were chosen arbitarily since the distribution of wall tension around both tubes and couplings were constant (see Fig. 5.3 and A1.3).

TABLE 5.2 - POSITIONS WHERE SHEAR FORCES WERE MEASURED

	MODEL NUMBER					
POSITIONS OF LOAD MEASUREMENTS	3	6	4	5	9	10
EVERY PITCH OF θ=						
FOR COUPLING	-	-	60,300	-	-	-
FOR TUBE	-	-	60,300 180	0,90,180, 270	0,90 180,270	0,90,180 270
NUMBER OF MEASUREMENTS IN LOADED COUPLING RUNOUT	5	-	5	0	0	0
MEASUREMENTS IN LAST LOADED THREAD	-	-	-	EVERY 30°	EVERY 30°	-
FURTHER MEASUREMENTS	-	IN 'BELLED-OUT' REGION	-	-	-	-

For Models 9 and 10, the θ=0, 90, 180 and 270 degree planes were chosen since they contained the minimum and maximum wall tensions (see Fig. A1.8 and A1.6). In addition, measurements were made every 30° in tne last pitch of Models 5 and 9 (the preloaded end of Model 9).

The shear force distribution was also measured in the 'belled-out' region of Model 6 in order to investigate the effect of thread clearance on load (see Section 8.3).

For Models 3, 4, 5, 6, and 9 the nominal thread load

$$V_F = \frac{\text{Applied Tension}}{\text{Spiral length of thread contact}}$$

$$\therefore V_F \doteq \frac{F}{(p^2+\pi^2 D_m^2)^{\frac{1}{2}} L/p} \qquad \ldots 5.11$$

Model 10 was analysed in order to determine whether the shear forces due to preload can be simply superimposed upon those due to tension to obtain the normal in service condition of tension and preload. Also tne effect of preload only (initial torquing up) was of interest.

Hence Model 9 represents tension and preload case. In order for Model 9 to be directly compared with Model 10, the preload had to be scaled down by a factor of $Q_{MODEL10}/Q_{MODEL9} = 1.55$ and normalised by the same tension as Model 9.

Hence, for comparison with Model 9, the nominal thread load for the preloaded Model 10

$$V_Q = \frac{1.55\ F_{model\ 9}}{(p^2+\pi^2 D_m^2)^{\frac{1}{2}} L/p} \qquad \ldots 5.12$$

In order to investigate the influence of preload the thread loads of Model 10 were also normalised by

$$\frac{Q_{MODEL10}}{(p^2+\pi^2 D_m^2)^{\frac{1}{2}} L/p}$$

5.3 Photoelastic Analysis of Stresses In Threads

5.3.1 Introduction

The surface stress distributions around several threads in different positions of models were obtained in detail. Fig 5.6 presents some of these normalised stress distributions. The greatest stresses occur in the loaded fillet and at the contacts. Fringe orders are differences of principal stresses; they are here defined as (stress tangential to thread profiles) - (stress perpendicular to thread profile). The compressive contact pressure therefore increases the fringe order and the values in the contact regions are upper bounds of tangential stress.

As expected, there are tensile maxima in the loaded fillets. The maximum contact fringe orders are of comparable magnitude with the fillet maxima. In Model 1, see Fig. 5.6a, contact was concentrated in the radii due to the machining errors of the thread profile, see Section 4.1.2. Significant negative fringe orders in the flat part of the loaded flank, where there was no contact, are attributed to radial compression due to the radial components of concentrated contact pressure in the fillets. In the correctly machined Model 4, a more even distribution of contact fringes was observed, see Fig. 5.6b.

The stresses in the unloaded fillets varied in both magnitude and sign along the thread spiral. In regions of large wall tensile force, i.e. near $z = 0$ in the tubes and near $z=L$ in the couplings, tensile stresses only were present but in regions of low or negative tensile wall force near $z = L$ in the tubes and near $z = 0$ in the couplings, compressive fillet stresses only were present. In between, tensile

stresses due to tensile wall force and compressive stresses due to thread bending were often present in the same fillet.

It was impracticable to measure the surface stresses in such detail on each thread, but from the above measurements it was concluded that the 'loaded' fillet (between thread root and contact face) and the contact were the only positions around the profile where extensive measurements along the thread spiral needed to be carried out.

Work has shown (23) that the stresses in screw threads or other similar loaded projections are due to a combination of the effects of i) the forces in the wall sections beneath the projection and ii) the shear forces applied directly to the projection.

In each photoelastic model, there were threads which were outside the region of thread contact and the wall beneath them carried the full wall force i.e. threads in the region $z<0$ for the tube and $z=L$ for the coupling. The stress distributions around these threads were analysed in detail using the AMP, see Section 5.3.2.

The effect of shear force on fillet stress distribution was examined in the loaded coupling runout threads between $z=0$ and $z=p/2$ of Models 2,3 and 4. These models had the full 180° of runout loaded, and hence a large range of w/b. Later models had truncated coupling runouts, see Table 3.1, and hence a reduced range of w/b. Loaded runout threads carried relatively large shear forces, but little wall tension was present, see Section 5.3.3.

The distribution of peak fillet stresses in the loaded fillets of both tube and coupling were measured for each model, see Section 5.3.4.

Distributions of contact stresses radially, axially and in the hoop direction were measured using the AMP in selected positions of Model 4.

Model 4 with its distributed contact stresses was considered representative of likely prototype contact stress conditions, see Section 5.3.5.

5.3.2. Stresses in Thread Fillets due to wall tension only

To investigate the effect of thread shape on the fillet stresses due to wall force only, the stress distributions in the fillets of unloaded runout threads were measured. Fig. 5.7 shows the shapes of tne threads analysed. These regions were chosen because of the large variations in w/b.

It was noticed that the peak fillet stress was consistently in the region of $0^{o} < \phi < 10^{o}$ and that the fillet stresses reduced as Ψ increased. Each thread analysed was positioned in the AMP and, using the program 'READARAD', measurements of fringe order were made at $\phi = 2\frac{1}{2}^{o}$ intervals from $\phi = 0^{o}$ to values of ϕ where the fillet stress $\sigma_a < 0.1$ fr/mm. These measurements were made 0.1 mm sub-surface so as to minimise any errors due to moisture effects. The AMP was also used to measure n and Φ radially from the fillet, see Fig. 5.8. These measurements showed large stress gradients $\partial\sigma_a/\partial r_f$, which were greatest at the value of ϕ where $\sigma_a = \hat{\sigma}_a$ (symbol o on Fig. 5.8). Hence the measurements 0.1 mm sub-surface underestimated the values of σ_a and overestimated $\partial\sigma_a/\partial\phi$, the surface stress gradient around the fillet.

Fig. 5.9 shows a typical set of fringe measurements taken 0.1 mm subsurface compared with surface measurements. For each thread analysed, radial lines of measurements were made at selected values of ϕ, similar to those shown in Fig. 5.8. The surface values were obtained by extrapolating to the edge, hence removing errors due to moisture absorption. These extrapolated surface values were used in the analysis. For each thread analysed, b and w were measured under the

high magnification of the A.M.P. and the outline of the fillet radius traced using the 100 x magnification shadow graph, so that R could be measured.

The mathematical KIRSCH solution (see Appendix 5) for a hole in an infinite plate loaded with tension σ_{sa}, shows that the surface stress

$$\sigma_a = \sigma_{sa}(1+2 \cos 2\phi) \qquad \ldots 5.13$$

This relationship was the basis for assuming that the thread fillet stresses due to wall tension should vary linearly with cos 2ϕ. Typical surface values of σ_a v cos 2ϕ are plotted in Fig. 5.10. For the threads with 'perfect' fillet radii (symbol + in Fig. 5.10), the stress distributions were linear with respect to cos 2ϕ but threads with non circular, compound radii (due to machining errors) were non-linear (symbol Δ in Fig. 5.10). For each thread, the fillet surface stress due to wall tension, σ_a was normalised by the mean through thickness wall tension σ_{sa} which were both non-dimensionalised by σ_{nom}, the mean full tube wall tensile stress. The fillet stress distribution can be characterised by the equation

$$\sigma_a = \sigma_{sa} (C_1 + C_2 \cos 2\phi) \qquad \ldots 5.14$$

where C_1 and C_2 are coefficients which Section 8.2 will show are dependent on the parameters w/b and R/b.

For the threads analysed, which were adjacent to the undercuts, $\sigma_{sa} = \sigma_T$, which had been obtained from the load calibrations (see Section 5.1).

5.3.3 Stresses in Thread Fillets due to Shear Forces

The stress distributions around thread fillets in the loaded runouts were measured using the AMP in a similar manner to threads loaded with wall tension only. In addition, the shear forces applied to

each thread were measured as described in Section 5.2. The distance of the centre of the contact fringes from the thread root, e, was also measured.

The loading of the thread on a tubular member creates both wall tension σ_{sa} and wall bending σ_{sf}. The magnitude of the bending moment at any position along the tubular depends on the distance e of the resultant shear force from the surface, the bending stiffness of the tubular defined by the diameter D_i and wall thickness b and of the distance z_m from the bending moment. The distribution of bending moment, $F(M_o)$ can be determined from 'beam on elastic foundation' type calculations, see Appendix 6. From the calculated bending moment at the thread $F(M_o)_{z_m=0}$ a nominal surface bending stress σ_{SF} was obtained from

$$\sigma_{SF} = \frac{6F(M_o)_{z_m=0}}{b^2} \qquad \cdots\cdots \quad 5.15$$

and σ_{SF} was used to normalise σ_F, the fillet stresses due to shear force. The fillet stresses due to the wall tension caused by the shear force had to be taken from the fillet stress distribution σ_L, to obtain the stress distribution due to shear force σ_F as shown in Fig. 5.11.

$$\sigma_F = \sigma_L - \sigma_a \qquad \cdots\cdots \quad 5.16$$

$$\sigma_F = \sigma_L - \sigma_{sa}\,(C_1 + C_2 \cos 2\phi) \qquad \cdots\cdots \quad 5.17$$

It can be seen from Fig. 5.11 (symbol x) that the peak fillet stress due to shear force only, σ_F occurs near $\phi=45^\circ$ and that σ_F reduces as ϕ tends to 0° and 90°.

Both σ_F and σ_{SF} were normalised by σ_{nom} and σ_F/σ_{SF} was plotted against sin 2ϕ, a typical example is shown in Fig. 5.12. Generally values of σ_F for $0^\circ<\phi<45^\circ$ were similar to $45^\circ<\Psi<90^\circ$ but differences did occur, particularly as e/R tended to 1. Since the measured peak fillet stresses due to combined loading occurred between $0^\circ<\phi<45^\circ$ only the values of σ_F in this region were plotted against sin 2ϕ . The linear region of the curve between $\phi=0^\circ$ and $\phi\simeq 40^\circ$ was characterised by the equation.

$$\sigma_F = \sigma_{SF} (C_3 + C_4 \sin 2\phi) \quad \ldots\ldots \quad 5.18$$

Due to the machining errors in the coupling thread fillets of Model 2, (see Section 4.1.2.) accurate values of σ_a could not be determined for this model hence values of σ_F could not be obtained.

5.3.4 Analysis of Peak Fillet Stresses

For each tube and coupling model the magnitudes of peak fillet stresses were measured manually at 30° intervals in the first and last loaded pitches and at 90° intervals in between, starting at $\theta=0^\circ$. The peak fillet stresses were normalised as described in Section 5.1. In several of the models the position of the peak fillet stress, ϕ_{max}, was measured at each of the above positions. This was done by positioning the isoclinic at the position of peak fillet stress and reading ϕ_{max} from the angle of rotation of the polariser and analyser.

5.3.5 Photoelastic Analysis of Contact Stresses

Contact stresses in the most highly loaded position (P=5.75) of the correctly machined Model 4 were studied in detail with the AMP. As would be expected from Hertz theory and experimental work (32), the greatest contact stresses occurred below the surface. It can be seen from Fig.

5.6b that contact occurred over the full extent of the loaded face but tended to be concentrated at a few distinct points, probably at surface asperities.

Using the AMP, distributions of fringe order and isoclinic angle were measured:-

i) parallel to the loaded face, at the sub-surface position of the peak fringe order and

ii) along several lines perpendicular to the loaded face in the region of the peak contact fringe order

From the above, the radial and axial stress difference gradients could be determined. In order to measure the hoop stress difference gradient, the 1.89mm thick slice at P=5.75 was cut into 2 slices 0.5mm and 1.0 mm thick. The distributions of fringe order were measured at the same positions in each of these slices.

Due to the change in sign of the shear stress gradients from one side of a contact point to the other and the very steep shear stress gradients in the hoop and axial directions, the Frocht shear stress difference method could not be used to accurately determine the cartesian stresses in the contact region.

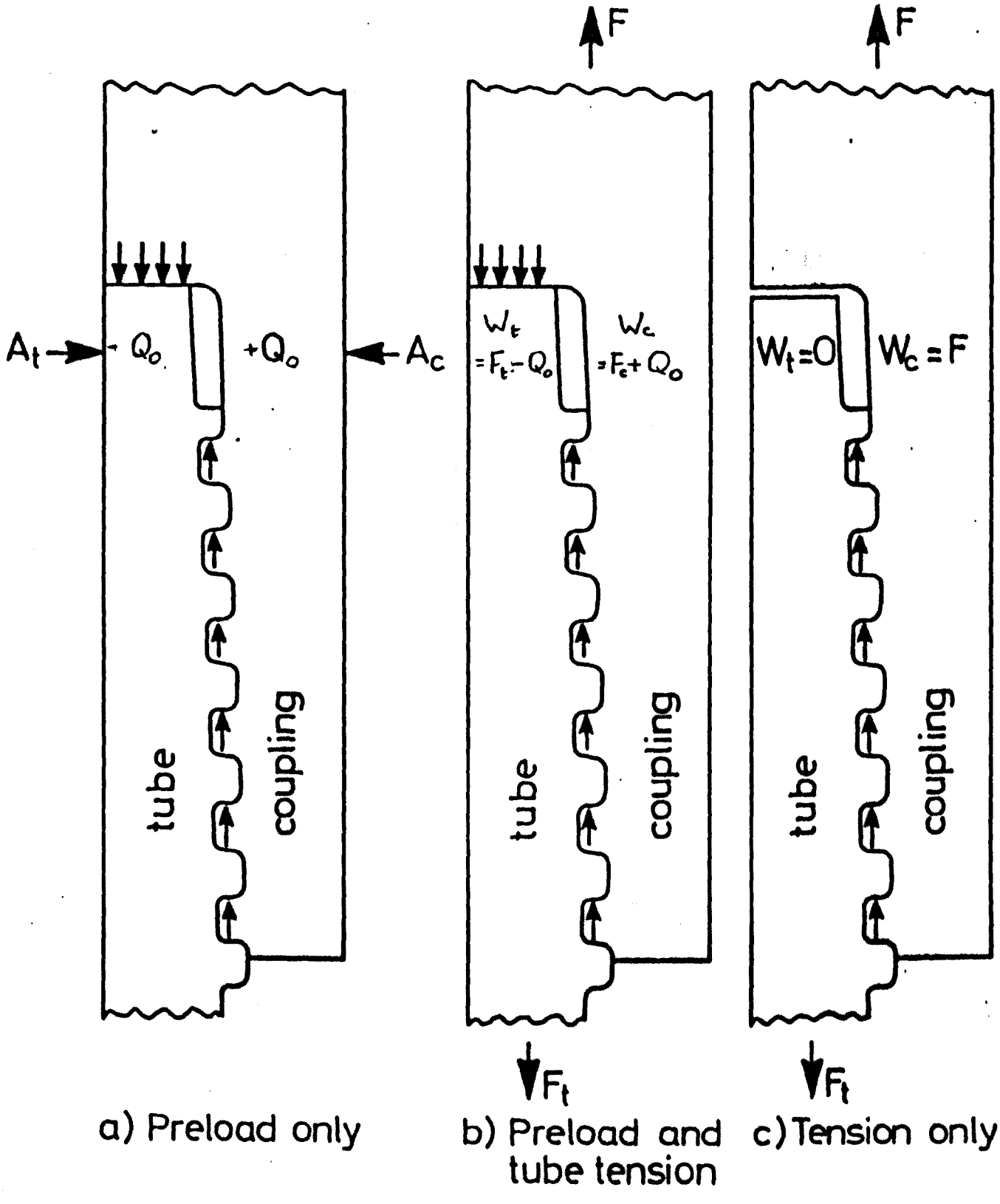

Fig 5.1

Loads In Tube Nose and Coupling Undercut

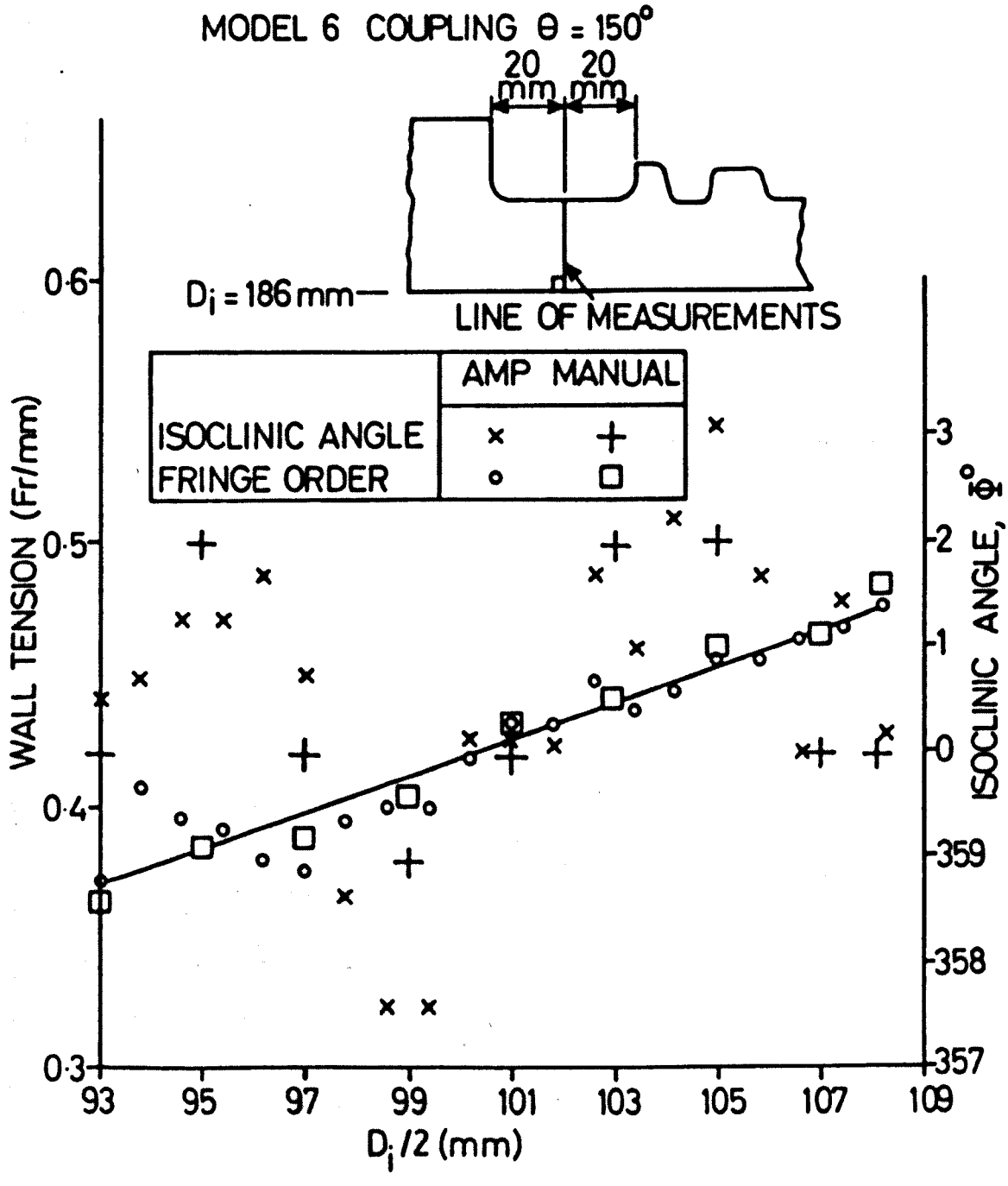

Fig 5.2

Typical Distributions of Fringe Order and Isoclinic Angle Across Model Undercut

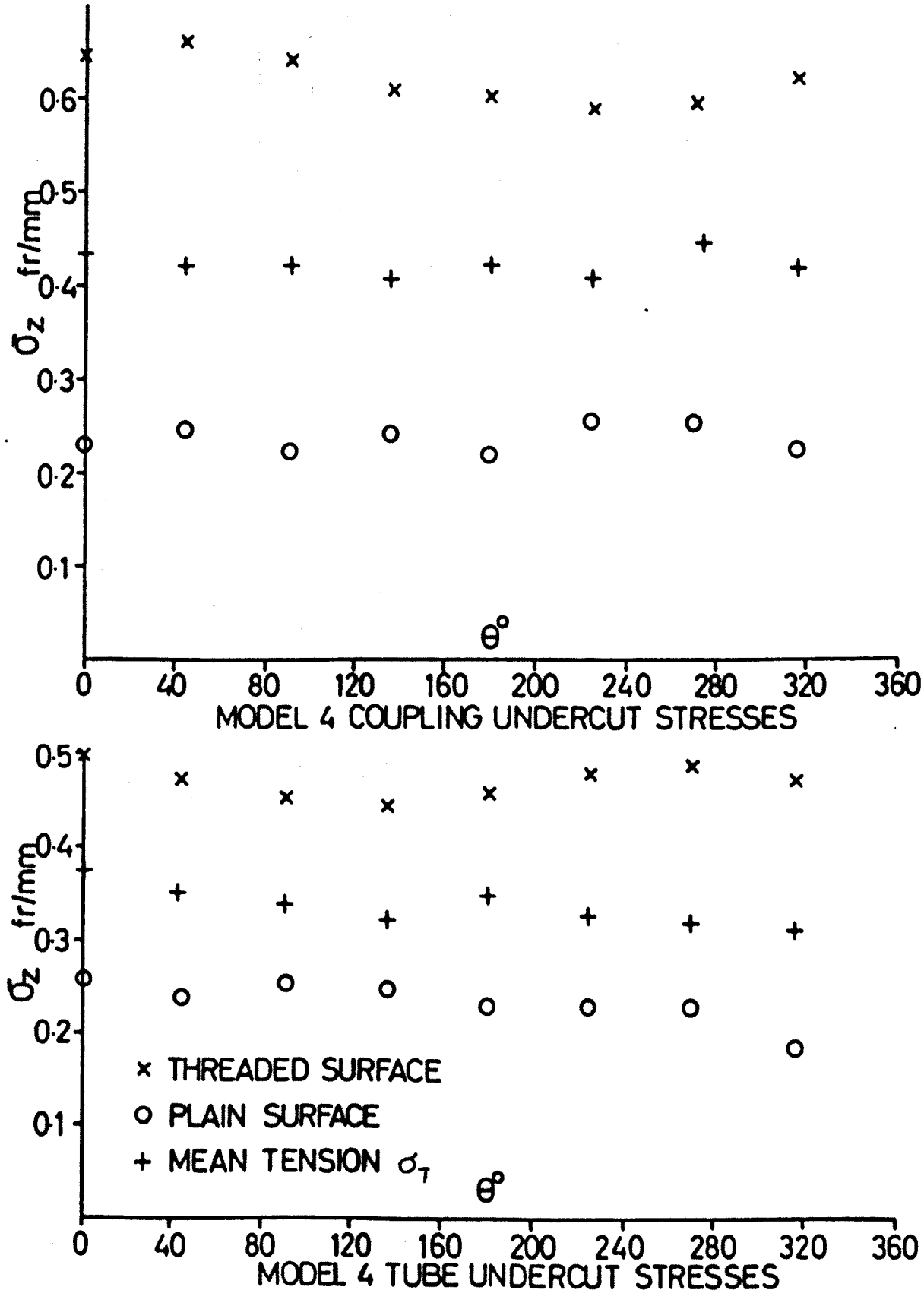

Fig. 5.3

Mean Through Thickness Axial Stresses and Surface Stresses in the Tube and Coupling Undercuts of Model 4

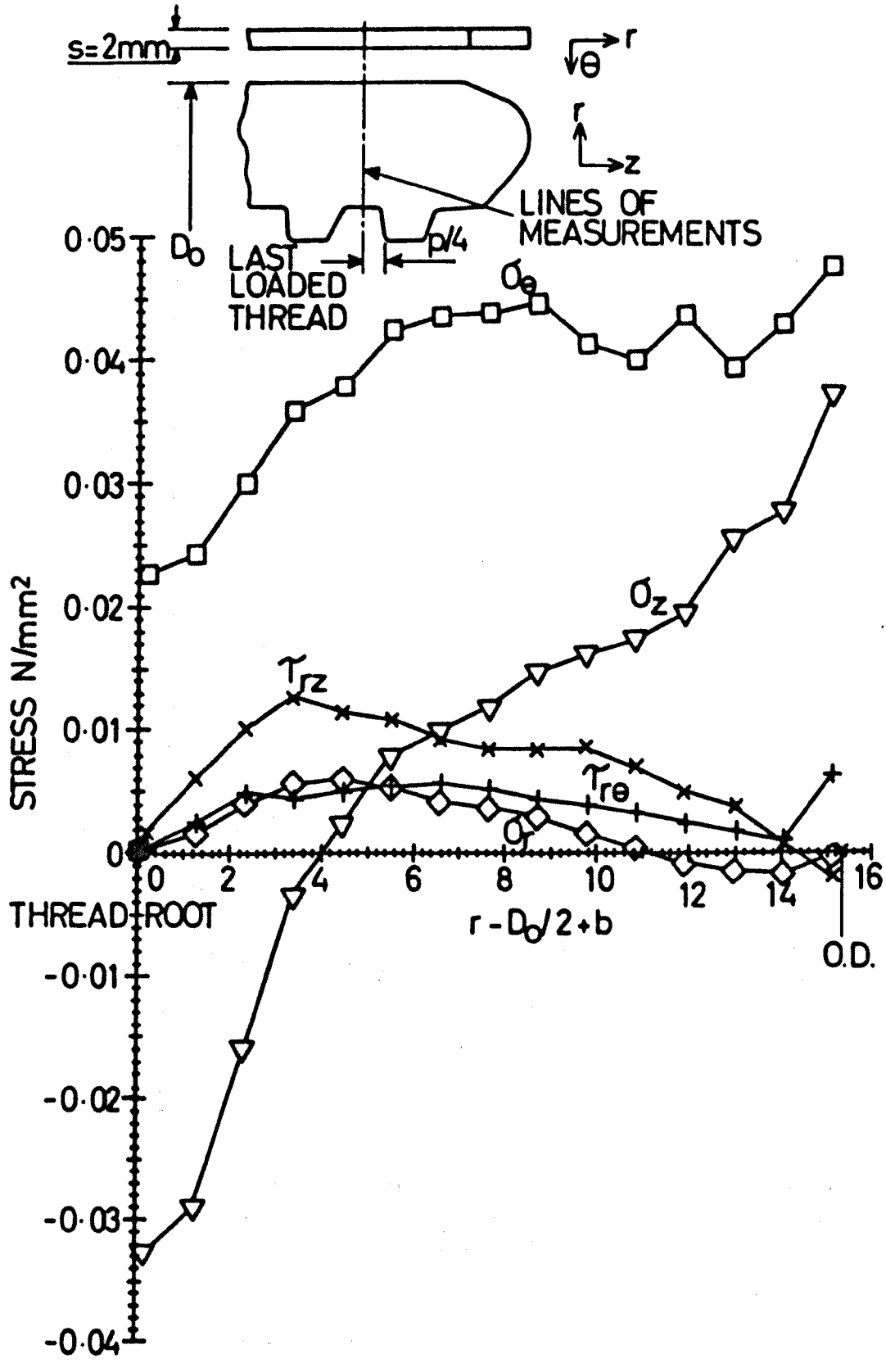

Fig 5.4

Through Thickness Stress Distributions in the $\theta = 180^{\circ}$ Position of the Tube Nose of Model 4 Obtained using the AMP

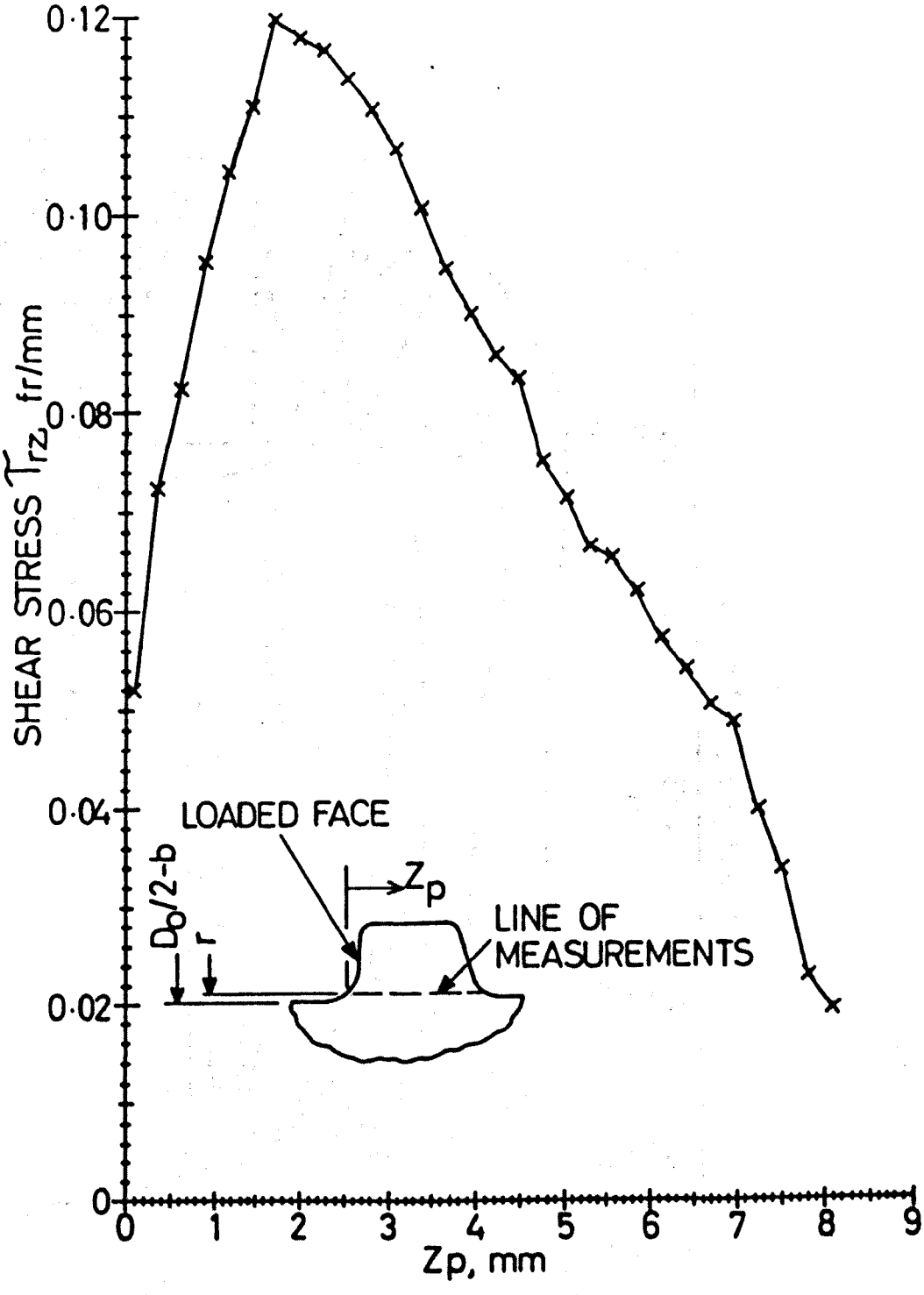

Fig 5.5

Distribution of Shear Stresses τ_{rz} Across the Tube Thread of Model 9 at z = 4.5P, $(\frac{D_o}{2} - b - r)/R = 0.97$

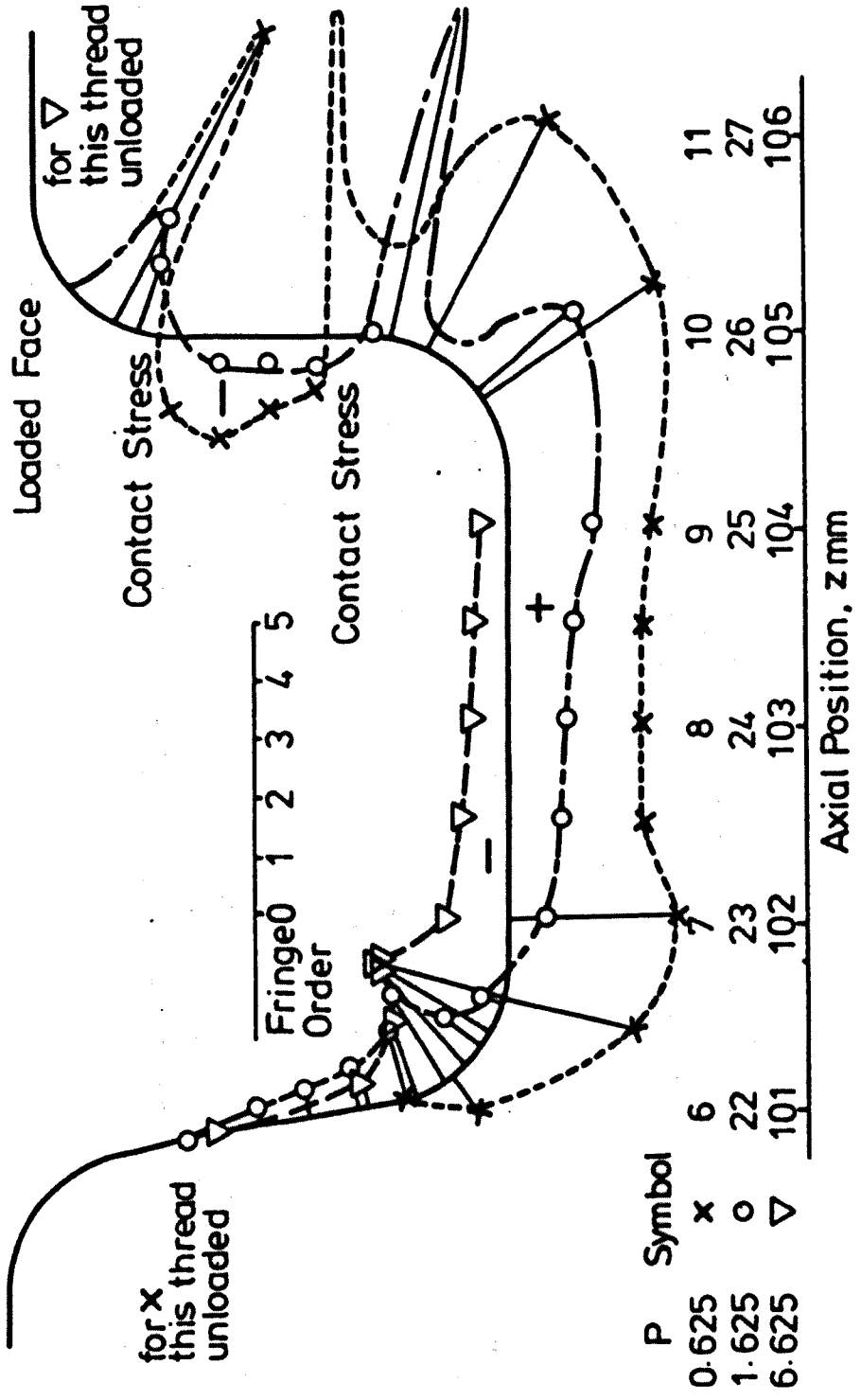

Fig 5.6a

Normalised Stress Distributions Around Loaded and Unloaded Tube Thread Roots in the $\theta = 45^{\circ}$ Plane of Model 1.

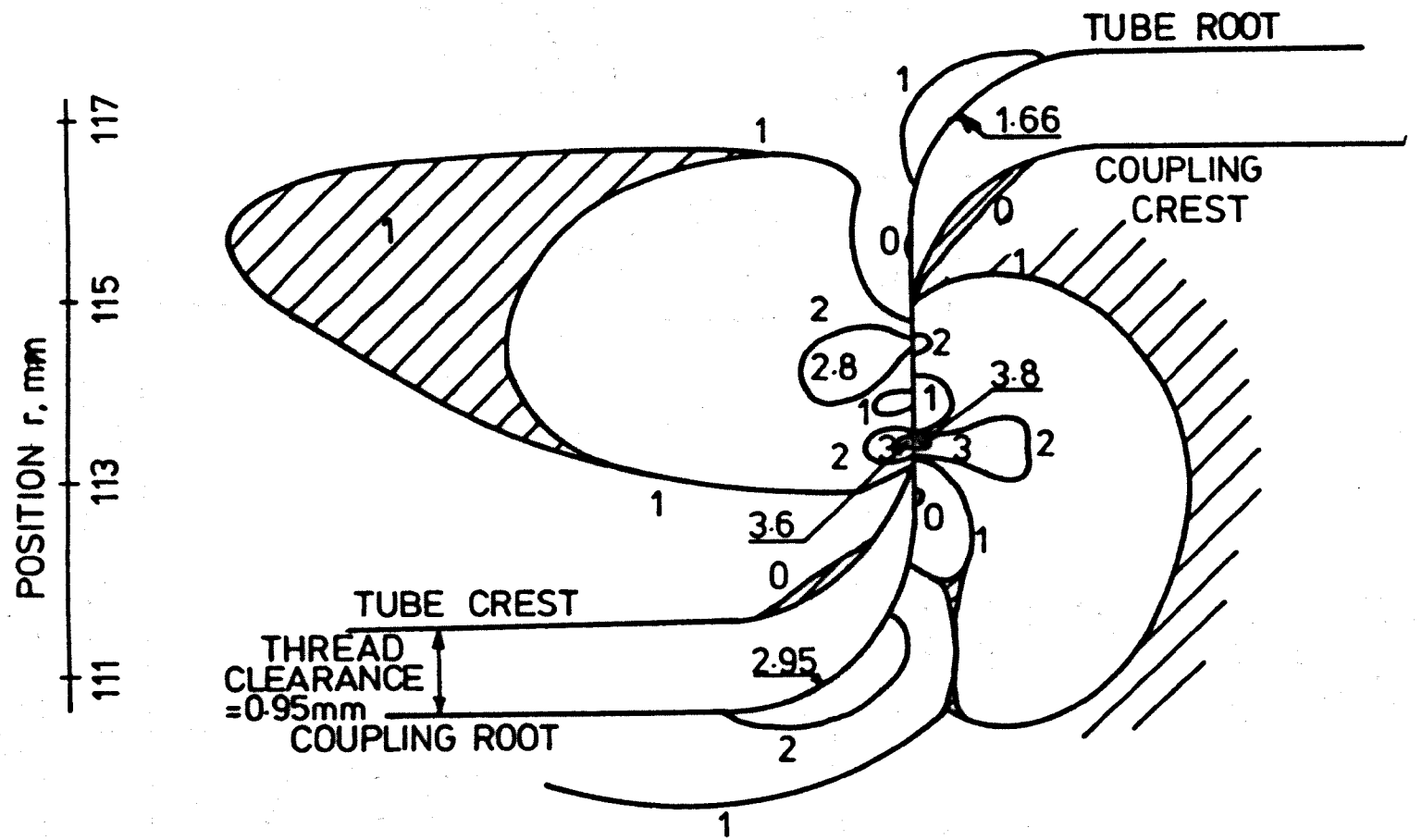

Fig 5.6b

Sketch of Fringe Pattern in mating Threads of Model 4, $\theta = 270^{\circ}$, P = 5.75, S = 1.9 mm. Numbers Refer to Fringe Orders

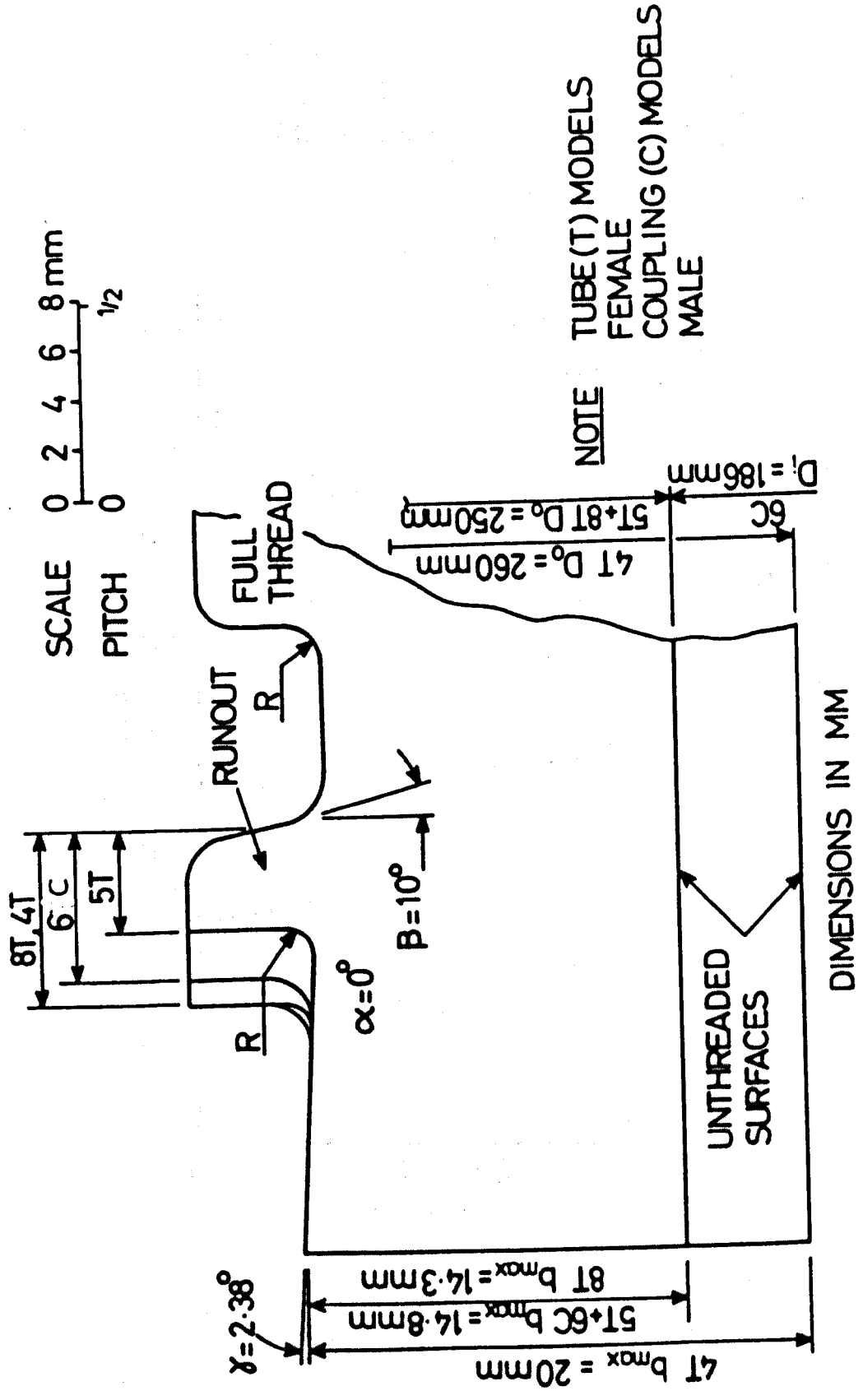

Fig 5.7
Unloaded Thread Sections Analysed

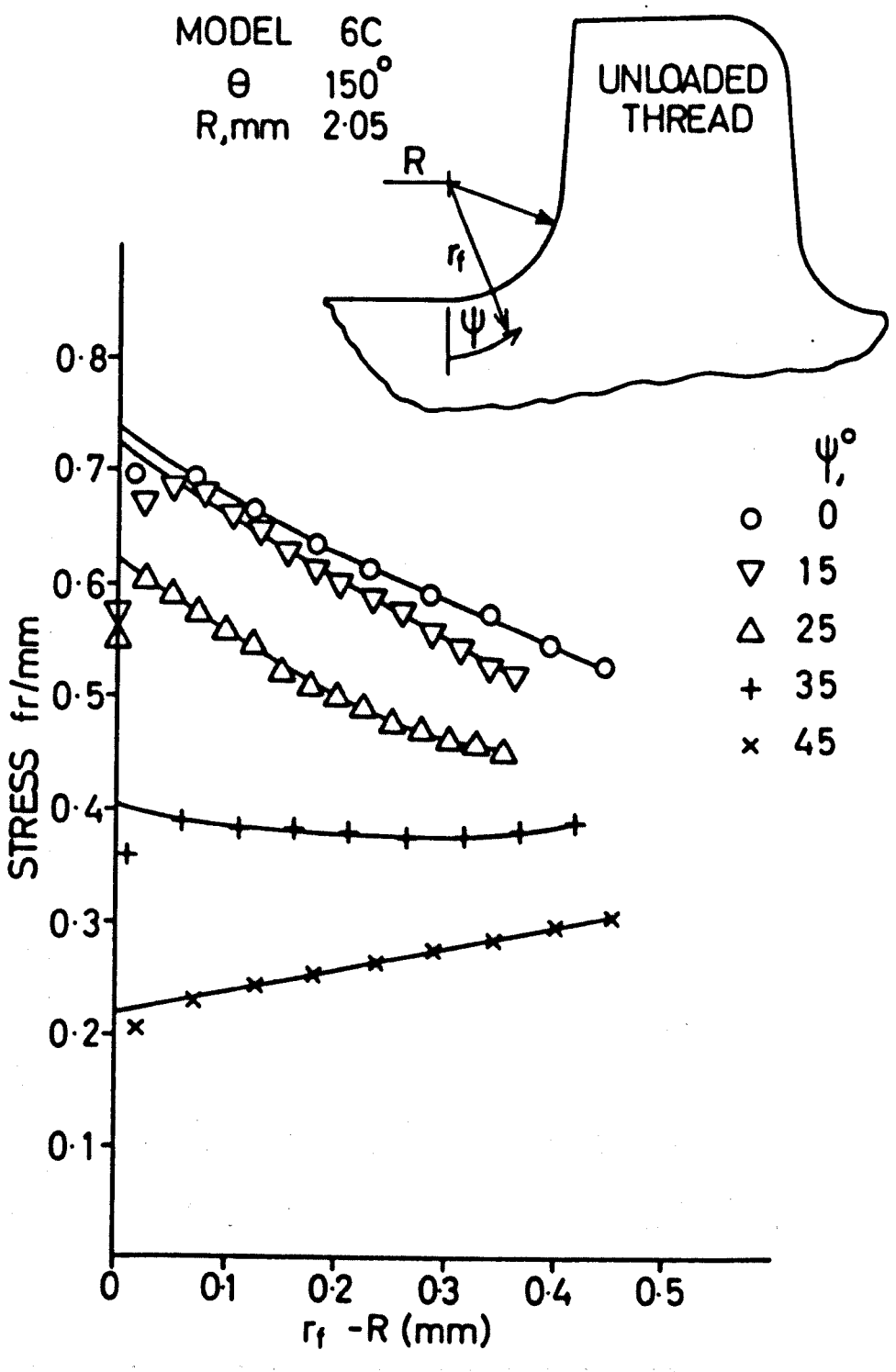

Fig 5.8

Distributions of Sub Surface Stresses in a Thread Fillet Loaded with Wall Tension Only

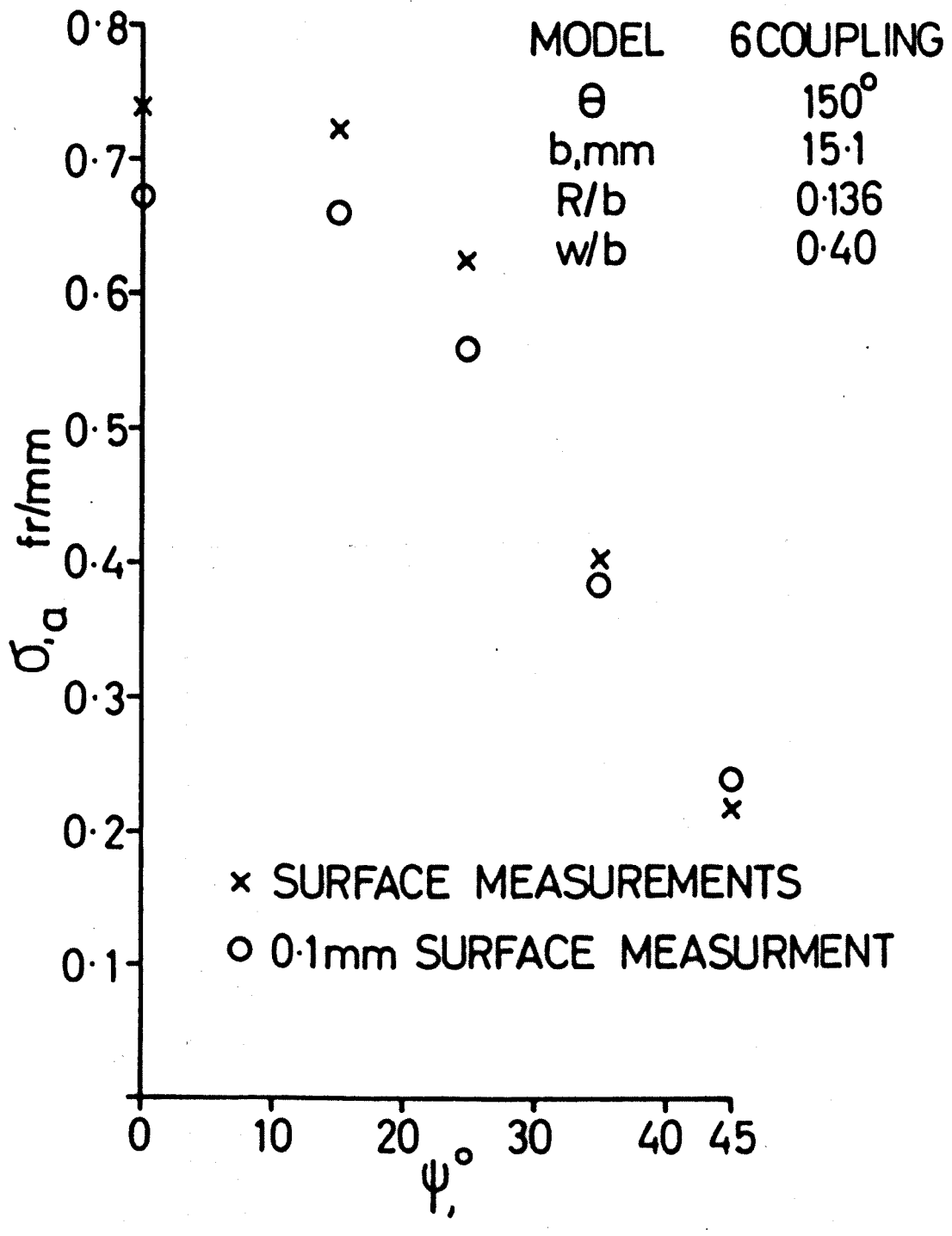

Fig 5.9

Distributions of Surface Stresses and Stresses
0.1 mm sub surface in a Fillet Loaded with Wall Tension

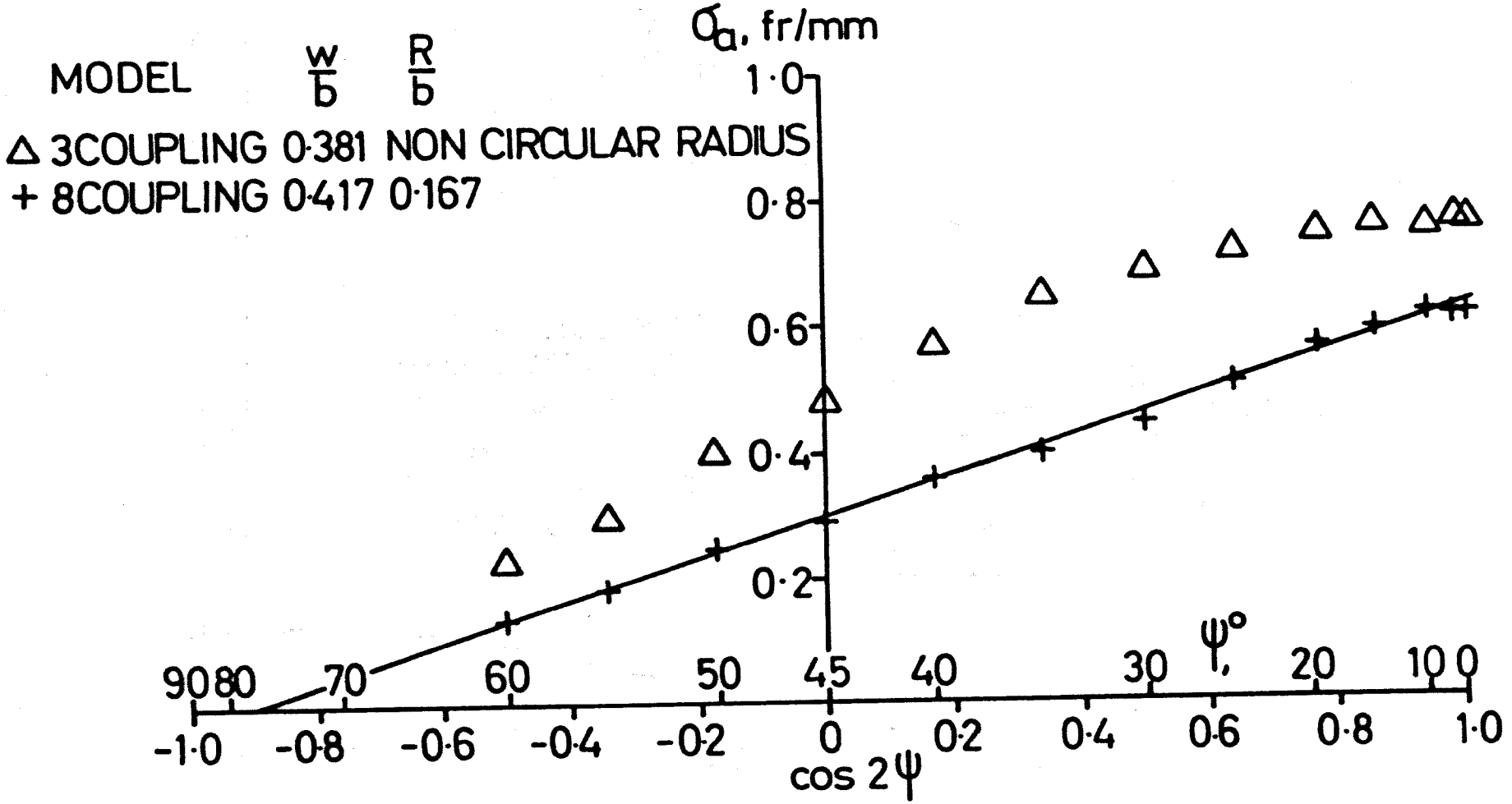

Fig 5.10

Distributions of Surface Stress Due To Wall Tension Only in 'Perfect' and 'Non-Circular' Fillet Radii

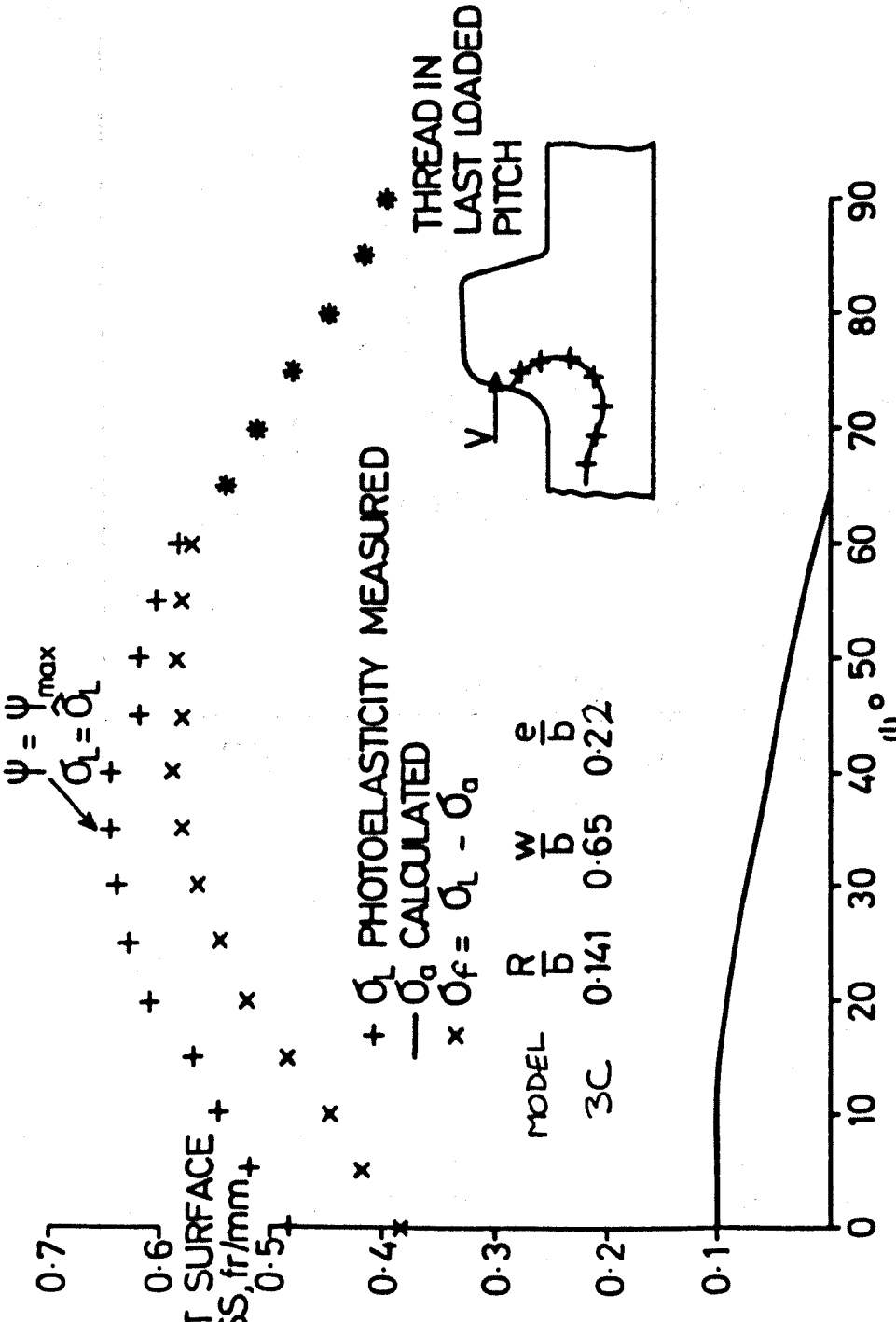

Fig 5.11

Surface Fillet Stresses Due to Wall Tension Only, Shear Force Only and Wall Tension Plus Shear Force

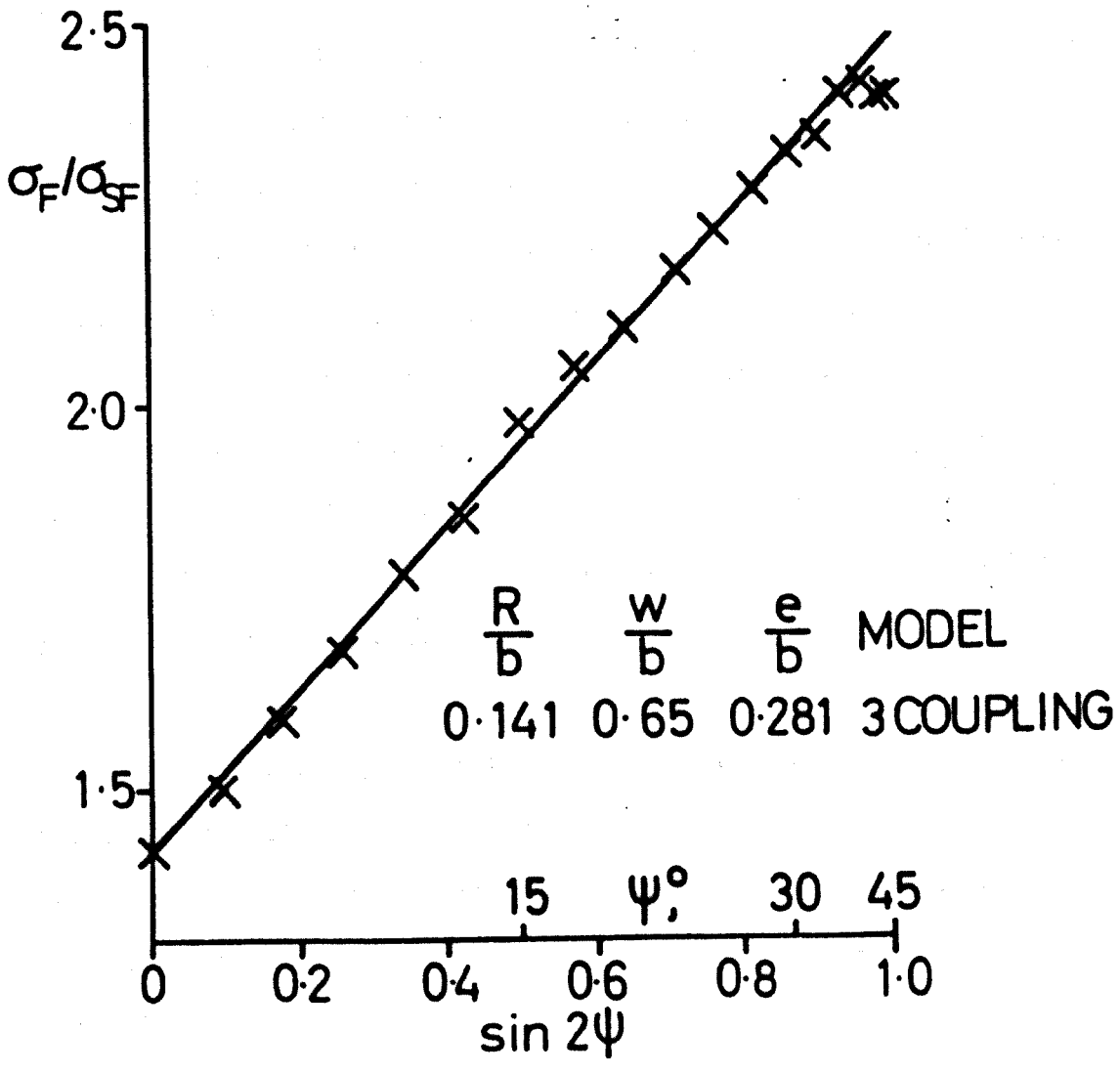

Fig 5.12

Distribution of Fillet Stresses Due to Shear Force Only Plotted Against Sin 2ϕ

CHAPTER SIX

FINITE ELEMENT WORK

6.1 Introduction

The walls of both tubes and couplings were loaded with tension due to the applied loads and also bending due to the couples caused by the thread loads. Tension and bending have different effects on the stress distribution around fillets. The influence of changes in thread shape on the different stress distributions could not be fully investigated using the photoelastic models because of the limited number of thread shapes and the slight imperfections in some of the thread fillets. The range of thread shapes investigated was extended using the PAFEC 75 finite element package. 8 noded isoparametric curvilinear quadrilateral type 36210 elements were used to generate the thread-like projections because:-

i) the thread helix angles of the photoelastic models and prototype screwed connections were small

ii) the stress gradients in the thread in the hoop direction were generally small (apart from at the beginning and end of thread contact)

iii) axisymmetric loading was to be applied.

The meshes were separately loaded with wall tension and thread shear force. In each of the photoelastic threads nominally loaded with wall tension only, wall bending was present to varying degrees. In order to investigate the effect of wall bending the F.E. meshes were also loaded with pure wall bending. The finite element material properties were defined to be as similar as possible to the photoelastic models i.e. $E = 13\ N/mm^2$, $\nu = 0.45$ (Note ν for Araldite = 0.5 but the nearest to 0.5 PAFEC will allow is $\nu = 0.45$.)

6.2 Choice of Shapes and Boundary Conditions

The peak fillet stresses in each photoelastic model have occurred in the loaded threads adjacent to the undercut where the influence of other threads is small. Because of this and so that fine meshes could be used, individual thread shapes only were analysed.

Wall tension and wall bending acts equally on both sides of the thread which for the finite elements was symmetrical about w/2. Hence, for these loading modes a line of symmetry was introduced at the w/2 position so as to minimise the mesh size. A typical mesh is shown in Fig. 6.1. For the meshes loaded with shear force the loading was not symmetrical, hence the full thread shape had to be defined. A typical mesh is shown in Fig. 6.2. There are several differences between the finite element shapes and the photoelastic thread shapes as listed below:-

i) the F.E. shapes had no tip radii but h/b was the same as in the P.E. threads;

ii) the F.E. shapes had no thread taper;

iii) only one thread shape was present which facilitated the measurements of σ_{sa}, the surface stress adjacent to the thread fillet which was used to normalise the fillet stresses of the wall tension loaded thread shapes

iv) the F.E. shapes were axisymmetric and hence there was no helix angle;

v) the F.E. loads were axisymmetric while the model screwed connections did show variations in load around a pitch.

vi) $\alpha = \beta = 0^{\circ}$ in the F.E. shapes while for the photoelastic threads $\beta = 10^{\circ}$ and $\alpha = 0^{\circ}$ or 3°.

vii) The meshes analysed generally had the thread type projection on the external surface, i.e. modelling a coupling. Tube type meshes of identical shape to coupling type meshes were analysed which showed very similar distributions of stress around the fillets.

viii) The F.E. meshes had D_i/b ratios = 10. Although this ratio was different for the photoelastic model threads, varying D_i/b on F.E. meshes of identical shape showed D_i/b had a negligible effect on the stress distributions around the fillet.

The effect of these differences on the fillet stress distributions was considered small.

Boundary Conditions

It was important that the finite element deformations model the screwed connection deformations as closely as possible. From Fig. 4.13 it can be seen that outside the threaded region the models deform primarily due to Poissons ratio and behave like infinitely long tubes. In the threaded region wall bending due to the thread shear forces predominates and there is some radial movement between the mating threads. The radial movement indicates that the tubes and couplings deform independently of each other and hence the radial stiffness of the connected models was less than the sum of the two individual models. The closest boundary conditions to those observed in the Araldite models were to allow the meshes to deform radially with the only restraint being that due to the hoop restraint of the tube.

The lengths of the tubes under the different loading conditions are considered below.

For the meshes loaded with wall tension, meshes with the same thread shape but with different 'tubular' length, l/b, varying from l/b=1 to l/b=5 were loaded and analysed. Variations in fillet stresses were negligible over the full range of l/b investigated.

For the meshes loaded with pure wall bending the loading had to be applied less than 1 wall thickness from the projection because the through-thickness distribution of bending decayed along the length of the mesh. Hence the tubular length was unimportant but distributions of surface stress between the projection and the application of load had to be measured so that the amount of bending decay could be determined.

For the meshes loaded with thread shear forces the length of tubular, l/b, between the thread and axial restraint was long enough to be effectively infinite, $l/b \gtrsim 4$ (see Fig. 6.2). The ratio l/b depends on D_i/b but for all the meshes analysed $D_i/b=10$. The length of tubular between the thread and the 'free' end of the mesh, m, was also important since this influenced the moment distribution (see Appendix 6). The beam-on-elastic foundations calculations indicated that if $(m+w)/b \gtrsim 4$ then the moment distribution was not affected by m. Hence, in order to obtain the coefficients C_3 and C_4, $(m+w)/b$ was always greater than 4, but for 1 shape of thread, m was varied from $(m+w)/b = 1$ to $(m+w)/b = 6$. The fillet stress distributions are shown in Fig. 6.3. The fillet stresses increased as the thread neared the free end of the tubular and the position of the peak fillet stress moved from $\phi \simeq 45^\circ$ to $\phi \simeq 35^\circ$. This is attributed to the increased nominal bending stress σ_{SF} which has been calculated and is shown in Table 6.1.

(see Appendix 6)

Table 6.1 - Variations of Calculated Bending Stress and Position and Magnitude of Peak Normalised Fillet Stress with Length of Tube for Threads Loaded with Shear Force

(m+w)/b	Nominal Calculated Bending Stress σ_{SF}, N/mm^2 x 10^{-3}	ϕ_{max} ^{o}	Peak Fillet Stress $\hat{\sigma}_L$, N/mm^2 x 10^{-3}
6.2	0.70	45	6.10
3.9	0.70	45	6.10
1.5	1.16	40	6.65
1.0	1.28	29-35	7.05

The increase in σ_{SF} is a measure of the increased tubular deflection and the stresses which occur due to the reduced stiffness of the tube between the point of application of the moment and the free end of the tube. But the presence of the thread and its stiffening effect on the tube becomes more significant as it nears the free end of the tube and hence the measured tubular surface stress is less than predicted by the beam-on-elastic-foundations calculations (See Fig. 6.3).

Due to the change in ϕ_{max} as (m+w)/b becomes small, the distribution of stress around the thread fillet cannot be characterised by the equation

$$\frac{\sigma_F}{\sigma_{SF}} = C_3 + C_4 \sin 2\phi \qquad \ldots\ldots 6.1$$

But most of the threads, particularly the most highly loaded ones, were more than 4 wall thicknesses from the free end of the models, hence $\phi_{max} \simeq 45^o$ for shear force loading only and Equation 6.1 is valid.

Shapes Analysed

The range of [illegible] shapes investigated was limited to buttress type threads with $\alpha = \beta = \gamma = 0$ and the significant parameters changed were w/b, R/b and for the [illegible] shapes with loads applied to the loaded flank, e/b.

Likely ranges of thread shapes were defined as:-

i) $2 < h/R < 7$

ii) $0.5 < h/w < 2$

iii) $0.10 < h/b < 0.5$

hence $0.015 < R/b < 0.25$

and $0.05 < w/b < 1$

For the thread shapes with loads applied to the loaded flank, $e/h = 0.5$ hence

$0.05 < e/b < 0.25$

A practical limit on the thread is that

$w/b > 2R/b$ since $w/b = 2R/b$ is a thread with a semi-circular root.

These ranges of shapes are shown in Fig. 6.4. The mesh shapes were chosen to cover the full range of shapes but some were also chosen to correspond with the shapes of photoelastic threads analysed.

Table 6.2 shows the range of shapes investigated for the loading modes of wall tension and wall bending. Table 6.3 shows the range of shapes investigated for thread shapes with loads applied to the loaded flank.

Table 6.2 - Shapes of F.E. Thread Type Projections loaded with Wall Tension and Wall Bending

R/b	w/b	h/b	D_i/b	Tube/coupling	D_o/b
0.02	0.1	0.06	10	Coupling	-
"	0.15	"	"	"	-
0.03	0.15	0.09	"	"	-
"	0.50	"	"	"	-
0.06	0.125	0.18	"	"	-
"	0.25	"	"	"	-
"	0.37	"	"	"	-
"	0.55	"	"	"	-
0.100	0.20	0.30	"	"	-
"	0.40	"	"	"	-
"	0.60	"	"	"	-
"	0.90	"	"	"	-
0.134	0.265	0.402	"	"	-
"	0.535	"	"	"	-
"	0.805	"	"	"	-
0.167	0.34	0.501	"	"	-
"	0.68	"	"	"	-
"	1.01	"	"	"	-
0.100	0.90	0.3	4.4	"	-
"	"	"	13.6	"	-
"	"	"	-	Tube	10

Wall tension was applied by a uniform through thickness tension at the end of the mesh, see Fig. 6.1, due to the line of symmetry no axial restraints were required.

Pure Wall bending was applied with tensile stresses at the projection side of the wall and the equal compressive stresses were on

the inside surface. Again due to symmetry no restraints were required.

For meshes loaded with shear forces point loads were applied at the mid thread height position and restrained at the end of the mesh, see Fig. 6.2.

6.3 Mesh Design

The objective of the finite element work was to accurately determine the distribution of stresses around the fillets. Sakaguchi et al (8) showed that a fine mesh was required in the region of the fillets. Nodes were specified every 11.25^{o} around each fillet which also allowed measurements of surface stress to be made every 5.6^{o} at the mid-side nodes. This fine mesh was extended beyond the fillet into the tubular wall and also radially to a depth of R/2 sub-surface. During the design phase of the meshes the fine density initially extended a subsurface distance =R but this did not affect the fillet surface stresses.

For all the meshes analysed R was kept constant and the other parameters altered. As w, b and the length of the meshes increased it became increasingly important to reduce the node density in the unimportant regions of the mesh so that the central processor time limit was not exceeded. Hence, transition blocks, Pafblock Type 5, were extensively used (see ref. 33).

For the meshes loaded with shear force the loads were concentrated axial ring loads and applied at nodes which were positioned in the mesh so that e = h/2. A fine mesh was specified between the end of the thread fillet and the point of application of the shear force, which was of similar node density to that in the fillet region. (see Fig. 6.2.)

6.4 Analysis

For each shape and loading mode the stress distributions parallel to the fillet surface σ_ϕ were measured and the stresses perpendicular to the surface σ_{rf} checked to ensure they were negligible. For the wall-tension loaded meshes the distributions of stress along the surface adjacent to the fillet and through the thickness were checked to prove equilibrium and to ensure bending was negligible. The mean through thickness stress σ_{sa} was used as the normalising stress. The fillet stresses were analysed in the same manner as for the photoelastic thread fillet stresses, see Section 5.3.,

i.e.
$$\sigma_\phi = \sigma_a \text{ and}$$
$$\sigma_a / \sigma_{sa} = C_1 + C_2 \cos 2\phi$$

The distributions of σ_a/σ_{sa} v $\cos 2\phi$ are presented in Appendix 7.

For the meshes loaded with shear forces, unit axisymmetric axial shear forces were applied and the shear force per unit length of thread

$$V = 1/\pi(D_i + 2b + 2e) \qquad \ldots\ldots 6.1$$

These shear forces created both thread bending and an axial stress

$$\sigma_{sa} = 1/\pi(D_i + b)b \qquad \ldots\ldots 6.2$$

the effect of which had to be considered when analysing the fillet stresses. The analysis was the same as that used on the threads analysed photoelastically, see Section 5.3.

For the meshes loaded with wall bending, the through thickness distribution of stress was measured between the thread and the position of application of load, to ensure pure bending had been applied. The distribution of axial stress on the surface adjacent to the fillet was measured and plotted against distance from the fillet, typical examples

are shown in Fig. 6.5. From these distributions the surface stress was extrapolated to the position of the thread fillet ignoring the stress raising effect of the fillet. This extrapolated stress, σ_{sb}, was used to normalise the fillet stresses σ_a in the equation

$$\sigma_a / \sigma_{sb} = C_1 + C_2 \cos 2\phi \qquad \ldots\ldots 6.3$$

Table 6.3 - Shapes of F.E. Thread, type Projection Loaded with Thread Load

R/b	e/b	w/b			
		0.15	0.35	0.6	1.0
0.02	0.06	12	13	14	15
	0.12	16	17	18	19
	0.17	23	24	25	26
	0.25	1	2	3	4
0.06	0.06	-	-	-	-
	0.12	-	20	21	22
	0.17	-	27	28	29
	0.25	-	5	6	7
0.17	0.06	-	-	-	-
	0.12	-	-	-	-
	0.17	-	33	30	31
	0.25	-	32	8	9
0.25	0.06	-	-	-	-
	0.12	-	-	-	-
	0.17	-	-	-	-
	0.25	-	-	10	11

- indicates impractical shape

$D_i/b = 10$, $l/b > 4$, $(m+w)/b > 4$ (see Fig 6.2)

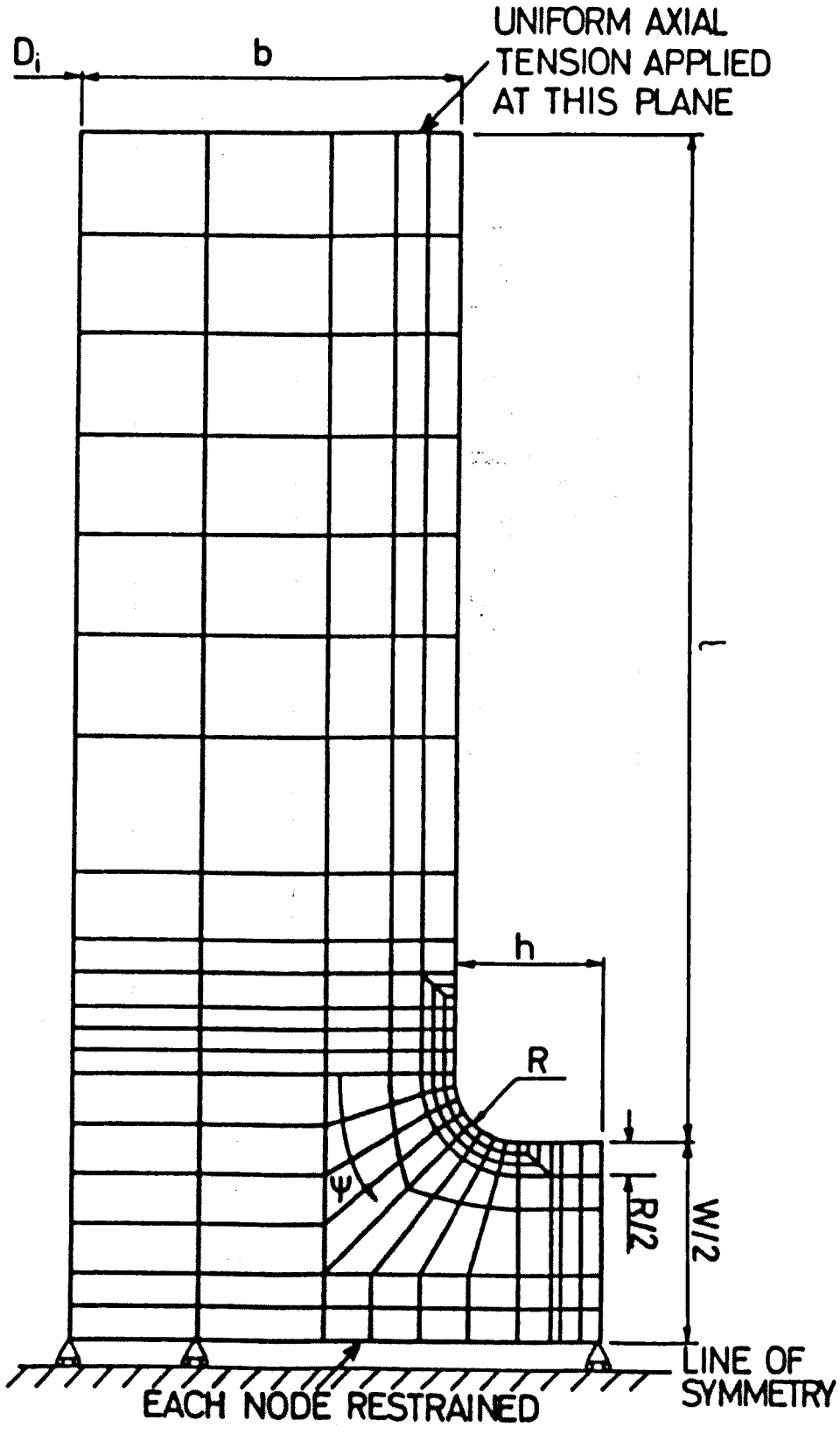

Fig 6.1

Typical Axisymmetric Finite Element Mesh
for Wall Tension And Wall Bending Loading

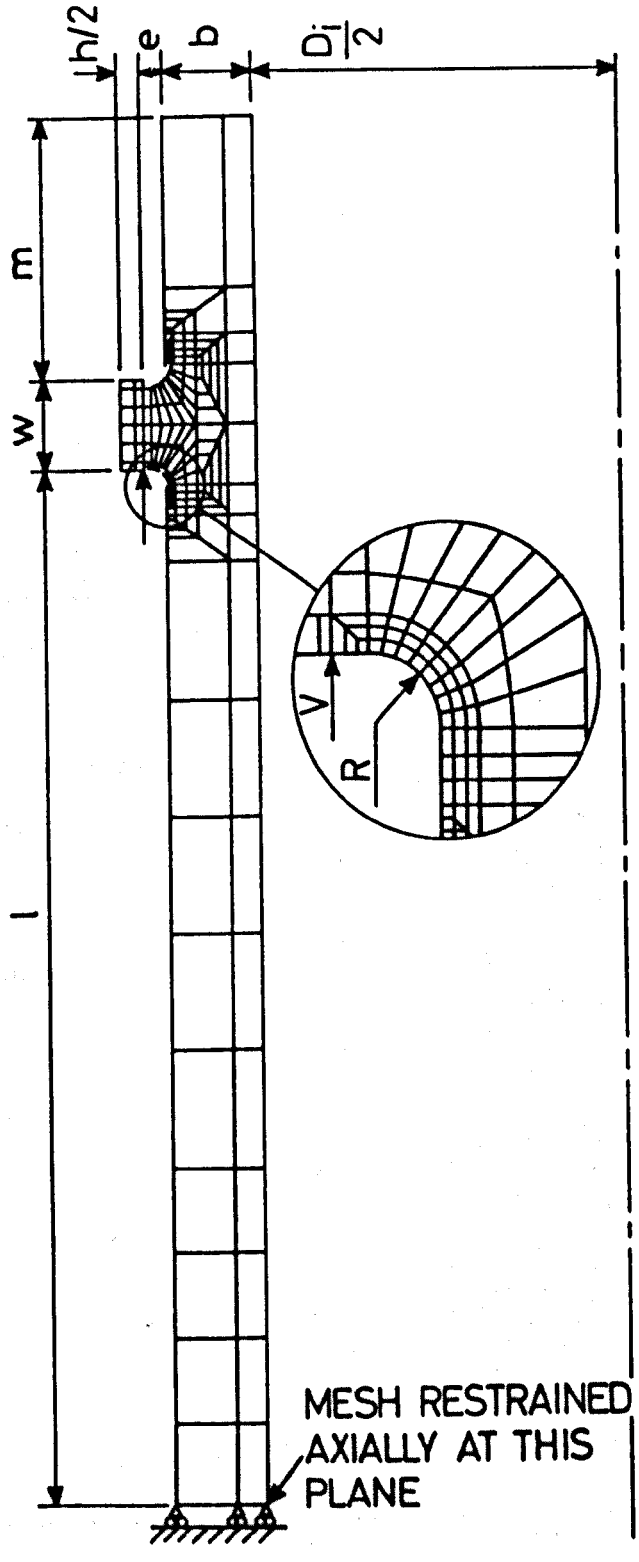

Fig 6.2

Typical Axisymmetric Finite Element Mesh Used to Analyse Shear Force Loading

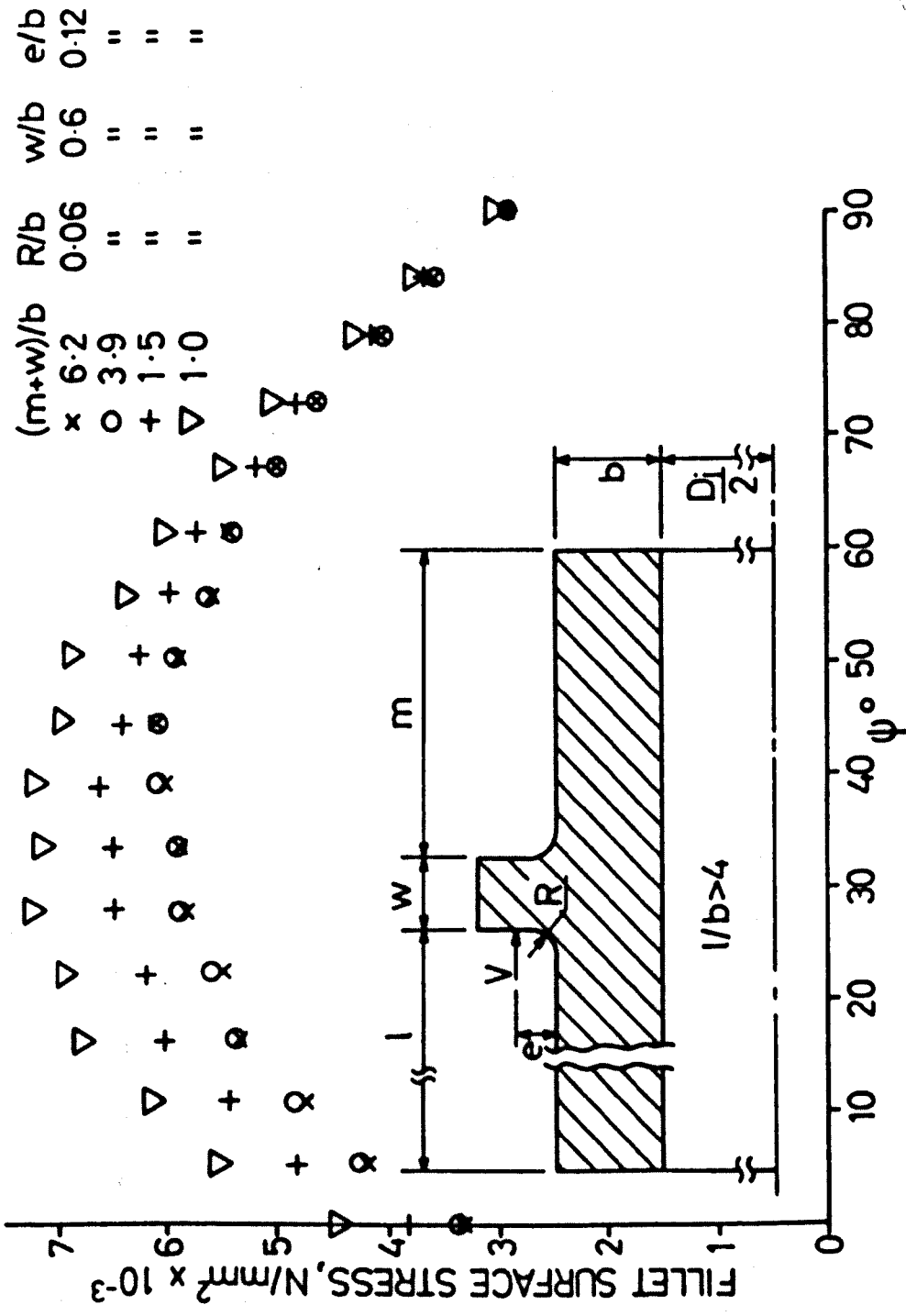

Fig 6.3
Stresses Around Shear Force Loaded Fillets In Similar Shape Projections Positioned at Different Distances from the Free End of the Tubular - From Finite Elements

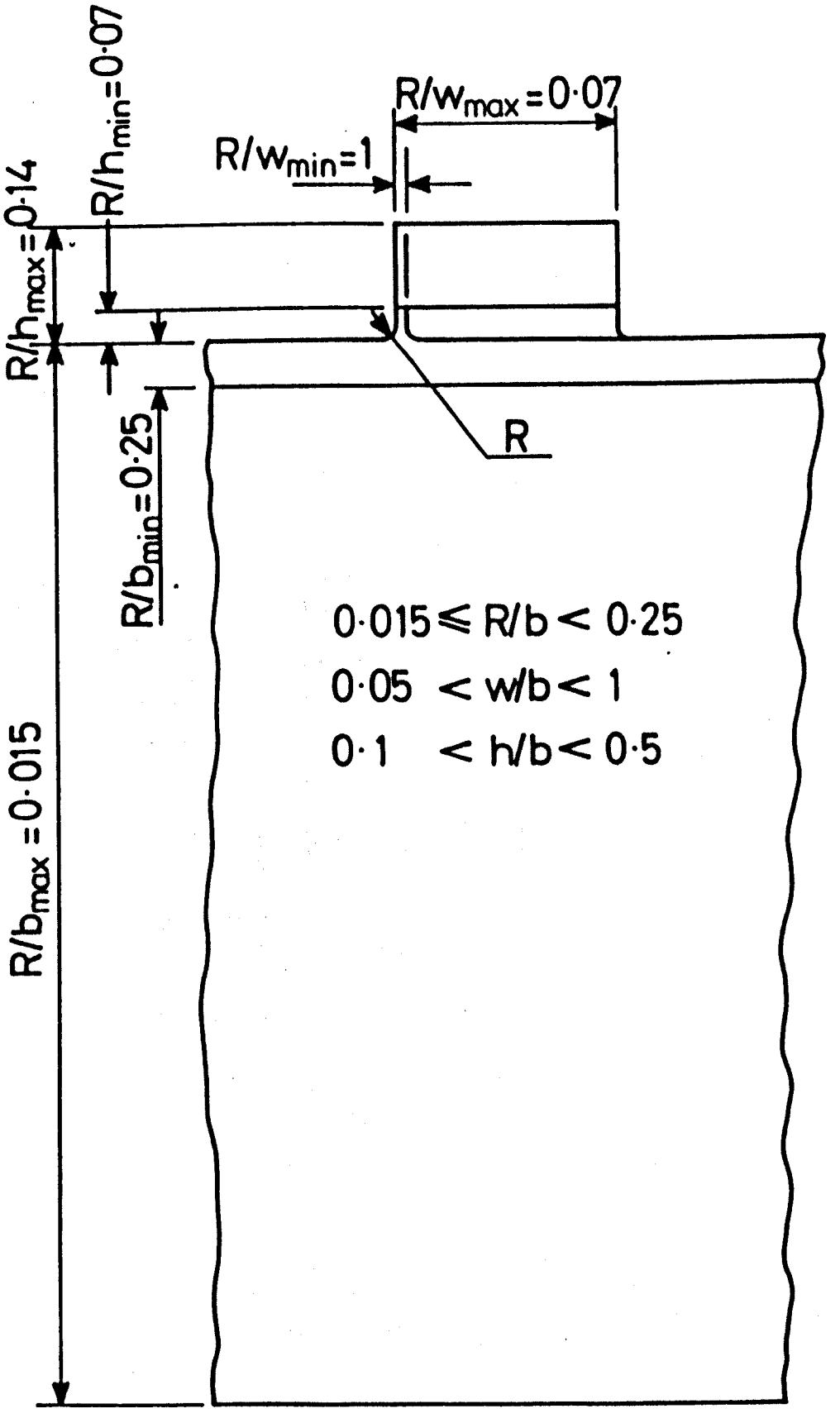

Fig 6.4

Range of Geometrically Possible Thread Shapes

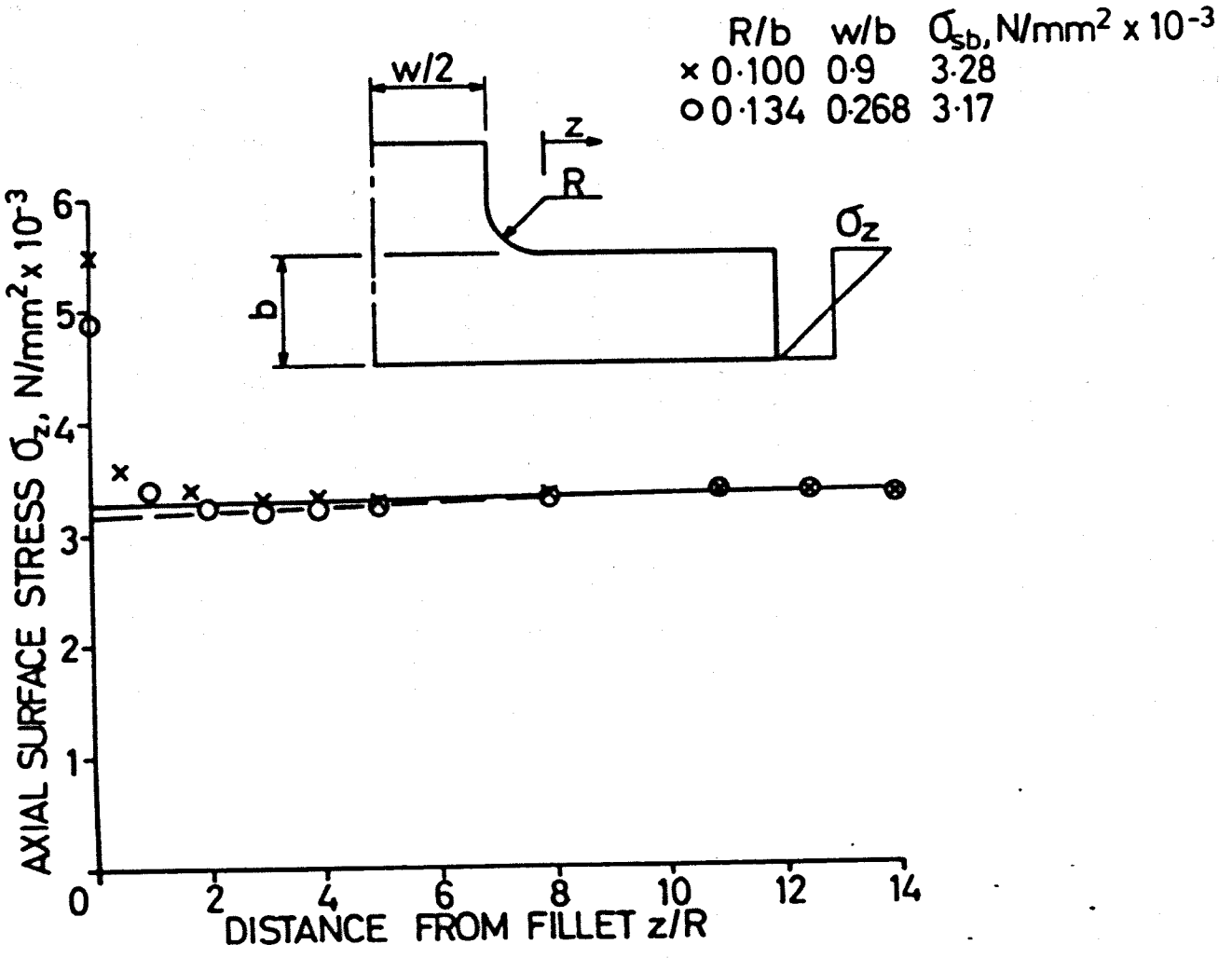

Fig 6.5

Surface Stresses Adjacent to Thread-like Shapes in Finite Meshes Loaded with Pure Wall Bending

CHAPTER SEVEN

ERROR ANALYSIS

7.1 Introduction

In this chapter consideration has been given to sources of experimental error involved in both determining the photoelastically measured peak fillet stresses and the errors associated with the proposed method of calculating the peak fillet stresses. Assuming that each individual error is random, they can be combined to give the probable error using the equation

$$e_{sd} = \sqrt{\sum_{i=1}^{n} e_i^2} \qquad \ldots\ldots 7.1$$

where e_{sd} is the standard error in either photoelastic measurement or in calculating the peak fillet stress and e_i are the individual errors.

Manual and automatic photoelastic techniques and axisymmetric finite elements have been used to analyse the stresses and loads in screwed tubular joints and the errors associated with each have been considered separately in this chapter.

A comparison between measured peak fillet stress and calculated fillet stresses has been made in Section 8.4

7.2 Errors in Manual Photoelastic Measurements

The likely random errors in the frozen stress photoelastic measurements of peak fillet stresses can be categorised as follows:-

i) divergence of model from measured shape and size,

ii) errors in measurements of applied loads,

iii) measurements of individual fringe readings.

7.2.1 Divergence of Models from Measured Shape and Size

The divergence of the thread parameters R, w, e and b from the designed shape will not have influenced the accuracy of the manual

photoelastic measurements. The unloaded dimensions D_o, D_i and t were measured in each of the machined Models 1 to 4 and also in Models 5 and 9 which were representative of the thin and thick walled precision cast models. Errors in these measurements, out of roundness of the models and variations in wall thickness will have created errors in the calculated values of the nominal stress σ_{nom}. For the measured dimensional errors of $\pm$ 0.1 mm in the machined models errors of $\pm$ 0.3% in σ_{nom} were likely, while for precisely cast models, greater variations of $\pm$ 0.5 mm were measured in D_o and $(D_o - 2t)$ which led to likely errors of $\pm$ 1.2% in σ_{nom}.

7.2.2 Errors in Measurements of Load

For each model loaded with pure axial tension and for the tube models loaded with tension and preload, the photoelastically measured stresses in the undercuts have been compared with the expected stresses calculated from weighing the applied loads as shown in Table 7.2.1. As was explained in Section 5.1 the axial stresses in the model undercuts were measured at N positions at regular intervals around the models and the mean of these axial stresses was used to evaluate the applied load. The standard deviation of the N measured axial stresses of each model is also shown in Table 7.2.1 as a percentage of the mean value.

The preload only models and the coupling models loaded with tension and preload have not been considered since the applied preload could not be accurately obtained from the applied torque.

The tube models loaded with tension and preload have been considered because preload did not effect the mean axial stresses in the tube undercut.

Table 7.2.1 - Accuracy of model load measurements for model undercuts with tension only

Model	Measured Mean Undercut Stress $\frac{1}{N}\sum_{\theta=0}^{\theta=360}\sigma_z$, F_r/mm	Standard Deviation of σ_z, %	Applied Stress, Fr/mm	% Difference Between Measured and Applied Stress
1 Tube	0.478	3.1	0.502	-5
1 Coupling	0.590	1.7	0.590	0
3 Tube	0.377	4.3	0.357	+6
3 Coupling	0.435	1.1	0.428	+2
5 Tube	0.440	2.4	0.452	+2
5 Coupling	0.481	2.1	0.474	-1
6 Tube	0.377	9.9	0.377	0
6 Coupling	0.436	11.0	0.396	-10
8 Tube	0.254	11.6	0.254	0
9 Tube	0.225	7.1	0.225	0
4 Tube	0.338	5.6	0.333	+1

From the standard deviations it can be seen that the uniformity of axial stress is fairly consistent around all the models considered, with the exception of Model 6 which was adversely effected by the presence of grooves on the plain surfaces of the tube and coupling.

The differences between the measured and applied stresses are attributed to:-

a) friction in the loading rig and errors in measuring the tension lever ratio,

b) errors in the measured material fringe values,

c) initial stresses in the models,

d) self weight effects.

The mean difference between the measured and applied stress = ± 2.3% and the mean standard deviation of the axial stress from the mean stress in the undercut for all the models was 5.4%.

The largest error in the application of preload would have been due to the torque cable not being horizontal and hence imparting either a tensile or compressive axial load to the models, see Fig. 7.1. During the loading cycle, the vertical position of the loading pulleys was adjusted so that the angle δ was kept to a minimum and it is unlikely that δ was greater than $\pm 2^{\circ}$. If the worst case is considered with δ = + 2° for 1 loading cable and -2° for the other, then the variation in axial tension would have been ± 0.035T, where T is the tension in the torque pulleys. For Models 7 and 10 loaded with preloaded only, T was measured by weighing the applied loads and since the preload Q was measured photoelastically for both models, the variation in Q can be found for $\delta = \pm 2^{\circ}$ and is shown in Table 7.22.

Table 7.2.2 - Maximum Errors in Preload Due to Non Horizontal Torque Cables

Model	Photoelastically Measured Preload Q,N	Weighed Loads T, N	% Error In Q, Due To $\delta = 2^{\circ}$
7	580	541	3.3
10	652	657	3.5

It can be seen from Table 7.2.2 that the worst variation in tube model nose compression and coupling model undercut tension due to preload was ± 3.5%, which is slightly worse than axial tension loading. This analysis does not consider any redistribution of variations in preload along the length of the extension tube and threaded region of the model.

7.2.3 Errors in Manual Photoelastic Fringe Measurements

These can be attributed to three factors:-

a) errors in fringe measurements,

b) errors in measuring slice thickness,

c) positional errors.

In considering the errors in fringe measurements errors of $\pm$ 0.03 fringes were found for surface measurements, which for typical peak fringe orders of 1.5Fr would give an error $\Delta n = 2\%$.

The loaded and trailing thread faces were not normal to the slices because of the thread helix angle where

$$\eta \simeq \tan^{-1}\left(\frac{p}{\pi D_m}\right) \qquad \ldots\ldots 7.2$$

Hence the measured fringe order

$$n = \frac{s}{f}\left(\sigma_1 - \sigma_3 \sin^2\eta\right) \qquad \ldots\ldots 7.3$$

where σ_1 is the principal stress parallel to the thread surface in the plane of the slice and σ_3 is the hoop principal stress both of which are defined in Fig. 7.2. However, $\eta \simeq 1.4^{\circ}$ hence $\sigma_3 \sin^2\eta$ was negligible.

The slice thickness was measured to an accuracy of $\pm$ 0.01 mm using a pointed anvil micrometer which for a typical slice thickness of 1.5 mm would give an error $\Delta s = \pm$ 0.7%.

Positional errors when measuring the peak fillet stresses were unimportant.

From the above, the standard error for manual photoelastic measurements of peak fillet stresses in both cast and machined models subjected to the three loading modes have been found and are shown in Table 7.2.3.

Table 7.2.3 - Standard Errors in Manual Photoelastic Measurements of Peak Fillet Stress

Loading Mode	Total % Error In	
	Machined Model	Precisely Cast Model
Tension Only	3.1	3.3
Preload Only	4.0	4.2
Tension+Preload	4.6	4.8

7.3 Errors in Automatic Photoelastic Measurements

The AMP has been used:-

a) to measure thread shear forces,

b) to measure surface stress distributions around thread fillets.

Each of the above applications have different errors associated with them.

7.3.1 Errors in Measuring Thread Shear Forces

Marston et. al. (18) have quantified the errors in measuring the fringe order and isoclinic angle with the AMP as $\pm$ 0.005 Fr and $\pm$ 0.2^{o} respectively. This takes into account repeatability of measurements and errors due to surface scratches which defract the light emitted from the slice.

The shear forces have been calculated from

$$V = \sum_{z=0}^{N} \tau_{rz} \, \delta z \qquad \ldots\ldots 7.4$$

where $\tau_{rz} = \frac{nf}{2s} \sin 2\Phi$ $\qquad \ldots\ldots 7.5$

The standard errors in τ_{rz} can be calculated from

$$= \Delta\tau_{rz} = \tau_{rz}\left[\left(\frac{\Delta n}{\bar{n}}\right)^2\left(\frac{\Delta f}{f}\right)^2+\left(\frac{\Delta s}{s}\right)^2+\left(\frac{\sin 2(\bar{\Phi}+\Delta\Phi)-\sin 2\Phi}{\sin 2\Phi}\right)^2\right]^{\frac{1}{2}} \quad \ldots 7.6$$

The average fringe order $\bar{n}$ and isoclinic angle Φ across a typical thread was 1 fr and 30° respectively. The usual slice thickness s was 1.55 mm and as stated earlier the accuracy in measuring s was $\pm$ 0.01 mm. The material fringe values f were measured from calibration strips cut from slices from each model. Tubes and couplings of each model were cast from the same mix of resin and hence should have had identical values of f. Table 5.1 does show differences in the measured values of f. The mean difference $\Delta f/f$ equals $\pm$ 1%. Using equation 7.6 the standard error $\Delta\tau_{rz}/\tau_{rz}$ equals $\pm$ 1.4%. The standard error in calculating the normalised shear force on each thread can be obtained from

$$\Delta V = \left[N(\Delta\tau.\delta z)^2 + (N.\tau.\Delta\delta z)^2\right]^{\frac{1}{2}} \quad \ldots\ldots 7.7$$

Initial positional errors $\Delta\delta z = \pm$ 0.01 mm and typical values of δz, N and τ_{rz} were 0.27 mm, 30 points and 0.072 N/mm^2 respectively. Using these values and equation 7.7.

$$\Delta V/V = \pm 3.7\%$$

For Model 4 the shear forces were measured at 17 positions in the mating tube and coupling threads. The mean difference between the nominally equal measurements was $\pm$ 4.9% which is of similar magnitude to the predicted error $\Delta V/V$ of 3.7%.

7.3.2 Errors in Measurements of Surface Stress Distributions Around Thread Fillets

The errors involved in measuring the distributions of surface stress around threads loaded with wall forces only and those loaded primarily with shear forces are similar in most respects. Contributory errors are:-

i) errors in the AMP measurements of fringe order,

ii) errors due to initial positioning of the slices,

iii) errors due to divergence of thread shapes from designed shape,

iv) errors due to moisture absorption and edge effects.

As was stated earlier the standard errors in measuring fringe order using the AMP was $\pm$ 0.005 fr. The measured fringe orders varied greatly from thread to thread and also around individual threads. We were primarily interested in the region $0^{\circ}<\phi<45^{\circ}$, where the fringe order generally varied between 1.5 fringes and 0.5 fringes. Hence maximum and minimum errors were $\pm$ 1% and $\pm$ 0.33%. The error in measuring the slice thickness was $\pm$ 0.6%.

The thread could be positioned accurately on the stage of the AMP to $\pm$ 0.01 mm, which for a thread with a typical radius of 2 mm led to an error in position around the thread $\Delta\phi$ of $\pm$ 0.25°. For threads loaded with wall tension only, the stress distribution around the thread can be characterised by

$$\sigma_a/\sigma_{sa} = C_1+C_2 \cos 2\phi \qquad \ldots\ldots 7.8$$

the error in σ_a/σ_{sa} due to $\Delta\phi$ at $\phi\simeq 0^{\circ}$ was negligible but at $\phi\simeq 45^{\circ}$ could lead to an error of $\pm$ 0.9%.

For threads loaded with shear force only the distribution of stress around the thread can be characterised by

$$\sigma_F/\sigma_{SF} = C_3+C_4 \sin 2\phi \qquad \ldots\ldots 7.9$$

Errors in σ_f/σ_{SF} due to $\Delta\phi$ near $\phi = 0^\circ$ would be $\pm$ 0.9% and negligible at $\phi \simeq 45^\circ$.

Due to the stress gradients normal to the fillet surface $\partial\sigma_1/\partial R_F$, shown in Fig. 5.8, the positional errors of $\pm$ 0.01 mm could lead to errors in σ_1 of $\pm$ 1% near $\phi = 0$ and negligible errors in σ_1 near $\phi = 45^\circ$ in the threads loaded with wall tension only. For threads loaded primarily with shear force, errors in σ_1 of $\pm$ 1% would occur near $\phi = 45^\circ$ and would be negligible near $\phi = 0^\circ$.

As was stated in Section 5.3.2, the radius R could be measured using the 100 x magnification shadowgraph to an accuracy of $\pm$ 0.01 mm which considering the gradients $\partial\sigma_1/\partial R_F$ could lead to errors of $\pm$ 1.0% in σ_1 in regions of high fillet stress.

Threads with non-circular radii caused by machining errors were not analysed, but threads in the loaded coupling runout with w tending to 0 showed large deflections and the large strains in the thread radii would have increased the radii and tended to make them non-circular. These bending deflections also pushed the position of peak fillet stress to nearer $\phi = 60^\circ$ and hence Equation 7.9 became inaccurate and the coefficients C_3 and C_4 could not be obtained.

Edge effects can be seen in Fig. 5.8 as reductions in stress near the surface. It is generally accepted that these edge effects are due to moisture absorption from the atmosphere which causes compressive stresses. Marston (34) has proposed a relationship between the depth of penetration of edge effect d,mm and the time out of a dry environment t in hours which is

$$d = \frac{t^{0.4}}{8} \qquad \ldots\ldots 7.10$$

From equation 7.10 it can be seen that measurements 0.01 mm subsurface would be effected in only a few seconds. Because of this, extrapolated surface values were used, see Section 5.3.2, which may have been $\pm$ 0.01 fr in error.

Using the above individual errors, the standard errors in measured surface stress at $\phi = 0^{\circ}$ and $\phi = 45^{\circ}$ have been calculated for threads loaded with wall tension only and threads loaded with shear force and are shown in Table 7.3.1.

Table 7.3.1 Standard Errors In Measured Fillet Surface Stress

	Standard Errors at ϕ =	
	0°	45°
Wall tension loaded thread	$\pm$ 1.7%	$\pm$ 1.5%
Shear force loaded thread	$\pm$ 1.5%	$\pm$ 1.7%

Taking the above errors into account, errors in C_1 and C_3 would be of the order of $\pm$ 1.7 % while the gradient of stress around the fillets C_2 and C_4 could have errors of the order of $\pm$ 2.3%.

7.4 Errors in Finite Element Work

The errors involved in modelling tubular screwed connections using Finite Elements can be separated into two categories:-

a) those due to the differences between the F.E. mesh shape and a screwed tubular connection,

b) those due to mesh design.

7.4.1 Errors Due to Differences in Shape Between F.E. Meshes and Screwed Tubular Connections

The differences between the F.E. meshes and a screwed tubular connection have been outlined in Section 6.2. The likely individual errors in evaluating the coefficients C_1 to C_4 due to these differences are difficult to quantify but a comparison has been made between the values of the photoelastically measured peak fillet stresses and the calculated values in Section 8.4. The calculated values are obtained using equations which describe the effects of thread parameters on the values of the coefficients and have been obtained using the Finite Element results.

7.4.2 Errors Due to Mesh Design

Errors in mesh design are generally due to insufficient mesh density and the element long side/short side length ratio being too large. Three checks were carried out on F.E. meshes with thread-type projections:-

i) equilibrium of loads checked,

ii) principal stresses at free surfaces checked,

iii) continuity of stresses over element boundaries checked.

To check equilibrium of the F.E. meshes loaded with wall tension only and with shear forces only the distributions of normalised through-thickness axial stresses σ_z/σ_{nom} were measured at several sections between the thread-like projections and the end of the mesh. Typical distributions are shown in Figs. 7.3 and 7.4. From these distributions the mean normalised axial stresses could be obtained and equilibrium checked. Typical root mean square equilibrium errors for meshes loaded

with wall tension were $\pm$ 0.1% and for meshes loaded with shear forces were $\pm$1.2%.

At the free surfaces of the F.E. meshes one of the principal stresses should have been zero. Around the fillets of the thread-like projections the magnitudes of the nominally 'zero' stresses σ_{rf} were measured and compared with the maximum principal stress σ_{ψ} for meshes loaded with wall tension only and loaded with shear force only. The root mean square value of the 'zero' principal stress around thread fillets loaded with wall tension only and with shear force only is

σ_{rf} which equals 0.05 σ_{ψ}

The stresses at any node on an element boundary are the averages of the stresses in the intersecting element nodes. Surface node stresses are the average of two stresses. Subsurface 4 nodes will intersect at a point and hence the stresses will be the average of 4 values. In the fillets of threads loaded with shear force and loaded with wall tension only the individual node maximum principal stress σ_1 was compared with the average maximum principal stress $\bar{\sigma}_1$ and the worst case and root mean square differences are shown in Table 7.4.1.

Table 7.4.1 - Continuity Errors in $\sigma_1/\bar{\sigma}_1$

	Standard Difference %	Worst Difference %
Thread Loaded with Tension only	$\pm$4	$\pm$8
Thread Loaded with Shear Force only	$\pm$2	$\pm$10

The worst continuity errors occurred at the intersection of the thread fillet and the root i.e. at $\psi = 0^{o}$.

The standard and worst errors in surface fillet stress at any node due to mesh design for meshes loaded with tension only and shear force only have been tabulated in Table 7.4.2.

Table 7.4.2. Errors Due to F.E. Mesh Design

	Standard Errors %	Worst Errors %
Threads Loaded With Tension Only	$\pm$3.4	$\pm$14.2
Threads Loaded With Shear Force Only	$\pm$2.7	$\pm$16.2

The potentially worst errors occur at $\phi = 0$ and much of the error is due to continuity problems at the blend of the thread fillet and root. Appendix 7 shows plots of σ_a/σ_{sa} v cos 2ϕ and plots of σ_f/σ_{sf} v sin 2ϕ and it can be seen from these distributions that the individual points were furthest from the best fit straight lines at $\phi = 0^\circ$.

7.5 Comparisons Between Photoelastic Model and Prototype Steel Screwed Tubular Connections

The major differences between Araldite models and steel prototypes are:-

i) differences in Poissons ratio,

ii) lack of plastic deformation with Araldite.

At the stress freezing temperature Araldite is in its rubbery state and $\nu = 0.5$ while for steel $\nu = 0.3$. The Finite Element work carried out to evaluate the coefficients C_1 to C_4 was done with $\nu = 0.45$, see Chapter 6. Two meshes were reanalysed and ν was changed to 0.3. One mesh was loaded with wall tension only and the other with shear forces only. The principal stresses σ_1 and σ_2 in the thread fillets from $\phi = 0^\circ$ to $\phi = 45^\circ$ were compared with the corresponding values for $\nu = 0.45$. The mean differences have been presented in Table 7.5.1.

Table 7.5.1 - Mean Differences Due to Differences in Poissons Ratio

Load	Difference	
	$\frac{\sigma_{araldite} - \sigma_{steel}}{\sigma_{steel}} \times 100\%$	
	σ_1	σ_2
Wall tension	3.8	18
Shear Force	4.2	22

These differences due to Poissons ratio are similar to those found by Edwards (35) in cast tubular joints.

Under high loads plastic deformations are likely in the steel connections which cannot be modelled by linear elastic Araldite. The effects of plasticity on the thread shear force distributions are discussed in Section 9.3.

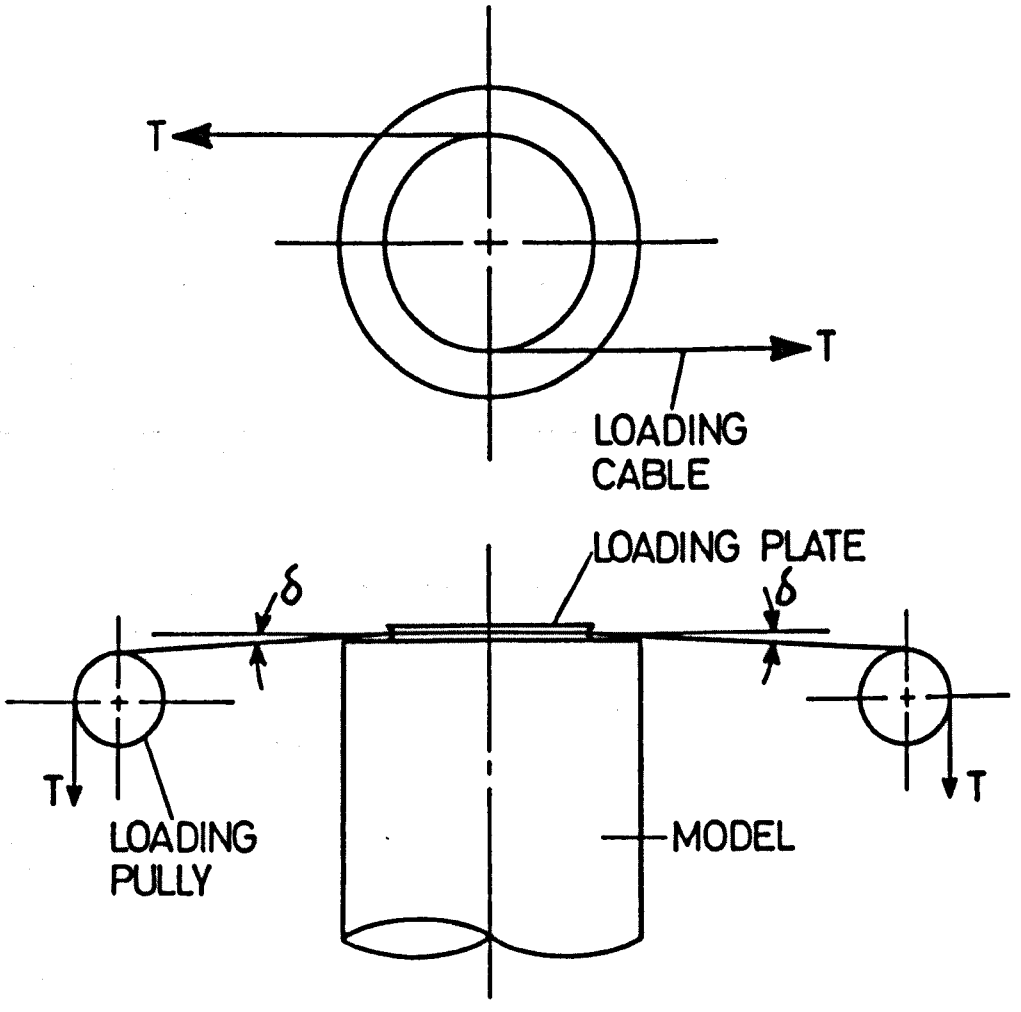

Fig 7.1

Potential Inaccuracies in Applying Preload

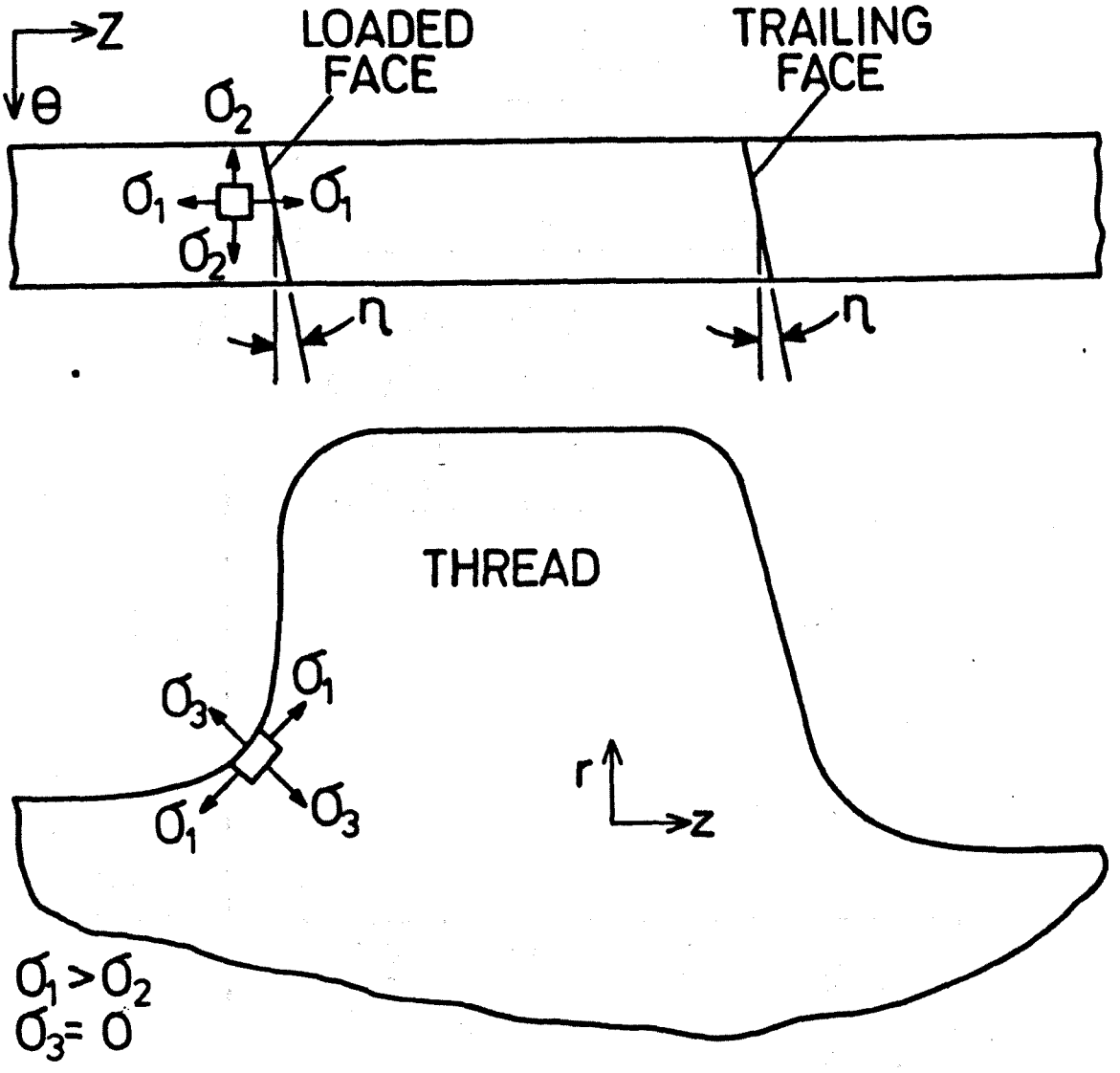

Fig 7.2

Definition of Principal Stresses at Model Surface

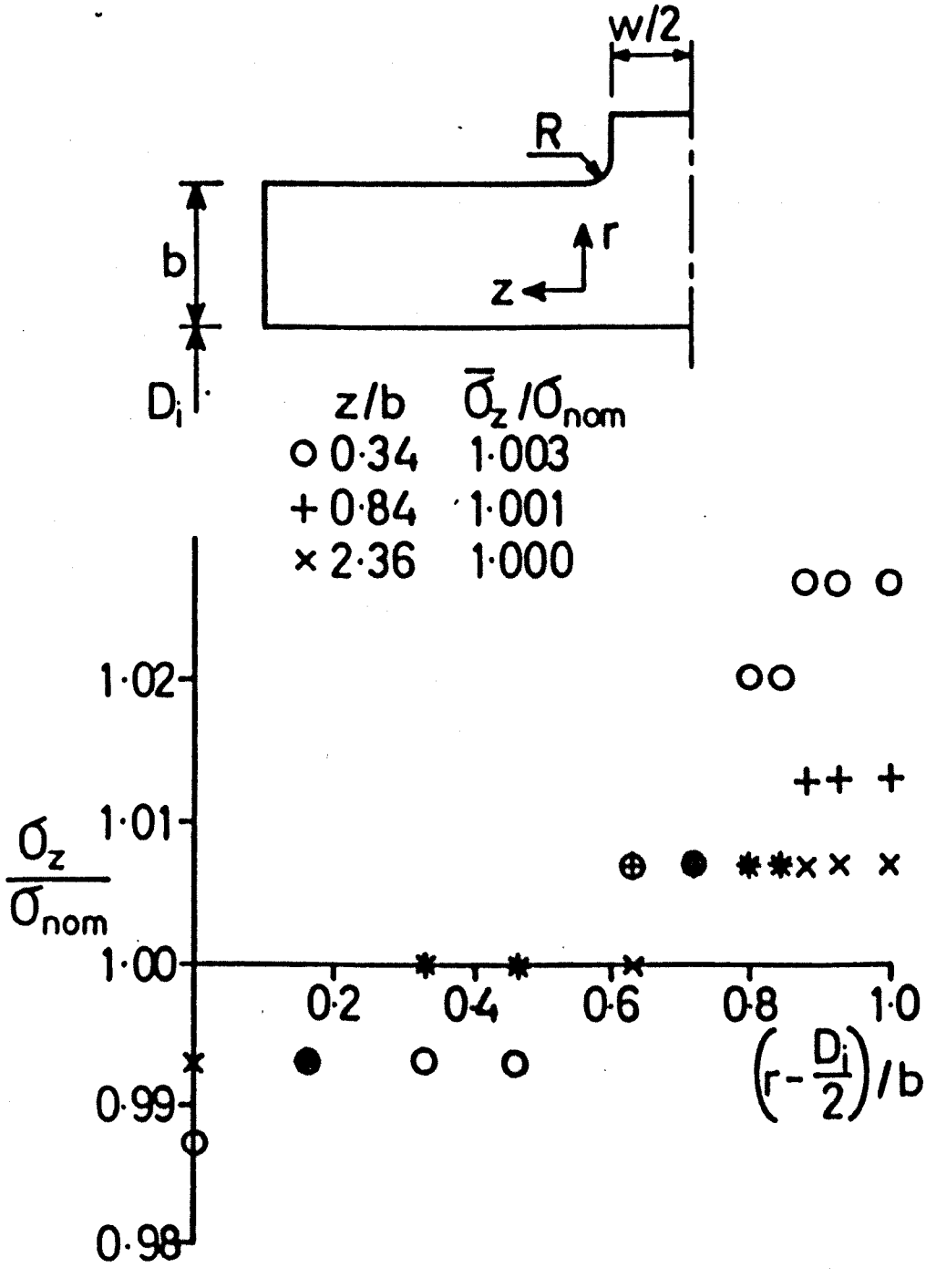

Fig 7.3

Through Thickness Distributions of Normalised Axial Stress at Various Positions in the Plain Region of a F.E. Mesh Loaded with Wall Tension Only to show how little Bending occurs.

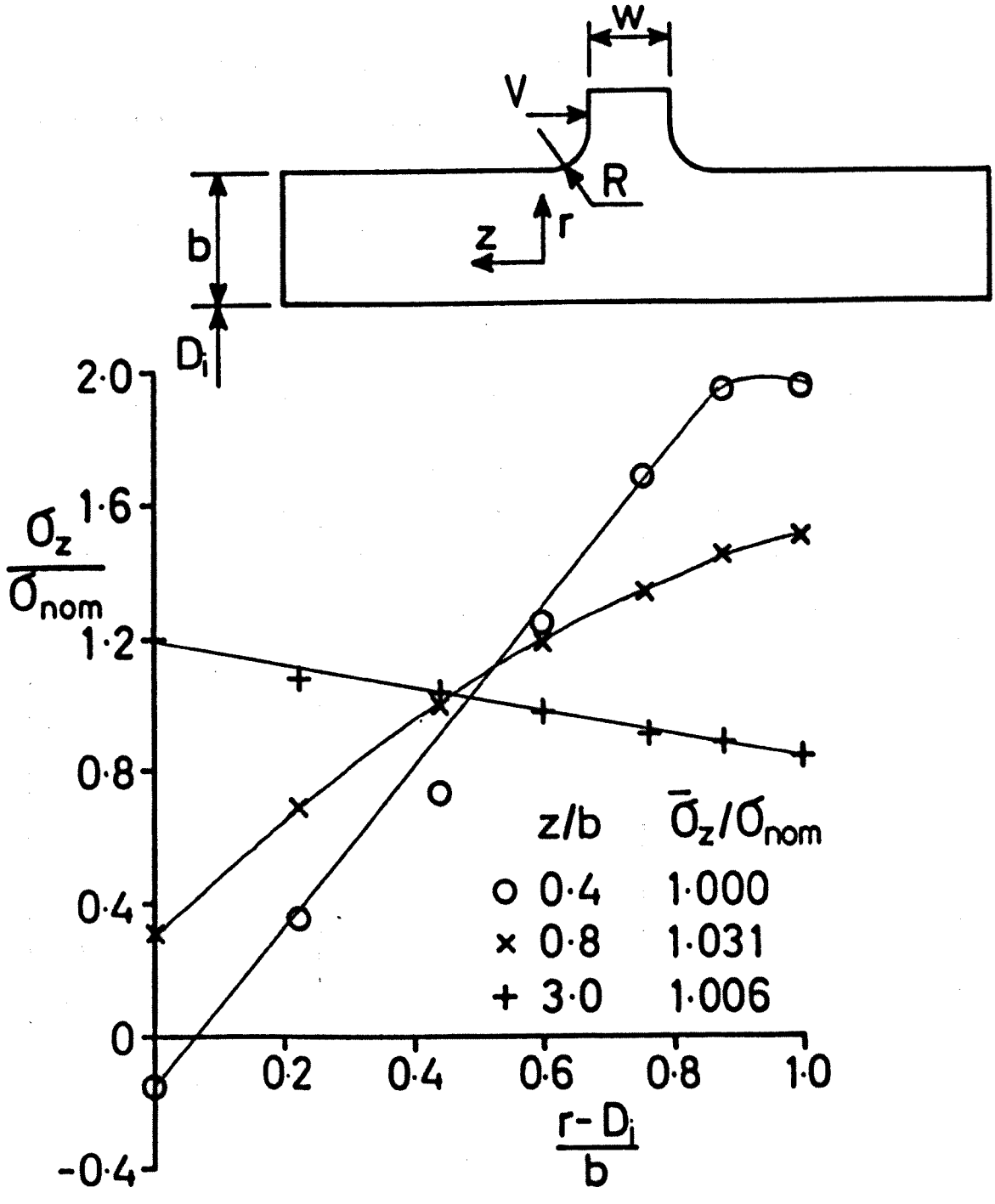

Fig 7.4

Through Thickness Distributions of Axial Stress at Various Positions in the Plain Region of a F.E. Mesh Loaded with Shear Force

CHAPTER EIGHT

RESULTS

8.1 Distributions of Thread Shear Forces, Wall Forces and Wall Stresses

In order to calculate fillet stresses due to shear forces, the distributions of shear force due to the different loading modes of tension and preload are required. Table 8.1.1 shows the shapes of the models for which measurements of shear force distribution were obtained. Also shown are the photoelastically measured applied loads obtained from the calibrations.

Table 8.1.1 Shapes of and Loads Applied to Models for which Full Shear Force Distributions were obtained

MODEL	4	5	9	10
SHAPE				
$b_{min(mm)}$	15.7	10.5	14.8	14.8
$b_{max(mm)}$	20.0	14.7	19.9	19.9
$p/b_{max.}$	0.79	1.08	0.79	0.79
R/b_{max}	0.097	0.17	0.12	0.12
h/b_{max}	0.294	0.4	0.294	0.294
L/p_{max}	6.5	6.3	7.54±0.04	7.75±0.04
EXTENT OF COUPLING LOADED RUNOUT, °	180	60	120	120
MEASURED LOADS				
TUBE UNDERCUT TENSION, F(N)	1510	1180	764	0
COUPLING UNDERCUT TENSION, F+Q (N)	1384	1206	1184	652
REMAINING PRELOAD Q(N)	-206	0	420	652

The negative preload indicates wall tension remaining between the last loaded tube thread and the tube nose due to friction at the conical joint (see Appendix 3).

8.1.1 Distribution of Shear Forces and Wall Forces due to Wall Tension

The measured thread shear forces V have been normalised for Models 4, 5 and 9 by the mean shear force due to the applied tension V_F

where V_F = Applied Tension / Spiral length of thread contact

i.e. $$V_F = \frac{F}{(L/p)\,(p^2 + D_m^2 \pi^2)^{\frac{1}{2}}} \qquad \ldots \quad 8.1.1$$

and the normalised shear force $\bar{V} = V/V_F$.

The measured normalised shear forces for these models are shown in Figs. 8.1.1, 8.1.2 and 8.1.3. Also shown are the distributions of pitch-average shear forces measured between P = i and P = 1 + i and plotted mid-way between at P = i + 0.5, e.g. the pitch average shear force for Model 5 between P = 3.25 and P = 4.25

= (1.02 + 0.82 + 0.9 + 0.88)/4 = 0.905

This is plotted as an x at P = 3.75 on Fig. 8.1.2.

For Model 4, the average of both tube and coupling measurements were used to calculate the pitch-average shear forces. Figs. 8.1.4 and 8.1.5 show the distributions of measured normalised shear force in the last pitch of Models 5 and 9. Measurements were generally taken every 30° in the tube model only. They show $\partial V/\partial\theta$ was smaller mid-pitch than at integral pitches from the end of the thread spiral. Also $\partial V/\partial\theta$ was generally larger in Model 9 than in Model 5 and $\partial V/\partial\theta$ in Model 9 showed distinct maxima at $\theta = 240^\circ$ and $\theta = 60^\circ$ and minima at $\theta = 330^\circ$ and $\theta = 160^\circ$. This indicated that the end of contact in Model 9 was nearer P = 7.416 than P = 7.5 due to the symmetry of the shear forces in the last pitch about $\theta = 150^\circ$.

For Model 10, loaded with preload only, Fig. 8.1.6 shows the actual measurements and pitch average measurements normalised by the appropriate mean shear force. V_Q = Preload / Spiral length of thread contact

hence $V_Q = \dfrac{Q_o}{(L/p)(p^2+Dm^2\pi^2)^{\frac{1}{2}}}$ 8.1.2

and $\bar{V} = V/V_Q$

The distributions of shear forces in Model 9 due to axial tension only have been presented in Fig. 8.1.7. These have been obtained by taking away the shear force distribution due to a preload of 420N from the full shear force distribution of Model 9.

The result has been normalised by

$$V_F = \frac{F \text{ model } 9}{(L/p)\,(p^2+Dm^2\pi^2)^{\frac{1}{2}}}$$

Each of the above figures has been plotted against P, the pitch number. The length of engagement varied from model to model.

From the measurements of shear forces the average normalised shear forces over the complete thread spiral have been calculated and are shown in Table 8.1.2 along with the applied loads.

Table 8.1.2 Averages of Normalised Shear Forces and Applied Loads

MODEL	AVERAGE NORMALISED SHEAR FORCE	F(N)	$\frac{W_C}{F}$ *
4 TUBE	0.85	1500	1.01+
4 COUPLING	0.88	1500	0.93
5 TUBE	1.02	1180	0.99
9 TUBE	1.56	764	1.55
10 TUBE	1.00	0	∞
9 - 10 TUBE	1.02	764	—

* W_C = Measured coupling undercut tension

+ 1.01 = Measured tube undercut tension/F

The pitch-average shear force distributions of Model 5 and Model 9 minus Model 10 have been plotted against z/L (symbols 0 and + on Fig. 8.1.8). This shows that the different lengths of thread contact and differences in shape and wall thickness have negligible effect on the normalised pitch-average shear force distributions due to tension only.

For Model 4, the pitch-average shear forces have been multiplied by 1/0.86 and also plotted on Fig 8.1.8 (symbol x). This assumes that the reduction in shear forces due to negative preload in Model 4 was evenly distributed over the whole of the thread length. In fact, from Fig. 8.1.8 it can be seen that this assumption is not correct since the shear forces of Model 4 were concentrated near z/L = 1 which was the preloaded end of the threads. Also shown on Fig. 8.1.8 is the curve of the equation.

$$\bar{V}_F = 0.81 + 15\,(z/L - 0.5)^4 \qquad \ldots \qquad 8.1.3$$

This equation has been obtained by plotting $\bar{V}_F - 0.81\,|z/L-0.5|$ on log-log paper, see Fig. 8.1.9. z/L - 0.5 was chosen because the distributions of shear force were reasonably symmetrical about z/L = 0.5. It was important that the power be an even integer as any other value would not have generated a symmetrical curve about z/L = 0.5. Symmetry of the shear force distribution was assumed because of the near symmetry of the axial stiffness of the models about z/L = 0.5. The area under the $\bar{V}_F$ v z/L curve should = 1 which was the normalised mean applied tension F.

Hence,

$$F = \int_{z/L=0}^{z/L=1} \bar{V}_F d\left(\frac{Z}{L}\right) = 1 \qquad \ldots 8.1.4$$

i.e. $$F = \left[0.81(z/L) + 3((z/L) - 0.5)^5\right]_0^1$$

$$= 0.81 + 3 \times 0.5^5 - 3 \times (-0.5)^5 = 1 \qquad \ldots 8.1.5$$

The values of 0.81 and 15 in Equation 8.1.3 were obtained from Fig. 8.1.9. These values also ensured that Equation 8.1.4 was satisfied.

From Equation 8.1.4 the values of the normalised tube and coupling wall forces due to tension W_{tF} and W_{cF} could be obtained at any section i

i.e.
$$W_{tF} = \int_{z/L=0}^{z/L=i} \bar{V}_F d\left(\frac{Z}{L}\right) \quad \ldots \quad 8.1.6$$

and
$$W_{cF} = \int_{z/L=i}^{z/L=1} \bar{V}_F d\left(\frac{Z}{L}\right) \quad \ldots \quad 8.1.7$$

The accuracy of the above equations in predicting the distribution of wall forces can be seen in Fig. 8.1.10 which plots

$1 - \sum_{z/L=0}^{z/L=i} \bar{V}_F d\left(\frac{Z}{L}\right)$ from i = 0 to i = 1 for Models 4, 5 and 9 - 10 and the curve of

$$W_{tF} = 1 - \int \bar{V}_F d\left(\frac{Z}{L}\right) \quad \ldots \quad 8.1.8$$

where $W_{tF} = 1-(0.81\left(\frac{Z}{L}\right) + 3\left(\frac{Z}{L} - 0.5\right)^5 + \text{constant})$ ... 8.1.9

The constant of integration was found from the conditions that at z/L = 0, W_{tF} = 1 and at z/L = 1, W_{tF} = 0 both of these conditions indicate that

$$W_{tF} = 1- (0.81\left(\frac{Z}{L}\right)+ 3\left(\frac{Z}{L} - 0.5\right)^5 + 0.094) \quad \ldots \quad 8.1.10$$

For the coupling model, at z/L = 0, W_{cF} = 0 and at z/L = 1, W_{cF} = 1

Hence

$$W_{cF} = 0.81\left(\frac{Z}{L}\right)+ 3\left(\frac{Z}{L} - 0.5\right)^5 + 0.094 \quad \ldots \quad 8.1.11$$

The distribution of coupling wall force are a mirror image of the tube wall forces about z/L = 0.5.

8.1.2 Distribution of Shear Forces and Wall Forces due to Preload

For the preloaded Model 10 shear force distribution, it can be seen from Fig. 8.1.6 that the shear forces were not symmetrical about z/L = 0.5. But at z/L = 0.5, $\bar{V}_Q$ was approximately 0.9 and $d\bar{V}_Q/d\ (\frac{Z}{L})$ was approximately 0.65 From this data,

$$\bar{V}_Q = 0.58 + 0.65\ (z/L) + f\ (z/L) \qquad \ldots \quad 8.1.12$$

where f(z/L) is a function of z/L which is different between $0 < z/L < 0.5$ and $0.5 < z/L < 1$

$\bar{V}_Q$-0.58-0.65 (z/L) has been plotted against $|\ z/L - 0.5|$ on log-log paper for the pitch-average shear forces on Fig. 8.1.11. For the values from 0 to z/L = 0.5 (symbol ■)

$$\bar{V}_Q - 0.58 - 0.65\ (z/L) = -1.4(z/L - 0.5)^2 \qquad \ldots \quad 8.1.13$$

adequately describes the results.

$$\therefore\ \bar{V}_Q = 0.58 + 0.65\ (z/L) - 1.4(0.5-z/L)^2 \text{ for } 0 < z/L < 0.5 \quad \ldots\ 8.1.14$$

From Fig 8.1.11 the values from z/L = 0.5 to z/L = 1 (symbol x) indicate that

$\bar{V}_Q - 0.58 - 0.65(z/L) = 59\ (z/L - 0.5)^5$ Hence

$$\bar{V}_Q = 0.58 + 0.65\ (z/L) + 59\ (z/L - 0.5)^5 \text{ for } 0.5 < z/L < 1 \quad \ldots\ 8.1.15$$

Equations 8.1.14 and 8.1.15 have been plotted on Fig. 8.1.6 and show good agreement with the experimentally obtained pitch-average shear forces. From Equations 8.1.14 and 8.1.15 equations for the distributions of tube and coupling wall forces can be obtained. As previously stated, preload puts the tube nose in compression and the coupling wall in tension. Hence

$$W_{tQ} = -\int \bar{V}_Q d\ (\tfrac{Z}{L}) \qquad \ldots \quad 8.1.16$$

and

$$W_{cQ} = \int \bar{V}_Q d\ (\tfrac{Z}{L}) \qquad \ldots \quad 8.1.17$$

For the tube anywhere in the thread spiral from $z/L = 0$ to $z/L = 0.5$

$$W_{tQ} = -\int [0.58 + 0.65\ (z/L) - 1.4\ (0.5 - z/L)^2]\ d\ (\tfrac{Z}{L})$$

$$\therefore\ W_{tQ} = -\ [0.58\ (\tfrac{Z}{L}) + 0.325\ (\tfrac{Z}{L})^2 + 0.466(0.5 - z/L)^3 + \text{constant}] \quad \ldots \quad 8.1.18$$

the constant of integration can be found from the fact that at $z/L = 0$,

$W_{tQ} = 0 \quad \therefore \quad \text{constant} = -\ \frac{1.4}{3} \times 0.5^3 = -\ 0.0586$

For the tube anywhere in the thread spiral from $z/L = 0.5$ to $z/L = 1.0$

$$W_{tQ} = -\int [0.58 + 0.65\ (\tfrac{Z}{L}) + 59\ (\tfrac{Z}{L} - 0.5)^5]\ d\ (\tfrac{Z}{L})$$

$$W_{tQ} = -\ [0.58\ (\tfrac{Z}{L}) + 0.325\ (\tfrac{Z}{L})^2 + 9.833(\tfrac{Z}{L} - 0.5)^6 + \text{constant}] \quad \ldots \quad 8.1.19$$

at $z/L = 1$, $W_{tQ} = -\ 1$

$$\therefore\ \text{constant} = +\ 1 - 0.58 - \frac{0.65}{2} - \frac{59}{6} \times 0.5^6$$

$$= -\ 0.0586$$

For the curve of W_{tQ} to be continuous through $z/L = 0.5$, the constants of integration in Equations 8.1.18 and 8.1.19 must be equal, which they are. Equations 8.1.18 and 8.1.19 have been plotted on Fig. 8.1.12 along with the distribution of wall force obtained from the summation of measured thread shear forces ie

$$W_{tQ} = -\ \Sigma\ \overline{V}_Q\ \delta\ (z/L)$$

Similar distribution of the coupling wall forces W_{cQ} could be obtained, these would be a mirror image of the tube wall forces about $W_{cQ} = 0$.

8.1.3 Distribution of Wall Stress due to Tension and Preload

From Equations 8.1.11, 8.1.18 and 8.1.19 the distribution of wall forces W_t and W_c due to any combination of normalised F and Q can be obtained

ie $$W_t = F\ W_{tF} + \frac{Q}{F}\ W_{tQ} \quad \ldots \quad 8.1.20$$

and $$W_c = F\ W_{cF} + \frac{Q}{F}\ W_{cQ} \quad \ldots \quad 8.1.21$$

From the measurements of the wall thickness b, the normalised mean wall stress can be found at any section. For the tube

$$\sigma_{sa} = W_t\ \frac{(D_o - t)\ t}{(D_o - b)\ b} \quad \ldots \quad 8.1.22$$

and for the coupling

$$\sigma_{sa} = W_c \frac{(Do - t)t}{(Di + b)\,b} \qquad \ldots \qquad 8.1.23$$

Distributions from Equations 8.1.22 and 8.1.23 have been plotted on Figs. 8.1.13 and 8.1.14 using the values of F and Q from Table 8.1.2. Also shown on Figs. 8.1.13 and 8.1.14 are distributions of mean axial wall stress, measured in a similar way to the undercut stresses, but only at one position per pitch, see Section 5.1 i.e. the measured mean axial wall stresses for the tube

$$r = Do/2$$

$$\sigma_t = \sum_{r = \frac{Do}{2} - b} \frac{\sigma_z \, \delta r}{b} \qquad \ldots 8.1.24$$

and for the coupling

$$\sigma_c = \sum_{r = Di/2}^{r = \frac{Di}{2} + b} \frac{\sigma_z \, \delta r}{b} \qquad \ldots 8.1.25$$

For the wall stresses of Model 4 the negative preload is assumed to act like a negative tension force

i.e. $W_t = W_{tF}$ and

$$W_{tF} = 1 - \int \bar{V}_F \, d\left(\frac{Z}{L}\right)$$

$$W_c = W_{cF}$$

and $$W_{cF} = \int \bar{V}_F \, d\left(\frac{Z}{L}\right)$$

The distributions of wall stress due to these wall force distributions have also been plotted on Fig. 8.1.13 and 8.1.14. The only wall stresses measured were at z/L = 0 and z/L = 1.

8.1.4 Distributions of Shear Forces in Thread Runouts

The shear forces were measured at various positions in the loaded coupling runouts of Models 3 and 4. These models contained the full runout i.e. w reduces from p/2 to 0 over 180^{o}. The measured shear forces were normalised using the applied tension for each model and have been plotted on Fig. 8.1.15 against both positions in the thread spiral and thread width, w. The normalised shear forces in Model 4 were lower than in Model 3 due to the Model 4 thread spiral not carrying the full applied tension. It can be seen that for both runouts the reduction in thread width caused an increasing rate of reduction in shear force. The shear force shed by the runout increased the shear forces in the rest of the thread spiral but the load shed

$$- \bar{V}_{max} \times p/2 - \int_{w=0}^{w=p/2} \bar{V}\, dw \qquad \ldots\ldots 8.1.26$$

where $\bar{V}_{max}$ is the shear force at w = p/2. A numerical integration of Equation 8.1.26 shows that the load shed by the runout equals approximately 3% of the applied tension.

8.2 Distributions of Stresses in Thread Fillets

8.2.1 Stresses due to Wall Tension

As was outlined in Sections 5.3.2 and 6.4 fillet surface stresses σ_a due to wall tension only were normalised by the mean tensile stress σ_{sa}, measured by photoelastic and axisymmetric finite element techniques, and plotted against cos 2ϕ. Typical examples are shown in Fig 5.10 the remaining distributions are shown in Appendix 7. The relevant stresses in both loaded and unloaded threads are defined in Fig. 8.2.1. The linear region of these curves has been characterised by the equation

$$\sigma_a/\sigma_{sa} = C_1 + C_2 \cos 2\phi \quad \ldots\ldots 8.2.1$$

Table 8.2.1 shows the shapes of the threads investigated, the values of C_1 and C_2 obtained and the ratio of surface stress adjacent to the thread fillet / mean tensile stress, σ_a/σ_{sa}. The values of C_1 have been plotted against w/b on Fig. 8.2.2 It can be seen that the values of C_1 obtained by photoelastic and finite element methods agree fairly well. The values of C_1 for varying w/b but constant R/b fit on smooth curves.

The values of C_1 obtained by F.E. techniques only were replotted on log-log paper against R/b, see Fig 8.2.3. From which it can be seen that $C_1 = a_1 (R/b)^{a_2}$. The gradient a_2 was nearly constant and the average value of - 0.56 has been used. a_1 was plotted against w/b on log-log paper on Fig 8.2.4 and the equation $a_1 \simeq 0.32\ (w/b)^{0.42}$ was obtained.

From these figures and by trial and error adjustment, the equation

$$C_1 = 0.38\ (w/b - 0.050)^{0.45}\ (R/b)^{-0.56} \quad \ldots \quad 8.2.2$$

was arrived at.

TABLE 8.2.1 SHAPES, LOADING AND RESULTS FROM THREAD SHAPES LOADED WITH WALL TENSION OR BENDING

Method	Thread shape R/b	Thread shape w/b	SURFACE STRESS MEAN TENSION σ_s/σ_{sa}	TENSION C_1	TENSION C_2	PHOTO E MODEL NUMBER	F.E PURE BENDING C_1	F.E PURE BENDING C_2
F.E.	0.02	0.1	1.00	0.96	1.22	-	0.98	1.19
"	"	0.15	"	1.20	1.22	-	1.28	1.20
F.E.	0.03	0.15	"	0.95	1.21	-	1.08	1.25
"	0.03	0.53	"	1.63	1.25	-	1.87	1.27
F.E.	0.06	0.125	"	0.58	1.27	-	0.57	1.27
"	"	0.25	"	0.87	1.24	-	0.95	1.14
"	"	0.37	"	1.09	1.24	-	1.21	1.13
"	"	0.55	"	1.32	1.25	-	1.39	0.97
P.E.	0.08	0.130	1.13	0.52	0.98	5T	-	-
"	"	0.165	1.13	0.62	1.13	"	-	-
"	"	0.205	1.16	0.80	1.12	"	-	-
"	"	0.243	1.25	0.81	1.06	"	-	-
"	"	0.380	1.07	0.85	1.09	"	-	-
F.E.	0.100	0.200	1.00	0.56	1.30	-	0.57	1.17
"	"	0.400	"	0.85	1.22	-	0.87	1.10
"	"	0.600	"	1.05	1.20	-	1.10	1.04
"	"	0.900	"	1.24	1.16	-	1.31	1.04
P.E.	0.113	0.08	1.14	0.40	0.91	4T	-	-
"	"	0.41	1.06	0.76	0.94	"	-	-
F.E.	0.134	0.265	1.00	0.56	1.29	-	0.60	0.96
"	"	0.535	"	0.83	1.22	-	1.00	1.02
"	"	0.805	"	1.00	1.18	-	1.19	0.93
P.E.	0.134	0.05	1.38	-0.04	1.43	6C	-	-
"	"	0.138	1.13	0.22	1.42	"	-	-
"	"	0.228	1.18	0.46	1.16	"	-	-
"	"	0.316	1.09	0.52	1.08	"	-	-
"	"	0.401	1.07	0.58	1.09	"	-	-

TABLE 8.2.1 SHAPES, LOADING AND RESULTS FROM THREAD SHAPES LOADED WITH WALL TENSION OR BENDING (continued)

Method	Thread shape		SURFACE STRESS MEAN TENSION σ_s/σ_{sa}	TENSION		PHOTO E MODEL NUMBER	F.E. PURE BENDING	
	R/b	w/b		C_1	C_2		C_1	C_2
F.E.	0.167	0.34	1.00	0.56	1.25	-	0.54	1.12
"	"	0.68	"	0.82	1.19	-	1.00	0.89
"	"	1.01	"	0.97	1.14	-	1.16	0.84
P.E.	0.167	0.076	1.30	0.36	1.28	8T	-	-
"	"	0.165	1.21	0.34	1.01	"	-	-
"	"	0.250	1.23	0.40	0.97	"	-	-
"	"	0.300	1.23	0.47	1.07	"	-	-
"	"	0.415	1.33	0.69	1.01	"	-	-
"	"	0.515	1.29	0.64	1.01	"	-	-

Note;- For the F.E. pure bending tests, $\sigma_s/\sigma_{sa} = \infty$

Equation 8.2.2 has been used to calculate values of C_1 for selected R/b values and over the range of w/b. Shown as continuous lines on Fig. 8.2.2, Equation 8.2.2 fits the data very closely for $0.05<w/b<0.7$ and in the range $0.02< R/b< 0.17$. Also shown on Fig. 8.2.2 are the values of C_1 for $w = 2R$ obtained using Equation 8.2.2. R=w/2 is a practical limit for circular-arc fillet radii and the values of C_1 for practical thread shapes lie above this line. It can be seen that many of the photoelastic threads analysed have $w< 2R$. This is because they were in the unloaded runout where w was reduced, see Section 3.3.

The R/b = 0 line has been drawn vertically since $\sigma_a = \infty$ for a sharp notch and through w/b = 0.05 to be consistent with Equation 8.2.2.

It should be noted that for w/b = 0.05, $C_1 = 0$, but stresses would still occur in a projection with this shape due to the effect of C_2. Thread shapes with $w/b< 0.05$ have not been analysed since it is unlikely that threads would be made with such a fine pitch. But it seems likely that C_1 would become negative since at w/b = -2R/b $\therefore$ no projection and $\sigma_a/\sigma_{sa} = 1$ $\therefore$ no stress concentration $\therefore$ $C_1 + C_2 \cos 2\phi = 1$ where $\phi = 0$ hence $C_1 = -C_2$

The coefficient C_2 has been plotted against w/b on Fig. 8.2.5.

For the finite element results

$$C_2 = (1.29 - 0.144\ w/b) \pm 0.05 \quad \ldots \quad 8.2.3$$

For $0.02 < R/b < 0.17$ and $0.1 < w/b < 1.0$

The photoelastically obtained values of C_2 were generally below the line described by Equation 8.2.3.

A major difference between the FE meshes and the PE threads was the wall bending present in the P.E. model walls. To investigate the effects of bending the FE meshes were loaded with pure wall bending i.e. $\sigma_s/\sigma_{sa} = \infty$ and were analysed in the same way as those loaded with pure tension, see Section 6.4.

The values of σ_a for wall bending were normalised by σ_{sb} the tensile surface stress due to wall bending which would have occurred if the stress raising fillet had not been present, see Section 6.4. Typical distributions of σ_a/σ_{sb} are shown in Fig. 8.2.6. For meshes with low values of w/b the distributions of σ_a/σ_{sb} were linear from $\psi = 10^o - 15^o$ to values of ψ where $\sigma_a/\sigma_{sb} \simeq 0$ (symbols V and o). As w/b increased the linear region was reduced hence Equation 8.2.1 less adequately described the fillet stress distributions, although the values of C_1 were generally very similar to the values of σ_a/σ_{sb} at $\psi = 45^o$.

The values of C_1 for the wall bending case were generally similar to those for wall tension loading and have not been shown. The values of C_2 along with Equation 8.2.3 have been plotted against w/b on Fig. 8.2.7 for bending From Fig. 8.2.7. it can be seen that the values of C_2 obtained from pure bending F.E. tests were lower than those predicted by Equation 8.2.3.

For a thread within the contact region the wall bending will be primarily due to the thread shear force applied at that section and will be taken account of when calculating the fillet stresses due to shear forces, see Section 5.3. Hence, Equation 8.2.3 will tend to overestimate C_2 and hence give safe conservative values of fillet stresses due to wall tension.

8.2.2. Fillet Stresses due to Shear Forces

The fillet stresses due to shear forces can be characterised by the equation

$$\sigma_F/\sigma_{SF} = C_3 + C_4 \sin 2\psi \qquad \ldots \qquad 8.2.4$$

Table 8.2.2 shows the shapes of F.E. thread-like projections investigated and the values of C_3 and C_4 obtained. For the F.E. thread-like shapes, axisymmetric unit shear forces were applied to the thread-like projections, see Section 6.2 . For the threads analysed photoelastically, the shear forces varied around the thread spiral and

they were measured at each section of thread analysed, see Section 5.2. The measured and applied shear forces were used to calculate the nominal bending stress which normalised the measured fillet stresses, see Appendix 4 . The photoelastically measured normalised shear forces, thread shapes and values of C_3 and C_4 obtained are presented in Table 8.2.3.

The distributions of σ_F/σ_{SF} plotted against sin 2ψ became increasingly non-linear as w/b reduced. Typical photoelastic and finite element linear and non linear distributions are plotted in Fig. 8.2.8. The remaining distributions of both photoelastic and finite element distributions are presented in Appendix 7.

As w/b reduced, thread bending became more important and ψ_{max} moved from 45^o to nearer 60^o. This effect was less apparent for small values of e/R at the same w/b. The shapes for which there were non-linear distributions of fillet stresses are shown in Tables 8.2.2 and 8.2.3.

Equation for C_3

The values of C_3 obtained by both photoelastic and finite element techniques have been plotted against w/b on Fig. 8.2.9.

The finite element values of C_3 were used to obtain a parametric equation and were plotted on log-log paper against w/b on Fig. 8.2.10 From this figure, C_3 can be characterised by

$$C_3 = a_3 (w/b)^{a_4} \quad \ldots \quad 8.2.5$$

the values of a_3, a_4 and thread shapes are shown in Table 8.2.4 for the Finite Element results only.

Table 8.2.2 Values of C_3 and C_4 for shapes of F.E. thread type Projection

Loaded with Shear Force

			w/b							
			0.15		0.35		0.60		1.0	
R/b	e/b	e/R	C_3	C_4	C_3	C_4	C_3	C_4	C_3	C_4
0.02	0.06	3	11.4	14.7	8.0	8.1	6.50	7.5	6.1	7.1
	0.12	6	*	*	6.90	8.5	4.90	5.30	4.00	4.60
	0.17	8.50	*	*	7.65	8.40	4.25	4.89	3.70	3.55
	0.25	12.50	*	*	6.60	11.4	4.20	5.6		
0.06	0.06	X	X	X	X	X	X	X	X	X
	0.12	2	X	X	3.45	5.05	2.85	3.45	2.45	3.05
	0.17	2.83	X	X	3.35	5.15	2.60	3.20	2.10	2.45
	0.25	4.16	X	X	3.25	5.85	2.47	3.23	2.00	1.95
0.17	0.06	X	X	X	X	X	X	X	X	X
	0.12	X	X	X	X	X	X	X	X	X
	0.17	1.00	X	X	1.55	3.10	1.32	2.18	1.05	1.90
	0.25	1.47	X	X	1.55	3.10	1.23	2.03	1.10	1.33
0.25	0.06	X	X	X	X	X	X	X	X	X
	0.12	X	X	X	X	X	X	X	X	X
	0.17	X	X	X	X	X	X	X	X	X
	0.25	1.00	X	X	X	X	1.0	1.73	0.9	1.27

X indicates impractical shape

For all shapes (Di+ 2b)/b = 10

* Non linear distributions of σ_F against sin 2 ϕ See Fig. 8.2.8 symbol +

TABLE 8.2.3 SHAPES AND PHOTOELASTICALLY OBTAINED RESULTS FOR THREADS LOADED WITH SHEAR FORCE

Model 3 Coupling b = 11.2 mm

θ	w/b	R/b	e/b	D_i/b	$\bar{V}$	C_3	C_4
180	0.65	0.14	0.22	16.6	1.20	1.50	0.50
135	0.59	"	"	"	1.18	0.70	1.40
90	0.41	"	"	"	1.04	1.45	1.60
67	0.33	"	0.21	"	0.90	*	*
22	0.15	"	0.15	"	0.81	*	*

Model 4 Coupling, b = 15.4mm

300	0.48	0.13	0.16	11.4	0.91	1.20	1.0
180	"	"	0.13	"	1.00	1.15	0.95
135	0.45	"	0.13	"	0.93	1.10	0.75
90	0.32	"	0.14	"	0.86	1.15	1.20
67	0.25	"	0.15	"	0.64	*	*
45	0.19	"	0.16	"	0.58	*	*

* Non linear distributions of σ_F against sin 2ϕ See Fig 8.2.8 symbol ▼

Table 8.2.4 Tabulated Values of a_3, a_4 and Thread Shape

R/b	e/b	a_3	a_4	Symbol (Fig 8.2.10)
0.02	0.06	5.25	-0.41	Δ
"	0.12	3.90	-0.52	▽
"	0.17	3.40	-0.70	◁
"	0.25	2.83	-0.80	▷
0.06	0.12	2.42	-0.33	▽
"	0.17	2.10	-0.45	▷
"	0.25	1.99	-0.45	<
0.17	0.17	1.07	-0.35	X
"	0.25	1.07	-0.35	0
0.25	0.25	0.9	-0.2	□

$-a_4$ has been plotted against R/b on log-log paper on Fig. 8.2.11 and

$$-a_4 = 0.154(R/b)^{-0.36}$$

or $$a_4 = -0.154\ (R/b)^{-0.36} \qquad \ldots\ldots\ 8.2.6$$

shows reasonable agreement with the data.

There appear to be other factors influencing a_4, but further refinement of Equation 8.2.6 would have had little effect on the calculated values of C_3.

The values of a_3 have been plotted against R/b on log-log paper on Fig. 8.2.12 and the equation

$$a_3 = 0.415\ (R/b)^{-0.56} \qquad \ldots\ldots\ 8.2.7$$

fits the data reasonably well, but e/b does influence the value of a_3.

$$\therefore\ C_3 \simeq 0.415\ (R/b)^{-0.56}\ (w/b)^{-0.154}\ (R/b)-0.36 \qquad \ldots\ldots\ 8.2.8$$

In order to determine the influence of e/b on C_3, the measured values of C_3 at each value of R/b and w/b were compared with the C_3 values calculated from Equation 8.2.8 and C_3 Measured/C_3calculated was plotted against e/b on Fig. 8.2.13. From this figure

C_3 measured = $0.75\ (e/b)^{-0.19} \times C_3$ calculated

$\therefore$ a new equation for C_3 has been obtained taking into account the influence of e/b.

ie $C_3 = 0.311\ (e/b)^{-0.19}\ (R/b)^{-0.56}(w/b)^{-0.154}\ (R/b)^{-0.36}$ ... 8.2.9

Equation 8.2.9 has been plotted on Fig. 8.2.9 for the values of R/b which were analysed and for maximum and minimum values of e/b, (the solid lines).

Also shown dotted is the curve for w = 2R and e = R obtained from Equation 8.2.9.

Equation for C_4

The values of C_4 obtained by both photoelastic and Finite Element techniques have been plotted against w/b on Fig. 8.2.14. The F.E. results have been plotted against R/b on log-log paper on Fig.8.2.15 and C_4 can be characterised by the equation

$$C_4 = a_5\ (R/b)^{a_6} \quad \ldots \quad 8.2.10$$

where a_5 and a_6 have been obtained from Fig. 8.2.15

The coefficients a_5 and a_6 are presented along with the shapes in Table 8.2.5

Table 8.2.5 Tabulated values of a_5 a_6 and Thread shape

w/b	e/b	a_5	a_6	SYMBOL (Fig 8.2.16)
1.0	0.25	0.78	-0.33	O
"	0.17	1.15	-0.28	□
"	0.12	1.15	-0.35	<
0.6	0.25	0.95	-0.45	>
"	0.17	1.15	-0.37	∇
"	0.12	1.22	-0.37	Δ
0.35	0.25	1.09	-0.59	U
"	0.17	1.45	-0.45	⌓
"	0.12	1.32	-0.47	D

$-a_6$ has been plotted against w/b on log-log paper on Fig 8.2.16 and the equation

$$-a_6 = 0.32\ (w/b)^{-0.43}$$

$$\therefore\ a_6 = -\ 0.32\ (w/b)^{-0.43} \qquad \ldots\ldots\ 8.2.11$$

shows reasonable agreement with the data. In a similar way to the equation for a_4, other factors may affect a_6 but further refinement of Equation 8.2.11 would have little effect on the calculated C_4 values.

The values of a_5 were plotted against w/b on Fig 8.2.17 and the equation

$$a_5 = (w/b)^{-0.25} \qquad \ldots\ldots\ 8.2.12$$

fits the data reasonably well. No simple function of e/b or e/R could be found to improve the accuracy of Equation 8.2.12 so the equation

$$C_4 = (w/b)^{-0.25}\ (R/b)^{(-0.32(w/b)^{-0.43})} \qquad \ldots\ldots\ 8.2.13$$

was used to generate curves of C_4 for equal R/b on Fig. 8.2.14

Also shown on Fig. 8.2.14 is the curve of w = 2R obtained using Equation 8.2.13.

8.2.3 Summary Of Individual Thread Fillet Stresses Due To Wall Tension And Shear Force

As explained previously the fillet stress σ_L, at any position ϕ in any thread section is made up of stresses due to wall tension, σ_a plus stresses due to thread shear force, σ_F

$$\text{ie.} \qquad \sigma_L = \sigma_a + \sigma_F \qquad \ldots\ldots\ 8.2.14$$

where the fillet stresses due to wall tension can be characterised by the equation

$$\sigma_a = \sigma_{sa}\ (C_1 + C_2 \cos 2\phi) \qquad \ldots\ldots\ 8.2.1$$

σ_{sa} is the mean wall stress at the section of the thread considered and is a function of the applied loads F and Q, the position along the thread spiral z/L and the cross-sectional area of the model wall, (see Section 8.1).

The fillet stresses due to shear force can be characterised by the equation

$$\sigma_F = \sigma_{SF}\ (C_3 + C_4 \sin 2\phi) \qquad \ldots\ldots\ 8.2.4$$

σ_{SF} is the nominal surface bending stress and is calculated from 'beam-on-elastic-foundations' type equations, see Appendix 4.

C_1, C_2, C_3 and C_4 are non-dimensional coefficients for which empirical relationships between them and the thread parameters have been obtained in Sections 8.2.1 and 8.2.2

$$C_1 = 0.38(w/b - 0.05)^{0.45} (R/b)^{-0.56} \quad \text{for } 0.05 < w/b < 0.7 \text{ and } 0.02 < R/b < 0.17 \quad \ldots 8.2.2$$

For $w/b < 0.05$, the value of C_1 is undefined but negative and for values of $w/b > 0.7$ and R/b outside the range given, the use of Equation 8.2.2 will approximate values of C_1.

$$C_2 = 1.29 - 0.144\ w/b \quad \ldots \quad 8.2.3$$

for $0.1 < w/b < 1.0$

and $0.02 < R/b < 0.17$

For values of w/b and R/b outside the ranges given, Equation 8.2.3 should be used to give approximate values of C_2.

$$C_3 = 0.311\ (e/b)^{-0.19}\ (R/b)^{-0.56}(w/b)^{(-0.154(R/b)^{-0.36})} \quad \ldots 8.2.9$$

For $0.15 < w/b < 1.0$

$0.02 < R/b < 0.25$

$0.06 < e/b < 0.25$

Practical limits on Equation 8.2.9 are:-

$e/b \geqslant R/b$ and $w/b \leqslant 2R/b$. Equation 8.2.4 does not accurately describe the fillet stress distribution when $e/b \geqslant w/b$

ie. when the thread shape becomes more like a cantilever in bending.

$$C_4 = (w/b)^{-0.25}(R/b)^{(-0.32\ (w/b)^{-0.43})} \quad \ldots \quad 8.2.13$$

for the same range of parameters and limits as Equation 8.2.9

The use of the above equations and relationships will enable the fillet stresses to be calculated at any position ϕ in the thread

and at any position z/L in the thread spiral as long as the model shape and applied loads are known. Also the position and magnitude of the peak fillet stress anywhere in the thread spiral can also be found using these equations and those developed in Section 8.1 for the applied loads, see Section 8.4.

8.3 Positions and Magnitudes of Peak Fillet Stresses Measured Photoelastically

8.3.1 Introduction

For models loaded with tension only, preload only and tension plus preload the position of the peak fillet stress, ϕ_{max}, was measured around the thread spiral of both the tubes and couplings. For each of the 10 models analysed the distributions of peak fillet stresses for both tube and coupling were measured. For all but the preload only models, the peak fillet stresses were normalised by the mean full tube wall stress.

$$\sigma_{nom} = \frac{F}{\pi(D_o - t)t}$$

For the preload only models, the peak fillet stresses were normalised by the stress which would have occurred in the full tube wall if the preload had been applied as a tension i.e.

$$\sigma_{nom} = \frac{Q}{\pi(D_o - t)t}$$

For each model the peak fillet stresses were measured, starting at $\theta = 0^o$ in the first loaded pitch and at $\delta\theta = 30^o$ in the first and last pitches and at $\delta\theta = 90^o$ between. For the purposes of comparing stresses in models with different shapes and different loading modes, the pitch-average peak fillet stresses have been calculated and tabulated. Comparisons between different model peak fillet stresses have generally been made in the middle region of the thread spiral, away from the high concentrations in the first and last pitches and away from the non-uniformities caused by the thread runouts.

8.3.2 Positions of Peak Fillet Stresses Due to Different Loading Modes

For the tubes and couplings of Models 5, 9 and 10, the position of the peak fillet stress ϕ_{max}, was measured at the same positions as the peak fillet stresses. Due to the small stress gradients around the fillets, the position of peak fillet stress could only be measured to an

accuracy of approximately $\pm 5^{\circ}$ by manual photoelastic techniques. Because of this, the average value of ψ_{max} in each whole pitch was calculated. These values are shown in Fig. 8.3.1.

For Model 5, loaded with tension only, ψ_{max} was similar for both the tube and coupling models and nearly constant at $\psi_{max} \simeq 20^{\circ}$ in all but the first thread of the coupling, i.e. $0<P<1$, and the last thread of the tube, i.e. $5<P<6$. In these regions, the thread shear forces were high but the wall tensions were low and as σ_{sa}/σ_{sF} tended to 0, ψ_{max} tended to 45°.

It can be seen from Fig. 8.3.1 that ψ_{max} was not measured over the complete thread spiral of the preloaded Model 10. This was because in regions of low fillet stresses ($0<P<4$ for the tube and $0<P<2$ for the coupling) the stress gradients around the fillet $d\sigma_L/d\psi$ were very low and the value of ψ_{max} was difficult to measure. But it can be seen that in the tube model the maximum tensile fillet stress occurred at $\psi \simeq 60^{\circ}$. In this region of the fillet the compressive fillet stresses due to the compressive wall forces were small compared with the tensile fillet stresses due to the shear force i.e.

$$\sigma_{sa}(C_1+C_2\cos 2\psi_{max}) \simeq 0$$

hence $C_1 \simeq -C_2 \cos 120^{\circ}$

For the coupling the wall forces were tensile, hence $\psi_{max} < 45^{\circ}$ and fairly constant at $\psi_{max} = 26^{\circ} \pm 3^{\circ}$. It can be seen from Fig. 8.1.6 and Fig. 8.1.10 that shear forces and wall forces were similar in the respect that both reduced as z reduced. Hence σ_{sF}/σ_{sa} was similar in the region of coupling thread analysed, even though both σ_{sF} and σ_{sa} were reducing.

For the tension and preloaded Model 9 tube, the distribution of ψ_{max} was similar to the values of ψ_{max} for the tension only model in the

region where tension predominated i.e. near P=0. At the other end of contact near z=L the values of ϕ_{max} for the tube tended to be larger and similar to those due to preload only. In the coupling model, the distribution of ϕ_{max} was similar to that due to preload only except in the last pitch, i.e. $6.5 < P < 7.5$ where ϕ_{max} for tension and preload was less than that due to preload only.

8.3.3 Peak Fillet Stresses Due to Tension Only

The peak normalised fillet stress distributions over the complete thread spirals of both tubes and couplings for Models 1, 3 and 5 loaded with tension only are shown in Figs. 8.3.2, 8.3.3 and 8.3.4. The results from Model 6, which was loaded with tension only, are presented later along with those of Model 7, which was identical in shape to Model 6 but loaded with preload only. The pitch-average peak fillet stresses have been calculated from these measurements and are presented later in Table 8.3.1.

The common features of the distributions of peak fillet stresses due to tension only were:-

i) the greatest fillet stresses which occurred in the pitches where shear forces and wall tensions were greatest

   i.e. from z = 0 to z = p in the tube models and

   from z = L-p to z = L in the coupling models where p is the model pitch,

ii) the small variations which occurred between z=p and z=L-p and there were little differences between the tube and coupling fillet stresses in this region.

Peak stresses in the connections of Models 1 and 3 occurred in the loaded coupling runout as the thread width w decreased to nothing, as z approached zero, see Section 3.3. The runout stiffness reduced compared with the tube thread in contact with it, (see Fig. N2). Hence the runout thread deflected more and the fillet stress increased. However, the increased deflection reduced the contact pressure and therefore the fillet stresses in the mating tube thread. At the other end of the contact, the coupling runout was not in contact since the loaded flank ended at z=L (see Fig. N2). The change from the loaded full thread to the unloaded undercut was abrupt. The effect of removing the last 120^{o} of the loaded coupling runout can be seen in Model 5, Fig. 8.3.4. Only a slight increase occurred in the coupling peak fillet stresses. This indicates that the remaining 60^{o} of loaded coupling runout, from w = p/2 to w = p/3 was only slightly more flexible than the full tube thread which was in contact with it.

Generally, disregarding the effects of the loaded coupling runout, the peak fillet stresses were uniform in any one pitch in a model loaded with tension only. Typical examples are the first and last loaded tube and coupling pitches of Model 5, see Fig. 8.3.5. The largest change in peak fillet stress with position, $d\hat{\sigma}_L/d\theta$ occurred at the ends of contact i.e. at z = 0 and z = L. The coupling thread was removed at z = 0 and the coupling loaded face was machined away at z = L, see Section 3.2. Hence the large $d\hat{\sigma}_L/d\theta$ near z = 0 in the tube model was due to the addition of shear force to the thread which already carried the full wall tension. At z = L the shear force was removed from the tube thread and beyond z = L, carried no wall force, nence the fillet stresses were zero. Very near to the ends of contact the peak fillet stresses were 10-15% greater than the pitch-average. $d\hat{\sigma}_L/d\theta$ was also significant at a whole pitch from the most highly loaded end of contact i.e. at z = p for

the tube and at z = L - p for the coupling. In all other regions of the thread spiral $d\hat{\sigma}_L/d\theta$ was small in both the tubes and couplings.

8.3.4 Peak Fillet Stresses Due to Preload Only

The features of the peak fillet stresses of the preload only Model 10, see Fig. 8.3.6, are:-

i) gradually increasing peak fillet stresses in both the tubes and couplings as the thread spiral approached the preloaded end and

ii) coupling peak fillet stresses were generally greater in magnitude than the tube.

The wall forces were tensile in the coupling and compressive in the tube hence the coupling fillet stresses were greater. In the region of tube thread with the highest negative wall forces, compressive fillet stresses were present near $\phi = 0$ in the same thread as peak tensile fillet stresses which occurred near $\phi = 60^{o}$.

i.e. at $\phi = 0^{o}$

$$\sigma_L = -\sigma_{sa}\,(C_1 + C_2) + \sigma_{sF}\,C_3$$

and since σ_L was negative

$$\sigma_{sa}\,(C_1 + C_2) > \sigma_{sF}\,C_3$$

8.3.5 Peak Fillet Stress Distributions In Models 6 and 7

The distributions of peak fillet stresses in Models 6 and 7 have been considered separately from the other models. The grooves in these models greatly increased the flexibility of the walls of the models and allowed the models to 'bell-out' radially which increased the thread radial clearances, see Figs. 4.14 and 4.15.

The distribution of peak fillet stresses are shown in Fig. 8.3.7 for the tension only Model 6 and in Fig. 8.3.8 for the preload only Model 7. The variations in peak fillet stress in the first and last loaded pitches of Model 6 are shown in Fig. 8.3.9.

The fillet stresses have been normalised by the mean tube wall stress and also by the local tube wall stress, which does slightly smooth out the fillet stress distributions but large variations do occur. These variations have been attributed to variations in shear forces which have been measured between $0.58p < z < 0.83p$ in the tube and plotted against angular position and radial clearance in Fig. 8.3.10.

8.3.6 The Effect of Preload and Tension on the Stresses and Deformations of Models 8 and 9

The peak tensile fillet stress distributions in the tension and preload loaded tubes and couplings of Models 8 and 9 were normalised by the applied tension F and show larger peak fillet stresses in the coupling threads nearest the preloaded end than in models loaded with tension only (see Fig. 8.3.11 and 8.3.12). This was due to the increased coupling wall tension. At the other end of contact, near $z = 0$, the influence of the preload was slight and the peak fillet stress distributions were similar to those in the models loaded with tension only. The distributions of peak fillet stresses in the first and last loaded pitches of Model 9 are shown in Fig. 8.3.13 and Model 9 was typical of the models with preload. In the first pitch, where the fillet stresses were primarily due to tension, the variations in peak fillet stresses were much smaller than in the last pitch, where preload had a considerable influence.

For Models 8, 9 and 10, with preload, local maximum peak fillet stresses in any pitch tended to occur 90° and 270° away from the last loaded thread position. Local minimum peak fillet stresses in any pitch tended to occur in the plane of the last loaded contact and 180° away from this position, see Fig. 8.3.13b.

These local maximum and minimum peak fillet stresses were more pronounced as the thread spiral approached the preloaded end. It can be seen from Fig. 8.1.5 and Fig. A1.8 (from Appendix 1) that the shear forces in the last pitch of Model 9 and the wall stresses in the coupling undercut of Model 9 both show peaks in the 90° and 270° planes and minima in the 0° and 180° planes. These variations in shear force and wall stress account for the variation in peak fillet stress.

It can be seen from Fig. A.1.8 that there were large variations in the coupling undercut threaded surface stress but small variations in the mean through thickness axial stress indicating that wall bending also varied around the undercut. Wall bending in axially loaded models is attributed to the thread shear force and it can be seen that the planes of minimum and maximum wall bending are the same as those of minimum and maximum shear force V.

Hoop slices were cut from wedges left after slicing in regions near the $\theta = 0^{\circ}$, 90°, 180° and 270° planes of the tube models. They were all cut at the same axial position i.e. 6mm from the seal. From each hoop slice the distributions of through-thickness fringe order and isoclinic angle were measured at selected θ values. At each θ value $\phi = 0^{\circ} \pm 5^{\circ}$ showing the principal stresses to be aligned in the hoop and radial directions with the minor radial principal stress being small compared with the hoop stress.

The distributions of through-thickness hoop stresses in the tube nose of Model 9 are shown in Fig. 8.3.14a. Through-thickness measurements of axial stress were also taken in the 0°, 90°, 180° and 270° slices at 6 mm from the tube nose and they have been presented in Fig. 8. 3.14b. Again in the radial slices the isoclinic angle ϕ was less than 5°, indicating radial stresses were small compared with the axial stresses. The axial stresses were compressive from the inside

diameter up to 5 mm from the outside diameter. This position was also the limit of contact in the seal region since the coupling seal outside diameter of Model 9 was D_o - 10 mm.

The mean hoop and axial through-thickness stresses in the tube nose were calculated from the through-thickness stress distributions which were measured at the positions of maximum and minimum fillet stresses (i.e. in the same planes as the other measurements). These stresses have been presented in Fig. 8.3.15.

The mean diametral strains due to Poissons ratio have been calculated for the tube nose which was in compression due to the preload, for the coupling undercut which was in tension due to the applied tension and preload, and for the coupling seal region which was in tension due to the applied tension only. The unloaded diameter was measured at several positions around the tube nose of Model 9 and after loading, the maximum and minimum tube nose diameters were also measured and their positions noted.

The calculated and measured strains are presented in Table 8.3.1.

Table 8.3.1 Calculated and Measured Model 9 Diametral Strains

POSITION	MEASURED STRAIN % MAX	MIN	MEAN	CALCULATED STRAIN % MEAN
TUBE NOSE	0.31	0.08	0.195	0.19
COUPLING UNDERCUT	-	-	-	-0.12
COUPLING SEAL	-	-	-	-0.43

Note:-

i) Unloaded tube nose diameter = 259.4 $\pm$ 0.1 mm.

The mean hoop stress in the tube nose of Model 9 equalled 0.13 fr/mm, which, if unrestrained, should have given rise to a mean hoop strain of + 0.32%.

Measurements were made of the positions and magnitudes of the contact fringes in the coupling seals of all the remaining slices of Model 9. Unfortunately the $\theta = 150^{\circ}$ and $\theta = 180^{\circ}$ had been used for other purposes and the contact regions could not be analysed. There was generally a peak concentrated contact fringe order n_1 which corresponded to the inner surface of the tube nose which was a distance j from the coupling seal outside diameter. Over the remainder of the contact surface, the fringe order n_2 was fairly constant. n_1, n_2 and j were all measured and have been presented in Fig. 8.3.16. There were only small variations in j and n_2 but there was a reduction in n_1 in the region of $\theta = 180^{\circ} \pm 30^{\circ}$. This corresponds to the positions at which the thread sprial ends.

Although a thorough investigation of the stresses in the tube nose region of the tension plus preloaded Model 9 was carried out, no satisfactory explanation of the observed phenomenon can be put forward.

The peak fillet stress distributions of Model 4 due to tension and negative preload, see Fig. 8.3.17 were very similar to the distributions of Models 1 and 3, although the magnitudes were generally slightly lower due to the reduced shear forces carried by the threads.

8.3.7 Peak Fillet Stresses Due to Eccentric Tension

The effect of bending is shown in Fig. 8.3.18 which presents the tube and coupling fillet maxima along the complete thread spiral of Model 2. The $\theta = 0^{o}$ and $\theta = 180^{o}$ fillet maxima for both tube and coupling (in the plane of zero bending) show quite close agreement with the $\theta = 0$ and 180^{o} values of the identical Model 1. The maximum peak fillet stresses varied from pitch to pitch and they generally occurred in the $\theta=270^{o}$ plane except between $z = 0$ and $z = p$ where the peaks in both tube and coupling occurred at $\theta=290^{o}$. This is attributed to the proximity of the loaded coupling runout which affected the load distribution. The minimum fillet stresses were nearly constant and very similar in the tube and couplings and they occurred, as expected, in the $\theta = 90^{o}$ plane.

Fig. 8.3.19 shows plots of normalised stresses (both fillet stresses and stresses in the undercut) v $\sin\theta$. These plots show a sinusoidal variation in unthreaded regions, in unloaded threads and in loaded threads where the normalised stresses were below about 5. In regions where the normalised peak fillet stress exceeded 5, i.e. from $z = 4.55p$ to $z = 4.9p$ and from $z = 5.55p$ to $z = 5.9p$ the distributions became increasingly less sinusoidal.

8.3.8 Comparisons Between Peak Fillet Stresses In Models with Different Load Conditions and Different Shapes

Due to the variations in peak fillet stresses, the pitch-average peak fillet stresses in each pitch of each model have been obtained and are shown in Table 8.3.1

TABLE 8.3.1 Normalised peak fillet stresses averaged over complete pitches

	Magnitudes of Peak Fillet Stresses In																			
	Tube Model										Coupling Model									
Loading	Tension				Preload		Tension+Preload			Ecc. Tens.	Tension				Preload		Tension + Preload			Ecc. Tens.
Pitch P	.1	3	5	6	7	10	8	9	4	2	1	3	5	6	7	10	8	9	4	2
0 - 1	4.04	3.89	4.54	4.08	1.48	0.4	4.45	3.53	3.17	3.81	3.11	2.87	2.48	2.87	1.51	1.37	3.31	3.41	2.87	2.84
1 - 2	3.06	3.08	3.09	3.38	1.59	1.23	3.68	3.16	2.71	3.17	2.42	2.48	2.48	2.80	1.90	1.50	3.65	3.51	2.20	2.88
2 - 3	2.69	2.80	2.70	3.14	1.85	1.55	3.30	3.13	2.54	2.90	2.56	2.69	2.51	3.09	2.29	1.86	3.84	3.64	2.31	3.13
3 - 4	2.65	2.74	2.61	2.77	2.18	1.80	3.03	3.10	2.48	3.12	2.62	2.90	2.54	2.84	2.62	2.08	3.79	3.68	2.36	3.35
4 - 5	2.72	2.75	2.57	2.21	2.35	1.88	2.65	3.56	2.53	3.28	2.84	3.09	2.87	2.80	2.59	2.25	3.49	3.85	2.57	3.79
5 - 6	3.18	2.89	2.44	2.23	2.56	1.91	2.46	3.51	2.65	4.32	3.74	4.08	4.14	4.20	4.25	2.33	3.41	4.16	3.62	4.97
5½ - 6½	3.89	3.07				2.00	2.28	3.45	2.65	4.50	4.99	5.30				2.69	3.64	4.41	4.62	5.38
6 - 7						1.91	1.97	3.90								2.94	4.14	6.17		
6½ - 7½						2.55	1.65	4.18								5.76	4.90	7.17		
Average	3.18	3.04	2.99	2.97	2.00	1.59	2.98	3.46	2.68	3.52	3.14	3.29	2.84	3.10	2.57	2.29	3.74	4.27	2.88	3.64

From Table 8.3.1 it can be seen that the peak coupling fillet stresses in the most highly loaded pitch of the tension only models were slightly higher than the corresponding tube. This is due to the smaller cross sectional areas of the coupling models.

The effect of removing the last 120^{o} of the loaded coupling runout in Model 5 can be seen by comparing the pitch average peak fillet stresses in the tubes and couplings of Model 5 with those of Models 1 and 3 which retained the full loaded coupling runouts. The tube fillet stresses in the first pitch of Model 5 were increased on average and the coupling fillet stresses reduced in Model 5 by the removal of the runout. No appreciable difference could be seen between the fillet stresses in Model 5 and those in Models 1 and 3 in the next pitch, P=1-2. This indicates that the effect of the runout was localised to the pitch it was part of. The peak fillet stresses between z=p and z=L-p in each model have been normalised by the mean stress in the relevant tube undercut and presented in Table 8.3.2.

TABLE 8.3.2 - AVERAGED PEAK FILLET STRESSES FROM z=p To z=L-p AS MULTIPLES OF THE TUBE UNDERCUT STRESS

MODEL	LOADS	TUBE UNDERCUT RATIO $\frac{b_{max}(D_o-b_{max})}{t(D_o-t)}$	COUPLING UNDERCUT RATIO $\frac{b_{max}(D_i+b_{max})}{t(D_o-t)}$	$\frac{R}{b_{max}}$	$\frac{P}{b_{max}}$	TUBE FILLET STRESS	COUPLING FILLET STRESS
1 COUPLING	TENSION	-	0.688	*	0.79	-	2.18
1 TUBE	"	0.833	-	0.078	0.79	2.32	-
3	"	0.738	0.630	0.105	1.05	2.10	2.06
5	"	0.719	0.613	0.170	1.08	1.97	1.87
6	"	0.719	0.613	0.170	1.08	2.07	2.08
7	PRELOAD	0.719	0.613	0.170	1.08	1.43	1.69
10	"	0.847	0.714	0.114	0.76	1.42	1.69
8 COUPLING	TENSION	-	0.629	0.158	1.06	-	2.55
8 TUBE	+PRELOAD	0.702	-	0.166	1.11	2.12	-
9 COUPLING	TENSION	-	0.706	0.115	0.77	-	3.01
9 TUBE	+ PRELOAD	0.800	-	0.122	0.81	2.63	-
4	TENSION -PRELOAD	0.800	0.659	0.096	0.79	2.05	1.89
2 COUPLING	ECCENTRIC	-	0.650	ǂ	0.79	-	2.70
2 TUBE	TENSION	0.820	-	0.079	0.79	2.56	-

* Due to machining errors there was a compound radius in this model R/b_{max} in the range 0.078 - 0.12

ǂ Due to machining errors there was a compound radius in this model R/b_{max} in the tubes and couplings of Models 8 and 9 they have been presented separately in this table.

For the tension only Models 3 and 5, it can be seen from Table 8.3.2 that increasing R/b_{max} from 0.105 to 0.17 only slightly reduced the fillet stresses; by 6% in the tube models and by 9% in the coupling models.

The results from the couplings of Models 1 and 3 indicate that increasing p/b_{max} from 0.79 to 1.05 had a negligible effect on the averaged peak fillet stresses. It can be seen that the grooves in Model 6 had only a slight effect on the pitch average fillet stresses, although the maximum peak fillet stress was greatly increased.

In the preloaded Models 7 and 10 the coupling fillet stresses were higher than the tube and this is attributed to the wall forces being tensile in the couplings and compressive in the tubes. The shape changes from Model 7 to Model 10 i.e. reductions in R/b_{max} and p/b_{max}, had a negligible effect on the averaged peak fillet stress. This indicates that the increase in peak fillet stresses which is associated with the reduction in R/b_{max} was equal to the reduction in peak fillet stress associated with the reduction in p/b_{max}. It can be seen from Tables 8.3.1 and 8.3.2 that the peak fillet stresses in both the tube and coupling models loaded with preload only (Models 7 and 10) were lower than models with similar shape loaded with tension (Models 6 and 9) in all but the thread pitch nearest the preloaded end of the spiral. This is because of the relatively high concentration of shear force near the preloaded end of the thread spiral and the consequently lower shear forces in the rest of the thread spiral of the preloaded models.

For Models 8 and 9 loaded with preload and tension the averaged peak fillet stresses were higher than those for models loaded with tension only or preload only. This was because the tension and preload model fillet stresses were normalised by the applied tension only but the threads carried shear forces due to tension and preload. Model 9

peak fillet stresses were greater than Model 8 because (F+Q)/F was greater for Model 9, i.e. (F+Q)/F = 1.48 for Model 8 and 1.55 for Model 9. The coupling fillet stresses were also significantly higher than the tube fillet stresses for both models. This is primarily because the tube wall forces were lower than the coupling wall forces due to the compressive effect of the preload on the tube. It can be seen from Fig. 8.3.1, that the distribution of ϕ_{max} was similar for coupling models loaded with preload only or tension only but for tube models loaded with preload only the distribution of ϕ_{max} was quite different from models loaded with tension only. Hence, for coupling models loaded with tension and preload, the peak fillet stress was very nearly equal to the peak fillet stress due to tension plus the peak fillet stress due to preload, but for tube models loaded with tension and preload the contribution of fillet stress from the tension and from the preload was less than their respective peak values.

The coupling fillet stresses of Model 4 were slightly lower than the tube fillet stresses. Due to the positive preload in the tube nose, the coupling wall forces were lower than the tube wall forces, hence the fillet stresses were lower.

For the eccentric tension loaded Model 2 peak fillet stresses were higher than for the similar Model 1, loaded with axial tension. The tube and coupling fillet stresses in Model 2 were similar to each other in the central region of thread contact.

8.4 Comparisons Between Calculated and Measured Peak Fillet Stresses and their Positions

Combining Equations 8.2.1 and 8.2.4 gives an expression for the fillet stress due to both wall tension and thread shear force at any position in a particular section of thread i.e.

$$\sigma_L = \sigma_{sa} (C_1 + C_2 \cos 2\phi) + \sigma_{sF} (C_3 + C_4 \sin 2\phi) \quad \ldots \quad 8.4.1$$

At the position $\phi = \phi$ max, $d\sigma_L/d\phi = 0$, and

$$d\sigma_L/d\phi = -2\sigma_{sa} C_2 \sin 2\phi + 2\sigma_{sF} C_4 \cos 2\phi \quad \ldots \quad 8.4.2$$

for $d\sigma_L/d\phi = 0$

$$\sigma_{sa} C_2 \sin 2\phi = \sigma_{sF} C_4 \cos 2\phi$$

$$\therefore \phi \text{ max} = \tfrac{1}{2} \tan^{-1} \left(\frac{C_4}{C_2} \frac{\sigma_{sF}}{\sigma_{sa}} \right) \quad \ldots \quad 8.4.3$$

For Models 5, 9 and 10, chosen to represent the loading modes of tension, tension plus preload and preload only, the measured pitch average values of ϕ max have been plotted in Fig. 8.4.1 against those calculated using Equation 8.4.3. The values of C_2, C_4, σ_{sa} and σ_{sF} were obtained from Equations 8.2.3, 8.2.13, 8.1.22, 8.1.23 and from Appendix 7. The shape parameters required to calculate the coefficients and stresses for Equation 8.4.3 were the pitch average values which had been measured in the models.

The values of $\phi=\phi$ max, calculated using Equation 8.4.3, were used in Equation 8.4.1 to calculate the peak fillet stress σ_L in each pitch of both the tubes and couplings of Models 5, 9 and 10. The measured pitch average peak fillet stresses have been plotted against the calculated peak fillet stresses in Fig 8.4.2. The peak fillet stresses in the last loaded pitch of the couplings and the first loaded tube pitch of Models 1, 3, 4 and 8 were also calculated and compared with their pitch average values in Fig. 8.4.2. These positions were chosen because the greatest fillet stresses in any screwed connection are likely to occur in these regions.

Appendix 8 shows a typical set of calculations required to obtain both ϕ_{max} and $\hat{\sigma}_L$.

The measured and calculated pitch-average peak fillet stresses have been plotted against position along the thread spiral for Models 5, 10 and 9 in Fig. 8.4.3, 8.4.4 and 8.4.5.

Fig. 8.4.2 shows the random scatter of the measured peak fillet stresses but the average of

$$\frac{\hat{\sigma}_L \text{ calculated}}{\sigma_L \text{ measured}} = 0.994$$

The distributions of calculated peak fillet stresses show a smooth curve when plotted against position along the thread spiral. The distributions of measured peak fillet stress do not exhibit such a smooth distribution. For tension only models, significant changes in $\hat{\sigma}_L$ only occur at integral pitches from the nearest end of contact, see Figs.8.3.2, 8.3.3 and 8.3.4 while for the preloaded models large variations in $\hat{\sigma}_L$ also occur within an integral pitch due to the runout effects on the preload distribution, see Section 8.3

Measured pitch-average peak fillet stress are distributed along the thread sprial in a similar manner to the calculated values. The largest differences between the pitch-average measured values and calculated values of $\hat{\sigma}_L$ are randomly positioned in the thread spiral.

8.5 Stresses In Contact Regions

Fig. 8.5.1 shows in detail the fringe pattern in the Model 4 thread analysed in detail and also the straight lines along which the AMP was used to measure the fringe orders and isoclinic angles. All the stress differences presented in this Section have been normalised by the mean tube wall stress σ_{nom}.

Fig 8.5.2 shows the distribution of normalised shear stress differences parallel to the loaded face of the thread and at a distance 0.15 mm below the surface of the 2 mm thick slice. The shear stress differences were also measured 0.15 mm subsurface in the tube thread and the peak shear stress differences are also plotted on Fig. 8.5.2. It can be seen that the measured peaks in the tube and coupling do not appear at the same radial positions. The distance 0.15 mm subsurface was arbitary and did not correspond to the sub surface position of the local shear stress difference maxima. The measured local maxima 0.15 mm subsurface were probably affected by radial shear stresses due to thread friction resisting relative radial movement of the mating threads.

Even under the highest magnification of the AMP (200x) no significant surface roughness in the thread contact regions was observed. Hence, the distance from asperity tips to troughs must have been less than about 0.0025 mm.

Fig. 8.5.3 shows the distributions of normalised shear stress differences in both the 1.05 mm and 0.50 mm thick slices, (which had been cut from the 2 mm thick slice) parallel to the loaded face and 0.05 subsurface in the region of the largest contact stresses. It can be seen that these distributions were very similar to each other, indicating small stress gradients in the hoop direction.

Fig. 8.5.4 to 8.5.9 shows the distributions of normalised shear stress differences, isoclinic angles and calculated shear stresses in the 6 lines perpendicular to the loaded face of the 1.05 mm thick slice starting at 0.05 mm subsurface. The measurements of normalised fringe order nearest the loaded face in these six lines are shown on Fig. 8.5.3 which also indicates the radial positions of these six lines of measurements and the high level of repeatability of measurements.

The shear stress gradients in the radial direction near to the peak contacts were too large to calculate the subsurface principal stresses accurately using the Frocht shear difference method and, since the loaded face was not a free surface, it would have been impossible to gauge the accuracy of any stresses calculated using the method since $\sigma_z \neq 0$ at the contact face. However from the measurements taken it can be seen that the stress gradients in the contact regions were small in the hoop direction, large in the axial direction and very large in the radial direction. Also, the contact stresses were localised at several distinct points (see Fig. 8.5.2). This suggests that surface roughness and thread shape in the contact region as well as the applied thread shear force influence the magnitude of the contact stresses.

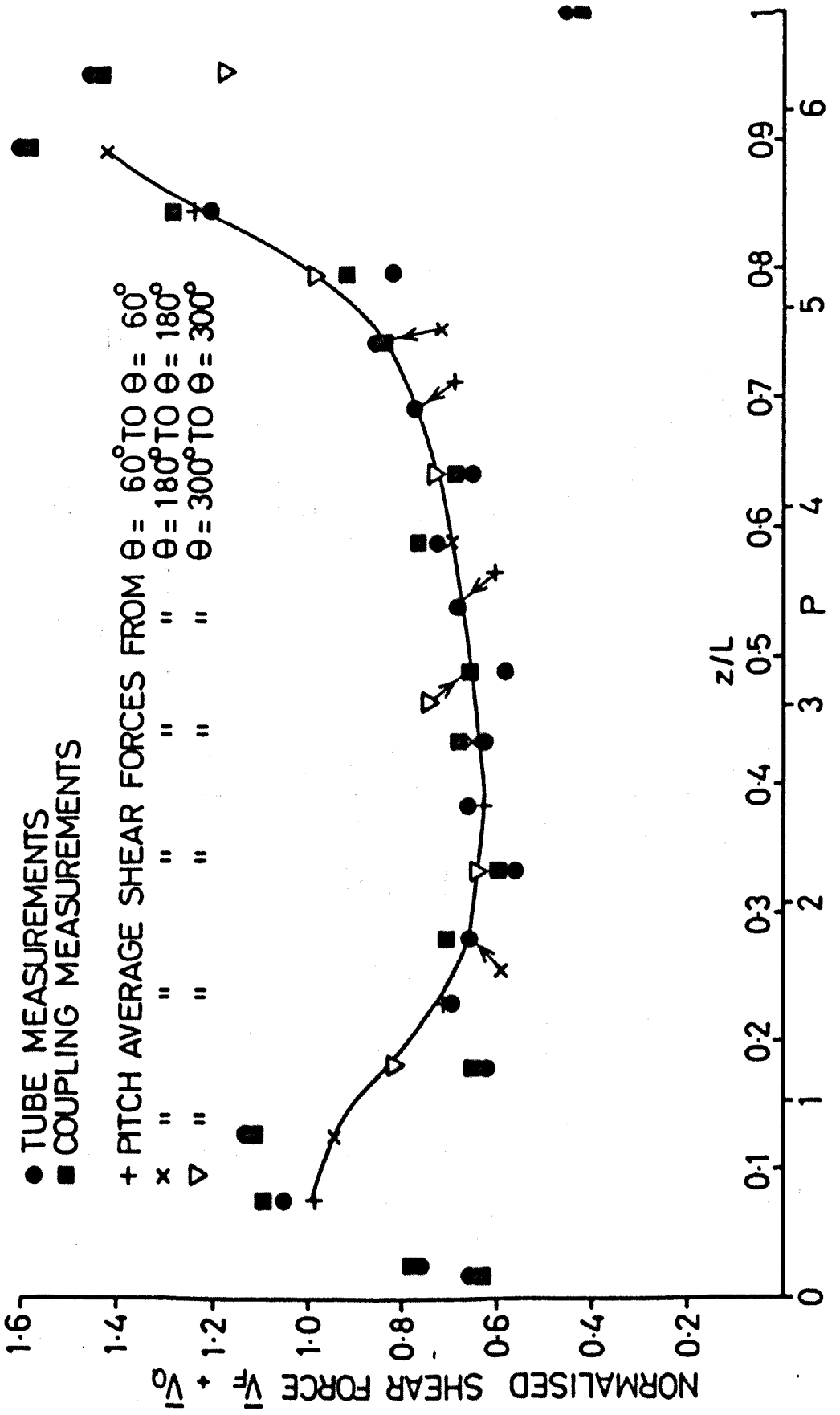

Fig 8.1.1

Normalised Shear Force Distribution Measured in Both the Tube and Coupling Threads of Model 4

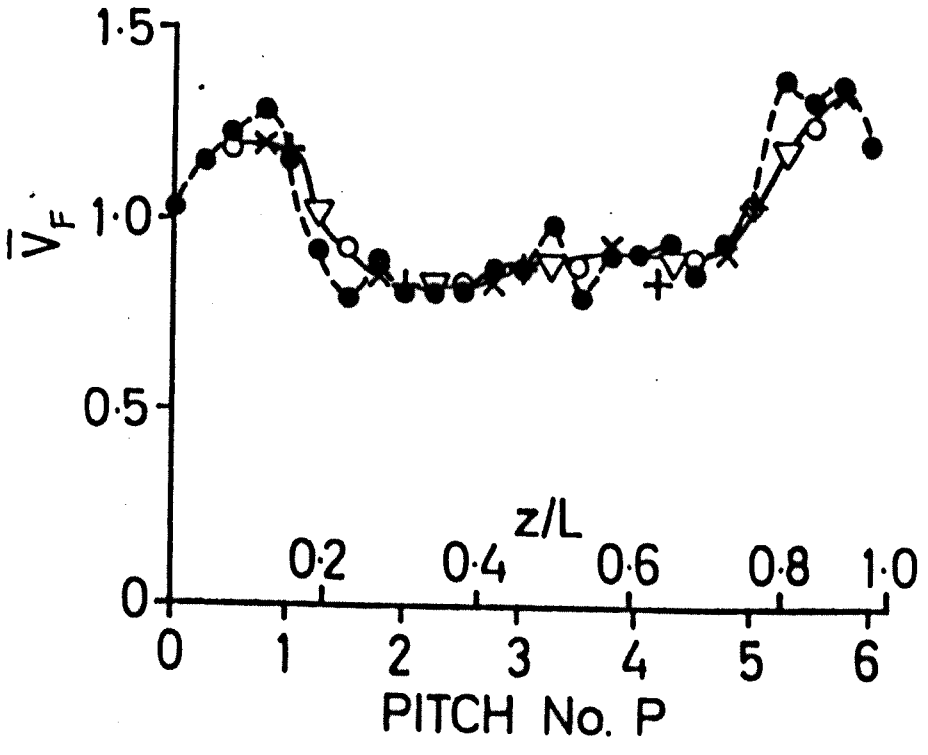

Fig 8.1.2

Normalised Shear Force Distribution Measured In
The Tube Threads of Model 5

o Pitch Average Shear Forces From θ = 0° to θ = 0°
x Pitch Average Shear Forces From θ = 90° to θ = 90°
+ Pitch Average Shear Forces From θ = 180° to θ = 180°
▼ Pitch Average Shear Forces From θ = 270° to θ = 270°
● Actual Measurements (Tube Only)

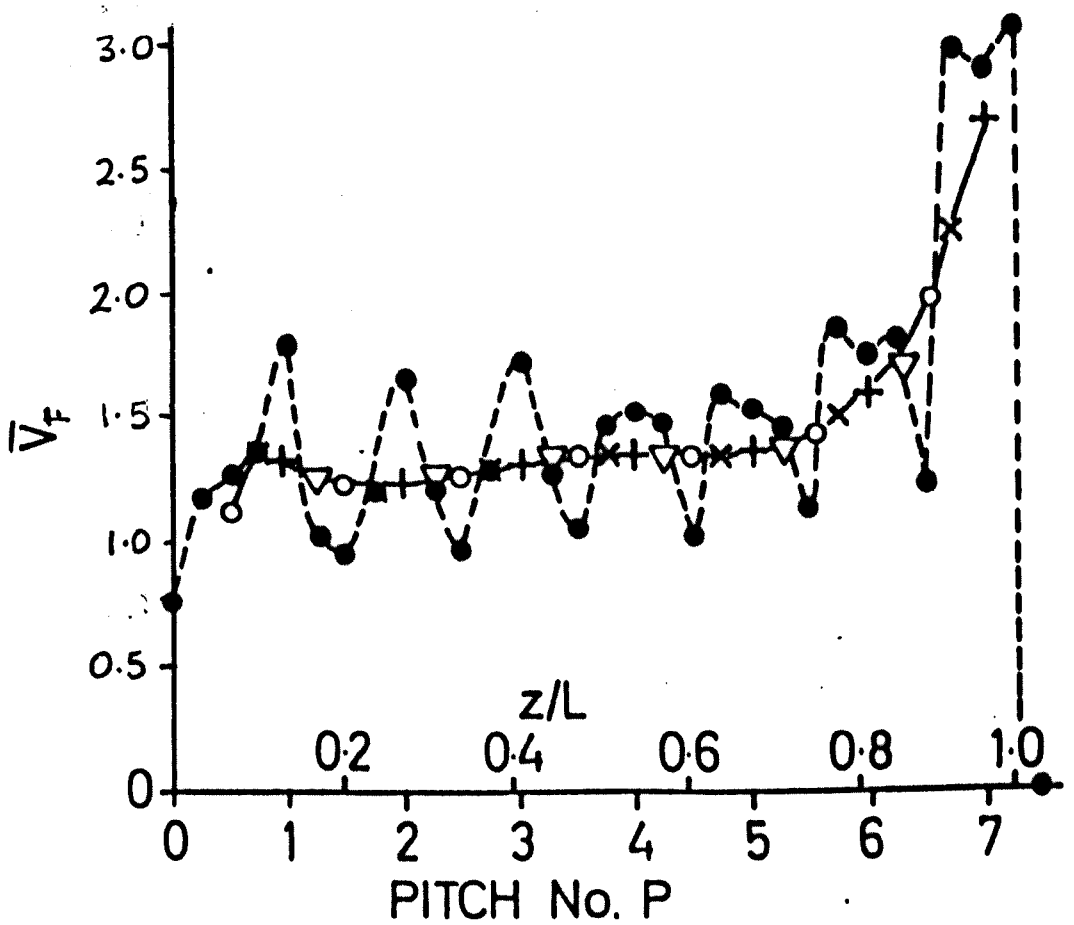

Fig 8.1.3

Normalised Shear Force Distribution Measured
In The Tube Threads of Model 9

o Pitch Average Shear Forces From $\theta = 0^o$ to $\theta = 0^o$
x Pitch Average Shear Forces From $\theta = 90^o$ to $\theta = 90^o$
\+ Pitch Average Shear Forces From $\theta = 180^o$ to $\theta = 180^o$
▼ Pitch Average Shear Forces From $\theta = 270^o$ to $\theta = 270^o$
● Actual Measurements (Tube Only)

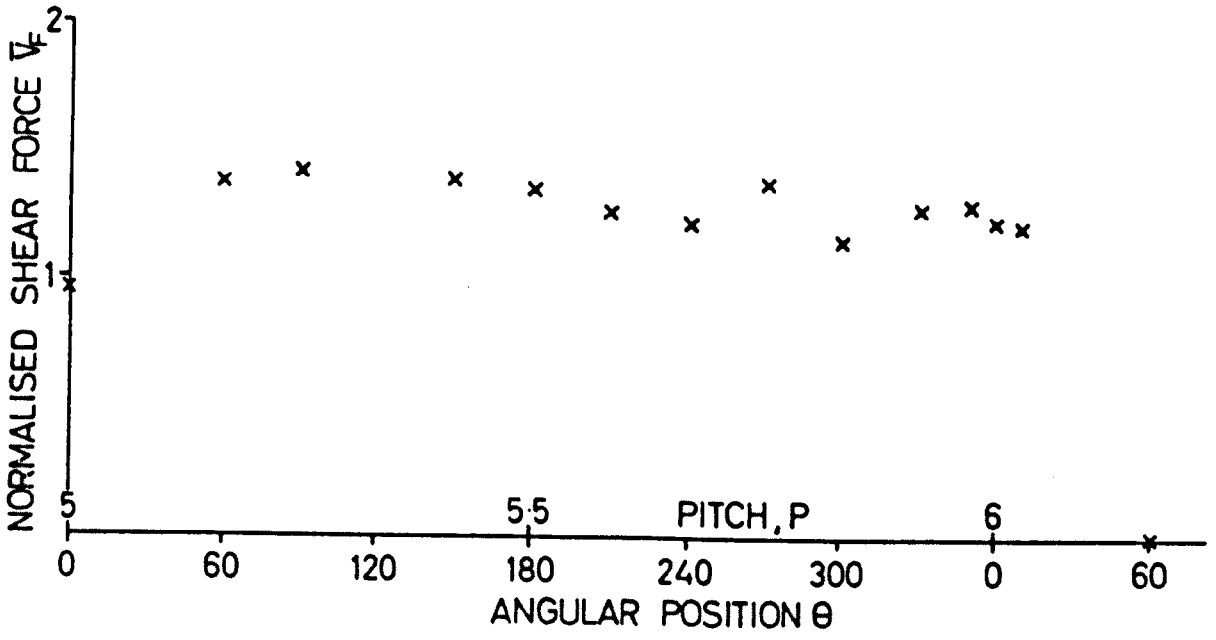

Fig 8.1.4

Normalised Shear Force Distribution Measured in the Last Loaded Tube Pitch of Model 5

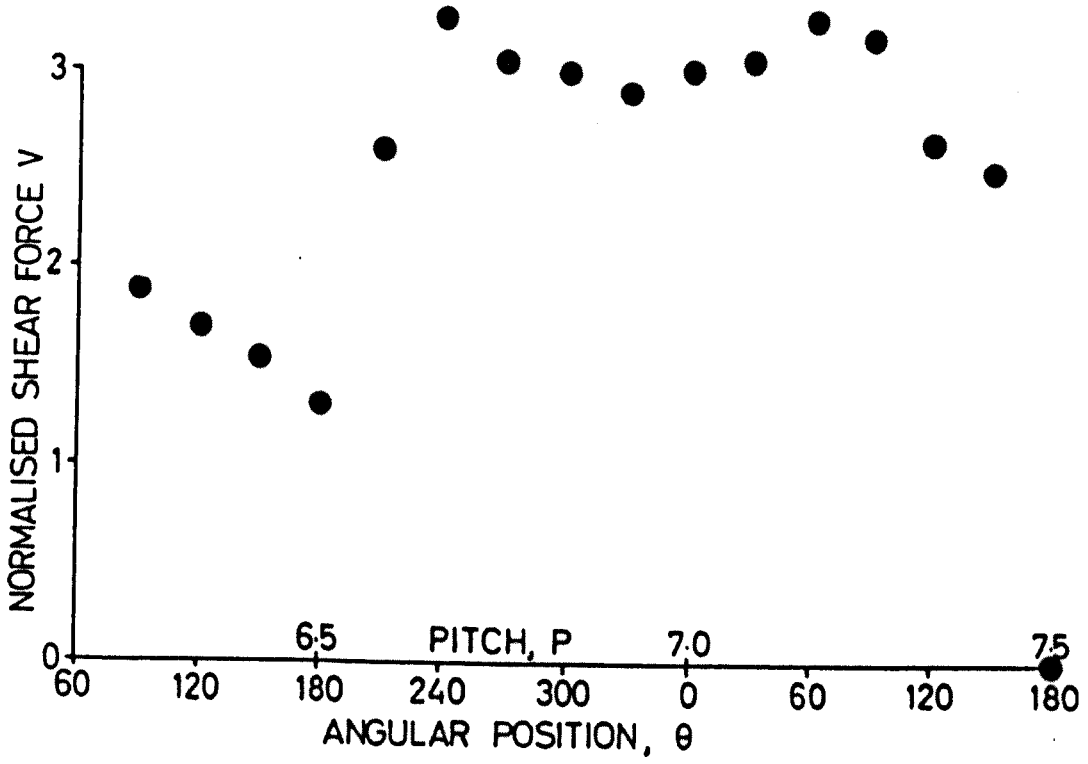

Fig 8.1.5

Normalised Shear Force Distribution Measured in the Last Loaded Tube Pitch of Model 9

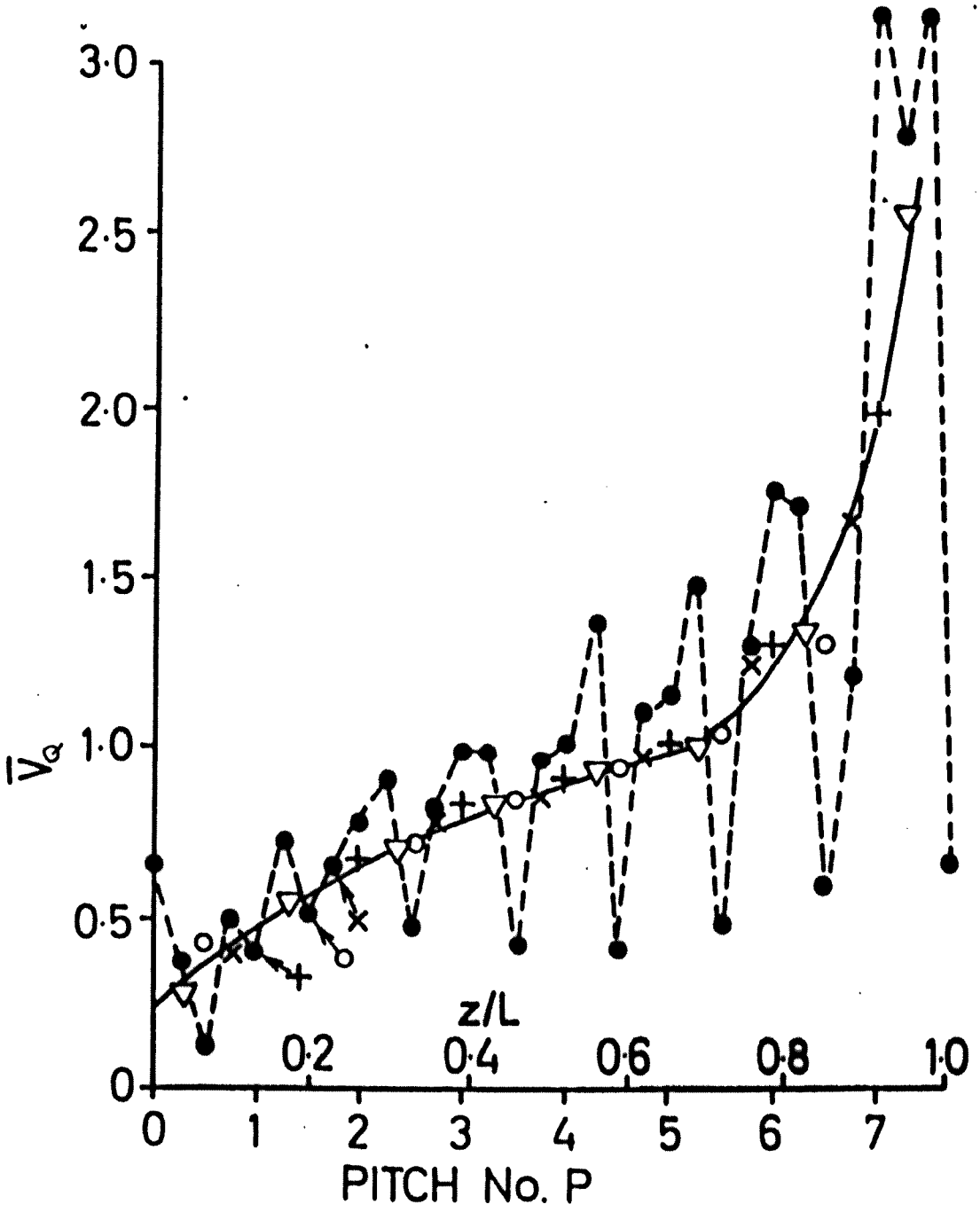

Fig 8.1.6

Normalised Shear Force Distribution Measured
In The Tube Threads of Model 10

o Pitch Average Shear Forces From θ = 0° to θ = 0°
x Pitch Average Shear Forces From θ = 90° to θ = 90°
\+ Pitch Average Shear Forces From θ = 180° to θ = 180°
▼ Pitch Average Shear Forces From θ = 270° to θ = 270°
● Actual Measurements (Tube Only)

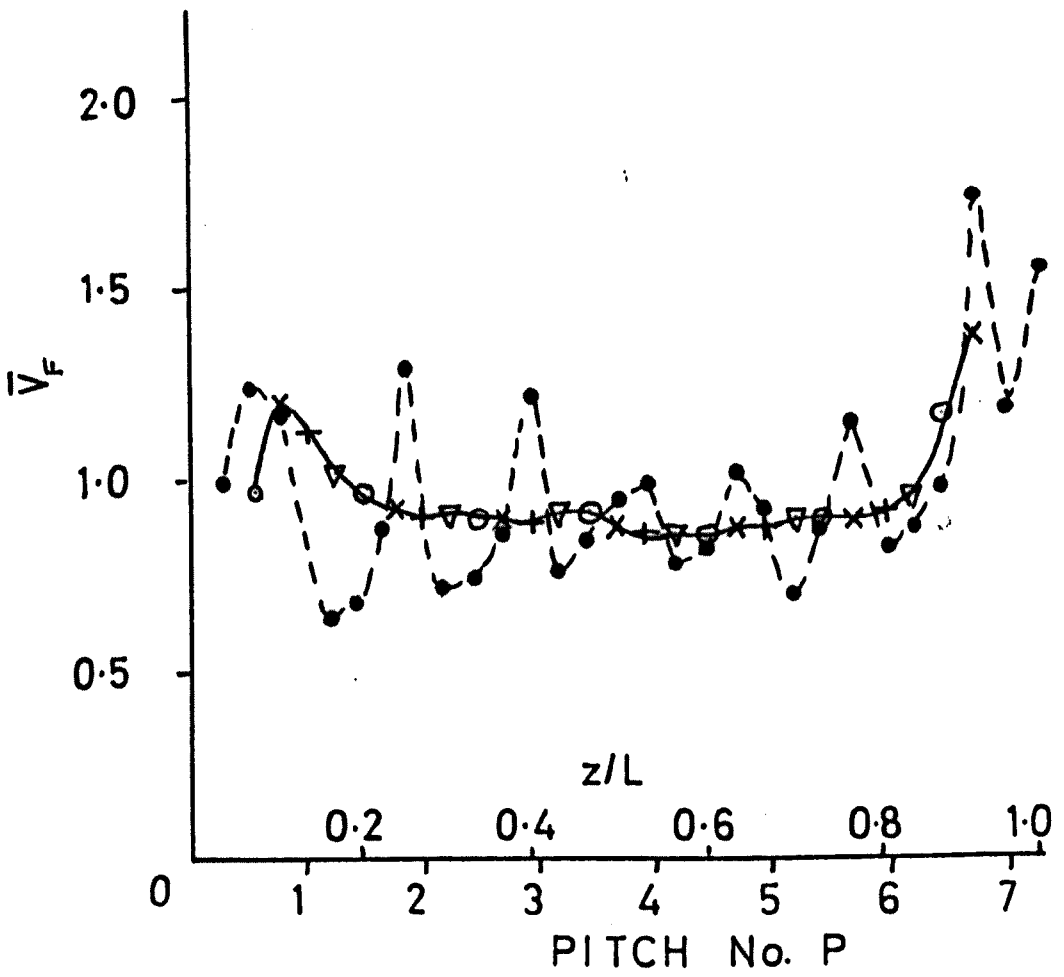

Fig 8.1.7

Normalised Shear Force Distribution in Model 9
Due to Tension Only

o Pitch Average Shear Forces From θ = 0° to θ = 0°
x Pitch Average Shear Forces From θ = 90° to θ = 90°
+ Pitch Average Shear Forces From θ = 180° to θ = 180°
▼ Pitch Average Shear Forces From θ = 270° to θ = 270°
● Actual Measurements (Tube Only)

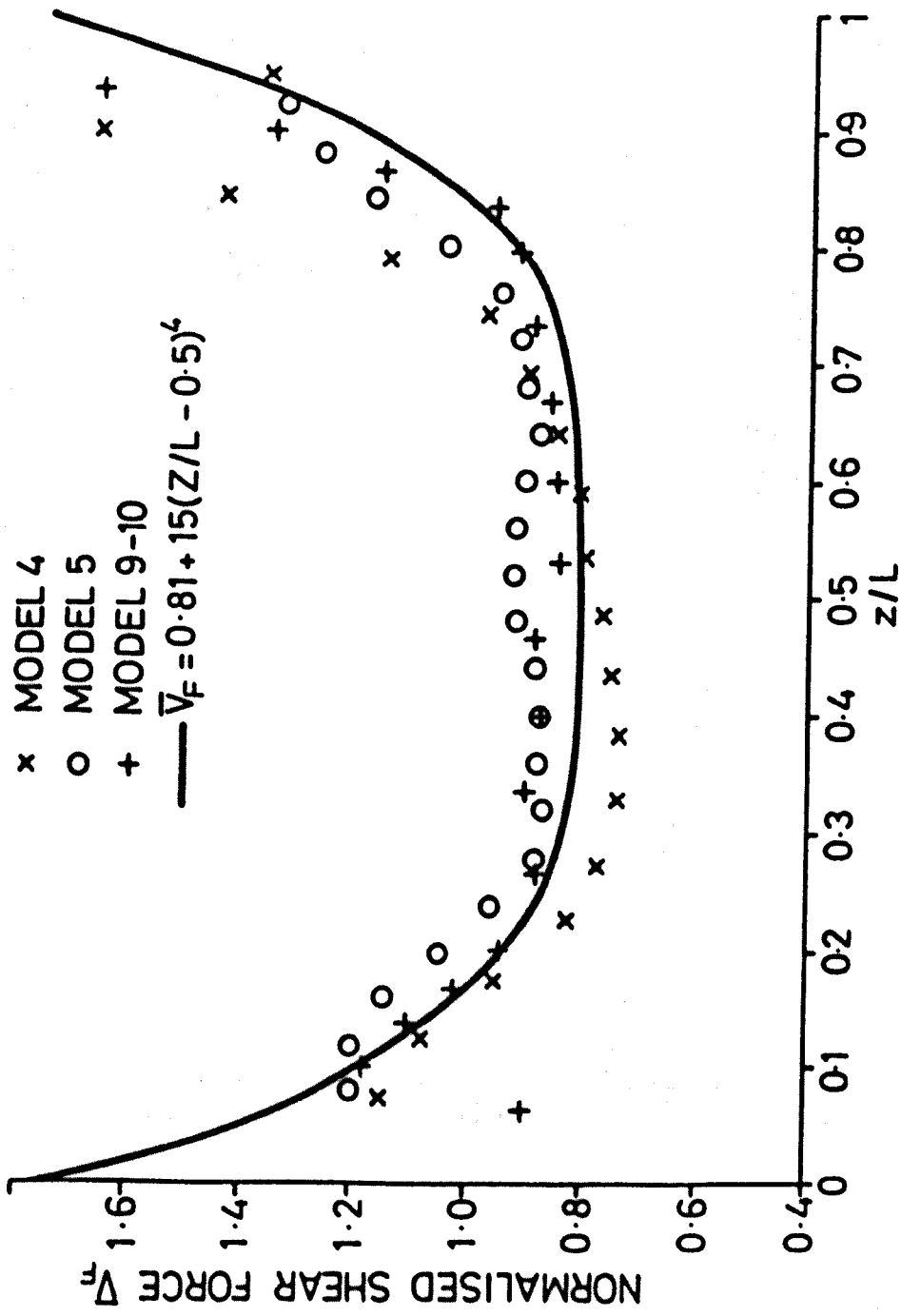

Fig 8.1.8

Pitch Average Normalised Shear Force Distributions Plotted Against Non Dimensionalised Distance from The Beginning of Thread Contact

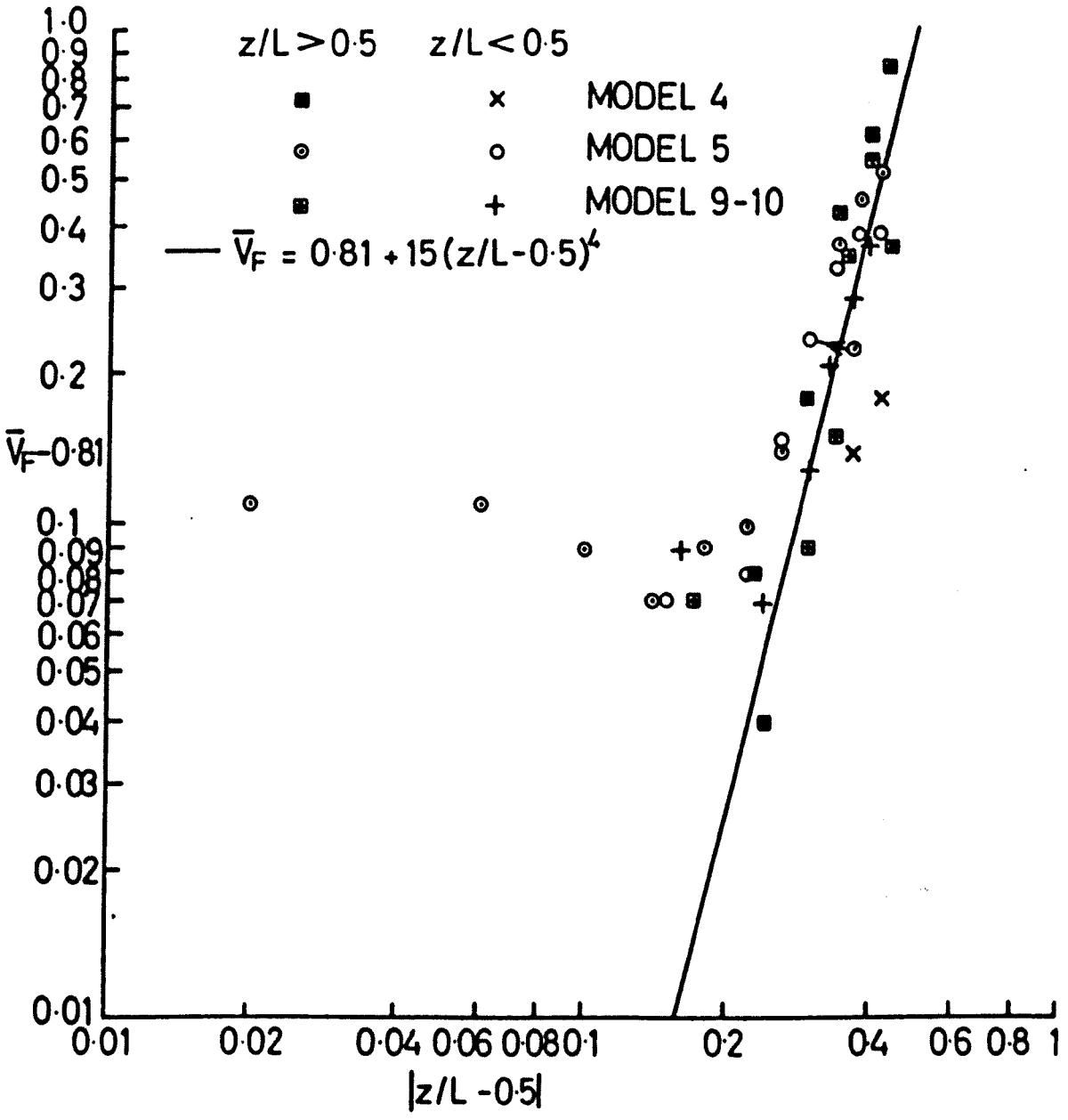

Fig 8.1.9

Pitch Average Normalised Shear Force Distributions For Tension Only Loaded Models Plotted on Log-Log Paper

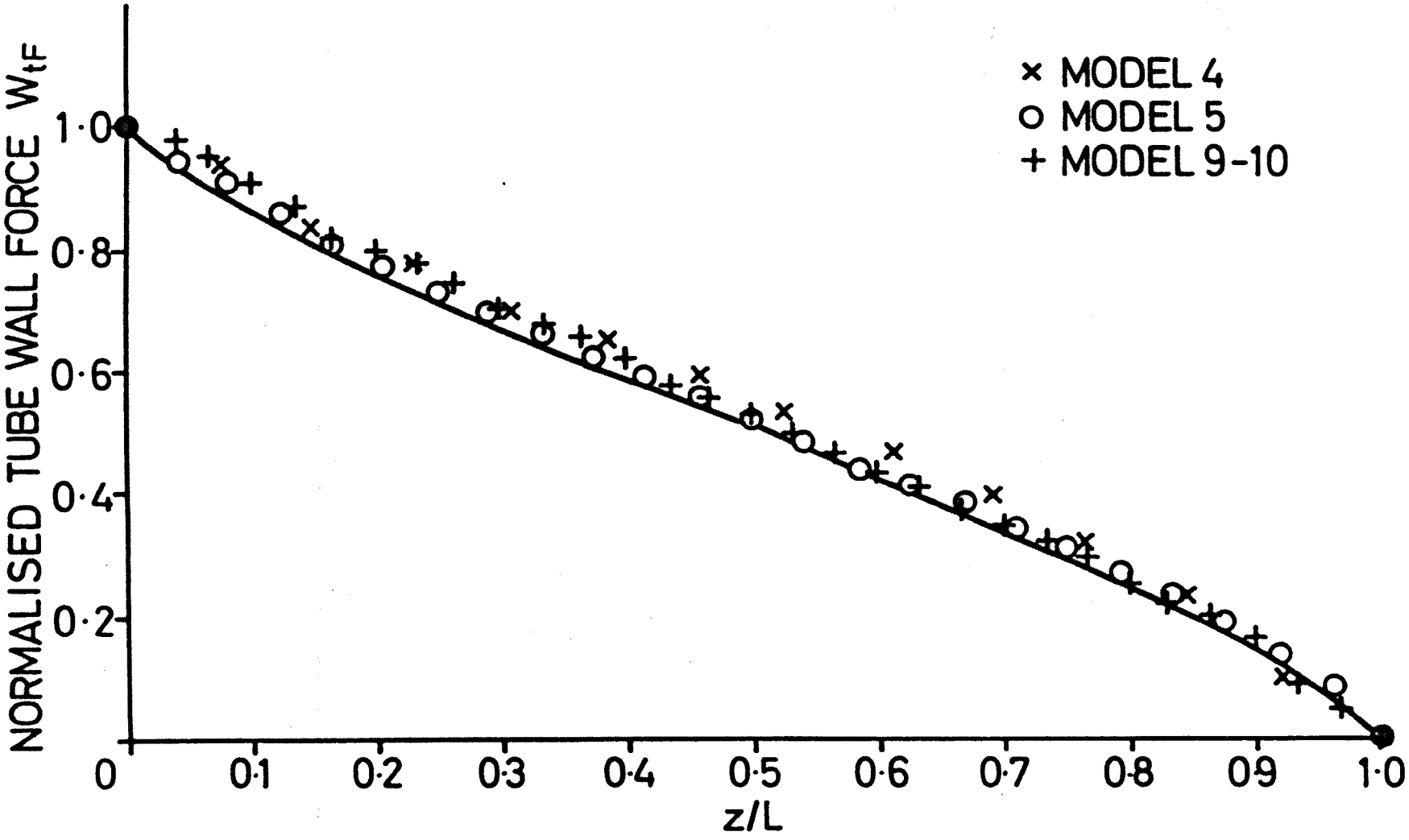

Fig 8.1.10

Measured And Predicted Tube Wall Forces for Tension Only Models. Solid Line is the Tube Wall Force Predicted Using Equation 8.1.10

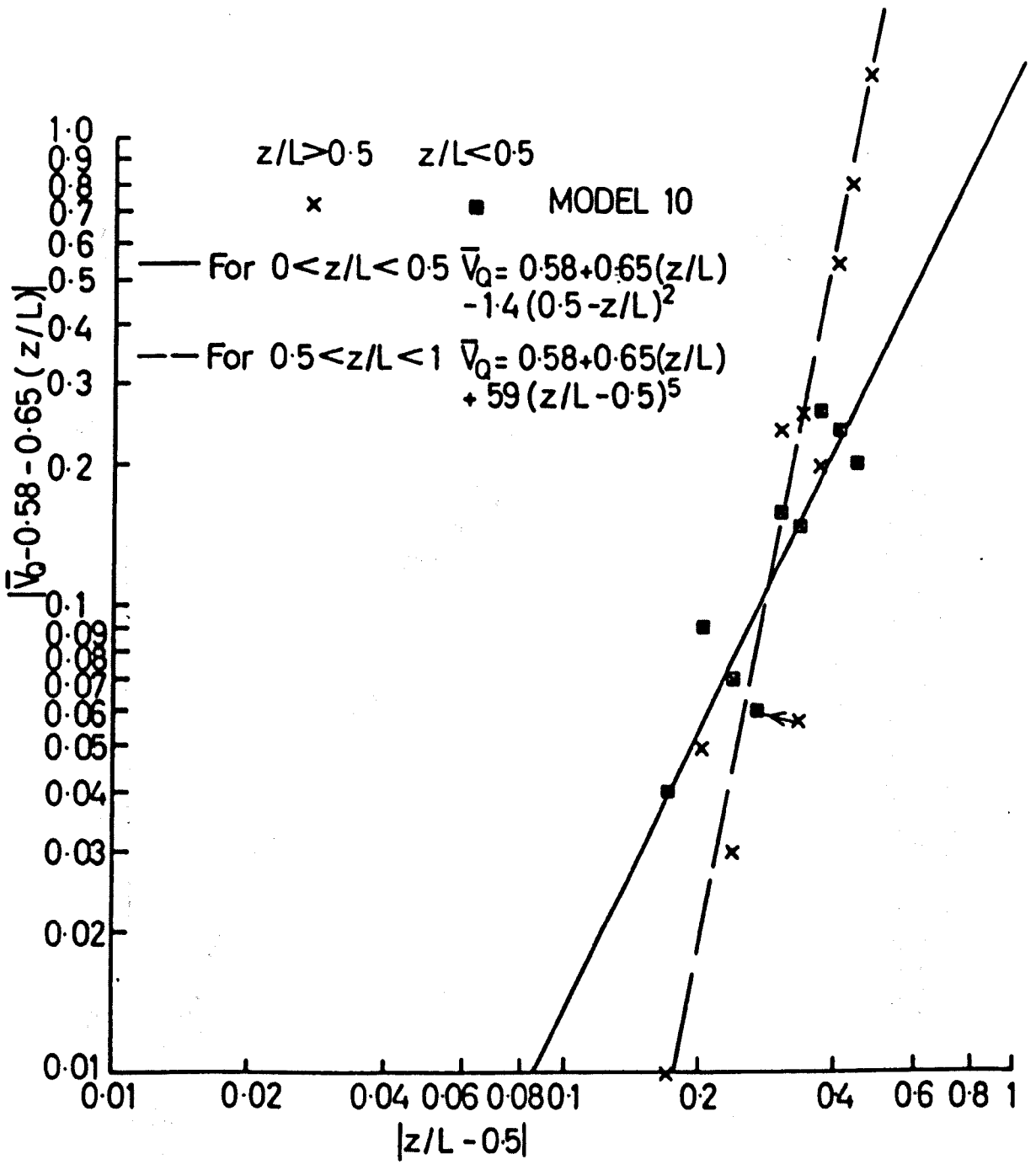

Fig 8.1.11

Pitch Average Shear Force Distribution for Preload Only Loaded Model 10 Plotted on Log-Log Paper

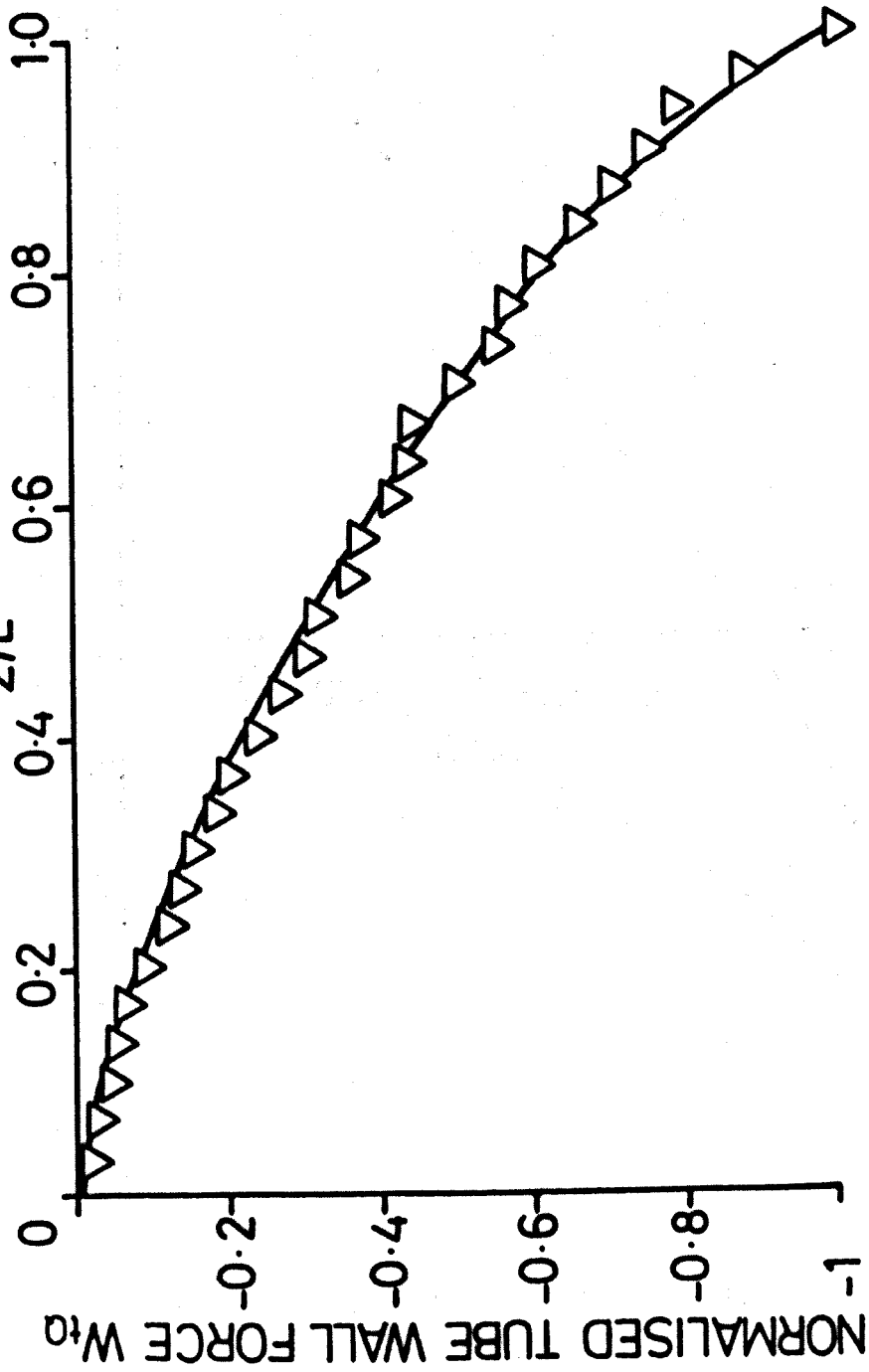

Fig 8.1.12

Measured and Predicted Tube Wall Forces For Preload Only Loaded Model 10. Solid Line is The Tube Wall Force Predicted Using Equations 8.1.18 and 8.1.19

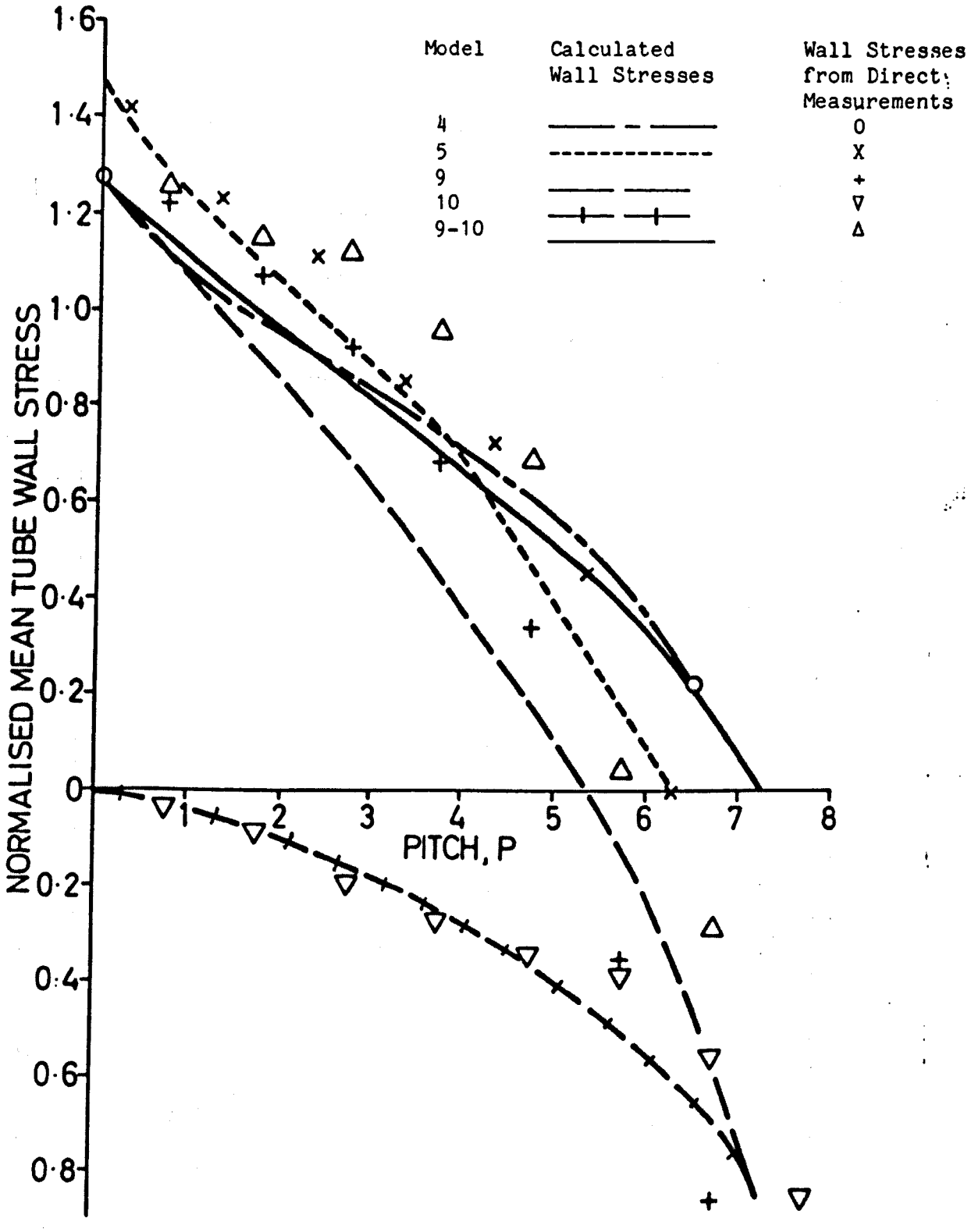

Fig 8.1.13

Distributions of Mean Axial Tube Wall Stresses
Obtained from Direct Measurements and from Calculations

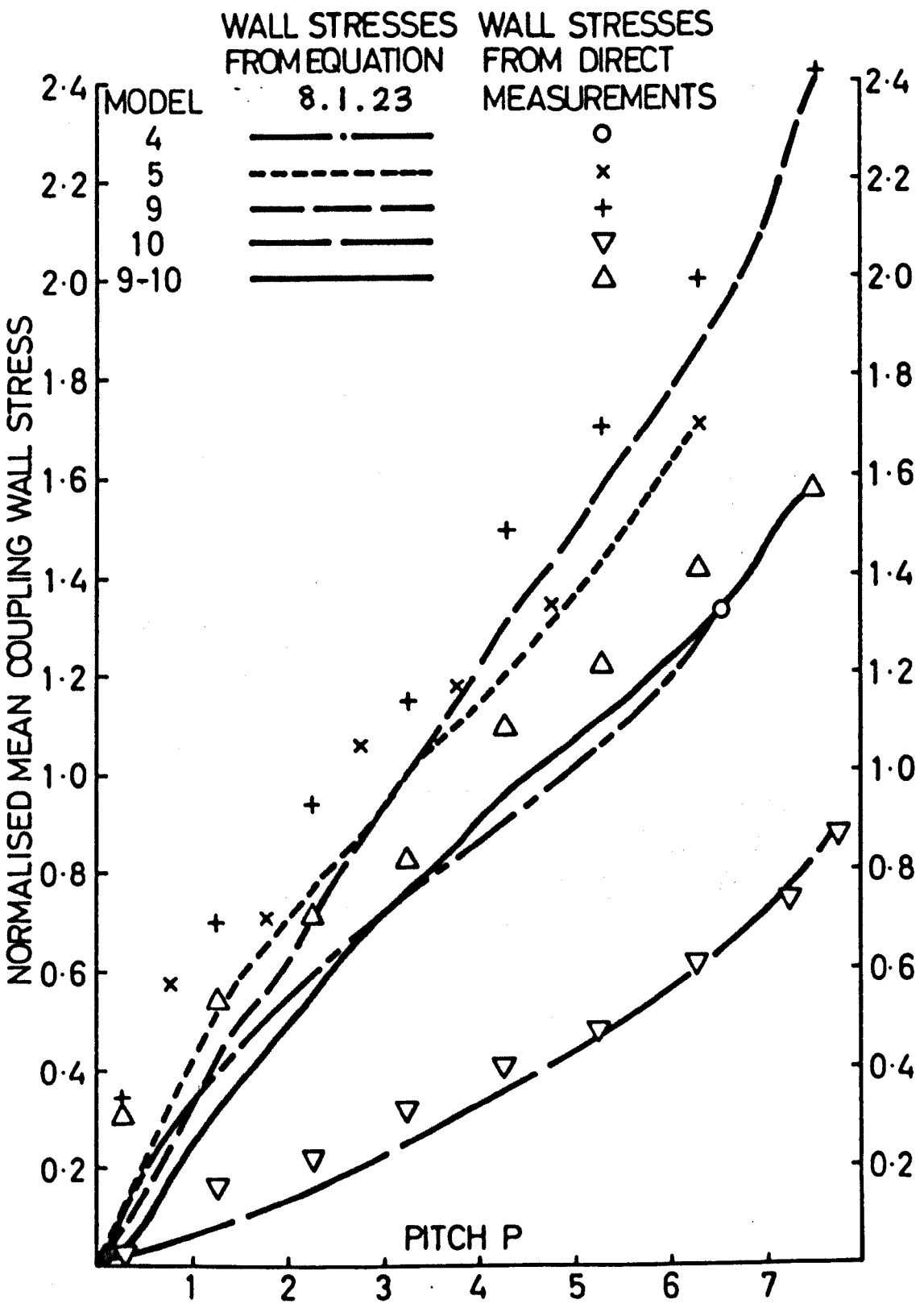

Fig 8.1.14

Distributions of Mean Axial Coupling Wall Stresses Obtained from Direct Measurements and from Calculations

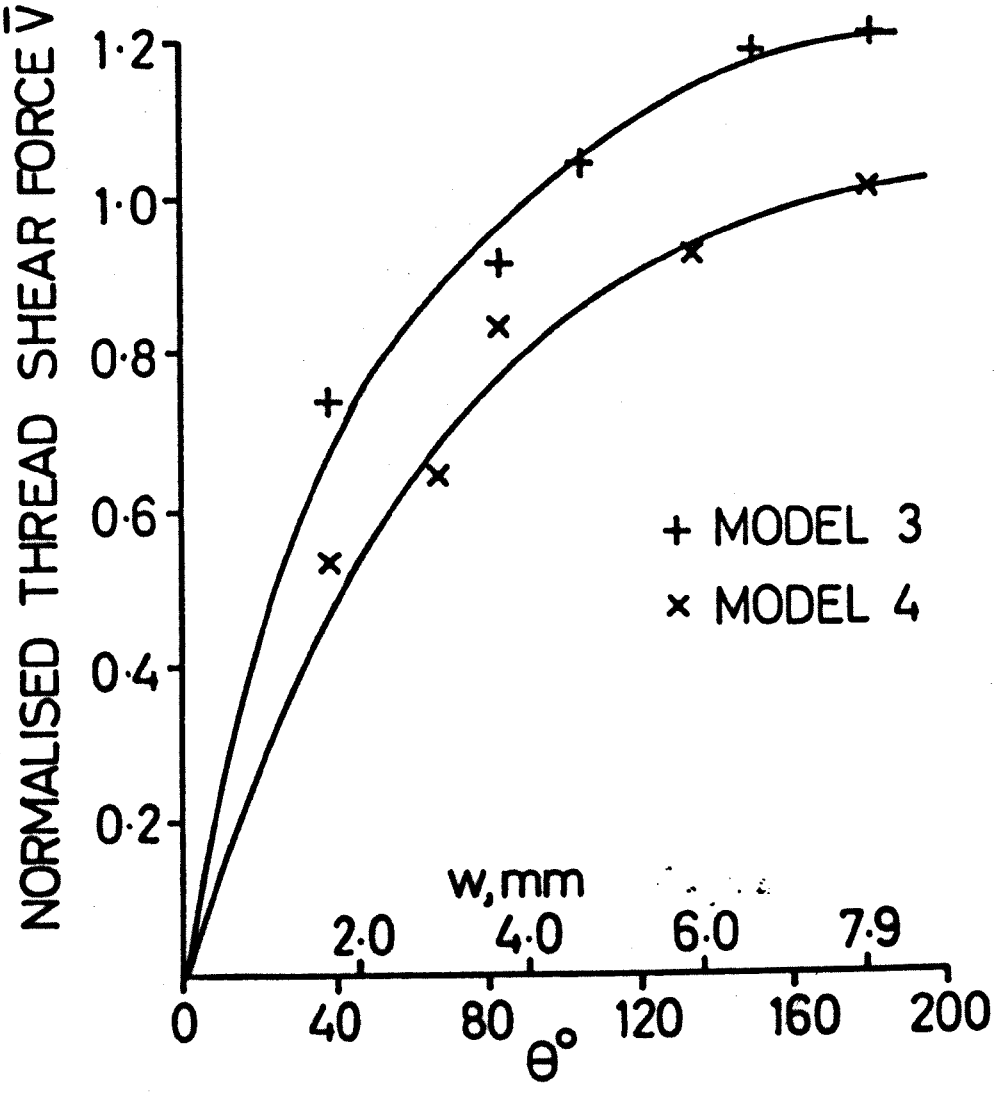

Fig 8.1.15

Normalised Shear Force Distributions in Loaded Coupling Runouts

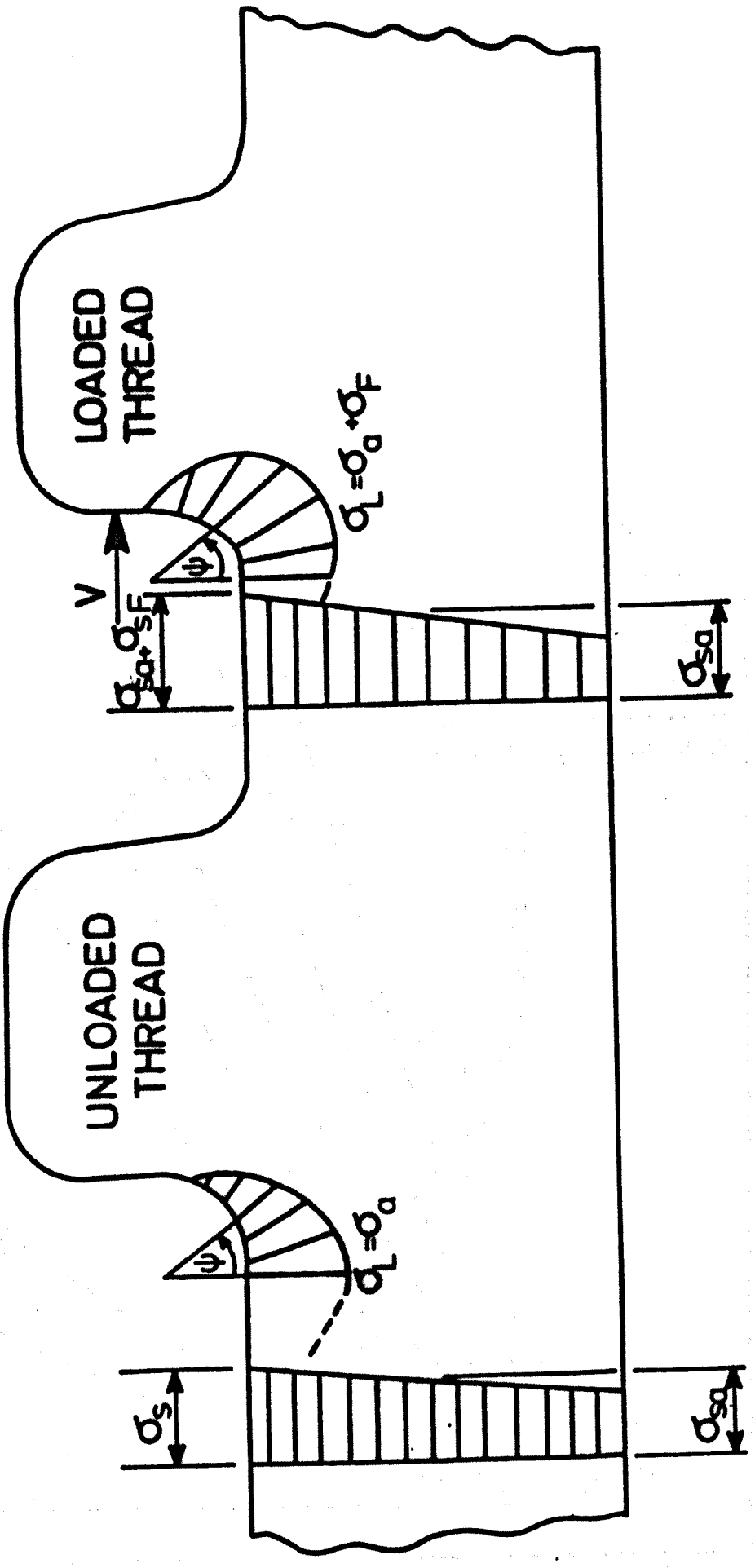

Fig 8.2.1

Definition of Stresses in Threads

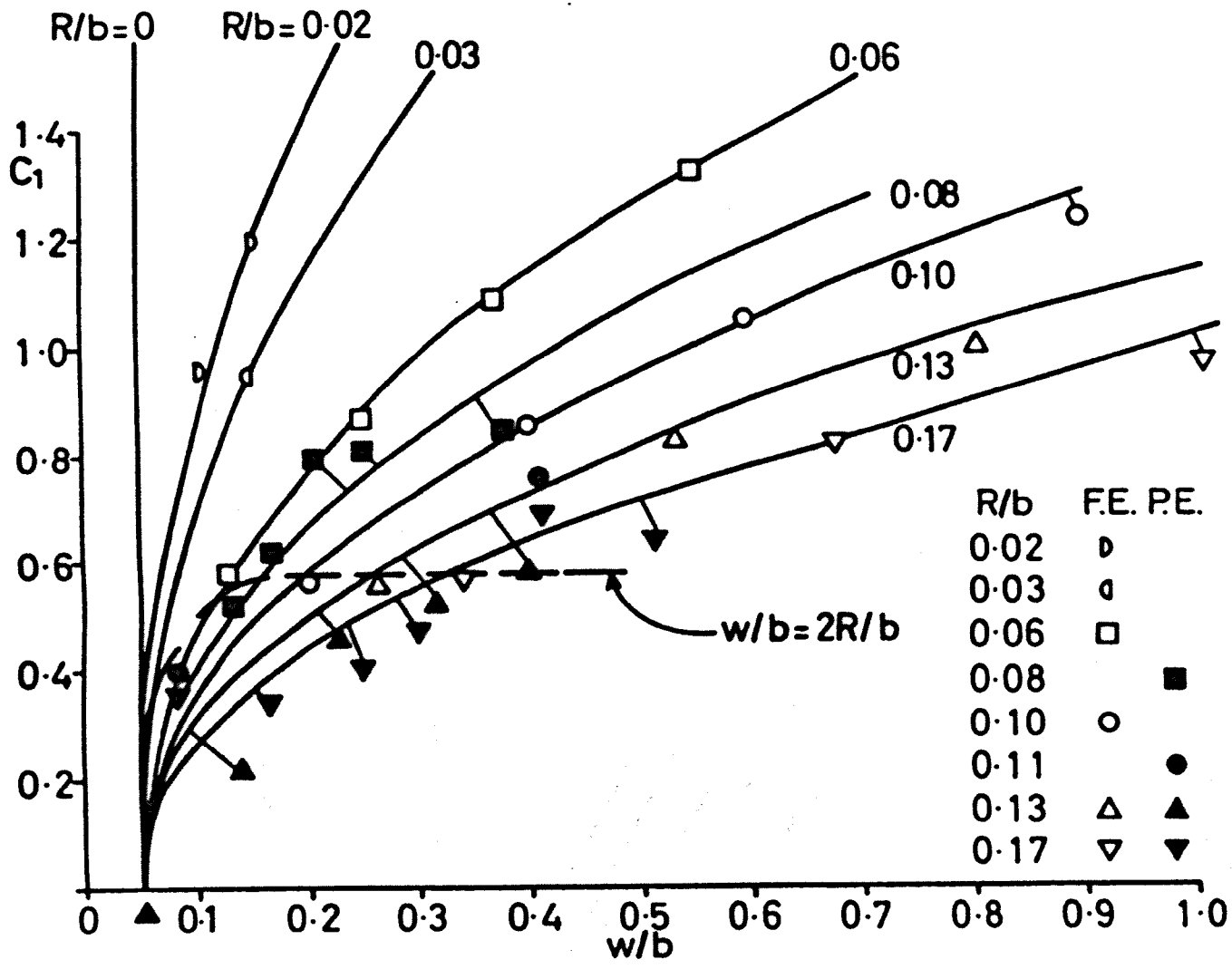

Fig 8.2.2 Plots of C_1 v w/b Obtained from Finite Elements and Photoelastic Measurements. Solid lines Obtained Using Equation 8.2.2

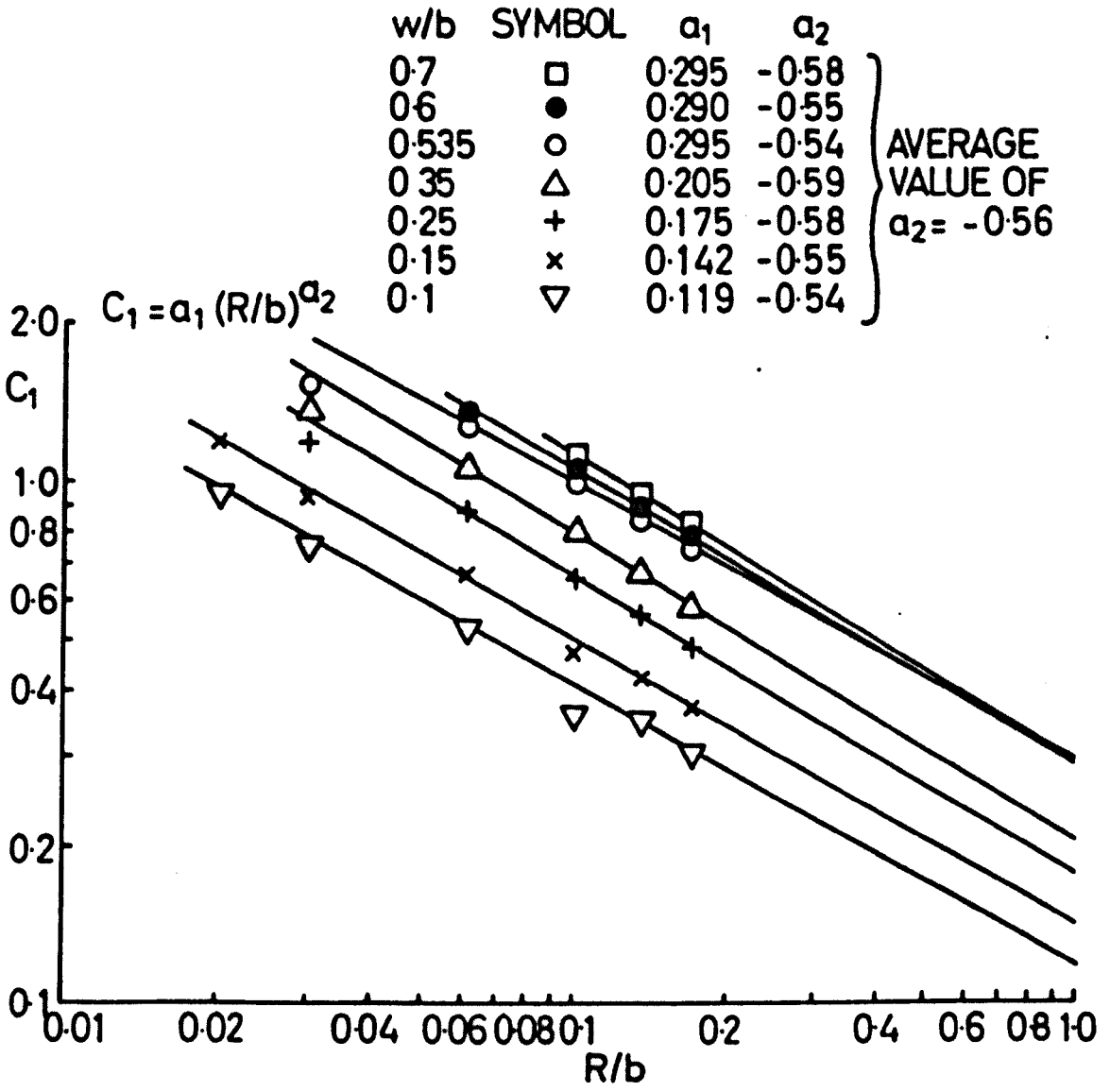

Fig 8.2.3

Values of C_1 Obtained by Finite Elements Plotted Against R/b On Log-Log Paper

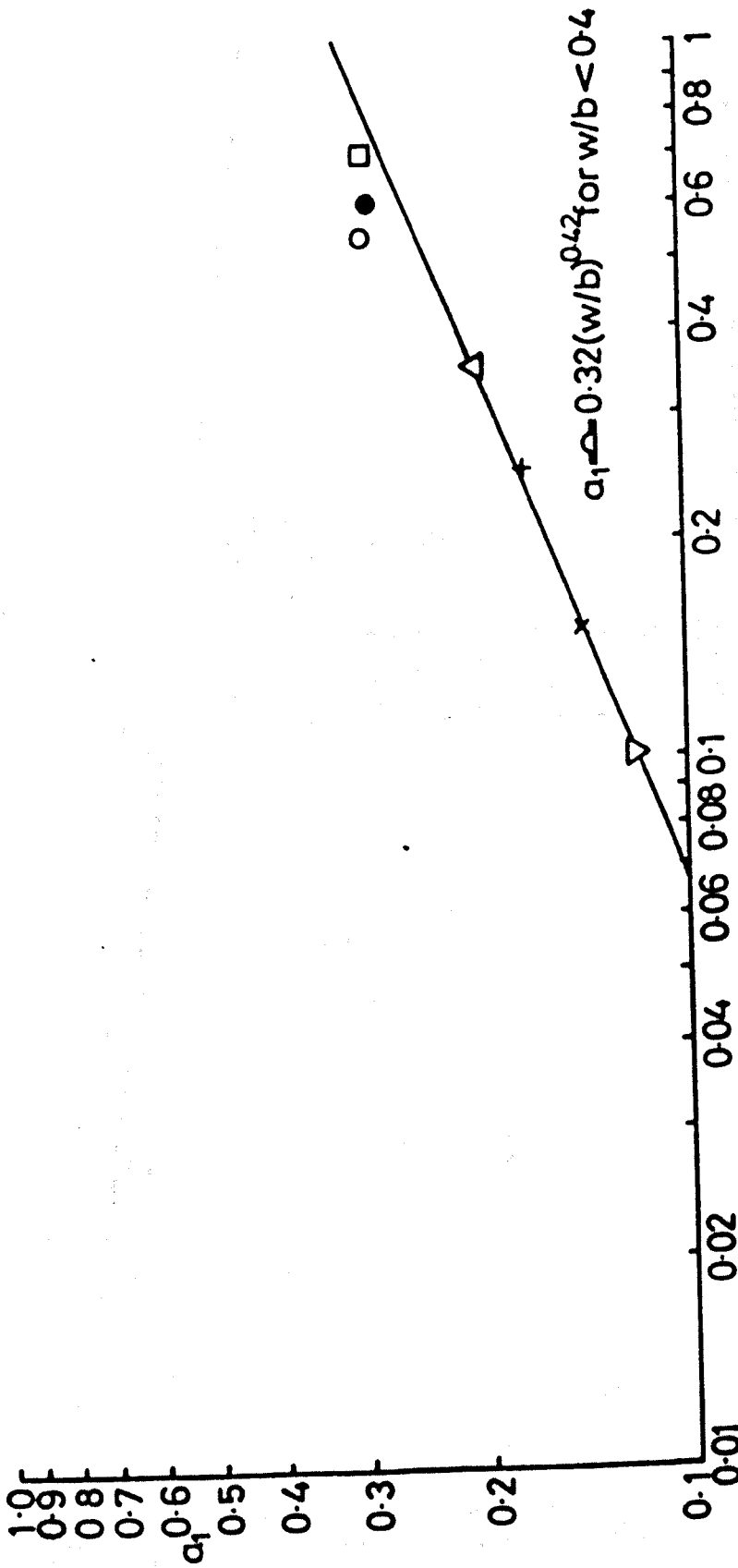

Fig 8.2.4

a_1 v w/b on Log-Log Paper

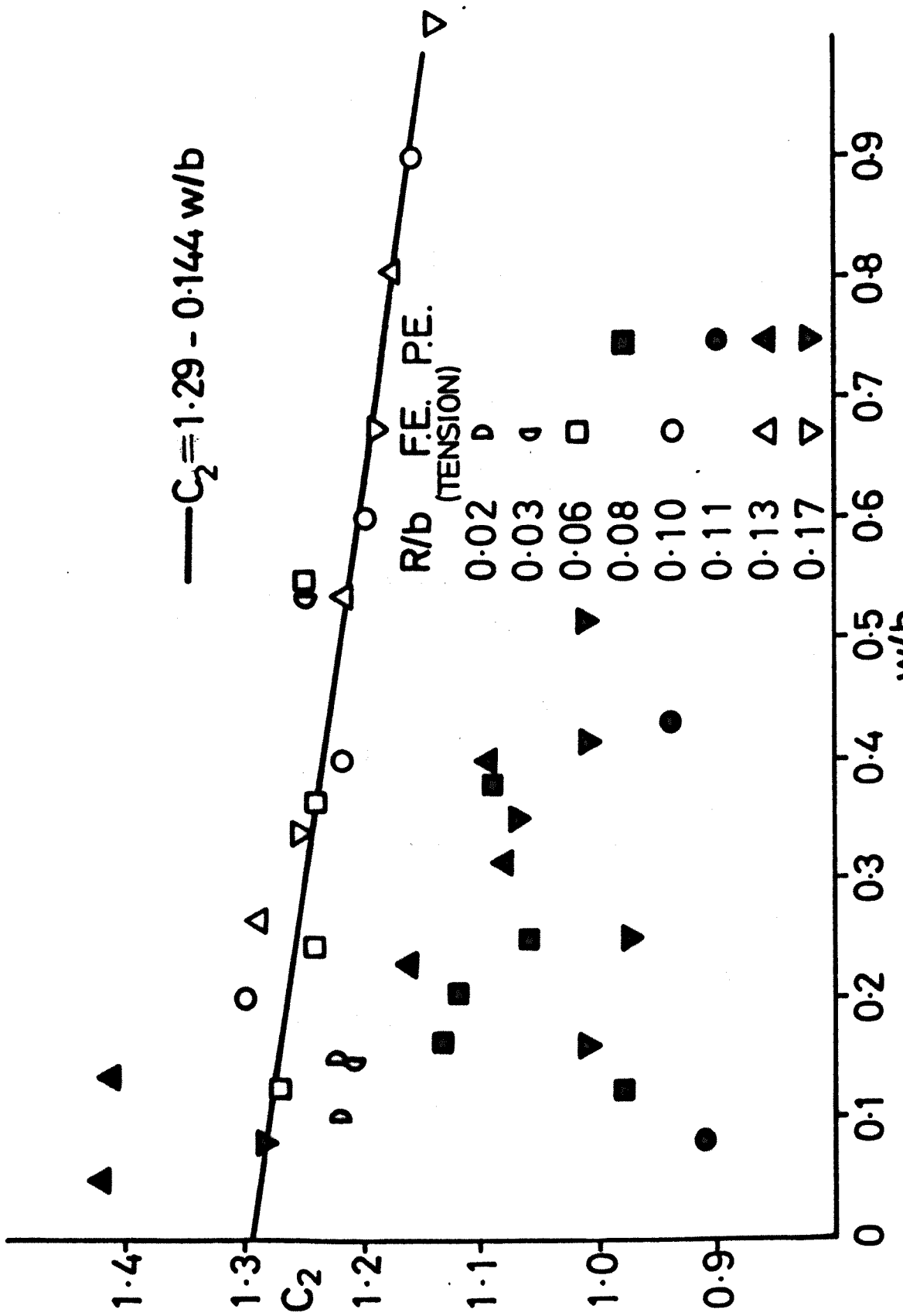

Fig 8.2.5

Parts of C_2 v w/b Obtained from Finite Elements and Photoelastic Measurements

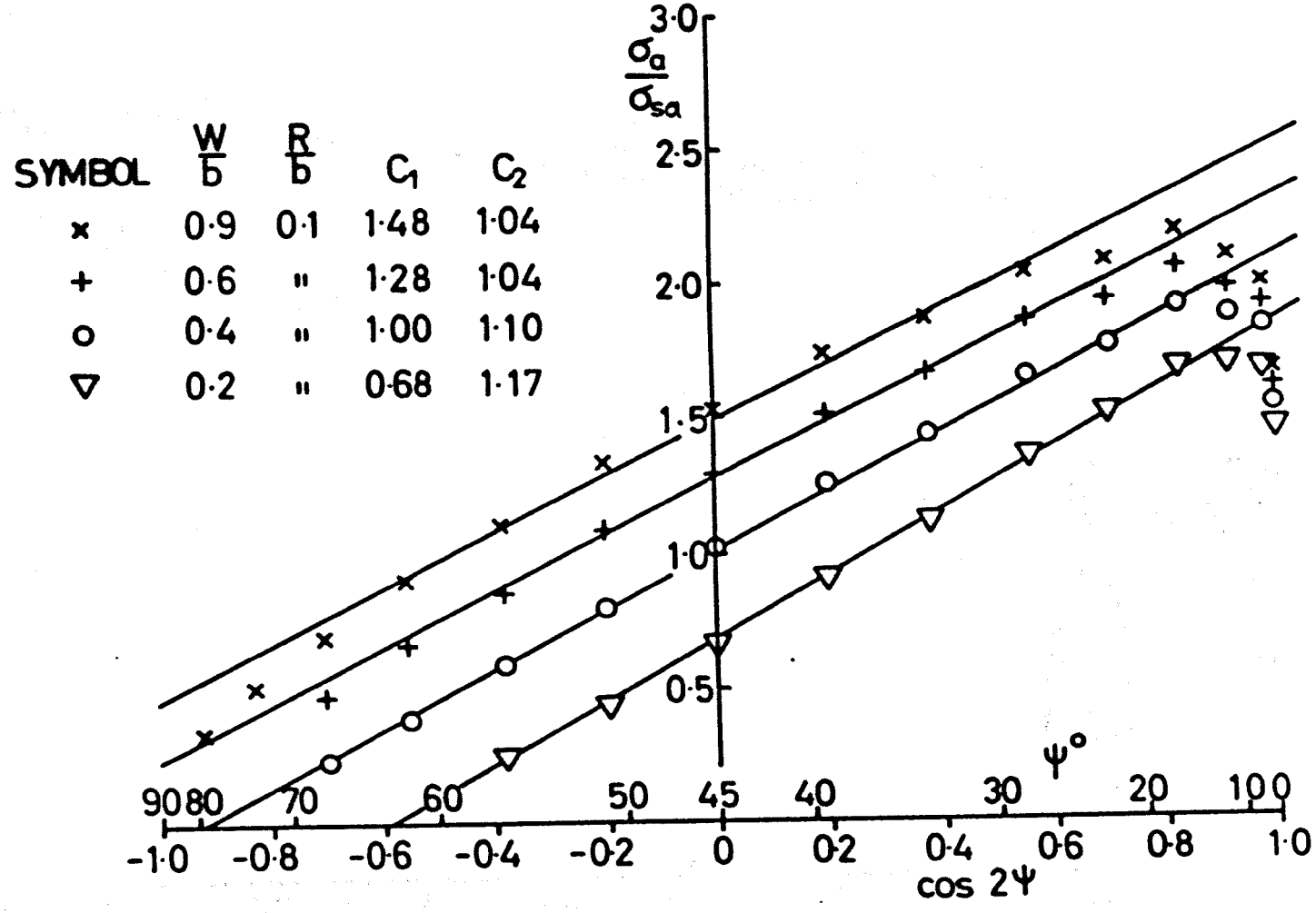

Fig 8.2.6 Typical Distributions of Normalised Surface Fillet Stresses Obtained Using Finite Elements for Thread-like Projections loaded with Wall Bending

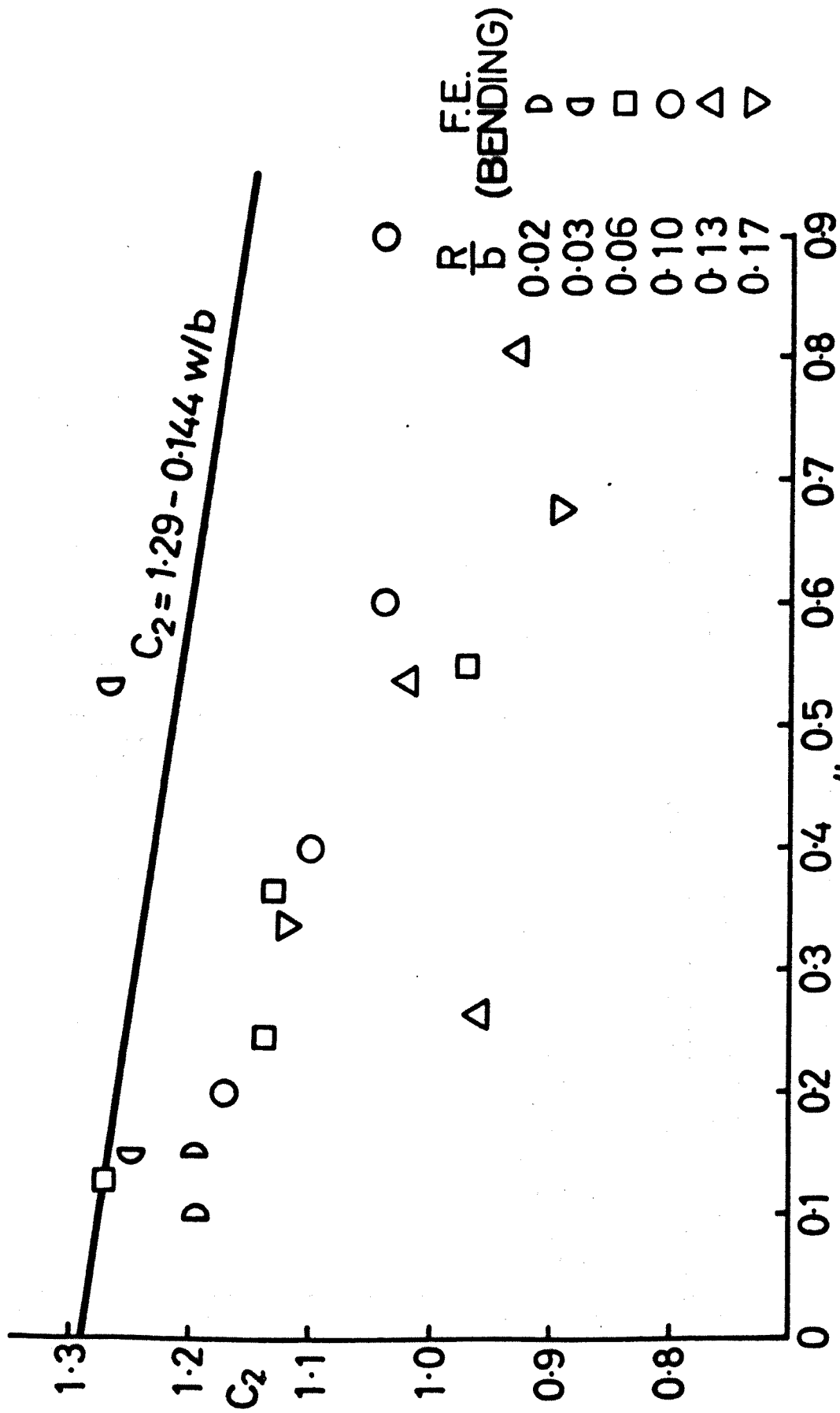

Fig 8.2.7

Plots of C_2 v w/b Obtained from Finite Elements for Wall Bending

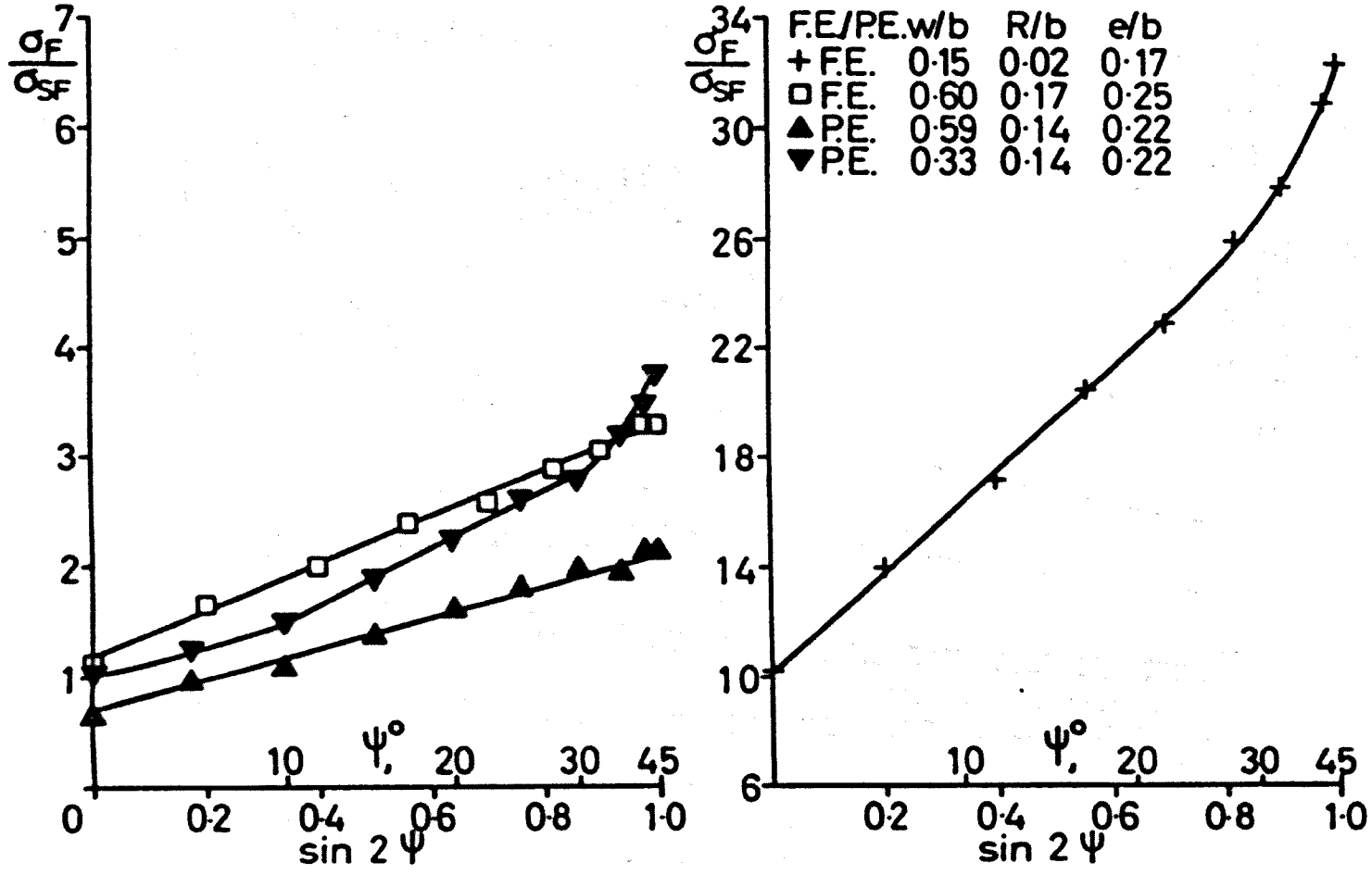

Fig 8.2.8 Plots of Normalised Fillet Stress v Sin 2ψ For Projections Loaded with Shear Forces Obtained from Finite Elements and Photoelastic Measurements

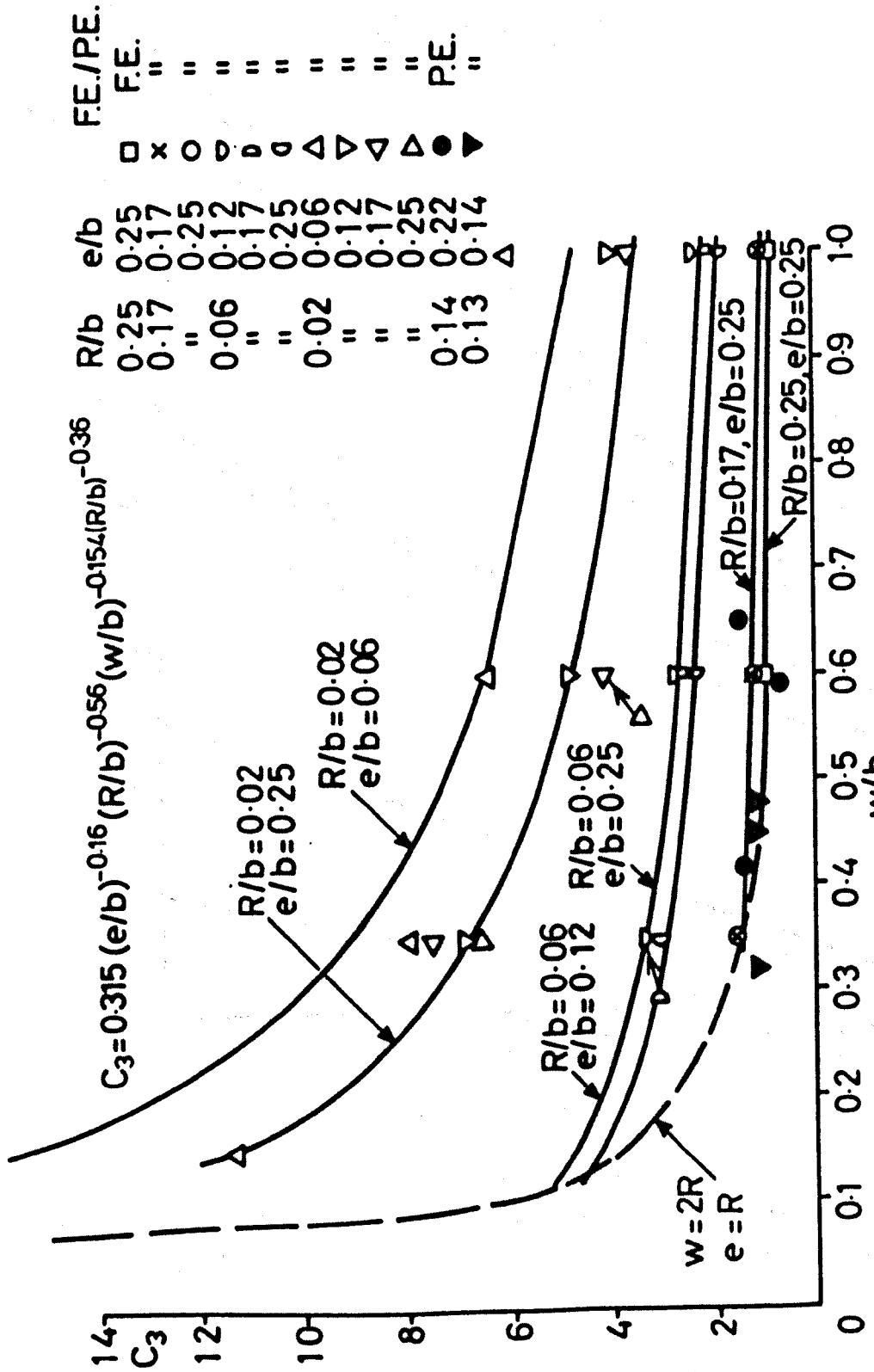

Fig 8.2.9 Plots of c_3 v w/b Obtained from Finite Elements and Photoelastic Measurements. Solid Lines Obtained using Equation 8.2.9

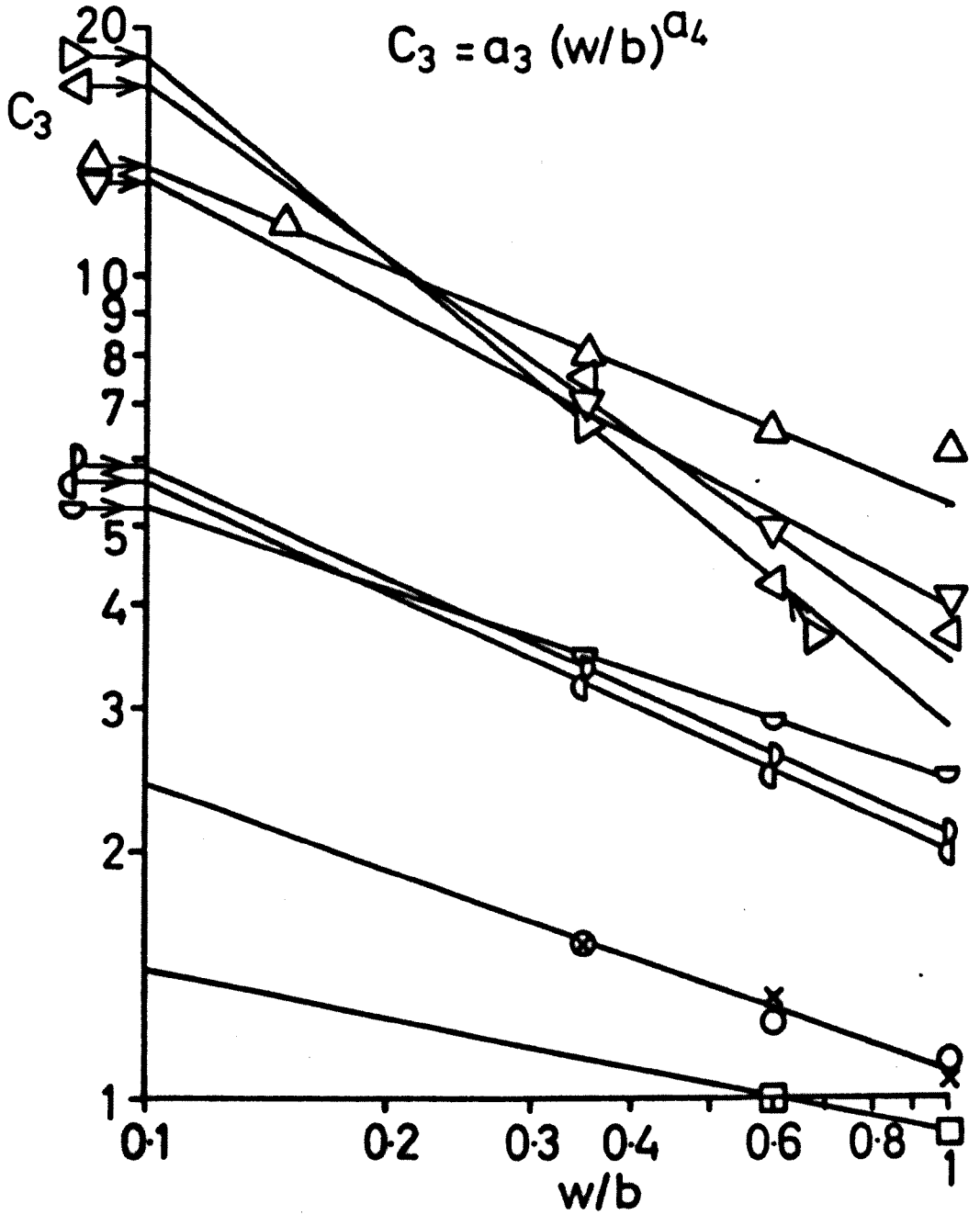

Fig 8.2.10

c_3 v w/b Plotted on Log-Log Paper. Values obtained from Finite Elements. Symbols Defined on Fig 8.2.9.

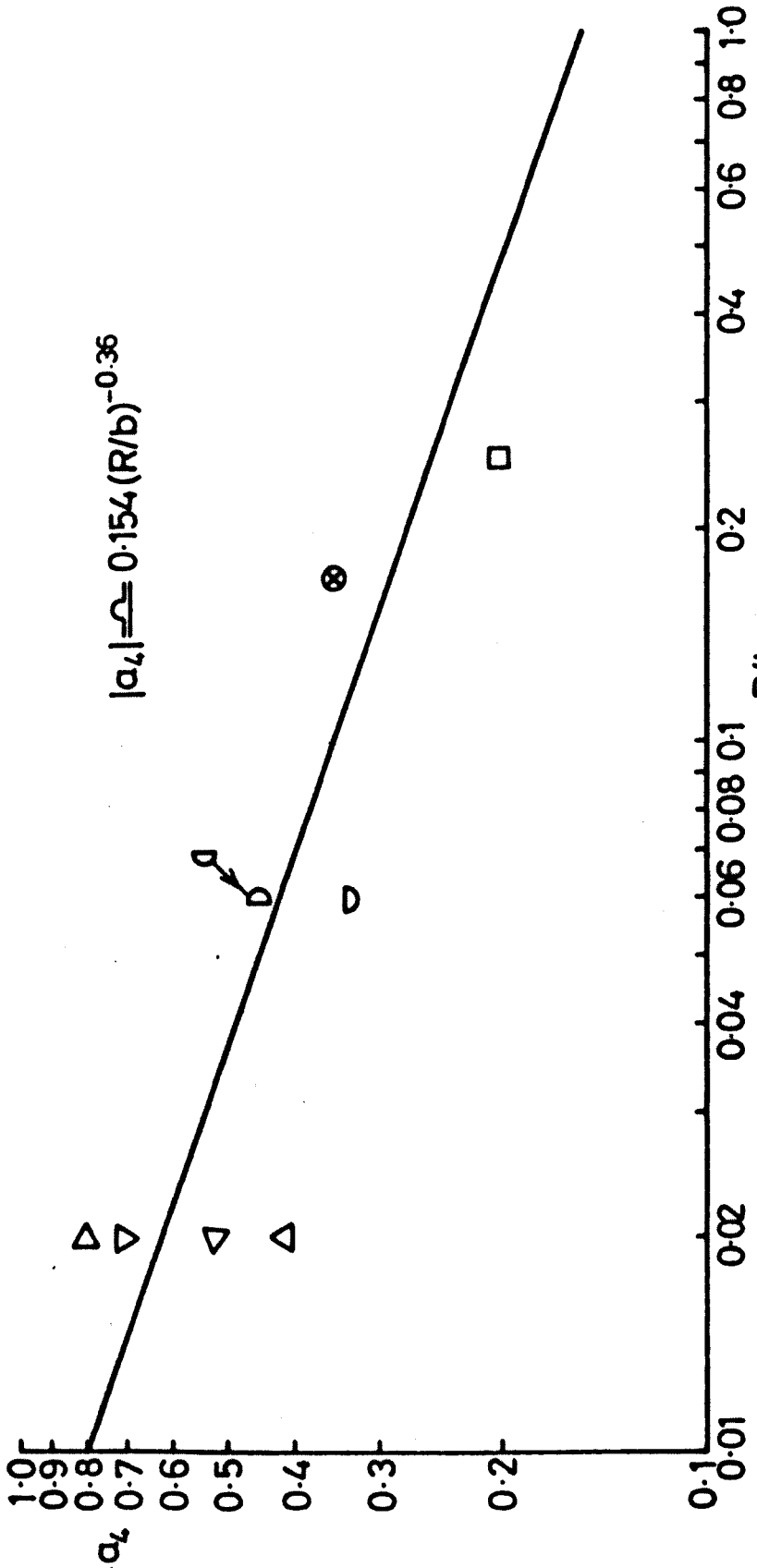

Fig 8.2.11

$-a_4$ v R/b Plotted on Log-Log Paper. Values Obtained from Finite Elements Symbols Defined on Fig 8.2.9

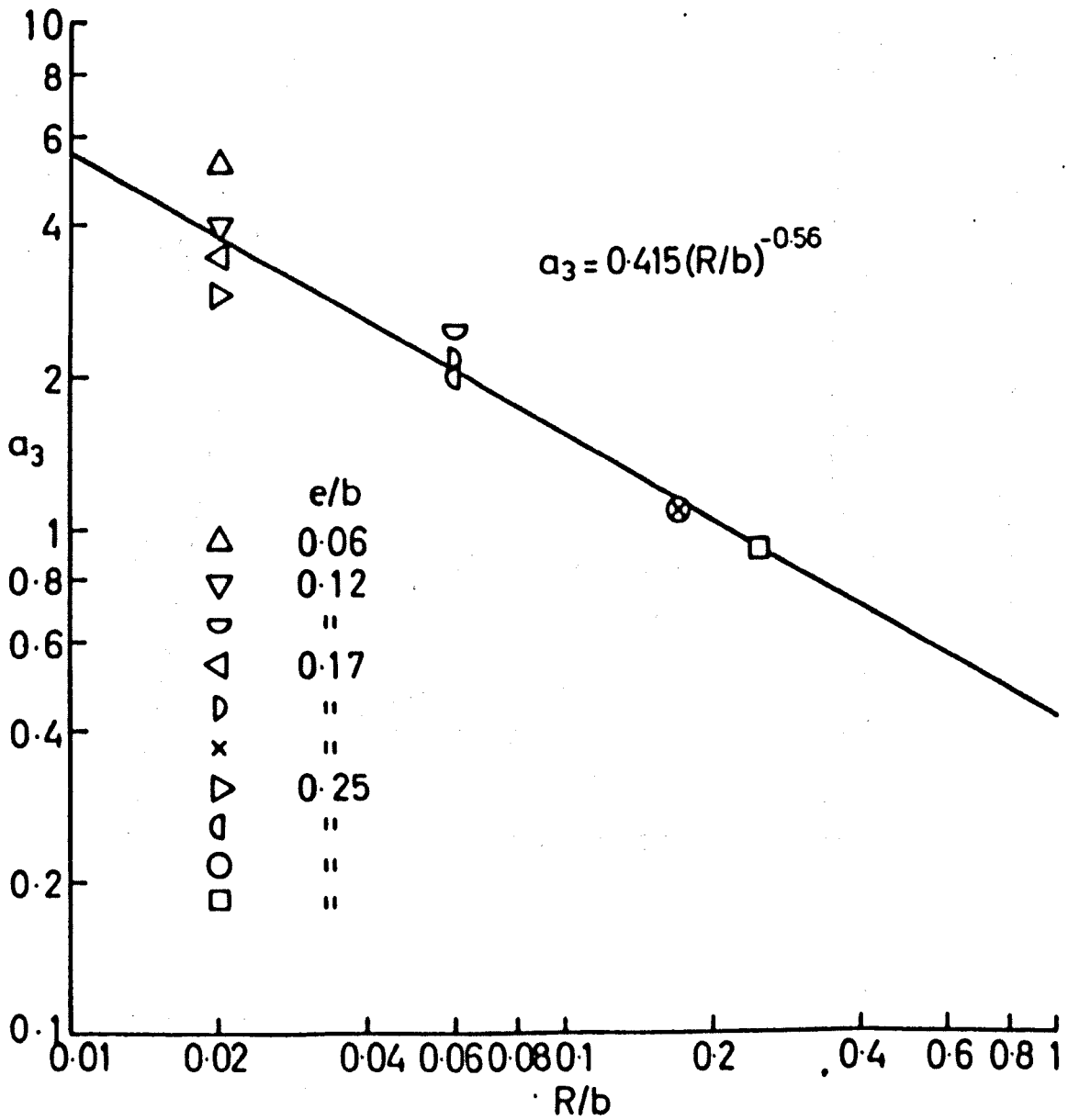

Fig 8.2.12

a_3 v R/b Plotted on Log-Log Paper. Values obtained from Finite Elements. Symbols Defined on Fig 8.2.9

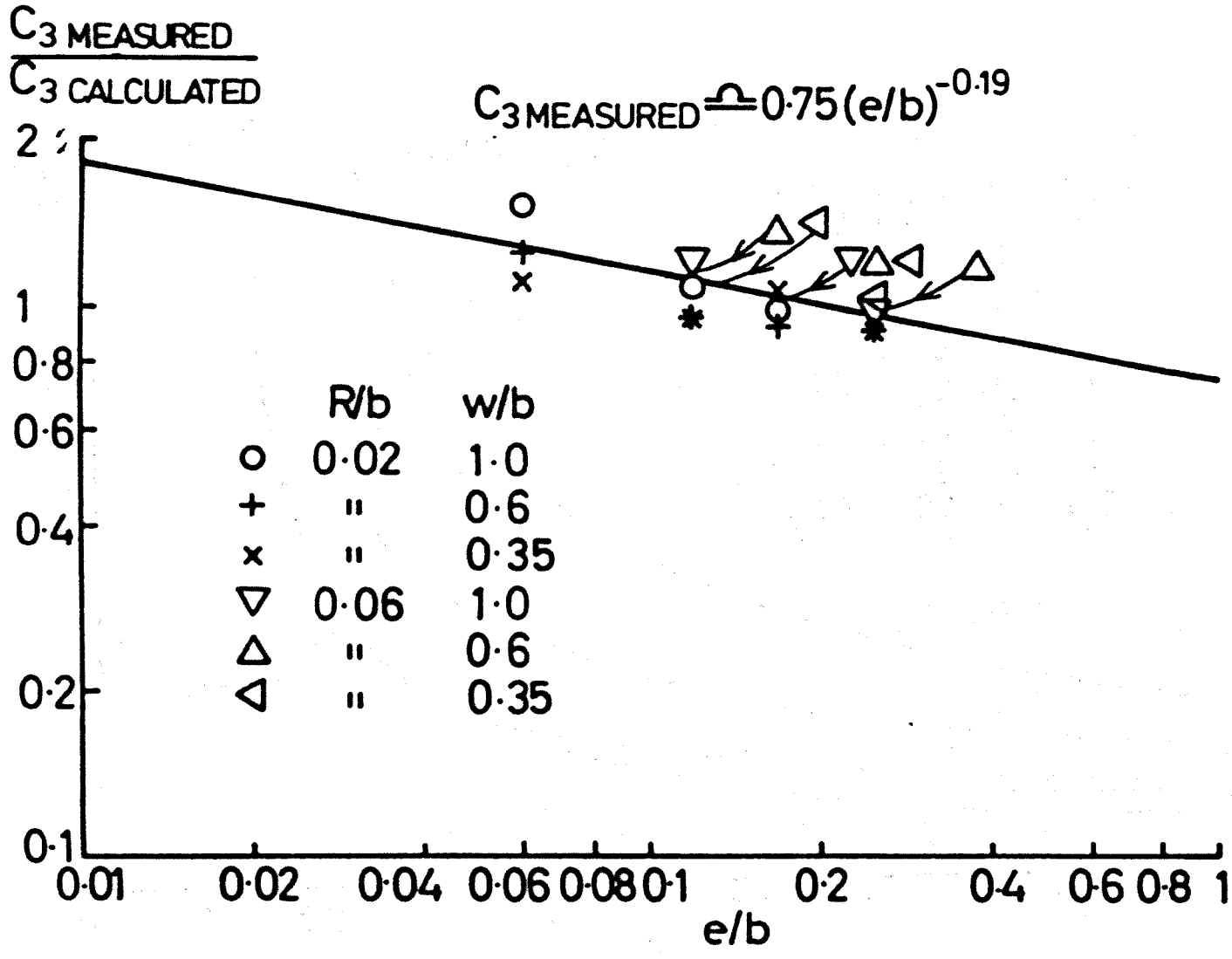

Fig 8.2.13

Measured c_3 (From F.E.)/ Calculated c_3 (from equation 8.2.8) Plotted against e/b

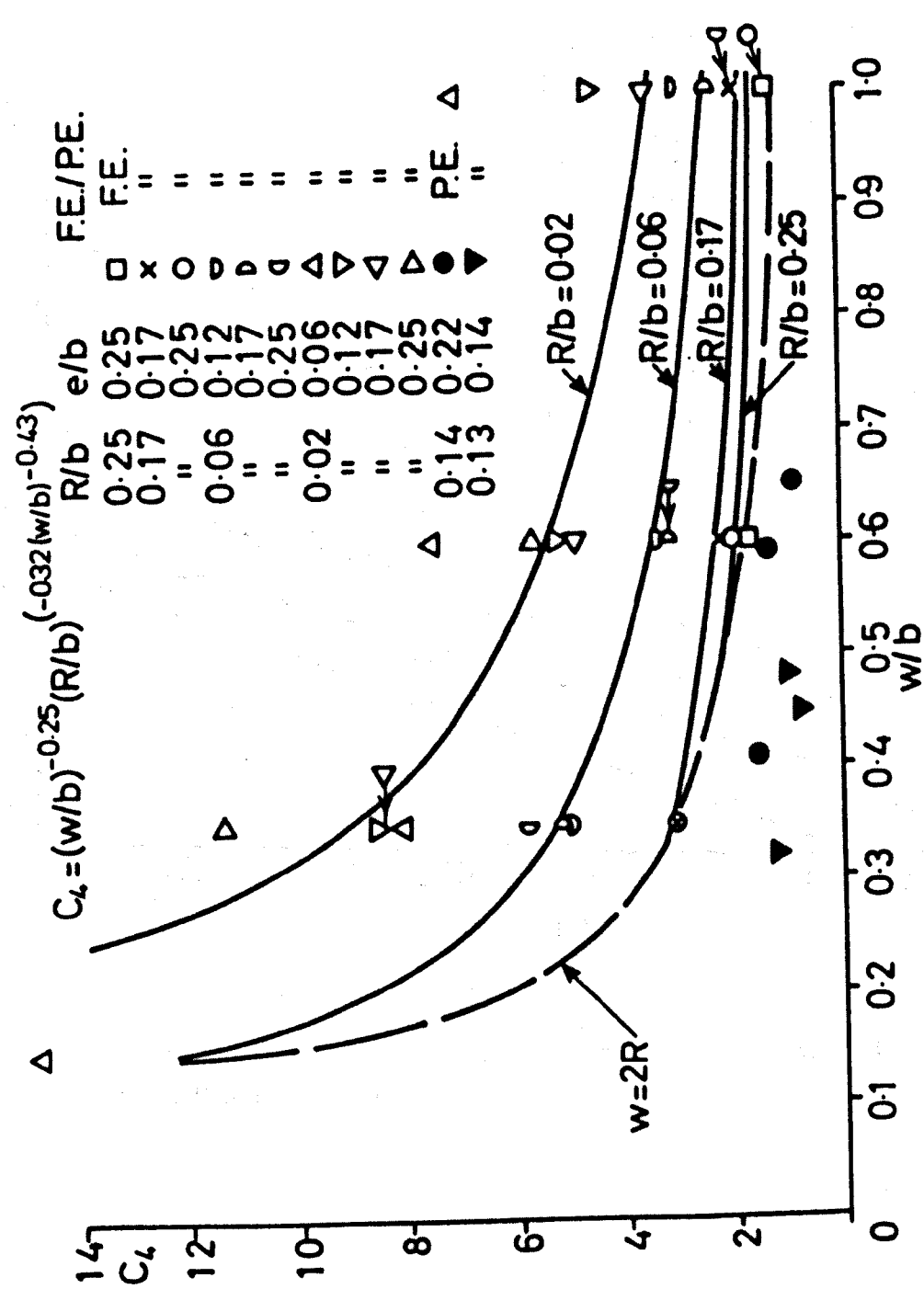

Fig 8.2.14

Plots of c_4 v w/b Obtained from Finite Elements and Photoelastic Measurements

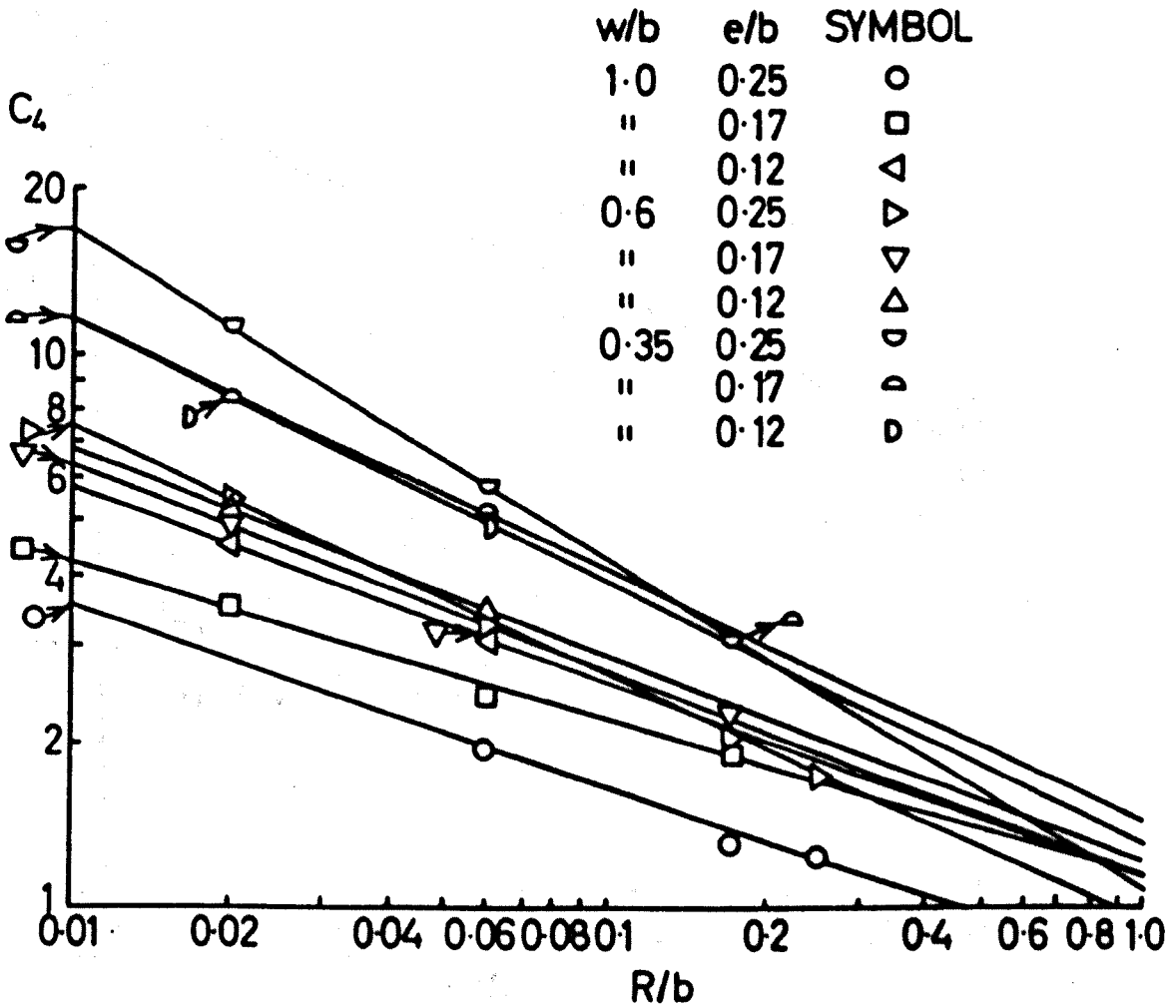

Fig 8.2.15

c_4 v R/b Plotted on Log-Log Paper. Values obtained from Finite Elements.

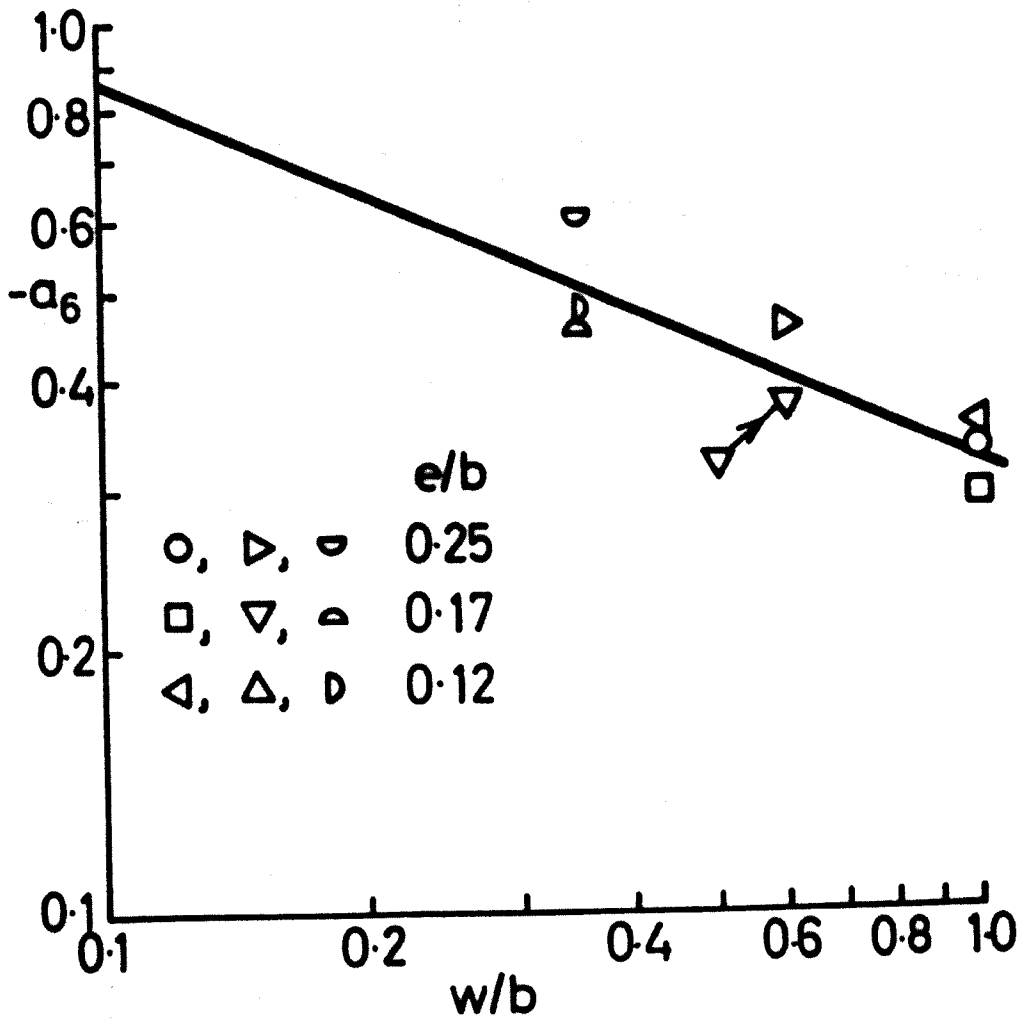

Fig 8.2.16

$-a_6$ v w/b Plotted on Log-Log Paper. Values Obtained from Finite Elements

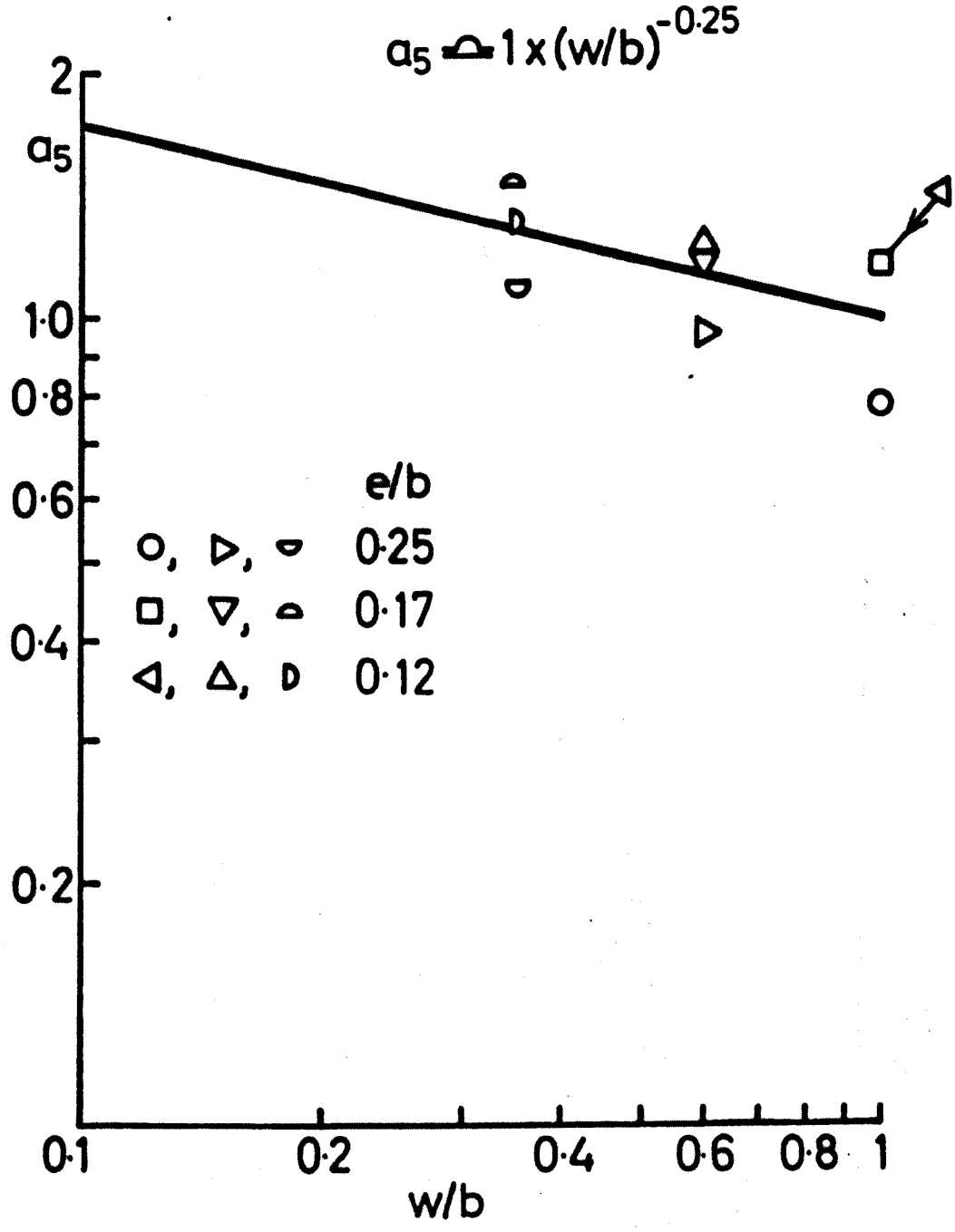

Fig 8.2.17

a_5 v w/b Plotted on Log-Log Paper, Values Obtained From Finite Elements

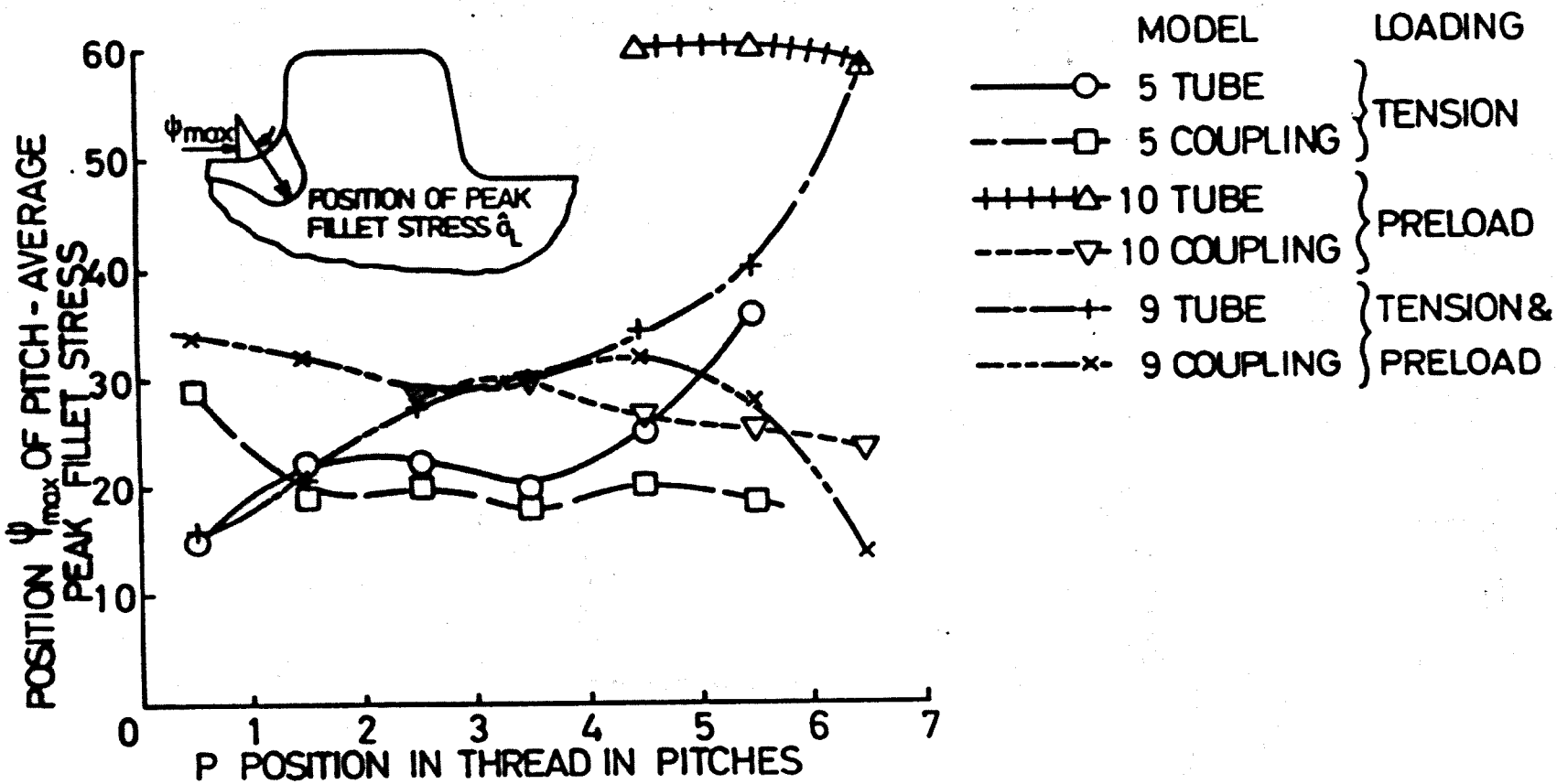

Fig 8.3.1 Pitch Average Positions of Peak Fillet Stress in Typical Models

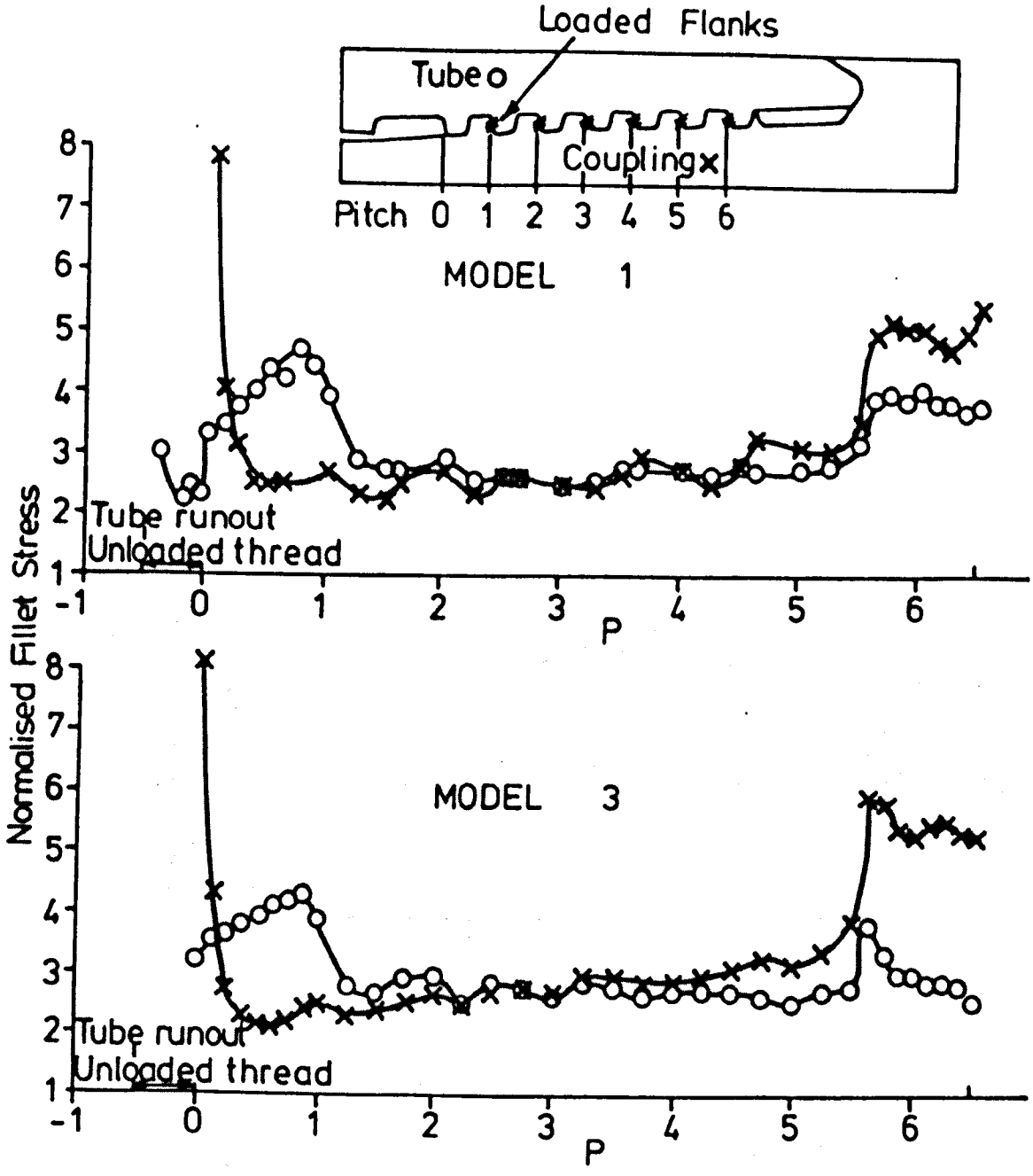

Fig 8.3.2 & 8.3.3

Normalised Peak Fillet Stress Distributions in the Tension Only Loaded Models 1 and 3

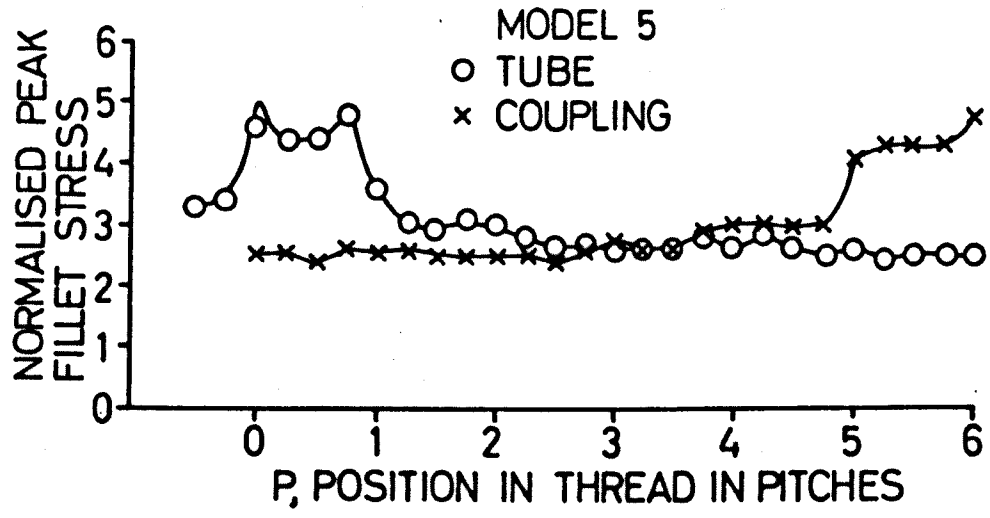

Fig 8.3.4

Normalised Peak Fillet Stress Distribution
In the Tension Only Loaded Model 5

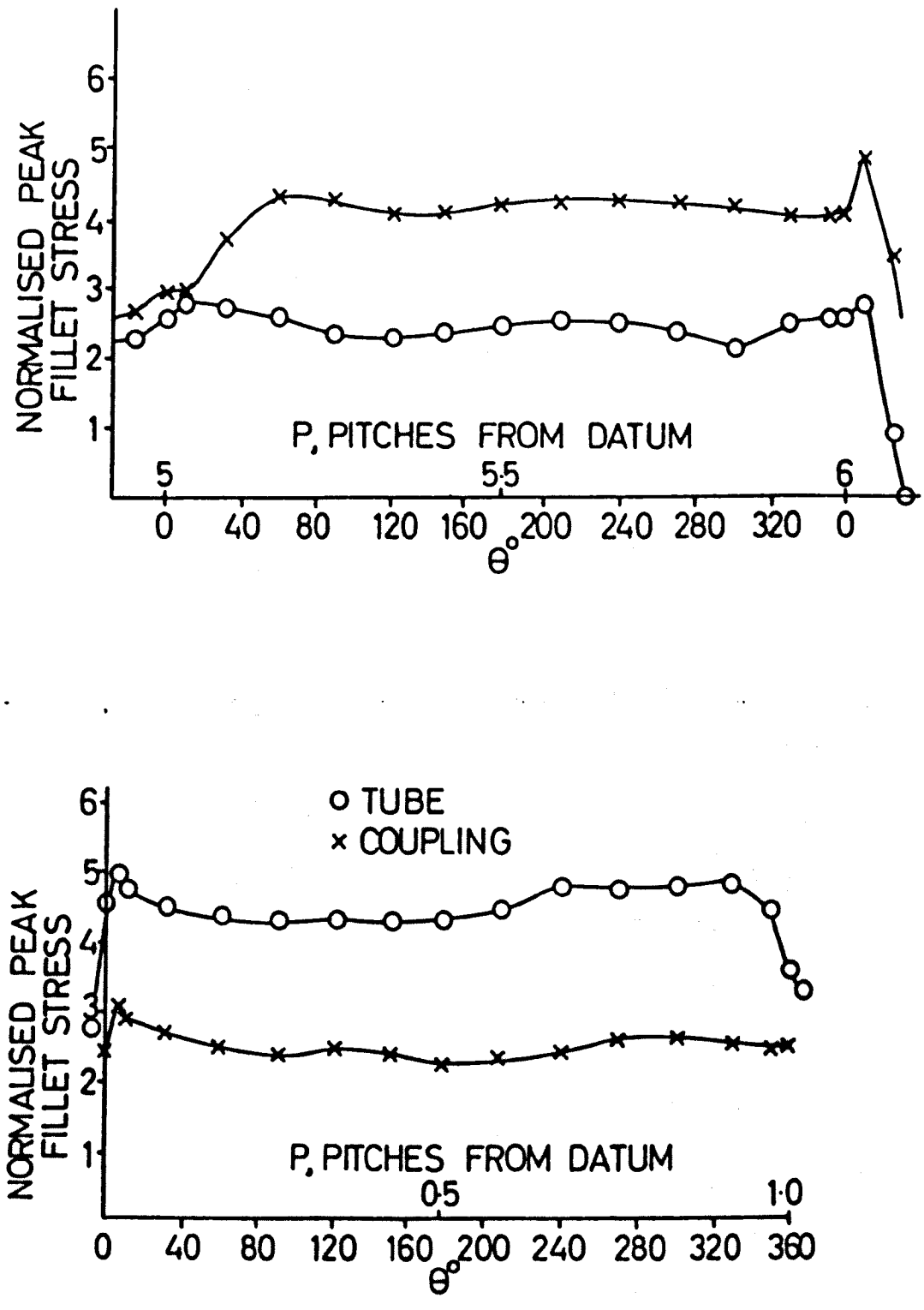

Fig 8.3.5

Normalised Peak Fillet Stress Distributions
In the Last and First Pitches of Model 5

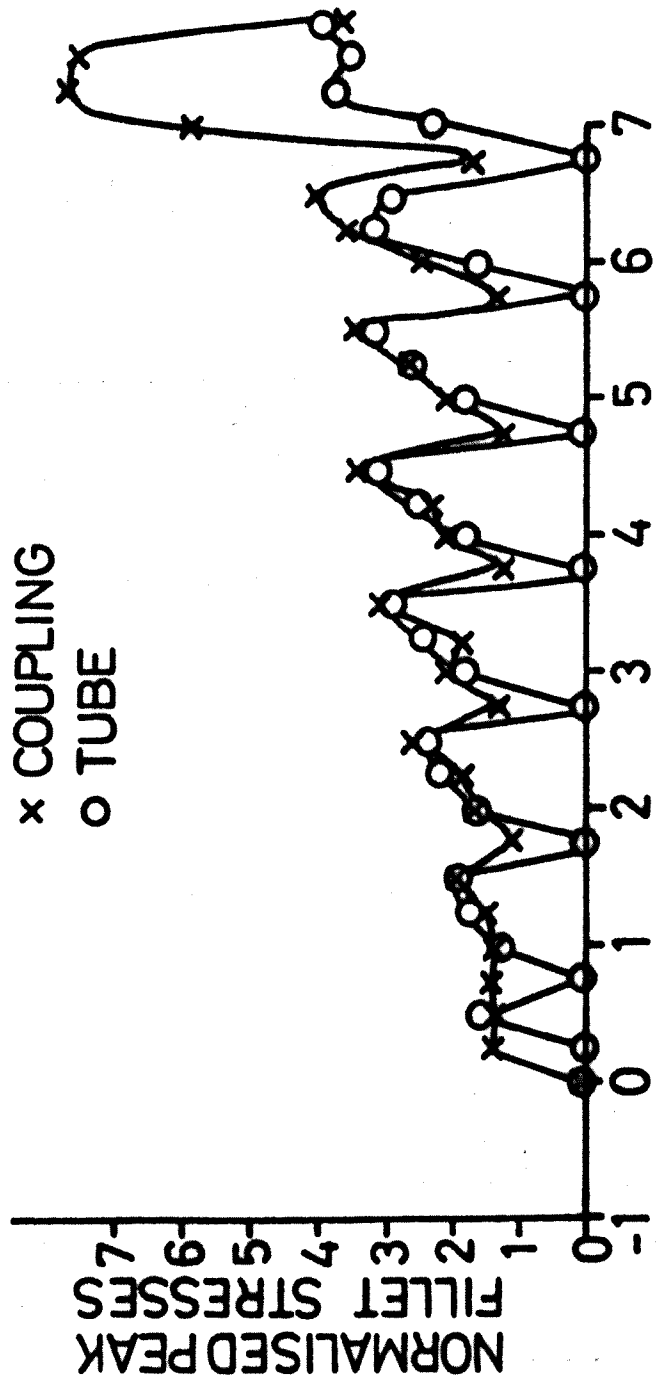

Fig 8.3.6 Normalised Peak Fillet Stress Distributions In the Preload Only Model 10

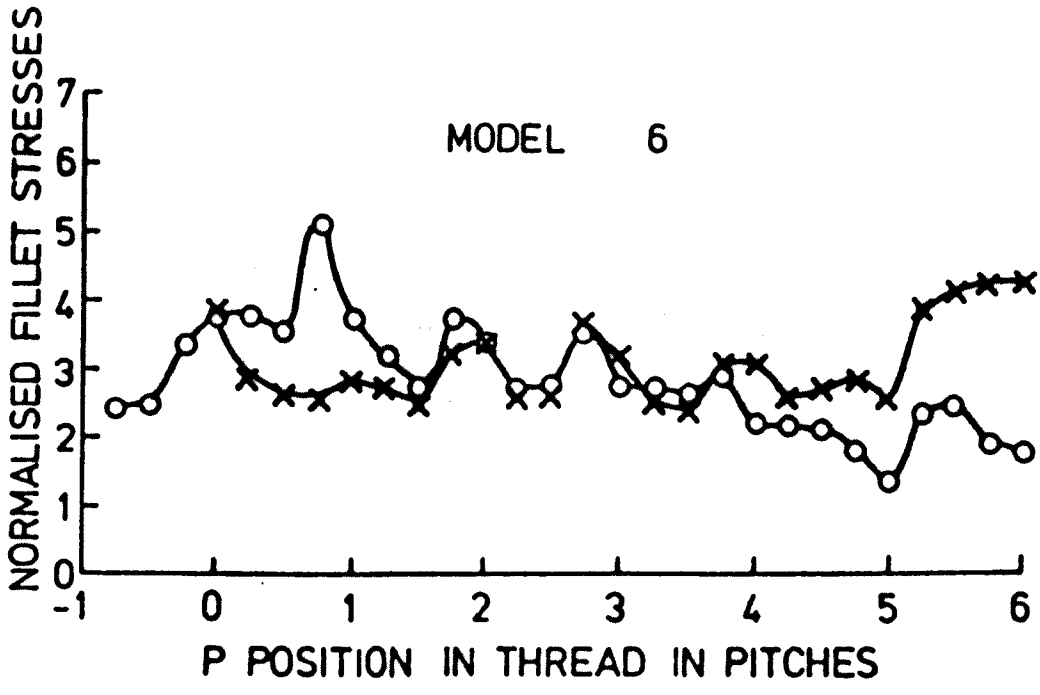

Fig 8.3.7 Normalised Peak Fillet Stress Distributions In the Tension Only, Grooved Model 6

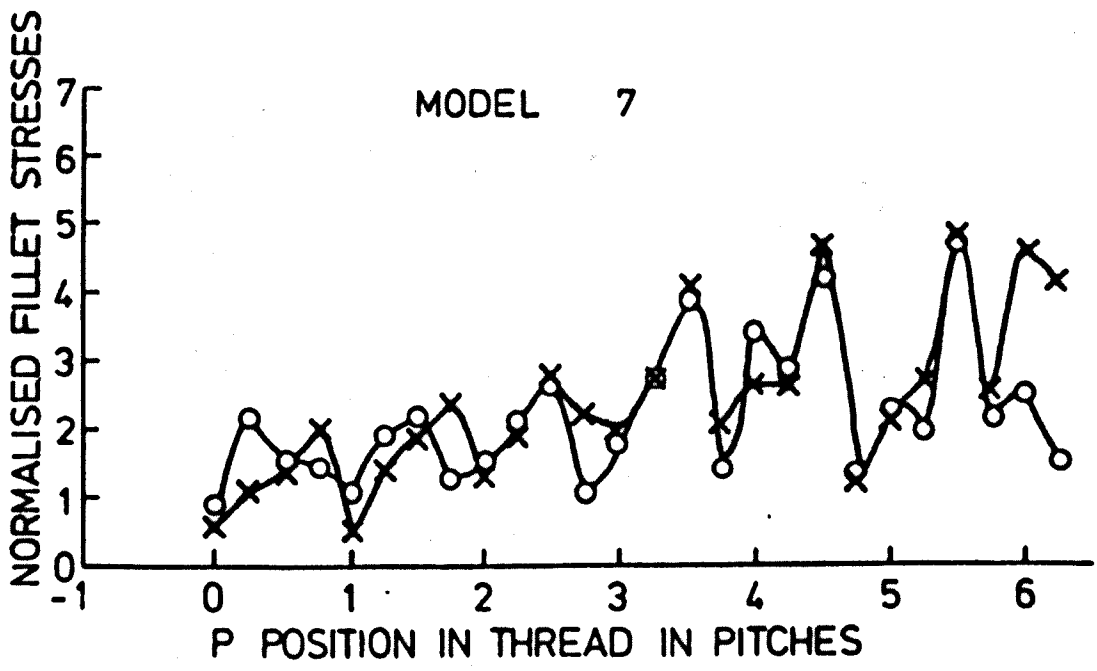

Fig 8.3.8 Normalised Peak Fillet Stress Distributions In the Preload Only, Grooved Model 7

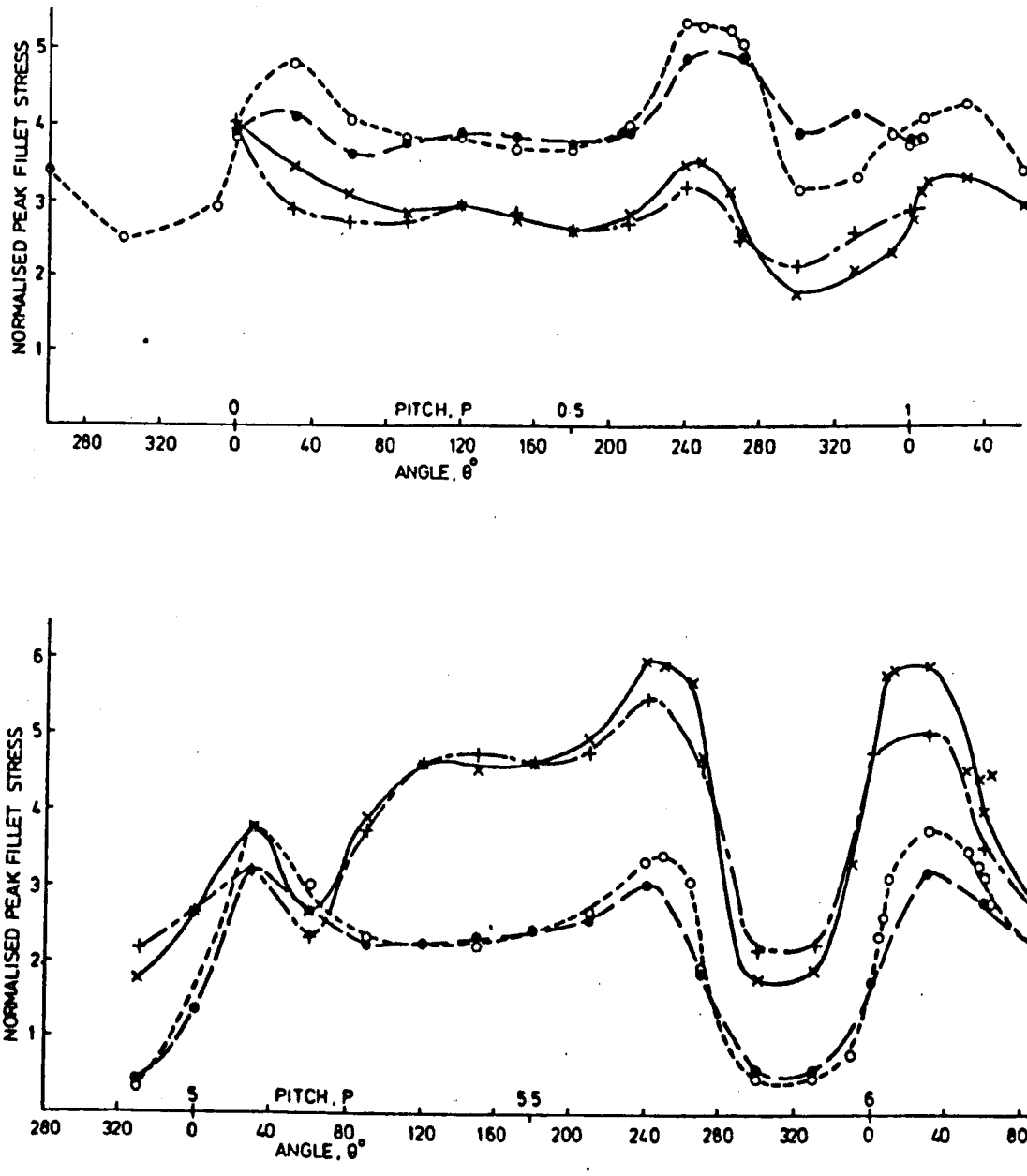

Fig 8.3.9

Normalised Peak Fillet Stress Distributions
In the First and Last Pitches of Model 6

- o Tube Fillet Stresses Normalised By Mean Tube Wall Stress
- ● Tube Fillet Stresses Normalised By Local Tube Wall Stress
- x Coupling Fillet Stresses Normalised By Mean Tube Wall Stress
- \+ Coupling Fillet Stresses Normalised By Local Tube Wall Stress

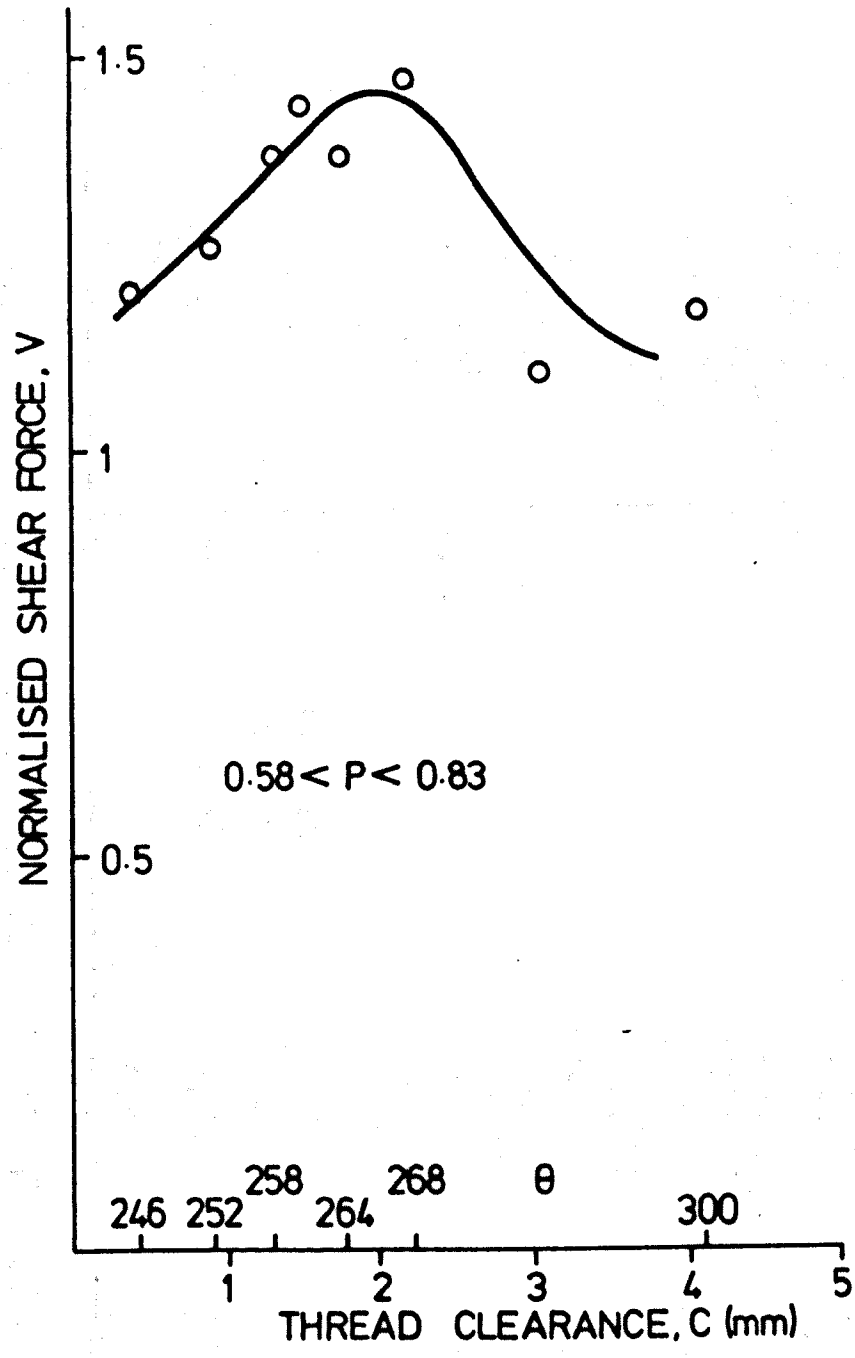

Fig 8.3.10 Variation of Normalised Shear Force with Clearance in a 'Belled Out' Region of Model 6

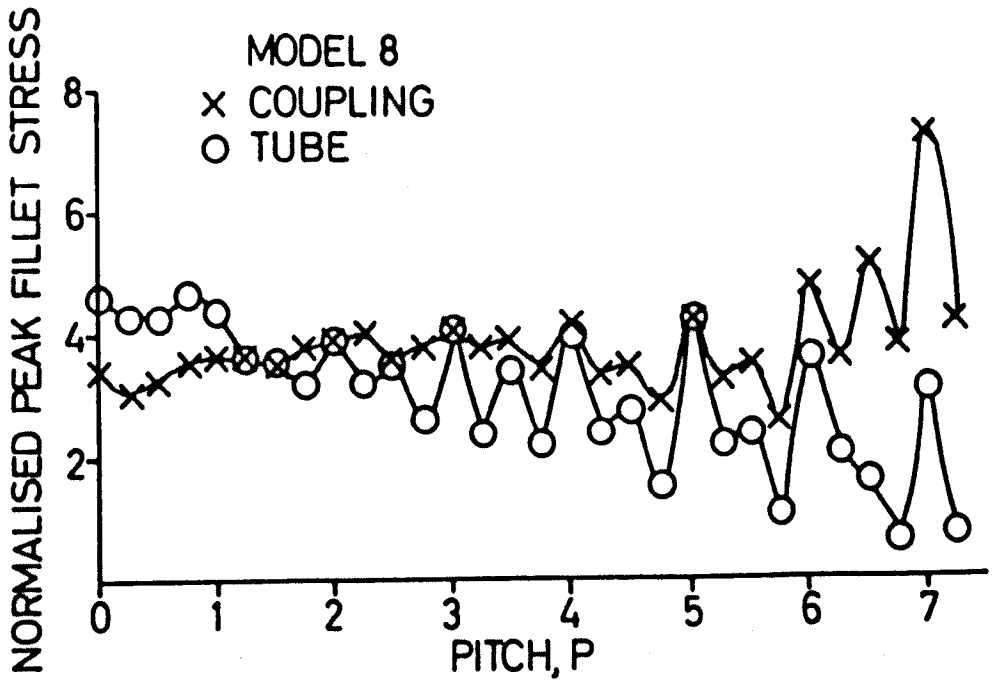

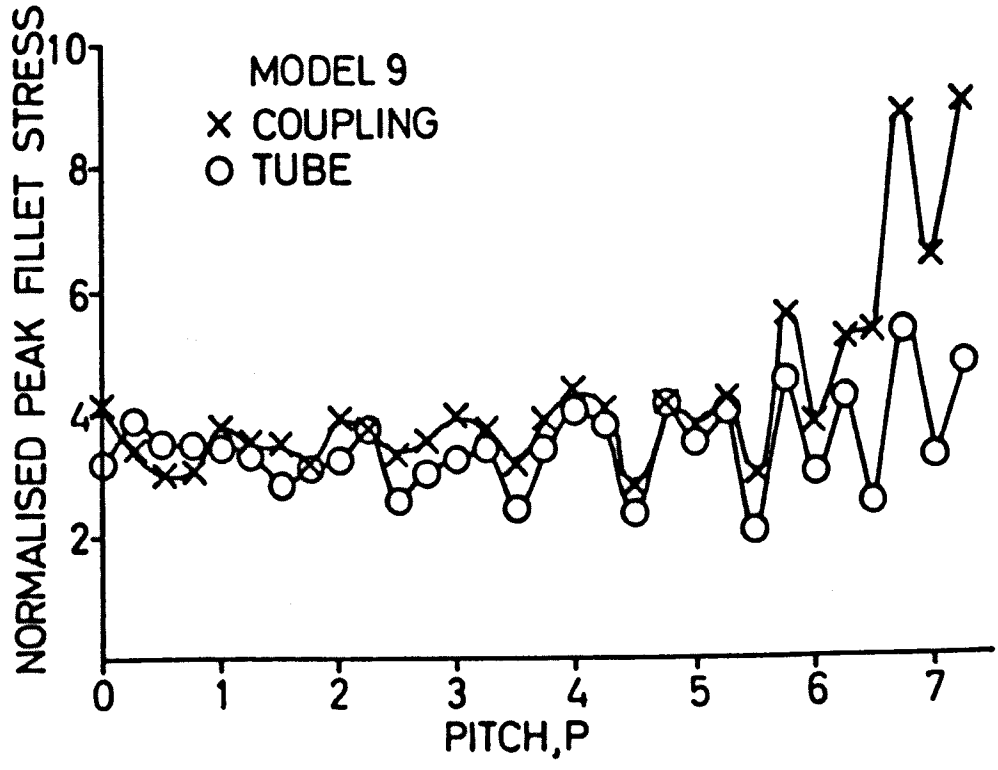

Fig 8.3.11 & 8.3.12 Normalised Peak Fillet Stress Distribution In the Tension and Preloaded Models 8 and 9

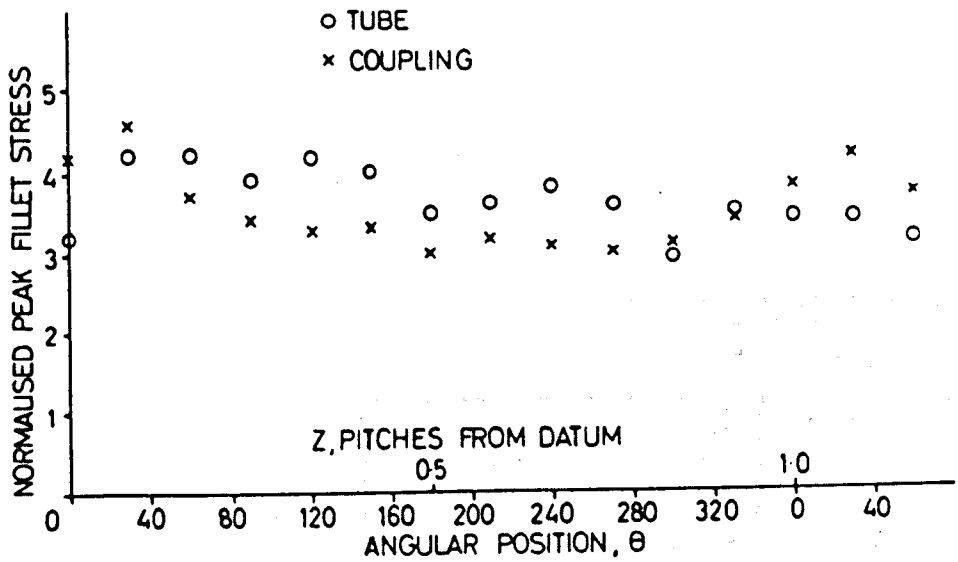

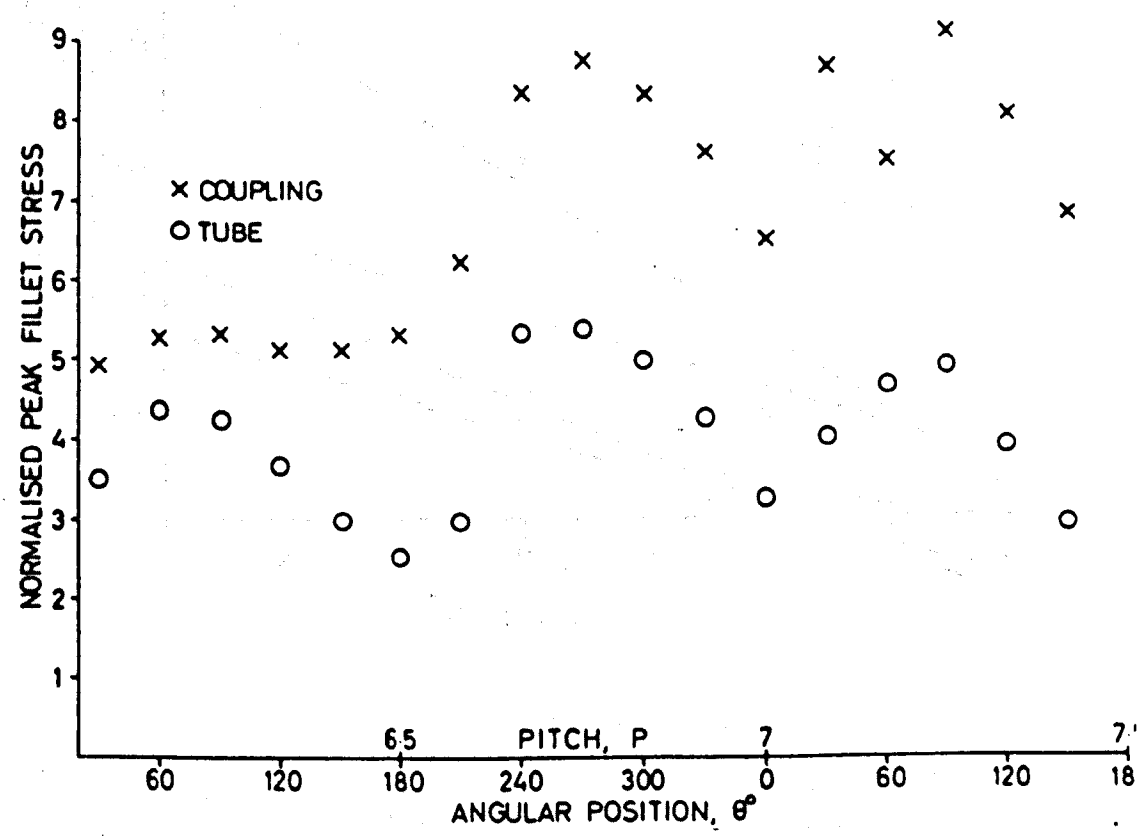

Fig 8.3.13a & b

Normalised Peak Fillet Stress Distribution In The First and Last Loaded Threads of the Tension and Preloaded Model 9

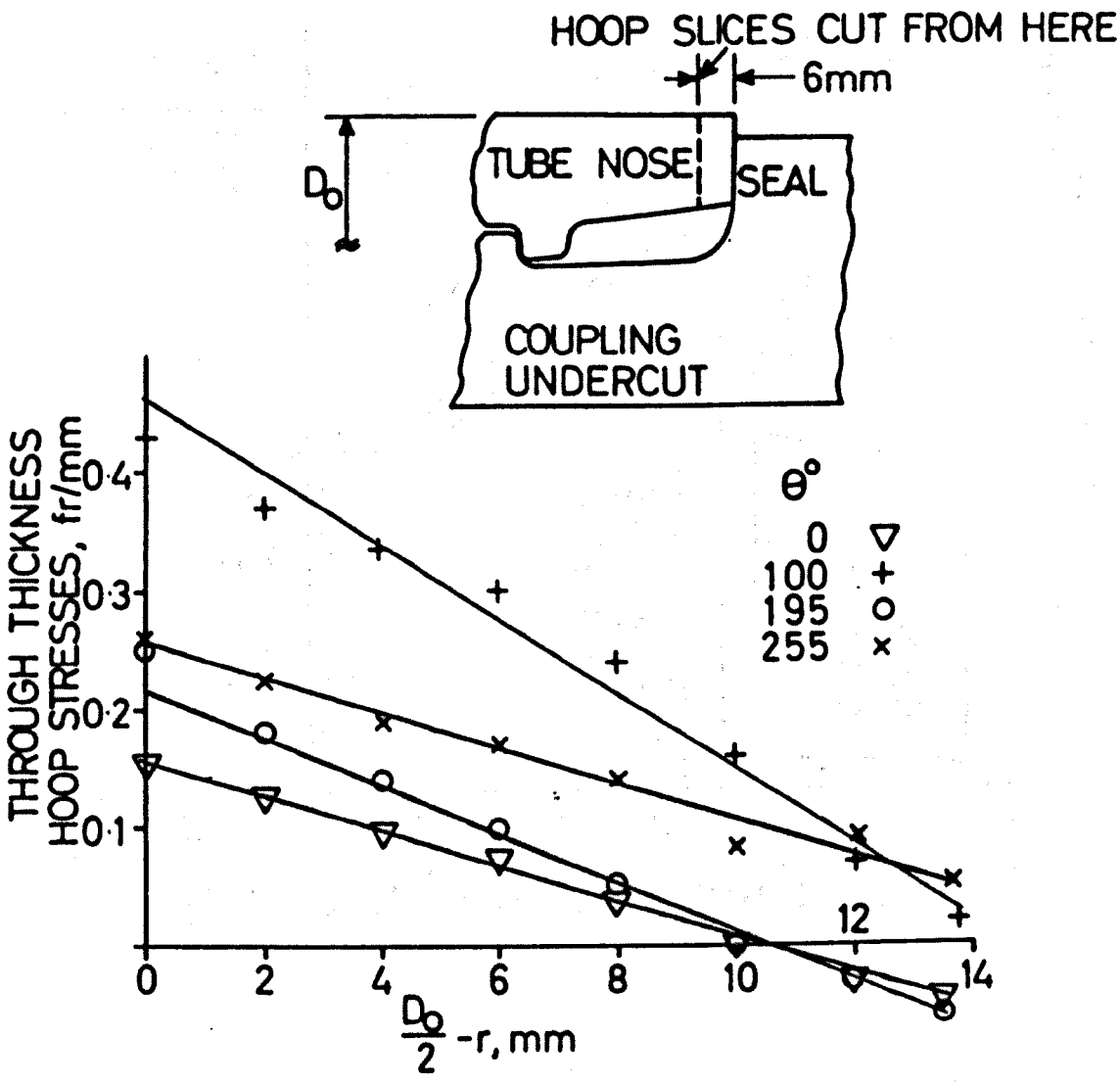

Fig 8.3.14a

Through Thickness Distributions of Hoop Stress in the Tube Nose of Model 9

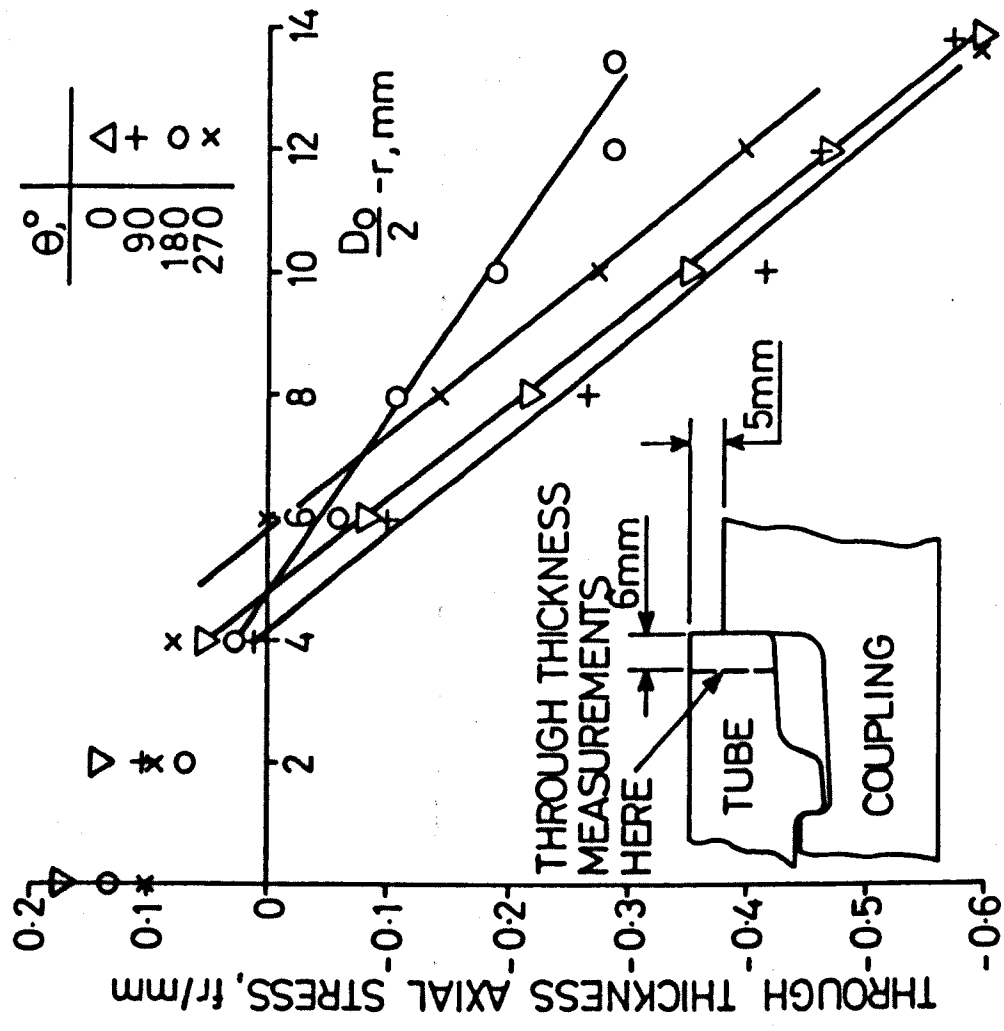

Fig 8.3.14b Through Thickness DIstributions of Axial Stress in the Tube Nose of Model 9

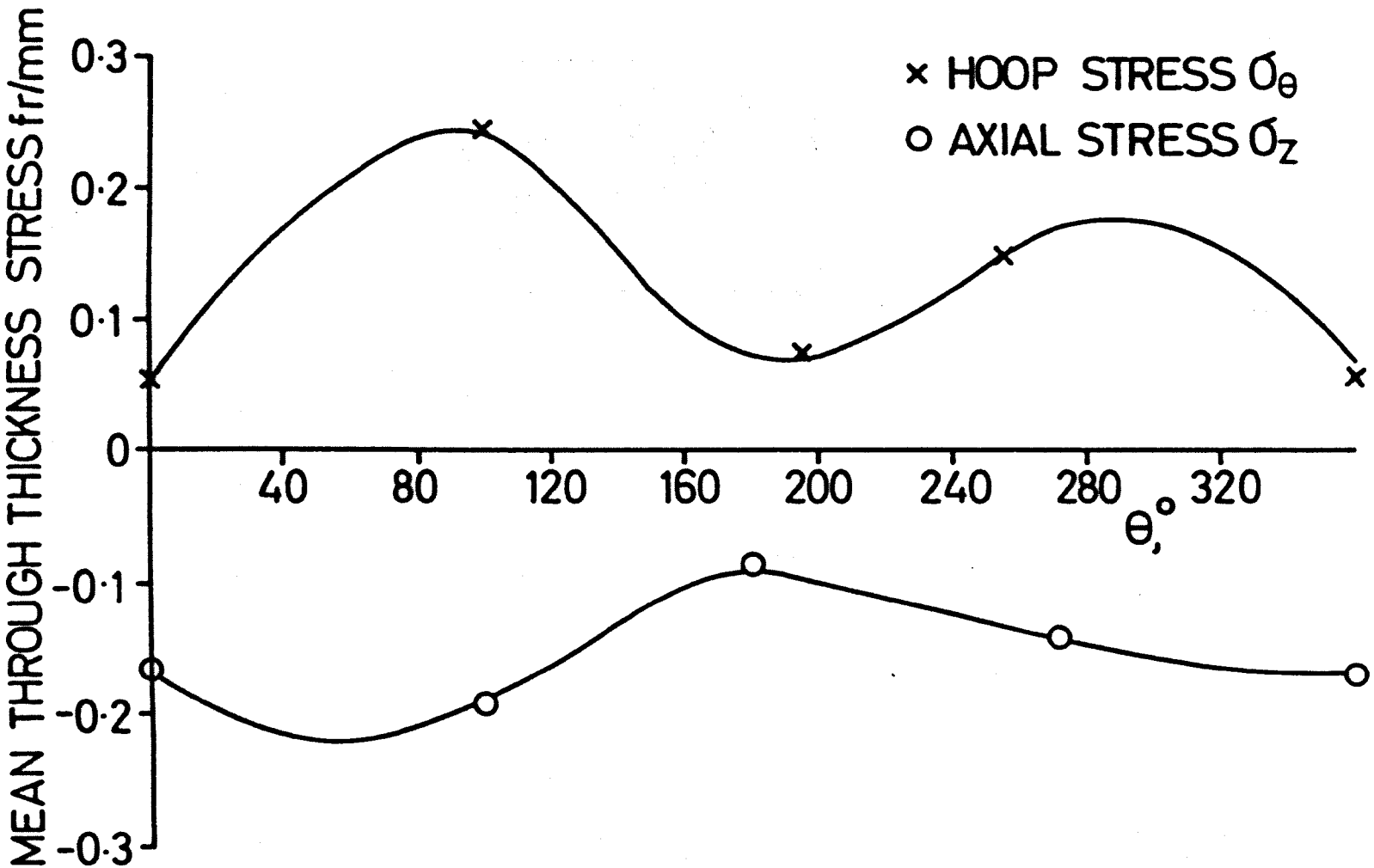

Fig 8.3.15

Mean Hoop and Axial Stresses in the Tube Nose of Model 9

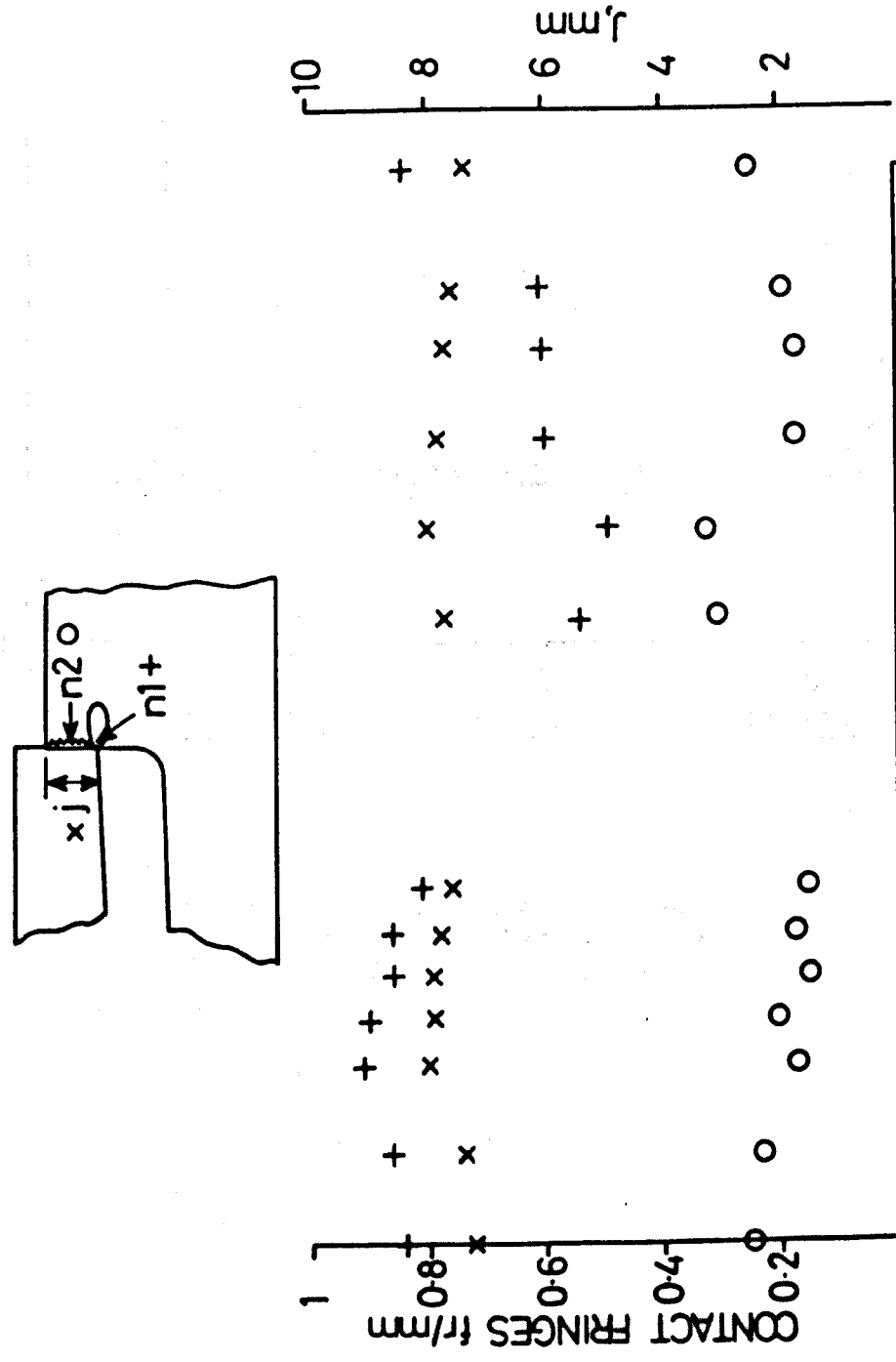

Fig 8.3.16 Contact Fringe Orders and Width of Contact in the Coupling Seal of Model 9

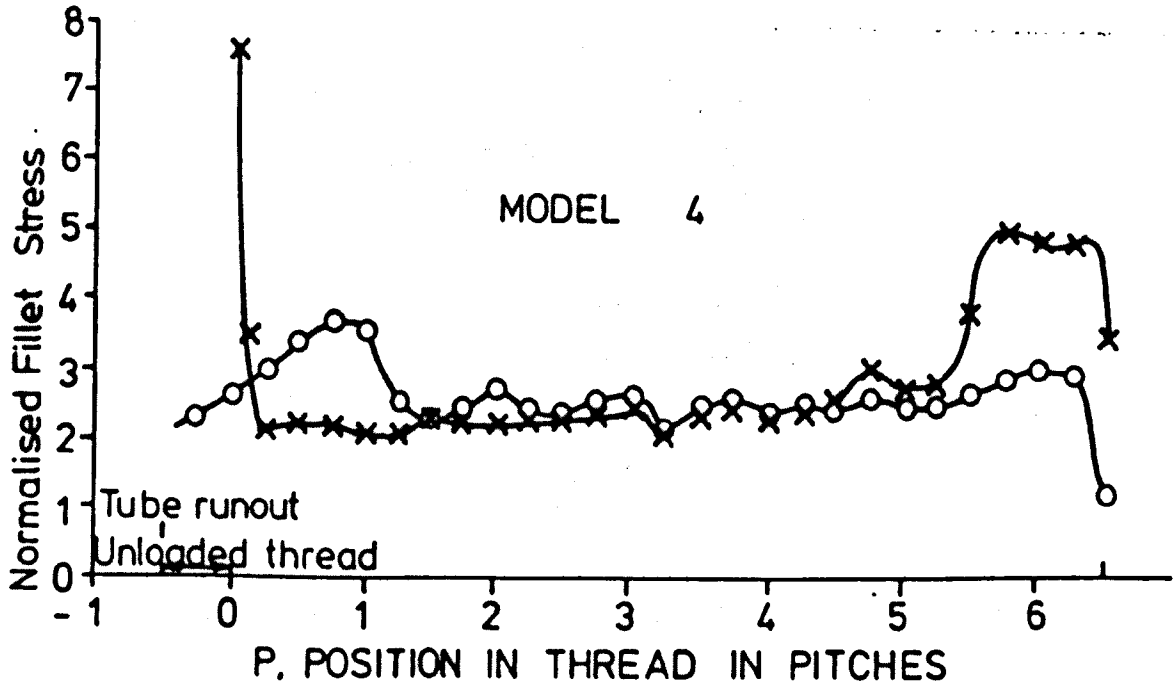

Fig 8.3.17

Normalised Peak Fillet Stress Distributions
In the Tension Plus Negative Preloaded
Model 4

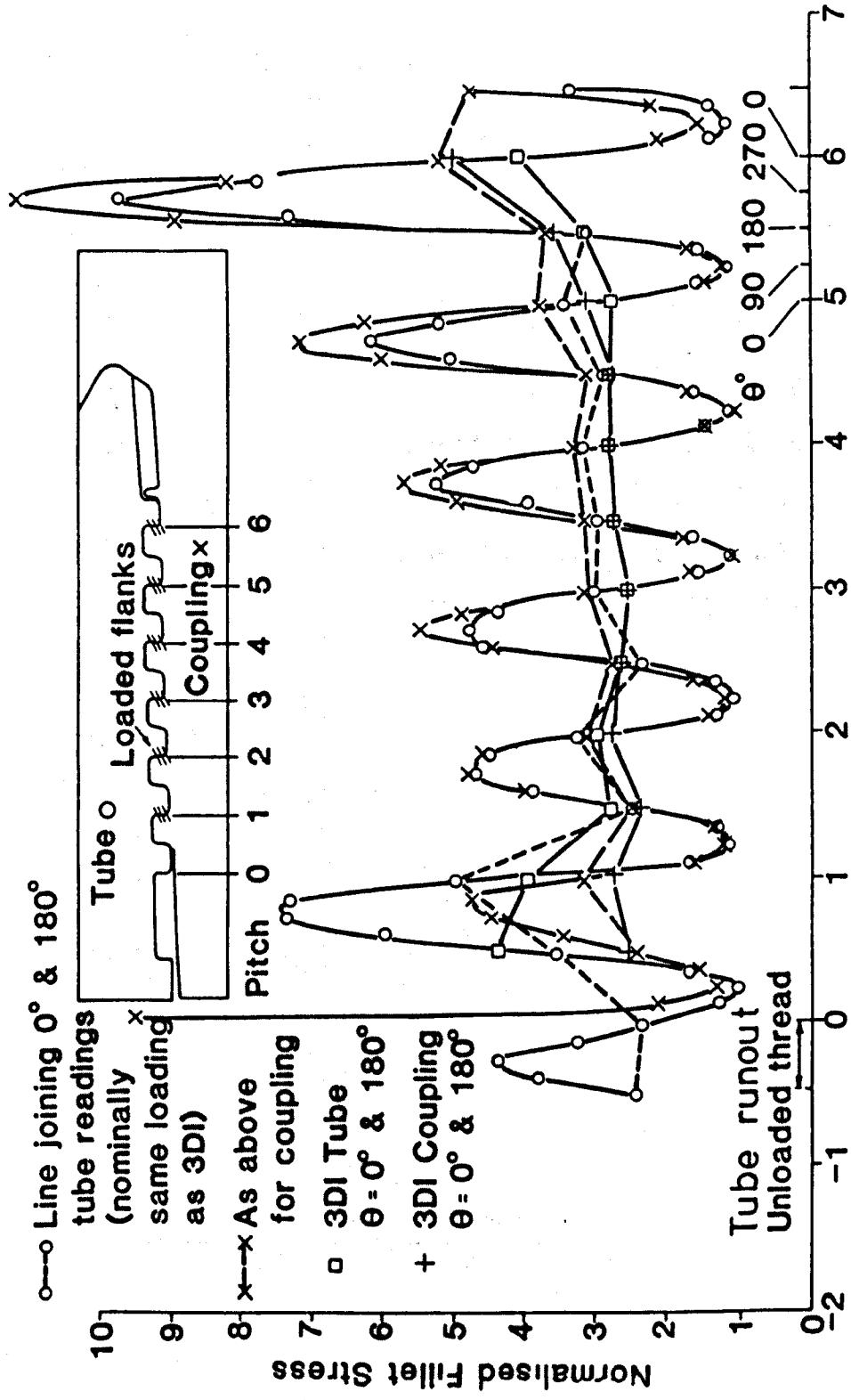

Fig 8.3.18 Normalised Peak Fillet Stress Distributions in the Eccentric Tension Loaded Model 2

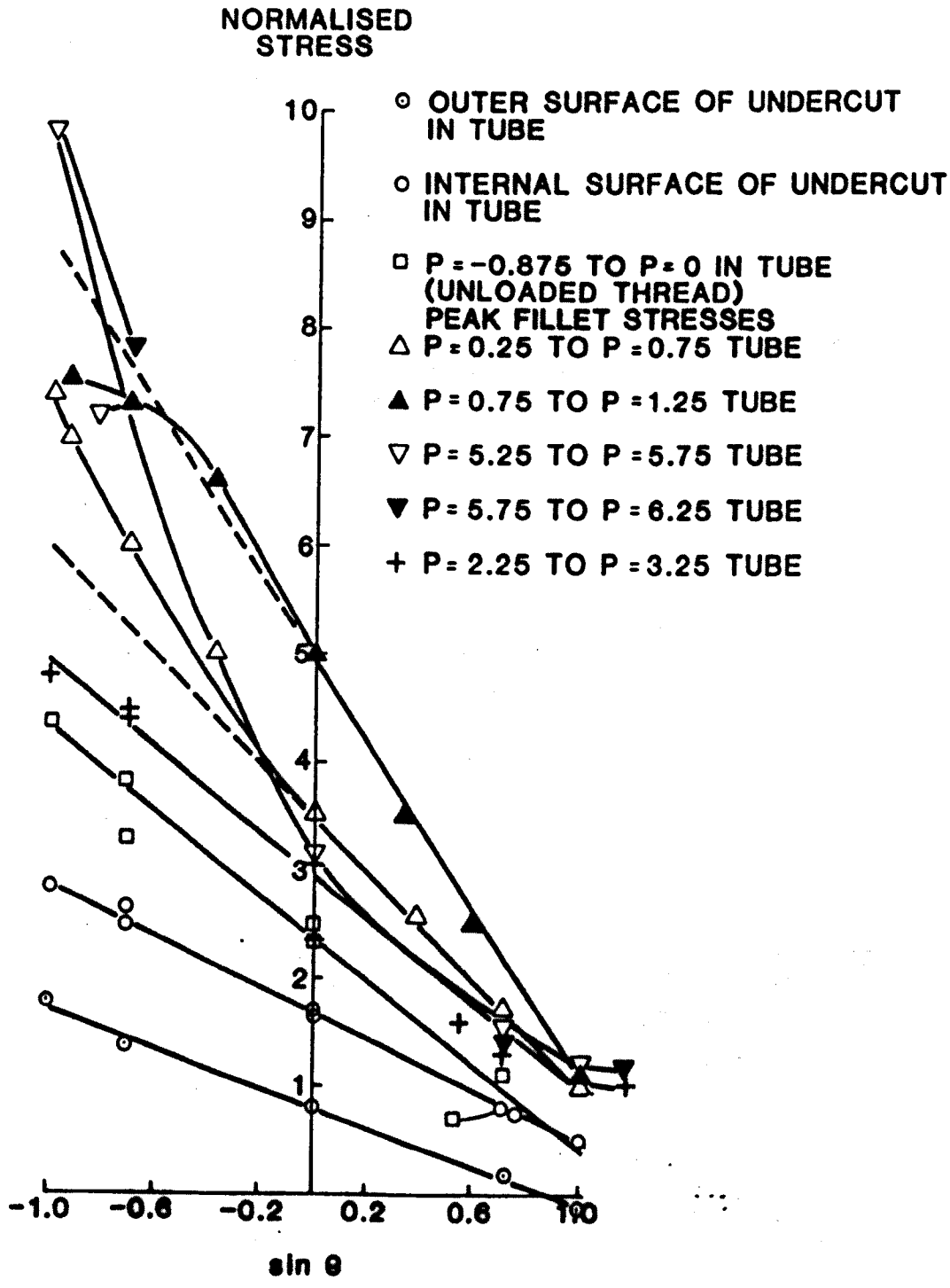

Fig 8.3.19

Normalised Stresses Distributions Plotted Against Sin θ
For the Eccentric Tension Loaded Model 2

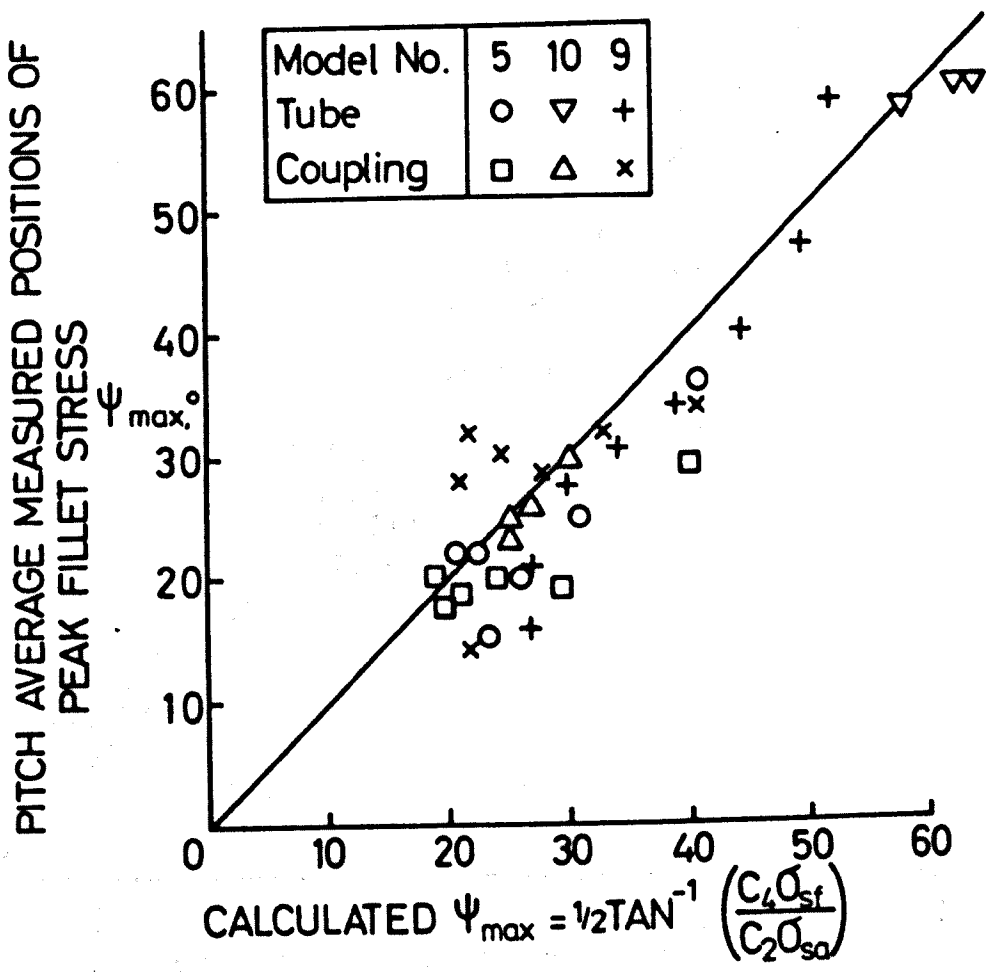

Fig 8.4.1

Measured Pitch Average Values of Position Of Peak Fillet Stress Compared with the Calculated Values

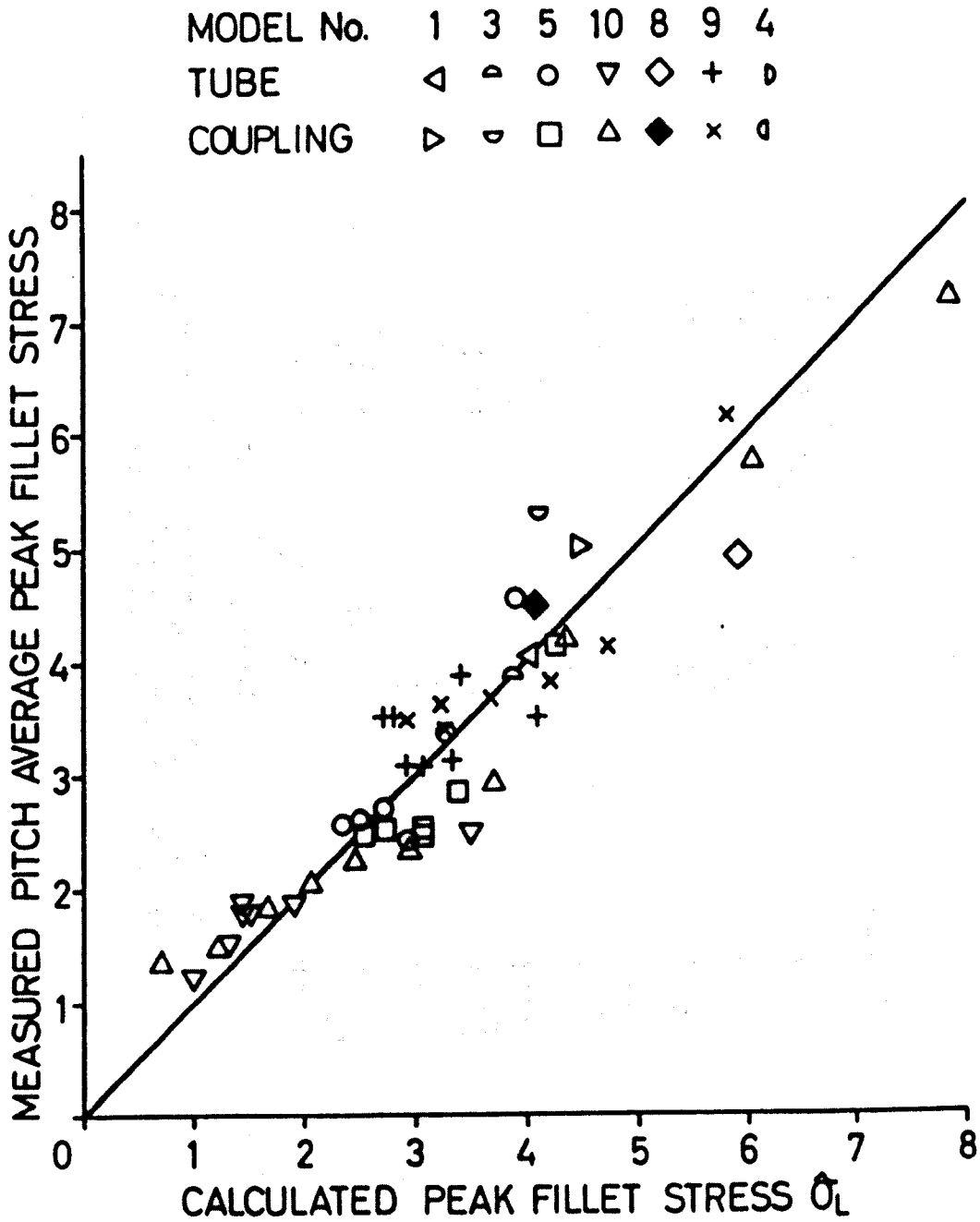

Fig 8.4.2

Measured Pitch Average Values of Peak Fillet Stress Compared with Calculated Values

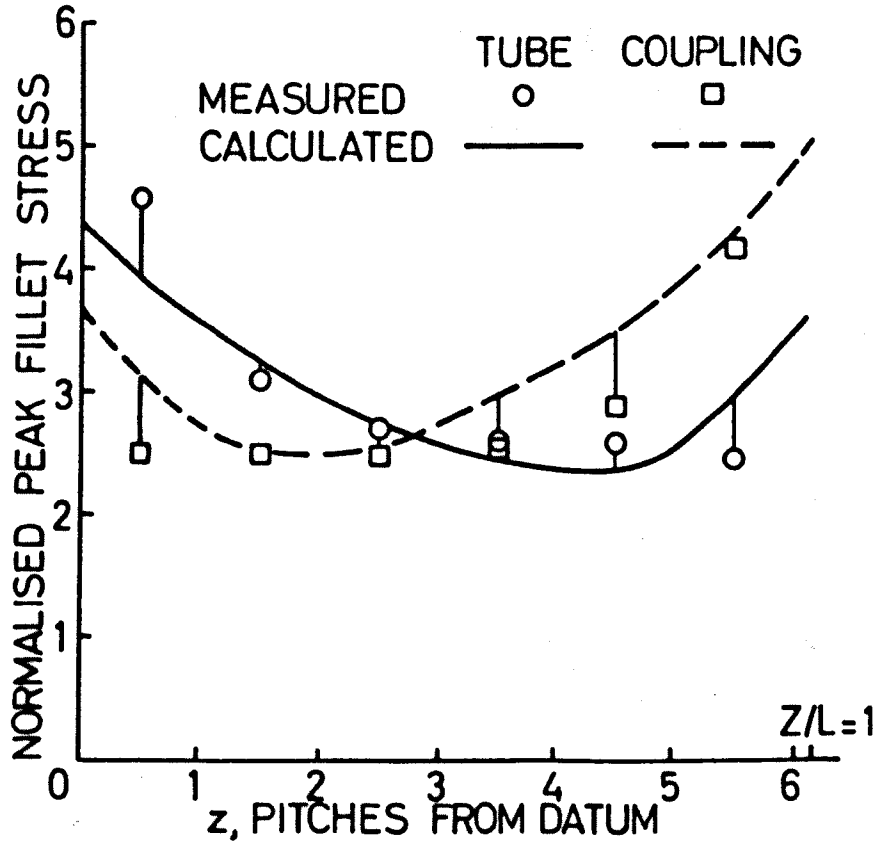

Fig 8.4.3

Measured and Calculated Pitch Average Peak Fillet Stresses in the Tensions Only Loaded Model 5

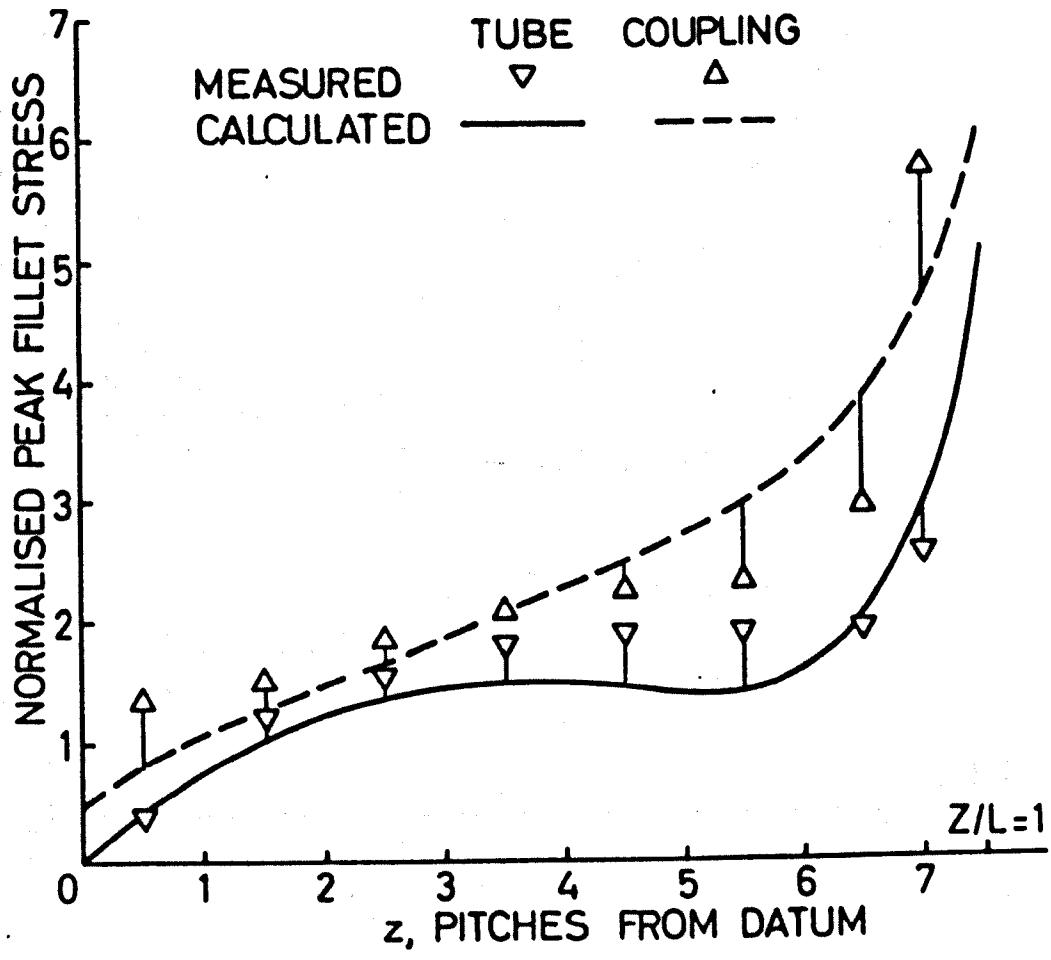

Fig 8.4.4

Measured and Calculated Pitch Average
Peak Fillet Stresses in the Preload Only
Loaded Model 10

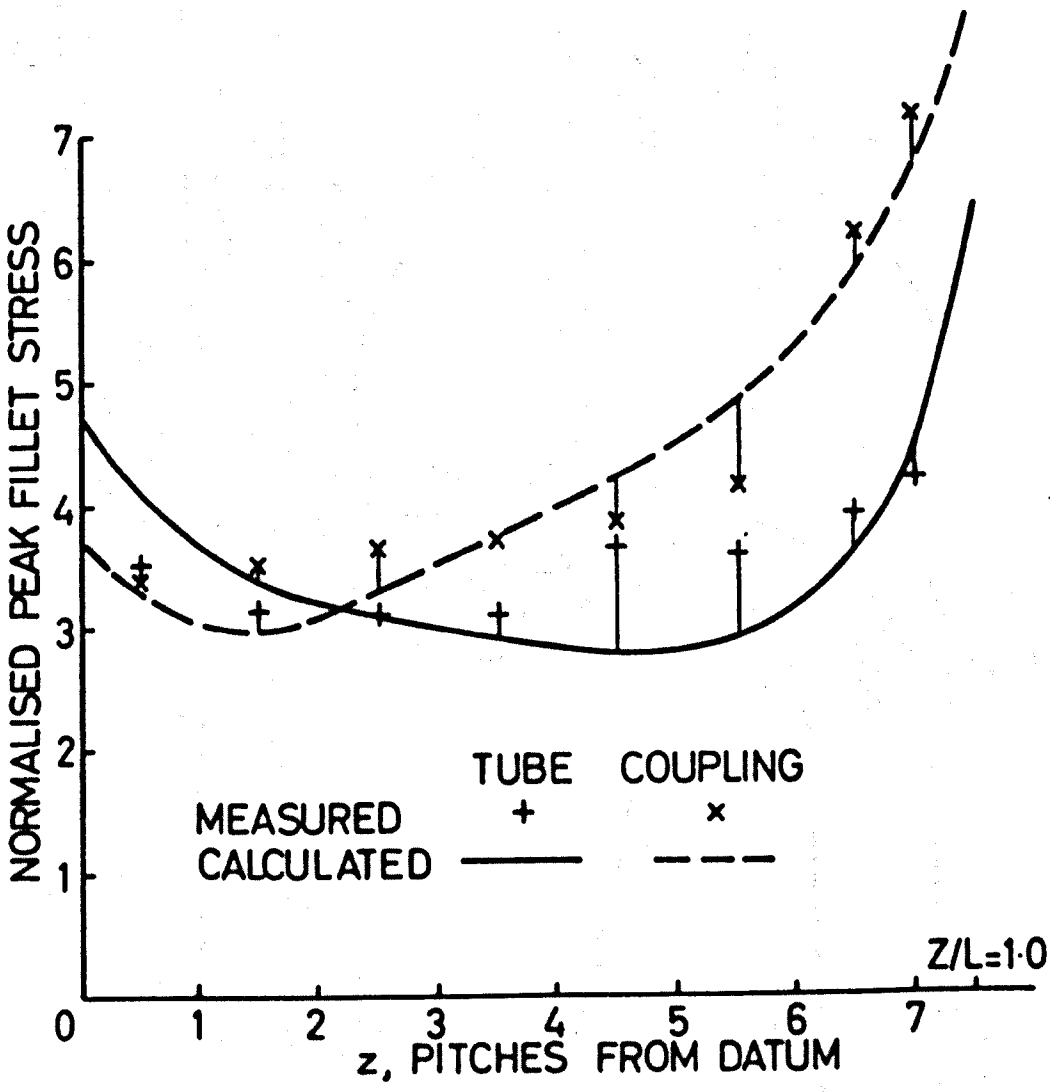

Fig 8.4.5

Measured and Calculated Pitch Average Peak Fillet Stresses in the Tension Plus Preloaded Model 9

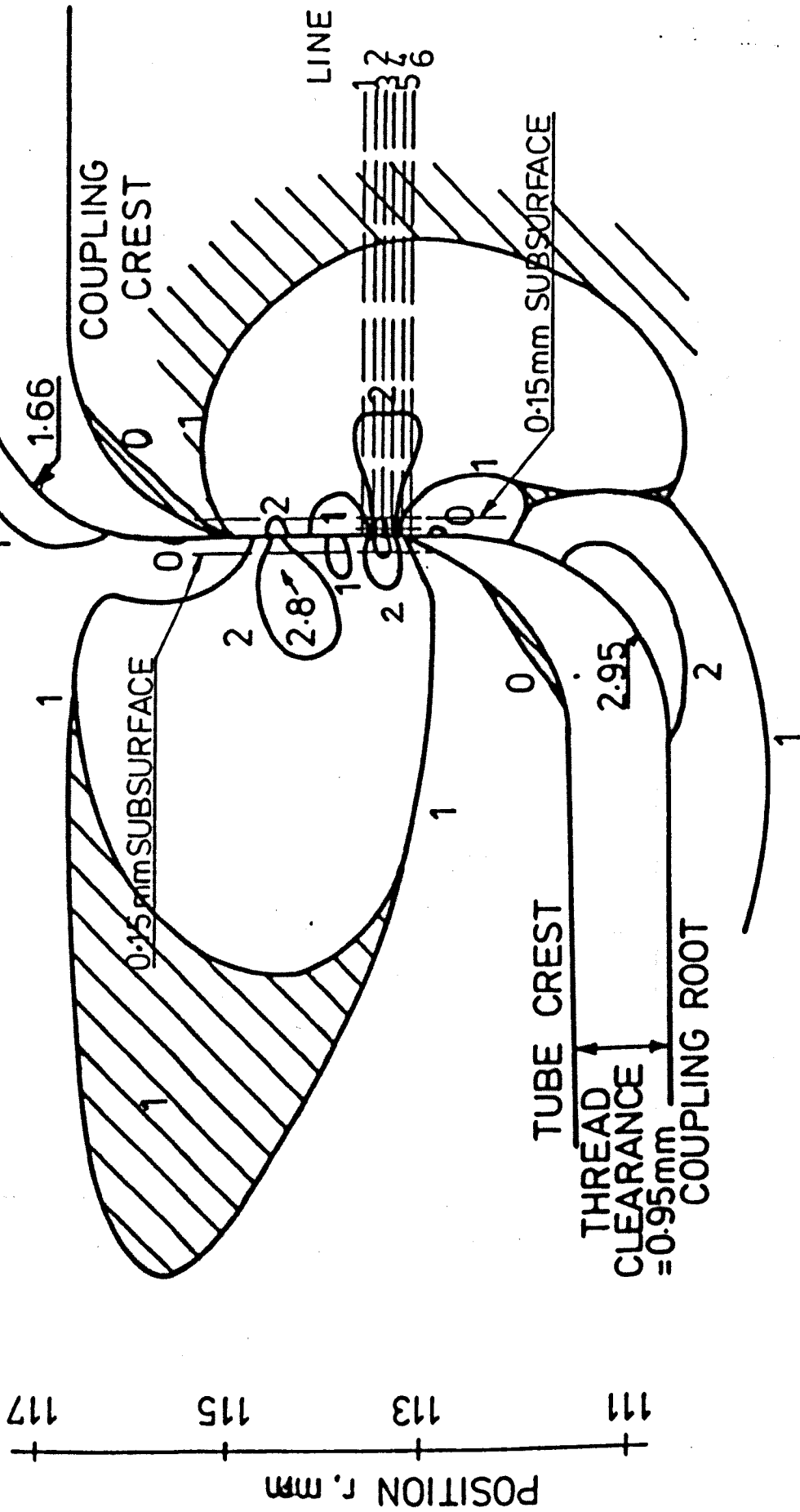

Fig 8.5.1 Sketch of Fringe Pattern in a Loaded Thread of Model 4. Slice Thickness = 1.9 mm
Numbers Refer to Fringe Orders

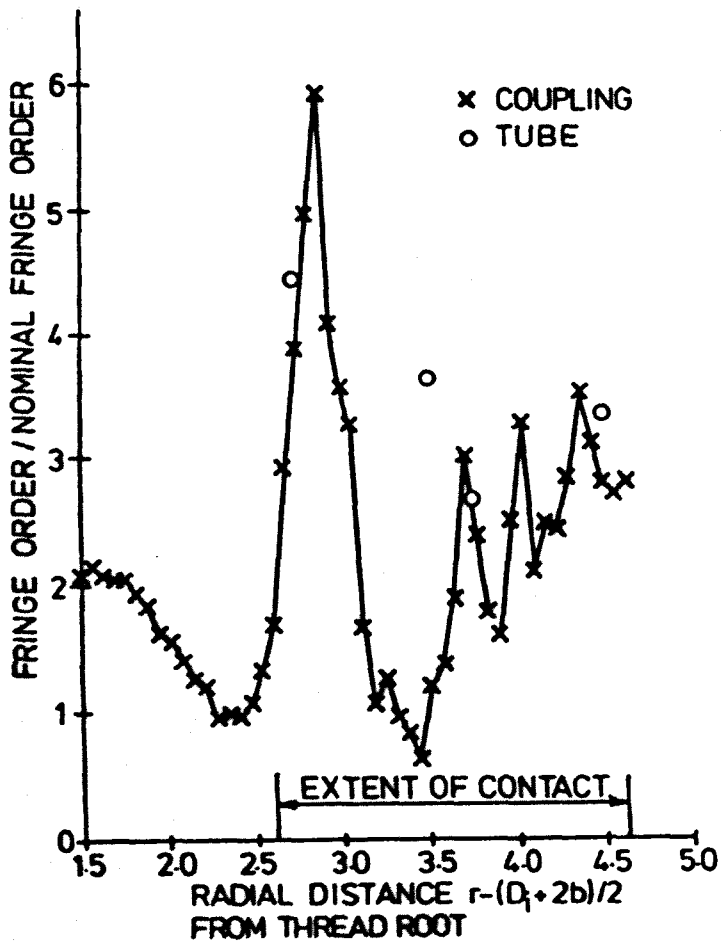

Fig 8.5.2 Distribution of Normalised Shear Stress Difference 0.15 mm Below Contact Surface of the 1.9 mm Thick Slice Measured Using the A.M.P.

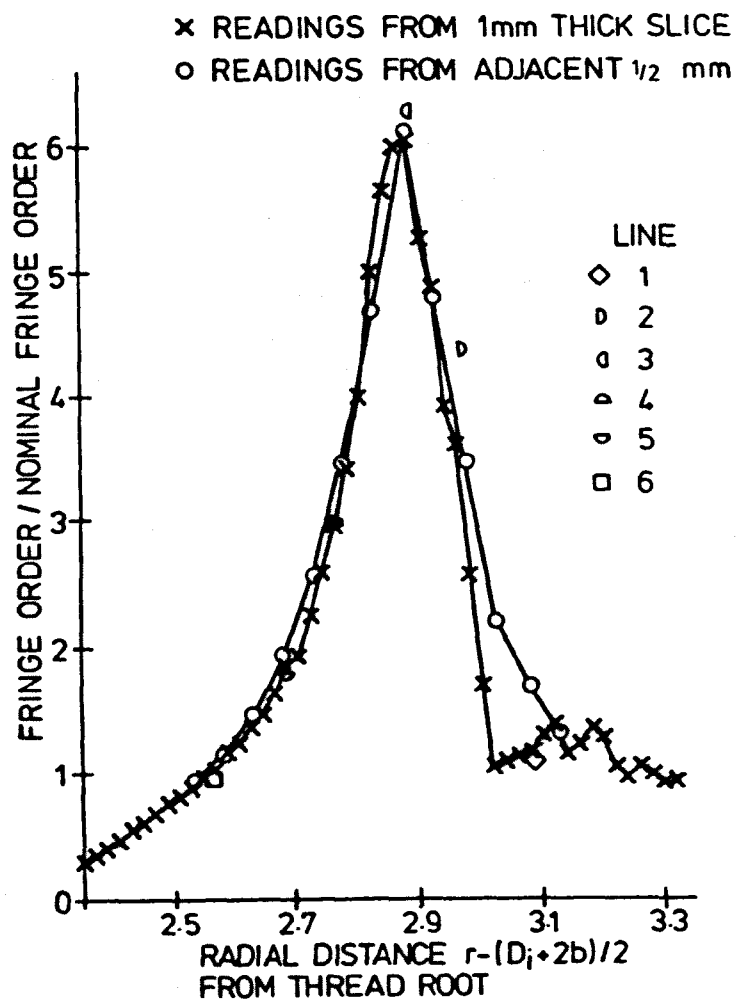

Fig 8.5.3 Distribution of Normalised Shear Stress Differences 0.05 mm Below Contact Surface In the Slice Cut From the 1.9 mm Slice Measured Using the A.M.P.

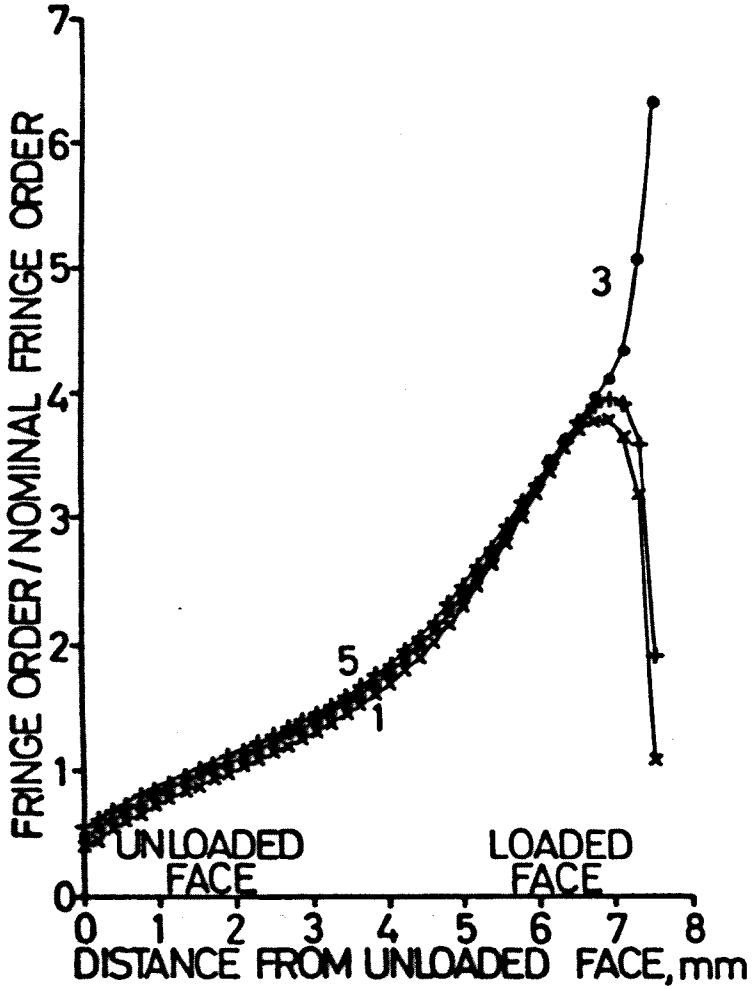

Fig 8.5.4 Distributions of Normalised Shear Stress Differences Perpendicular to the Contact Surface Along Lines 1,3 and 5 defined in Fig 8.5.1 & 8.5.3

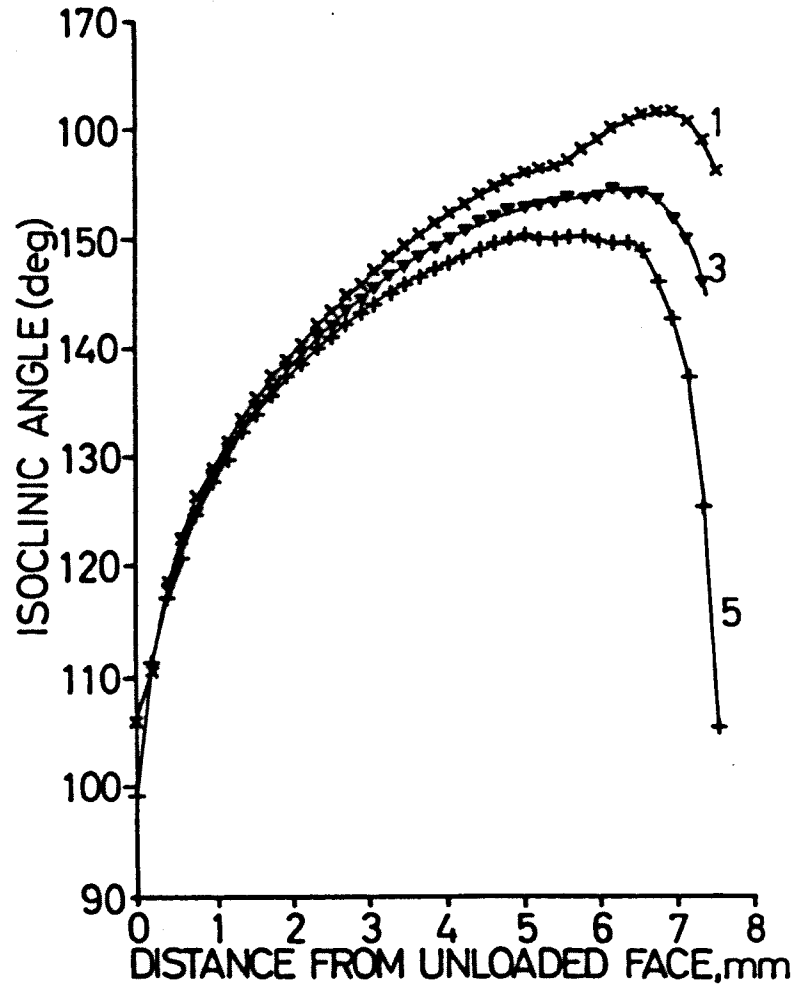

Fig 8.5.5 Distributions of Isoclinic Angle Perpendicular to the Contact Surface to the Contact Surface Along lines 1, 3 and 5 defined in Fig 8.5.1 & 8.5.3

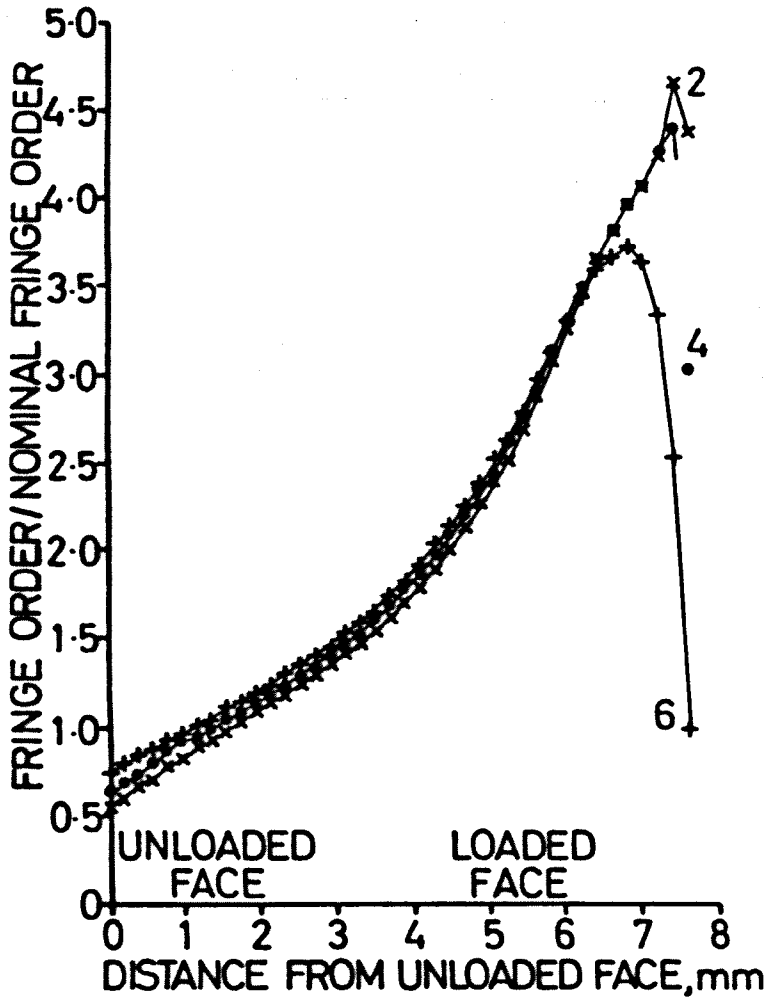

Fig 8.5.6 Distributions of Normalised Shear Stress Differences Perpendicular to the Contact Surface Along Lines 2, 4 and 6 Defined in Fig 8.5.1 & 8.5.3

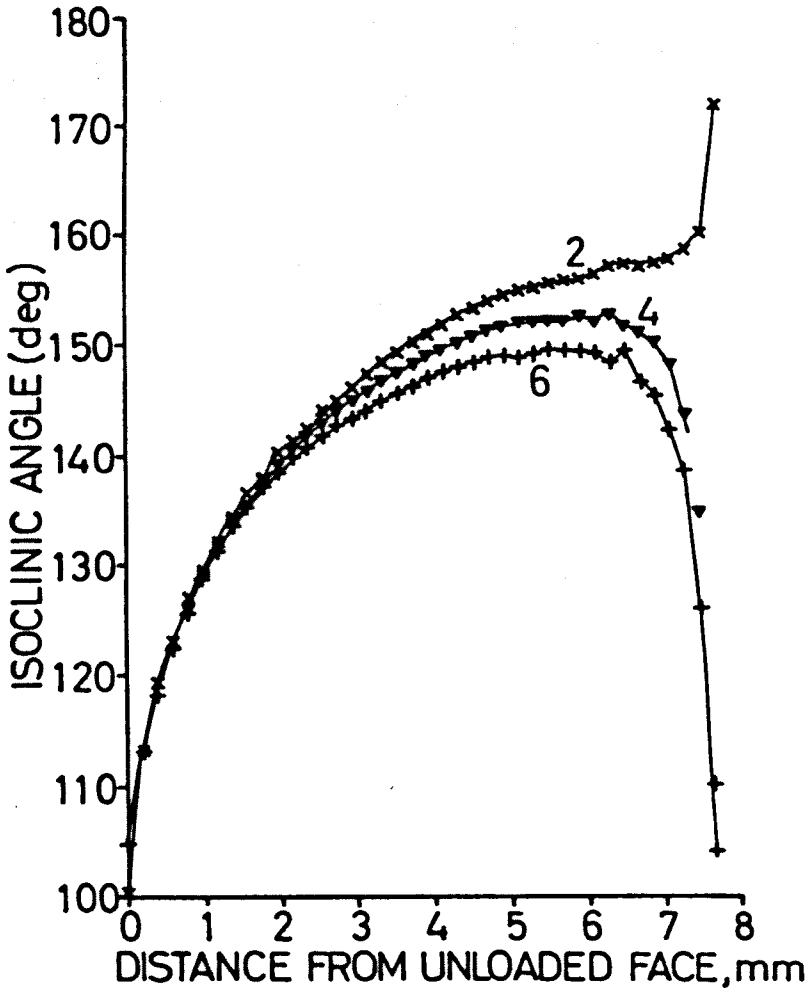

Fig. 8.5.7 Distributions of Isoclinic Angle Perpendicular to the Contact Surface Along Lines 2, 4 and 6 Defined in Fig 8.5.1 & 8.5.3

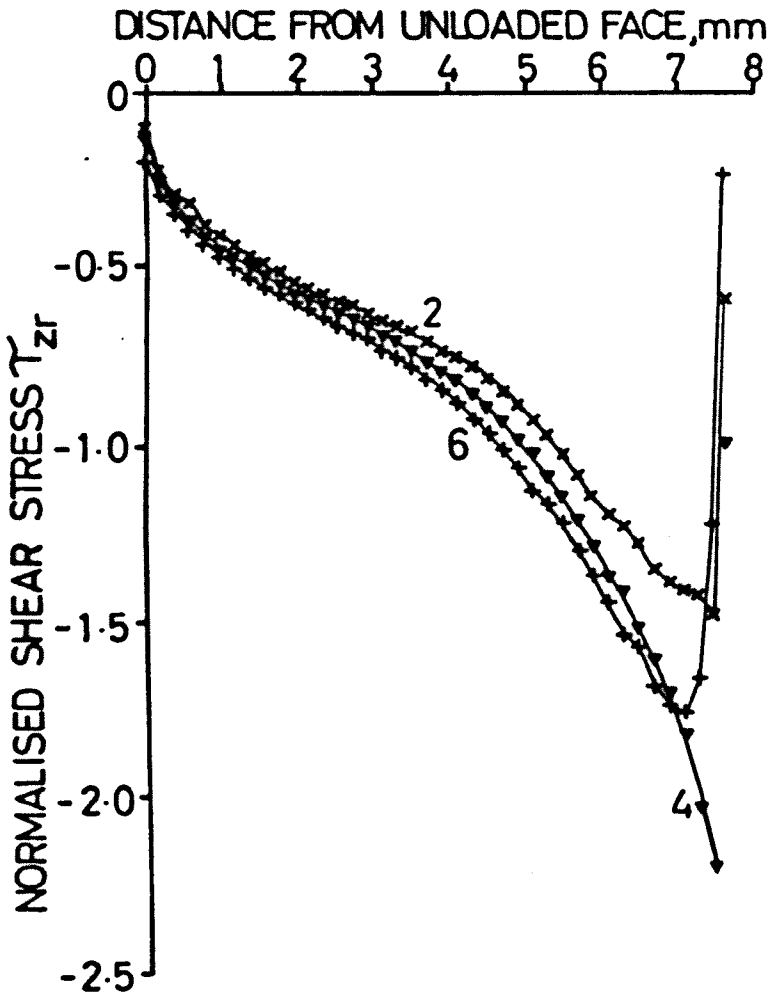

Fig 8.5.8 Distributions of Normalised Shear Stresses τ_{zr} Perpendicular to the Contact Surface Along lines 2, 4 and 6 Defined in Figs 8.5.1 & 8.5.3

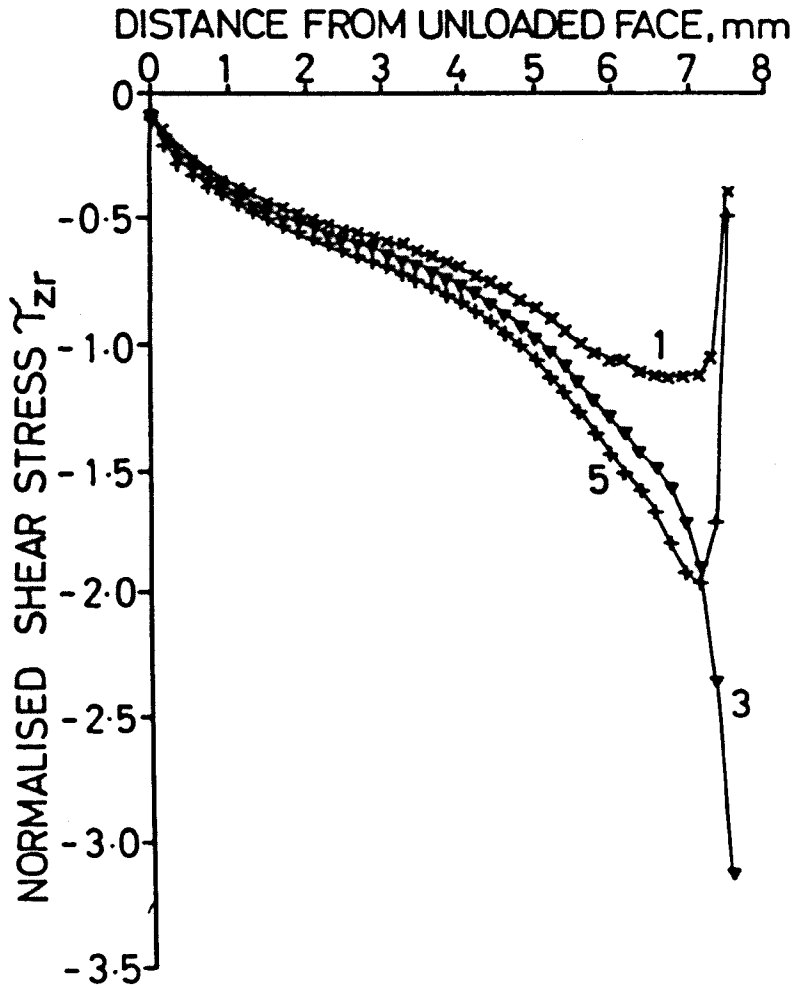

Fig 8.5.9 Distributions of Normalised Shear Stresses τ_{zr} Perpendicular to the Contact Surface Along Lines 1, 3 and 5 defined in Figs 8.5.1 & 8.5.3

CHAPTER NINE

DISCUSSION

9.1 Techniques

Originally, the experimental work was going to consist of a parametric analysis of the thread form using flat plate 2-dimensional photoelastic techniques. The best thread forms would then have been studied in thin-walled screwed connections using 3-dimensional photoelasticity. The effect on the fillet stresses of the loading modes of axial tension, preload, eccentric tension (bending plus tension) and pressure, both internal and external, would also have been investigated using 3-dimensional photoelastic techniques.

It soon became obvious that the lack of hoop restraint was giving much greater wall bending in the 2-dimensional models than would occur in a 3-dimensional joint. Also, accurate distributions of shear forces between several threads in contact could not be consistently reproduced in the 2-dimensional models due to the relatively large Young's Modulus of Araldite at room temperature, (approximately 250 x that of Araldite above the stress freezing temperature). Hence, the proportion of pitch errors to pitch strains was much larger in the 2-dimensional models than in the 3-dimensional models. Hence it was decided to carry out the parametric analysis using axisymmetric Finite Elements and to analyse more thread shapes using 3-dimensional photoelastic models.

Increasing the number of different thread shapes to be analysed reduced the number of 3-d models which were given over to the study of loading modes. Pressure was unlikely to affect the stress concentration and although external pressure acting on empty tubes will cause hoop compression and probably increase the Tresca and Von Mises effective stresses, it was decided not to investigate pressure loading.

Since axial tension is the most important load, comparisons between different thread shapes were generally carried out under axial tension loading only. The results of Model 2, which was loaded with a large eccentricity of tension indicated that generally there was a sinusoidal variation of peak fillet stresses and the magnitudes of the fillet stresses on the neutral axis of bending were similar to those in Model 1, which was a similar shape and loaded with axial tension only. Hence further analysis of bending became a low priority.

The attempt at reducing the peak fillet stresses in the most highly stressed threads of Models 6 and 7 by reducing the axial stiffness of the wall of the threads in contact with these highly stressed threads was not successful. Although the pitch-average peak fillet stresses of Model 6 were made no worse or even slightly better than Model 5, (which was identical apart from the reductions in wall area), local maximum peak fillet stresses were considerably greater than in Model 5. It was concluded that the reduction in area was too great for such a thin-walled tubular joint and no conclusions can be drawn as to whether the technique will be successful at redistributing shear forces in other, thicker-walled joints.

The method of manufacture of the models was dependent on the thread shape. Since the shape of the thread was changed in Models 1, 3 and 4, casting the thread regions precisely to shape would have been costlier and more time consuming than machining since new threaded moulds and cores would have to have been made for each model. But, once it was decided to limit analysis to the thread shape of Model 5, casting precisely became the most attractive option. The potential problems of extracting the castings from the moulds and cores were designed-out of the system and once the moulds and cores had been manufactured, then machining time and cost were reduced by about 90% and the model

turnaround time was also improved by several weeks.

The method of application of axial and eccentric tensions was simple and accurate as shown by the good agreement between the photoelastic measurements of load and the weighing of the applied loads.

Application of preload was by the same technique as used for applying preload to the Hutton platform tether connections (6) i.e. after screwing the connection together to a hand-tight position the connections were further tightened by a pre-set angular displacement. Due to the stick-slip nature of the relative movement of the models during preload application, the magnitudes of the applied preloads were not easy to control and were as much as 20% greater than the designated preloads. This did not cause problems in comparing different preloaded models since the preloads were always measured photoelastically. Variation in the degree of lubrication and the coefficient of friction meant that the torque loads, T, required to produce the same preload, were different from model to model.

From Chapter 7 it can be seen that the likely variations in preload around the seal due to incorrect positioning of the torque loads were $\pm$3.5%. This variation was not considered serious and the variations in preload are unlikely to have produced the variations in shear forces and peak fillet stresses which were observed in the models loaded with preload and outlined in Section 8.3.

The differences between the photoelastically measured axial tensions and those measured by weighing the applied loads were $\pm$2.3%. Also, the average standard deviation of axial tension at any section from the mean undercut tension was 5.4% for all the tube and coupling models loaded with axial tension only. A similar value was obtained for the tube models loaded with axial tension and preload.

The use of the Automatic Micropolariscope (AMP) has been extended

by the author beyond that of Marston (34). The AMP has shown itself to be flexible and an invaluable tool in the analysis of complicated 2 and 3-dimensional stress fields. The degree of accuracy of the measurements taken using the AMP is so good that the major errors are in measuring slice thickness and other practical considerations such as moisture effects and material inhomogeneity. But, for all its simplicity of operation there are still instances when manual photoelastic readings are preferable to using the AMP. The most obvious instance is measuring a peak surface stress when the position of the peak stress in the slice is relatively unimportant and due to the time required to set up the slice and AMP, manual measurements can be made much more quickly and with only small reductions in accuracy.

Using axisymmetric Finite Elements to analyse the effect of thread shape changes on thread fillet stresses had several advantages over the other possible analysis techniques. Once the basic mesh had been created, changing the parameters b, w, h and e was relatively simple. In most cases it meant just adding on or taking off rows of elements. In all the meshes the size of R and the density of elements around the fillet was kept constant. Hoop restraint was defined by the symmetry of the mesh about the centre line. Only one thread was modelled in each mesh since the highest fillet stresss in the 3-dimensional models analysed photoelastically was in the threads adjacent to the model undercuts. Using the equations developed from these single thread Finite Element mesh results, the fillet stresses in threads in both the central region of the thread spiral and at the ends of contact could be predicted with similar accuracy. This indicates that the threads in the Finite Element meshes would not have been greatly affected if other threads had been modelled in the meshes.

If time had allowed other parameters such as the thread face angles

α and β and the cone angle γ could have been investigated. But the results obtained could not have been verified since these parameters, which were considered to have been of secondary importance, were not investigated using 3-dimensional photoelasticity.

9.2 Presentation of Results

The shear force distributions in Models 5 and 9-10 are very similiar when plotted against non-dimensional distance along the thread spiral, z/L. This is despite Model 9-10 having 1.25 times the number of engaged pitches than Model 5 and w/b and R/b of Model 5 being 1.35 times that of Model 9-10. This indicates that length of engagement, pitch and fillet radius have negligible effect on shear force distributions in models loaded with tension, with large pitch/wall thickness ratios and with relatively few pitches in contact. With hindsight a shear force distribution for a model with different shape to Model 10 would have been useful to confirm that the same can be said for models with preload. Model 7 was not analysed because of the problems associated with the grooves which were machined in that model.

The equations developed in Section 8.1 accurately described the measured pitch-average shear force distributions between z = p/2 and z = L-p/2 for both preload and tension. The actual shear force measurements can be seen as systematic variations superimposed upon the smooth curves, see Figure 8.1.1, 8.1.2, 8.1.3 and 8.1.6. For tension loading, these systematic variations were small unless a loaded coupling runout was present. Measurements of shear forces in the loaded coupling runouts of Models 3 and 4 (see Fig. 8.1.15), show the reduction in shear force carried as the coupling thread flexibility increases. This type of runout, although not normal in screwed tubular joints, would entail less machining and reduced assembly time than the runout of the VAM joint (5) in which the threads run out on the cone angle over several

pitches. For example, this type of runout would have extended over 7 pitches for Models 5 to 10. The reductions in shear forces in the loaded runout were beneficial to the fillet stresses of the threads in contact with the runout. If the runout is truncated properly, i.e. the region of runout with the smallest thread width is removed, say from w = 0 to w ≃ p/8 then significant reductions in shear force and hence peak fillet stresses could be achieved in the most highly stressed pitch of the tube model. There is no practical reason why the tube thread should not runout in a similar manner at the other end of the thread spiral, hence reducing the peak coupling fillet stresses which are in contact with a tube runout.

At the preloaded end of a thread spiral, the differences between the measured shear forces and the best fit curve through the pitch-average values were greater than for tension loading only for reasons which are not fully understood, see Section 8.3. The measured maximum shear force and peak fillet stress occurred 90° from the end of the spiral and, as can be seen from Table 9.1.1, were considerably greater than the pitch-average values. Calculated maximum values of shear force and peak fillet stress have been obtained at the end of the thread spiral (at z = L) and compared with the calculated values at z = L-p/2, which are equivalent to the pitch-average values. It can be seen from Table 9.1.1 that the calculated maximum/pitch-average shear force is greater than that measured for all three loading modes. Also the calculated Maximum fillet stress/pitch-average fillet stress is within 8% of the measured value.

Table 9.1.1 Comparison of Measured and Calculated Peak/Pitch-Average Shear Forces and Maximum Fillet Stresses in the Last Pitch

Model	Loading	Maximum Pitch Average			
		Shear Force		Fillet Stress	
		Measured	Calculated	Measured	Calculated
5C	Tension	1.08	1.32	1.17	1.26
10C	Preload	1.23	1.46	1.58	1.46
9C	Tension & Preload	1.16	1.38	1.20	1.28

The terms in the equation for the shear forces, wall forces and the coefficients C_1 to C_4 have all been obtained using manual rather than automatic curve fitting techniques. This is because the manual techniques gave good agreement between simple functions of the expected parameters and the observed data. Any improvements in the accuracy of equations obtained by computer optimisation would have been slight. Only for the coefficients C_3 and C_4 did the functions become more complex and it is doubtful whether better agreement could have been obtained between the calculated fillet stresses and the measured pitch-average fillet stresses. The equations for the shear force distributions could possibly have been modified to show the observed variations from the pitch-average values. A possible modification would have been a Taylor series in terms of θ, multiplying the pitch-average shear forces, but this would have led to complicated and cumbersome equations, particularly for threads loaded with tension and preload.

It can be seen from Section 8.4 that the Equations developed in Sections 8.1 and 8.2 can be used with equal accuracy in regions of the tube models where the wall forces were compressive.

9.3 Effect of Parameter Changes on Peak Calculated Fillet Stresses

Introduction

The peak fillet stresses in the pitch nearest the preloaded end of the thread spiral have been calculated for shapes similar to coupling models and loaded with preload and tension using the equations developed in Chapter 8. This position was chosen because the maximum peak fillet stresses in a screwed connection are likely to occur there. The loading ratio, Q/F = 0.55, was the same for each shape investigated and equal to the Model 9 ratio. The tube dimensions D_o and t were kept constant for each shape at the Model 9 values, so that the nominal stress σ_{nom} was constant and hence direct comparisons could be made between the shapes investigated.

It was very difficult if not impossible to differentiate the equations for the peak fillet stresses with respect to the thread parameter considered, hence optimum values of thread parameters could not be obtained mathematically. Indeed, zero gradients of peak fillet stress with respect to thread parameter may not even exist. Hence the important parameters of fillet radius R, thread width w = p/2, number of pitches in contact N, axial length of engagement L and coupling wall thickness b were all varied indpendently and the peak fillet stresses calculated. The shapes investigated are shown in Table 9.3.1. For all the shapes considered, the constraints of $R < p/4$ and $e \geq R$ were observed. Although the axial length of engagement L is not an independent parameter since L = N.p, it is important since the non-dimensional position in the thread spiral = z/L and both the loads of shear force V and wall force W are functions of z/L.

Table 9.3.1 Thread Shapes and Coupling Sizes for which Coupling Peak Fillet Stresses have been calculated (See Fig N3 for definitions of Parameters)

SHAPE	R, mm	e, mm	p/2, mm	Number of Pitches, N	L, mm	b, mm	Di, mm	Calculated peak fille stresses σ_L
1 (1)	2.50	2.50	7.9	7.5	119	20.00	176	7.14
2	1.35	2.50	7.9	7.5	119	20.00	176	9.81
3 (2)	0.66	2.50	7.9	7.5	119	20.00	176	14.10
4	3.95	3.95	7.9	7.5	119	18.55	176	6.66
5	2.50	3.95	7.9	7.5	119	18.55	176	8.01
6	1.35	3.95	7.9	7.5	119	18.55	176	10.60
7	0.66	3.95	7.9	7.5	119	18.55	176	15.15
8	2.50	2.50	5.0	7.5	75	20.00	176	8.15
9	2.50	2.50	12.5	7.5	188	20.00	176	6.08
10	2.50	2.50	17.0	7.5	255	20.00	176	5.84
11	0.66	2.50	5.0	7.5	75	20.00	176	17.19
12	0.66	2.50	12.5	7.5	188	20.00	176	10.86
13	0.66	2.50	17.0	7.5	255	20.00	176	10.01
14	2.50	2.50	5.0	11.9	119	20.00	176	6.00
15	2.50	2.50	12.5	4.8	119	20.00	176	7.10
16	0.66	2.50	1.32	45.1	119	20.00	176	17.19
17	0.66	2.50	2.50	23.8	395	20.00	176	12.64
18	0.66	2.50	5.00	11.9	119	20.00	176	13.40
19	0.66	2.50	12.50	4.8	119	20.00	176	14.21
20	2.50	2.50	7.9	4.8	76	20.00	176	8.23
21	2.50	2.50	7.9	12.5	198	20.00	176	6.09
22	2.50	2.50	7.9	25.0	395	20.00	176	5.10
23	0.66	2.50	7.9	4.8	76	20.00	176	18.41
24	0.66	2.50	7.9	12.5	198	20.00	176	11.64
25	0.66	2.50	7.9	25.0	295	20.00	176	8.38

Table 9.3.1 Continued

SHAPE	R, mm	e, mm	p/2, mm	Number of Pitches, N	L, mm	b, mm	Di, mm	Calculated Peak Fille Stress σ_L
26	2.50	2.50	7.9	7.5	119	15	186	8.40
27	2.50	2.50	7.9	7.5	119	30	156	6.60
28	2.50	2.50	7.9	7.5	119	40	136	6.68
29	2.50	2.50	7.9	7.5	119	50	116	7.15
30	0.66	2.50	7.9	7.5	119	15	186	15.12
31	0.66	2.50	7.9	7.5	119	30	156	14.49
32	0.66	2.50	7.9	7.5	119	40	136	15.77
33	0.66	2.50	7.9	7.5	119	50	116	19.21

Notes:-

(1) Shape of Model 9 coupling thread nearest the preloaded end

(2) Shape of an API buttress thread

For all but shapes 25 to 32, b values were equal for both tube and coupling.

The calculated peak fillet stress in Model 9 was almost identical to the measured pitch-average peak fillet stress and the Model 9 shape of thread has been used as the basis for comparison with other snapes.

The parameter e has been used rather than the thread height h, since the equation for C_3 has a term of e/b in it. But for the purpose of this investigation it is assumed that e = h/2. e was not varied independently of the other parameters because its effect on peak fillet stress would have been small compared with that of the other parameters.

Effect of Fillet Radius

The effect of fillet radius was investigated for 2 different e/p ratios with shapes 1 to 7 shown in Table 9.3.1. Increasing e over the Model 9 value allowed a larger radius to be defined but it did reduce the wall thickness b, since b = t-h, where h = 2e. 2e/p = 0.31 was chosen since both the API thread and Model 9 have values of 2e/p = 0.31. The fillet radius was increased from the small API value to the maximum allowable Model 9 value of R = e, see shapes 1 to 3. An increased value of 2e/p = 0.50 was also investigated, so that a larger value of R at R = e could be analysed, see shapes 4 to 7. This value of e/p was chosen since R=e = p/4 which is the maximum allowable. Four values of R were investigated for 2e/p = 0.5 and they are defined in Table 9.3.1.

The calculated peak fillet stresses for the 2 sets of 2e/p values are shown on Fig 9.3.1. As expected, increasing R reduces the peak fillet stresses. It can also be seen that the reductions in b caused by the increased value of e, increases the fillet stresses for a given value of R, e.g. compare shapes 1 and 5. This increase in peak fillet stress is due to the increased wall stress σ_{sa} and bending stress σ_{sf} which both have inverse relationships with b, see Section 8.1 and Appendix 6.

Effect of Pitch, Number of Pitches and Length of Engagement

Because L = N.p all three parameters have been investigated in turn with one of the three parameters constant at the Model 9 value while the other two were altered.

The effect of keeping N constant and altering p/2 and L was investigated with shapes 1, 3 and 8 to 13 for two different values of R, which were those of Model 9 and the API shape. Four different pitches were investigated for each value of R and the calculated peak fillet

stresses plotted on Fig. 9.3.2 against both pitch p and p/b. From this figure it can be seen that increasing p/b generally reduced the calculated peak fillet stresses. This is because, as w/b increases, the reductions in σ_L due to reductions in C_3 and C_4 are greater than increases in σ_a due to increases in C_1, see Section 8.2. For the larger value of R/b, the reductions in peak fillet stress as w/b increased were less marked than for the thread shapes with the smaller R/b value. Finally, reductions in peak fillet stress were small for increases in p/b over 1.2. But values of p/b as large as 1.2 are unlikely to be made.

The effect of keeping pitch constant and increasing N, the number of pitches in contact, was examined for the Model 9 and API values of R defined earlier. N was increased from the very small value of N=4.8 to N=25. The shapes are defined in Table 9.3.1 and referred to as shapes 1, 3 and 20 to 25. The peak fillet stresses have been plotted against N on Fig. 9.3.3. It can be seen that increasing N reduces the fillet stresses and that for the larger value of R, these reductions in fillet stresses are less pronounced. Also, as N becomes large, further increases in N give a relatively small reduction in peak fillet stress. The peak fillet stresses reduce as N increases because the shear forces per unit length of thread spiral reduces as the spiral length of engaged thread increases.

The effect of keeping the axial length of engagement L constant and altering p and N was investigated with shapes 1, 3 and 14 to 19. Again, the same two values of R were analysed. For each value of R, pitch was varied from the minimum value of p = 4R to the large value of p for which N=4.8. The calculated peak fillet stresses have been plotted against p and p/b on Fig. 9.3.4. Also shown on this figure is the line of calculated peak fillet stresses for p = 4R. For the shapes with

large radius it can be seen that the calculated peak fillet stress reduced as pitch reduced and tended to a minimum value at p = 4R which was equivalent to p/b = 0.5.

For the shapes with the smaller API radius, a slight reduction in calculated peak fillet stress occurred as pitch reduced from the maximum. The minimum peak fillet stress occurred near p/b = 0.5. If pitch was reduced further, the fillet stresses increased rapidly until p = 4R.

There are two conflicting effects as pitch reduces and the number of threads in contact increases:-

i) due to reductions in w/b, increases in C_3 and C_4 tend to increase the fillet stresses, this can be seen on Fig. 9.3.2.

ii) due to increases in the spiral length of thread contact, the shear forces per unit spiral length of thread reduce and tend to reduce the fillet stresses, see Fig. 9.3.3.

The different combinations of parameters give rise to the apparently contradictory effects on peak fillet stress as pitch is varied. But it seems likely that there is an optimum value of pitch for each value of L and R/b.

Effect of Wall Thickness

The coupling wall thickness beneath the thread b has been increased for the two values of R investigated earlier. The tube dimensions D_o and t were kept constant and hence the coupling values of b were different from the tube in all but shape 1 and shape 3. This also meant that the mean contact diameter D_M remained the same and as b was increased, the coupling inside diameter D_i reduced to accommodate this since

$$D_i = D_M - 2e - 2b$$

Table 9.3.1 shows the shapes 1, 3 and 26 to 33 investigated and Fig. 9.3.5 shows the calculated peak fillet stresses obtained using the parameters defined. It can be seen that for both values of R there is an optimum value of coupling wall thickness b. The larger the radius, the larger the optimum value of b and also the smaller the changes of peak fillet stress with b, i.e. $\partial\hat{\sigma}_L/\partial b$

As b changes so the thread parameters R/b, w/b and e/b and the normalising stresses σ_{sa} and σ_{sf} also change.

For the b values which were lower than the optimum value, reductions in fillet stresses due to the reduction in the coefficients C_1, C_3 and C_4 were less than the increases in fillet stresses due to increases in σ_{sa} and σ_{sf}. For b values greater than the optimum value, the increases in fillet stresses due to increases in the coefficients were greater than the reduction in fillet stresses due to reduced values of σ_{sa} and σ_{sf}.

Decreasing the tube undercut area A_t/A_c had the beneficial effect of reducing the preload applied Q_o, which is required to maintain a preload W_t under the same axial tension F. Since from Section 5.1, in the tube nose

$$W_t = \frac{FA_t}{A_c+A_t} - Q_o \qquad \ldots 5.6$$

and in the coupling undercut

$$W_c = \frac{FA_c}{A_c+A_t} + Q_o \qquad \ldots 5.7$$

From either Equation 5.6 or 5.7

$$Q_o = \frac{FA_t}{A_c+A_t} - W_t \qquad \ldots 9.3.1$$

9.4 Fatigue Considerations

For a fatigue life assessment to be made of any structure both the mean stress level and the stress range are required. Although such an assessment is outside the scope of this work, an assessment of the effects of the maximum and mimimum loading magnitudes on peak fillet stresses can be made.

The load spectrum that a TLP will undergo is complicated, see Ref. 37, but it can be considered as a high cycle fatigue system, due to variations in buoyancy caused by the rise and fall of waves which is superimposed upon a low cycle fatigue system due to the drift of the platform.

For a prototype screwed connection to retain its integrity against seawater intrusion into the threaded region, contact must be maintained in the seal region under the greatest axial tensions and bending moments and therefore some preload must be present in the seal region at this condition. Because of this, the threads nearest the preloaded end of the thread spiral would carry the greatest shear forces and the coupling would carry the greatest wall forces. The loading magnitudes in the threads of a coupling nearest the preloaded end have been found under the maximum and minimum in-service wall tensions and the positions and magnitudes of the peak fillet stresses calculated for both these wall tensions using the equations developed in Chapter 8. The thread shape analysed being that of Model 9 which was considered typical for a thin-walled connection.

Webster (1) in his 1981 review of available information on TLP tethers has reported that the maximum tensile stresses due to tether bending are expected to be 1/7 of those due to axial tension. In order to retain seal contact, the applied preload in a TLP screwed tubular connection

$$Q_o = F_{max}(1+1/7)\frac{A_t}{A_c+A_t} + Qp \qquad \ldots 9.4.1$$

where F_{max} is the maximum axial tension in a tether

Q_p is the preload required to ensure seal contact pressure is greater than the sea-pressure at the maximum water depth and contains a safety margin which must be large enough to accommodate any non-uniformities in the application of preload

A_c is the coupling undercut area

A_t is the tube nose area

The other loading requirement is that the tethers must be in tension even in a dead calm sea at low tide. This ensures stability of the platform. Webster (1) has presented data from wave tank studies of different TLP models which indicates that the minimum axial tension per tether

$$F_{min} = 0.08 \times F_{max} \qquad \ldots 9.4.3$$

from wave tank studies of different TLP models.

From Section 5.1, the remaining preload Q in the seal when a tension F is applied can be found from

$$-W_t = Q = Q_o - \frac{FA_t}{A_c+A_t} \qquad \ldots 9.4.3$$

Q/F is required to calculate the shear forces on the section of thread considered. From equation 9.4.3

$$Q/F = \frac{Q_o}{F} - \frac{A_t}{A_c+A_t} \qquad \ldots 9.4.4$$

If we assume that Q_p in Equation 9.4.1 is a factor of F_{max}, say 0.2 F_{max} and substituting Equation 9.4.1 into Equation 9.4.4 we obtain

$$Q/F = 1.14\left(\frac{A_t}{A_c+A_t}\right)\frac{F_{max}}{F} + \frac{0.2F_{max}}{F} - \frac{A_t}{A_c+A_t} \qquad \ldots 9.4.5$$

and Q/F can be found for the maximum and minimum load conditions of $F = F_{max}$ and $F = 0.08F_{max}$

ie for $F = F_{max}$, $Q/F = 0.14 \frac{A_t}{\overline{A_c}+A_t} + 0.2$ ... 9.4.6a

and for $F = 0.08F_{max}$, $Q/F = 13.25 \frac{A_t}{\overline{A_c}+A_t} + 2.5$ ... 9.4.6b

The dimensions A_t and A_c and the parameters for Model 9 have been used, see Table 7.1, to calculate the position ϕ_{max} and magnitude of the normalised peak fillet stress $\hat{\sigma}_L$ for the loading magnitudes in Equation 9.4.6a and 9.4.6b. Both calculated peak fillet stresses have been normalised by $F_{max}/\pi\, t(Do-t)$ so that a direct comparison can be made between the two calculated stresses. The positions chosen were $z = L-0.5p$ for the coupling and $z = 0.5p$ for the tube, i.e. the highest loaded threads.

Table 9.4.1 Magnitudes and Positions of Maximum Peak Fillet Stresses for Maximum and Minimum Applied Tensions

LOADING	MODEL	ϕ_{max} °	$\hat{\sigma}_L$
Maximum Tension $F = F_{max}$	Tube	25.7	4.08
	Coupling	23.5	5.75
Minimum Tension $F = 0.08F_{max}$	Tube	39.0	0.74
	Coupling	28.5	4.01

It can be seen from Table 9.4.1. that for the coupling threads the position of the peak fillet stress varies only slightly and that the peak fillet stress reduces by only 30% despite a 90% reduction in wall tension. This indicates the importance of preload in reducing the peak fillet stress ranges in the coupling threads.

For the tube threads, the peak fillet stresses are less than the coupling peak fillet stresses for the same loading condition. The value of ϕ_{max} changes significantly with the wall tension. The values of fillet stress at the angular positions $\phi = 25.7^{o}$ for the minimum tension of $F = 0.08F_{max}$ and at $\phi = 39.0^{o}$ for $F = F_{max}$ have been calculated so that the stress ranges can be found. Since the calculated values are at a free surface, the direction of the calculated maximum principal stress does not change since $\sigma_1 = \sigma_L$ and $\sigma_2 = 0$. The calculated values of σ_L are shown in Table 9.4.2.

It can be seen from Table 9.4.2 that the range of calculated fillet stresses for the maximum and minimum wall tensions at $\phi = 25.7^{o}$ was slightly greater than if the maximum fillet stresses only were considered, irrespective of their position. Similar calculations have not been done for the coupling threads since $\partial\sigma_L/\partial\phi$ wouldbe negligible from $\phi = 23.5^{o}$ to $\phi = 28.5^{o}$.

From Table 9.4.2 the reduction in fillet stress at $\phi = 25.7^{o}$ is 83% for a 90% reduction in wall tension. Because of this large calculated fillet stress range in the tube threads they should also be considered in any fatigue life assessment of a screwed tubular joint.

Table 9.4.2 Magnitudes of Fillet Stresses at Selected Positions in Tube Threads for Maximum and Minimum Applied Tensions.

LOAD	CALCULATED FILLET STRESS σ_L AT THE POSITIONS	
	$\phi = 25.7^{o}$	$\phi = 39.0^{o}$
$F = F_{max}$	4.08	3.84
$F = 0.08F_{max}$	0.69	0.74

The peak fillet stresses in a preloaded coupling will be greater than in the mating tube, if they are of similar cross-sectional areas, see Table 9.4.1. The simplest way to reduce the coupling peak fillet stresses independently of the tube is to change the coupling wall thickness, see Fig. 9.3.5. But, it can be seen from this figure that great care should be taken, since increasing the wall thickness beyond a certain value will tend to increase the peak fillet stresses due to the reduction in the R/b and w/b ratios.

9.5 STRESS GRADIENTS IN AND AROUND THREAD FILLETS

It has been shown in Chapter 8 that the thread fillets exhibit high elastic stresses. The elastic stress or stress difference distributions have been measured in the Hoop direction and parallel and perpendicular to the surface in the r-z plane. From these elastic stresses an insight into the likely growth of plasticity can be obtained.

Measurements of peak thread fillet stresses have shown generally small gradients in the hoop direction, see Section 8.3. Stress gradients perpendicular to the fillet surface vary around the fillet but generally are large at values of ϕ where the maximum principle surface stress $\hat{\sigma}_L$ is large and stress gradients are small where σ_L is small, see Section 5.3. The equation developed by Glinka (22) for the subsurface stress σ_1 ahead of a notch tip is

$$\sigma_1 = \frac{\hat{\sigma}_L}{2\sqrt{2}} \left[\left(\frac{R}{r_f - \frac{R}{2}} \right)^{\frac{1}{2}} + \frac{1}{2} \left(\frac{R}{r_f - \frac{R}{2}} \right)^{3/2} \right] \quad \ldots\ldots 9.5.1$$

where $\hat{\sigma}_L$ is the peak stress at the notch tip and r_f is the distance from the Radius centre, see Fig. 2.1. Figure 9.5.1 shows the stress distribution calculated radially from the thread fillet surface at the position of maximum fillet stress, $\phi = \phi_{max}$ using Equation 9.5.1 and compares it with the photoelastically measured subsurface stress distributions at $\phi = 0^\circ$ and $\phi = 15^\circ$ in a thread loaded with wall tension only; these photoelastic measurements were shown in Fig. 5.8. Photoelastic measurements of surface fillet stress showed $\partial\sigma_L/\partial\phi$ was negligible between $\phi = 0^\circ$ and $\phi = 15^\circ$ and that $\hat{\sigma}_L$ occurred in that region. Generally, up to about R/4 subsurface, the radial stress σ_3 was negligible compared with σ_1, and hence fringe order measurements were measurements of the maximum principal stress subsurface.

It can be seen from Fig. 9.5.1 that Equation 9.5.1 accurately predicts the sub-surface stress distribution for thread fillets loaded with wall tension only when measured from the position of peak surface fillet stress.

Fig. 9.5.2 compares the stresses predicted using Equation 9.5.1 with those measured photoelastically at $\phi=\phi_{max}$ in a thread fillet loaded with wall tension and shear forces. The thread position chosen was in the loaded region of the coupling of Model 6, and adjacent to the thread analysed in Fig. 9.5.1. It can be seen that Equation 9.5.1 over-estimates the magnitude of the measured sub-surface stress in thread fillets loaded with shear force and wall tension.

Also shown on Fig. 9.5.1 and 9.5.2 is Ω, which is the value of maximum subsurface principal stress, normalised by the peak surface fillet stress

$$\Omega = \sigma_1/\hat{\sigma}_L \qquad \ldots\ldots 9.5.2$$

where $\hat{\sigma}_L$ is the peak surface fillet stress and σ_1 is the maximum principal stress and hence $\Omega < 1$. If the point considered is close to the fillet surface then Ω equals the fringe order at the point/max fringe order in the fillet.

Fig 9.5.3 shows a typical contour of Ω, and also the distances r_f-R and d_2 which have been used to define the shape of the contour. r_f - R is the distance subsurface from the position of peak fillet stress i.e. $\phi=\phi_{max}$; d_1 is the circumferential distance around the fillet surface measured from the position $\phi=\phi_{max}$ in the direction of increasing ϕ and d_2 is the circumferential distance around the fillet surface measured from $\phi=\phi_{max}$ in the direction of decreasing ϕ.

Distributions of $(r_f - R)/d_1$ v Ω , measured photoelastically, have been plotted on Fig. 9.5.3 for the 2 different threads whose subsuface

stress distributions have been shown in Fig. 9.5.1 and 9.5.2. The distributions of surface stresses for the two threads are shown in Fig. 9.5.4 and 9.5.5 and from these figures values of d_1 and d_2 were obtained. For the thread loaded with wall force only (symbol 0), $\psi_{max} \simeq 10^{\circ}$ and hence the maximum value of d_2 was small and has not been plotted on Fig. 9.5.3. For the thread loaded with shear force and wall tension (symbol x) $d_2 = d_1$ for each value of Ω considered since σ_L was symmetrical about $\psi = \psi_{max}$ in this particular position.

Fig. 9.5.3 shows almost linear distributions of $(r_f - R)/d_1$ against Ω. The low values of $(r_f - R)/d_1$ indicates the way the contours of equal stress tended to follow the fillet surface. As Ω reduced, the relative depth subsurface of the stress contour increased, although d_1 was still several times the value of $r_f - R$, even for the smallest values of considered. It can also be seen that the gradient of $(r_f - R)d_1$ with respect to Ω is greater for the thread loaded with wall tension only. This indicates the shallower subsurface stress gradients in this thread. The relative magnitudes of the shear force and wall tension for the 2 threads have been represented by the ratio of nominal bending stress to mean through-thickness tensile stress, σ_{sf}/σ_{sa}.

Although these results are for 1 shape of thread under 2 different loading ratios Schijve (37) has shown that d_2/d_1 v Ω was similar for several notches of different severity which were loaded with wall tension only i.e. $\sigma_{sf}/\sigma_{sa} = 0$.

If $\Omega\ \hat{\sigma}_L > \sigma_y$ the prototype material yield stress, then the regions of plasticity are likely to conform to the region of the fillet defined by d_2 and d_1 for the value of Ω considered. Since the highest values of σ_L are likely to occur in the highest loaded coupling threads then the regions of plasticity in the thread fillets are likely to be wide and shallow in the r-z

plane but extend a long way in the hoop direction. This wide, shallow region of plasticity means that crack initiation could occur within a relatively large region of the thread fillet. This is supported by the fatigue crack shapes and crack growth observed by Glinka et al (10), which showed crack initiation at several distinct sites which then grew into long shallow cracks before joining up prior to final fracture.

9.6 Comparison with Published Data

Table 9.6.1 shows the peak fillet stresses published by Glinka et al (10) and those calculated by the author using the equations developed in Chapter 8 for the same thread shape reported by Glinka. Although there are other published results for fillet stresses in screwed tubular connections (7,8,15) no direct comparisons can be made using the method of calculating fillet stresses proposed by the author because the thread shapes were too dissimilar to the buttress threads analysed by the author (7,15) or insufficient data was presented (8).

Table 9.6.1 - Comparison of Fillet Stresses from Glinka (10) and those calculated by the Author

Shape					Results From		
					Glinka	Author	
R/b_{max}	w/b_{max}	e/b_{max}	L/p	D_i/b_{max}		$\hat{\sigma}_L$	σ_L AT $\phi=0^o$
0.021	0.067	0.021	25	2	4.0	10.3	3.0
0.010	"	"	"	"	5.2	22.7	6.0
0.005	"	"	"	"	7.0	45.8	11.0

There are several reasons why the authors method has generated fillet stresses which are larger than those measured by Glinka:-

i) the parameter w/b_{max} was outside the range of applicability for the

equation

$$\sigma_F = \sigma_{SF} (C_3 + C_4 \sin 2\phi)$$

ii) the method of calculating the nominal bending stress σ_{SF} is applicable only to thin-walled tubulars.

It is also uncertain from Ref. 10 where Glinka et. al. measured the fillet stresses. If they were measured at the blend of fillet and root, $\phi = 0^\circ$, then a serious underestimate of the peak fillet stress would have occurred, see Table 9.6.1. The author has calculated the peak fillet stress to have occurred very near to $\phi = 45^\circ$.

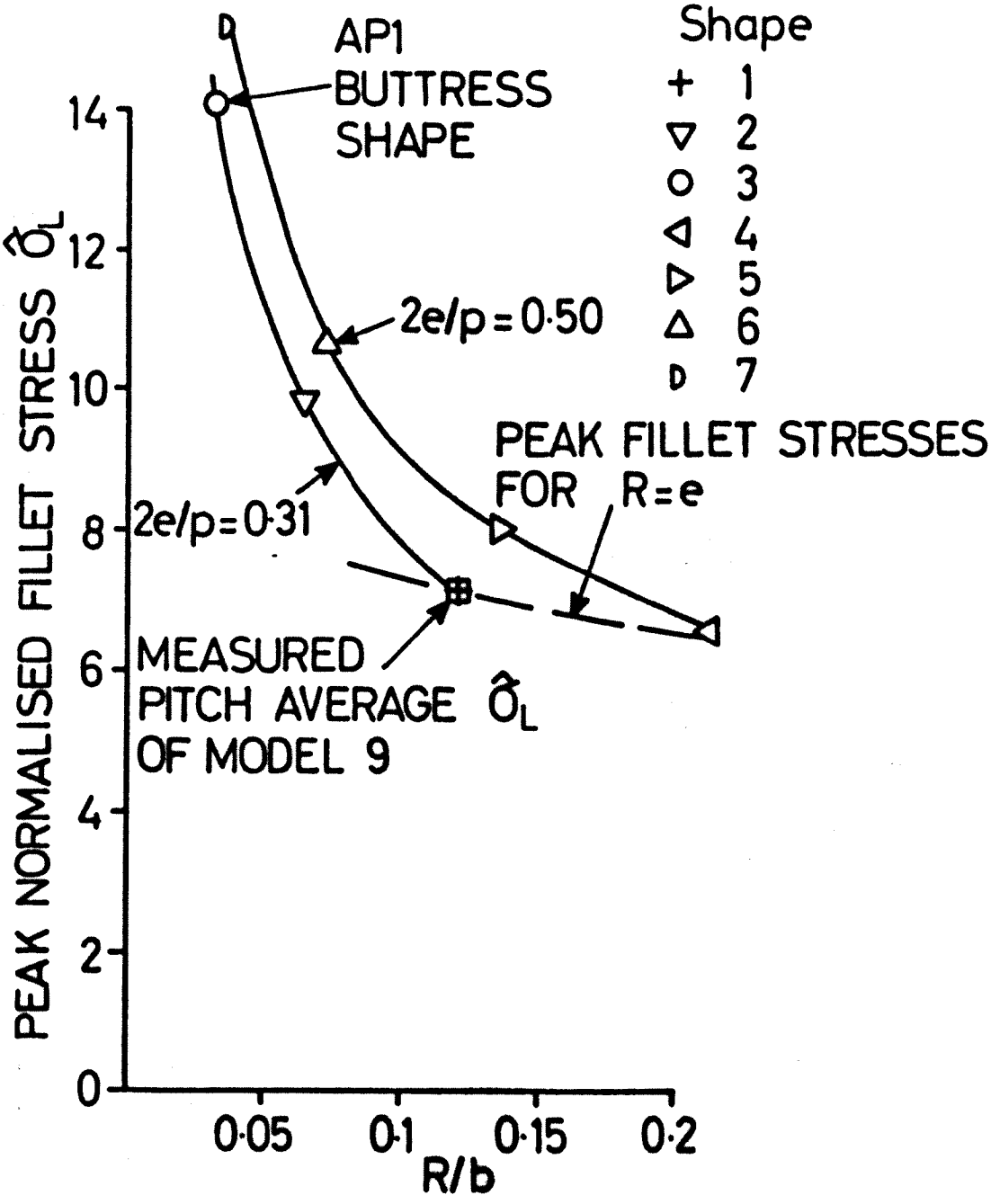

Fig 9.3.1

Effect of Thread Fillet Radius on Calculated Peak Fillet Stress

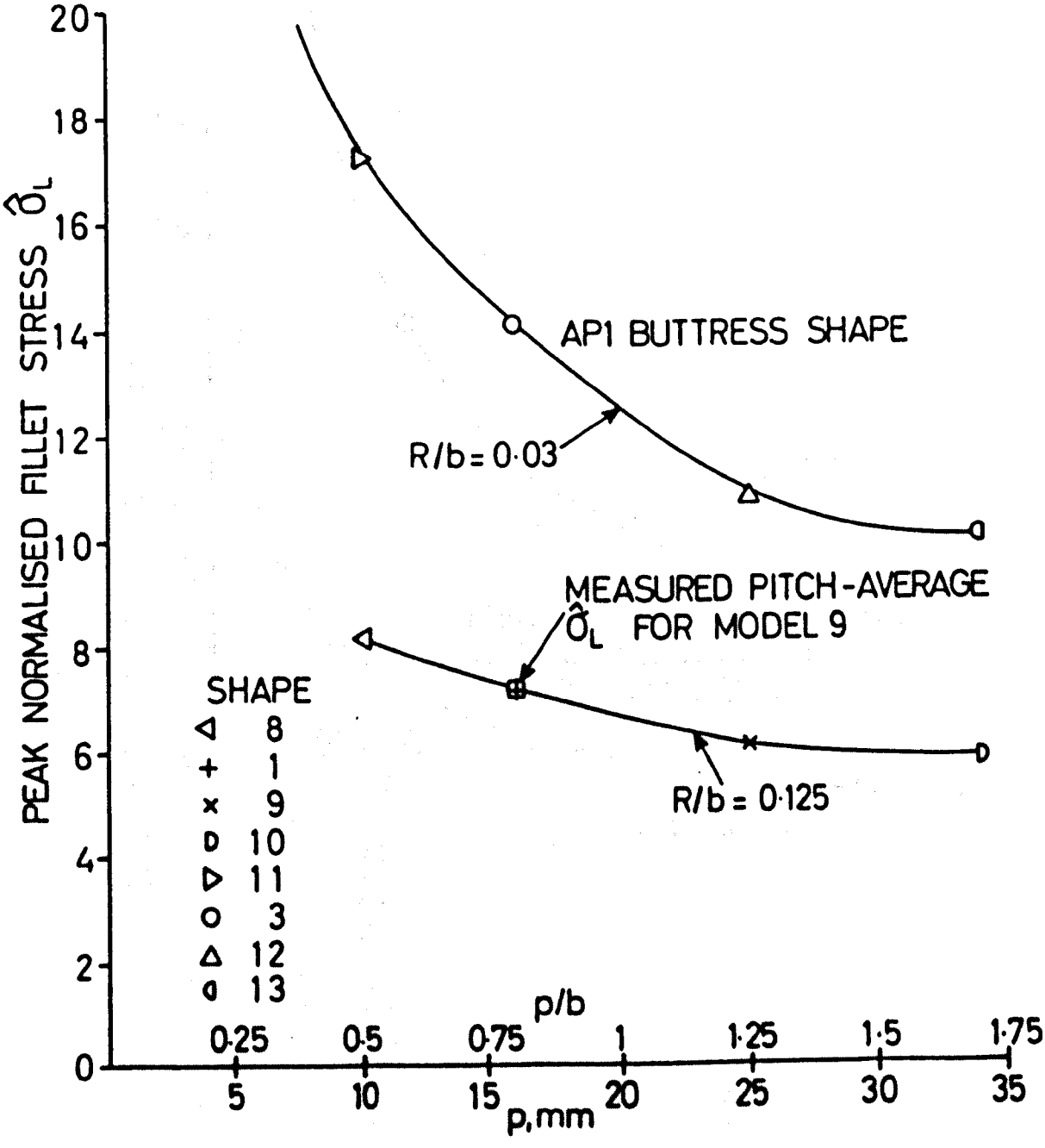

Fig 9.3.2

Effect of Thread Pitch on Calculated Peak Fillet Stress for A Constant Number of Pitches = 7.5

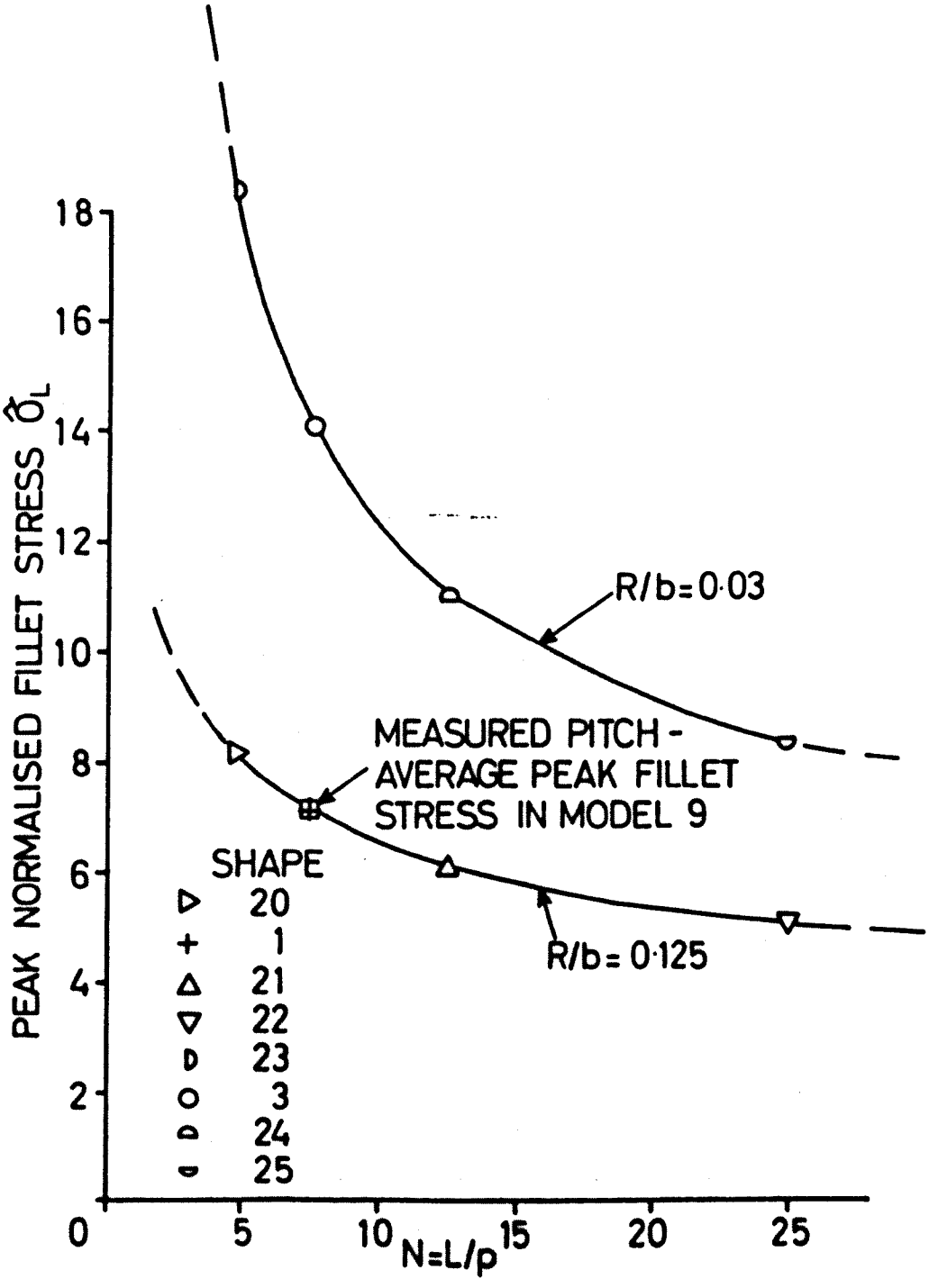

Fig 9.3.3

Effect of Number of Pitches on Calculated Peak Fillet Stress for a Constant Pitch of p/b = 0.395

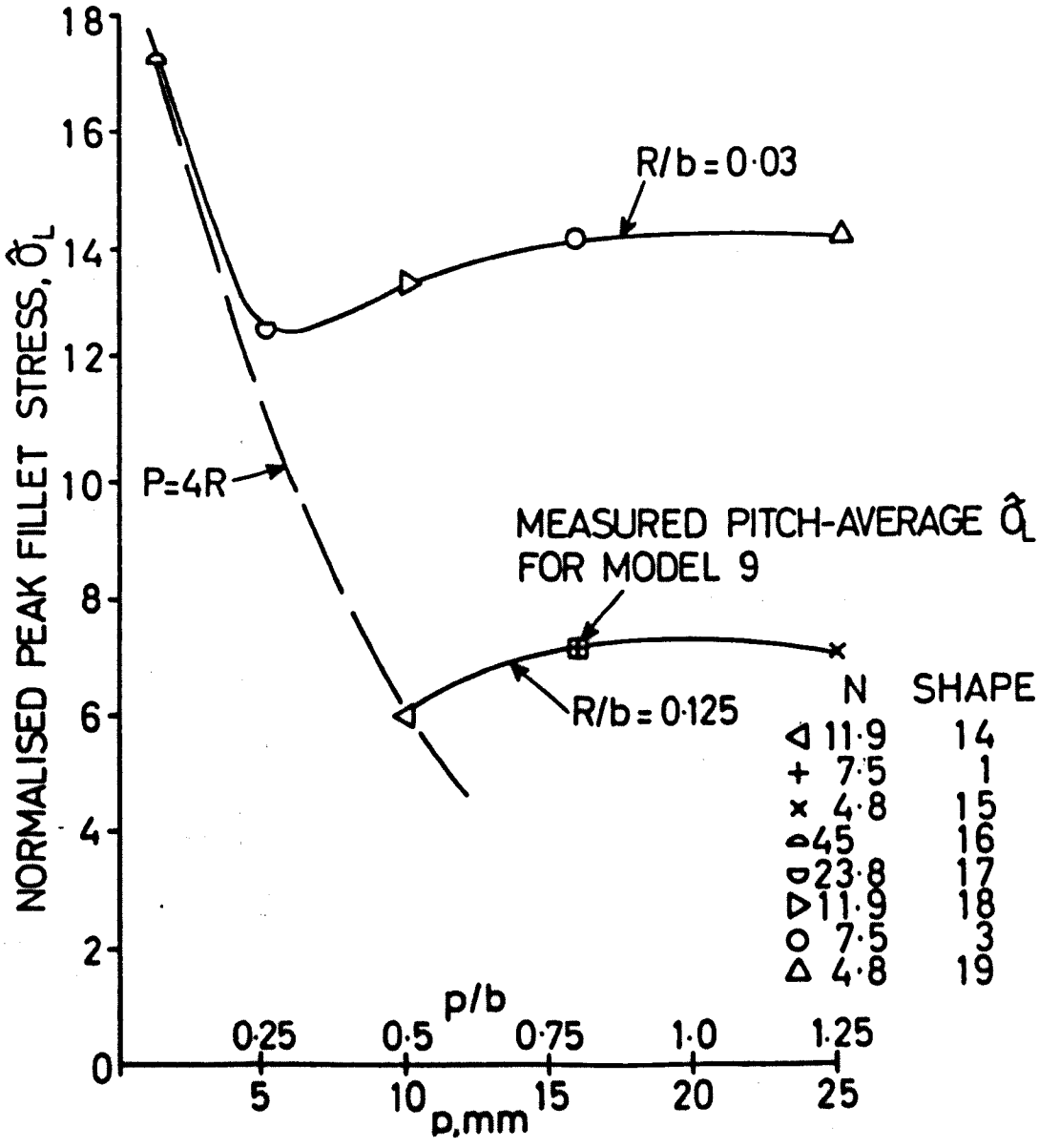

Fig. 9.3.4

Effect of Thread Pitch on Calculated Peak Fillet Stress for a Constant Length of Engagement L/b = 5.95

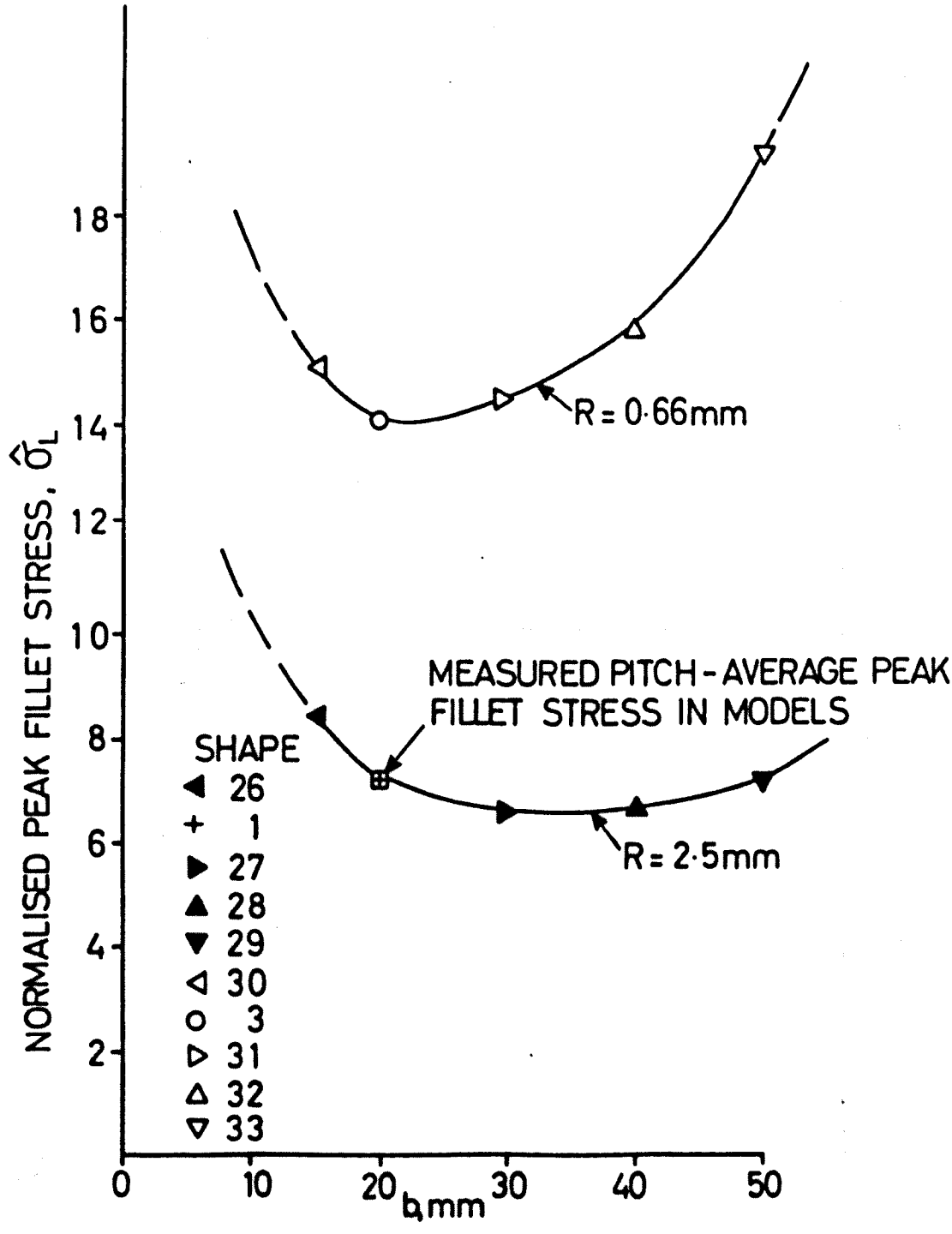

Fig 9.3.5

Effect of Altering Wall Thickness on Calculated Peak Fillet Stress

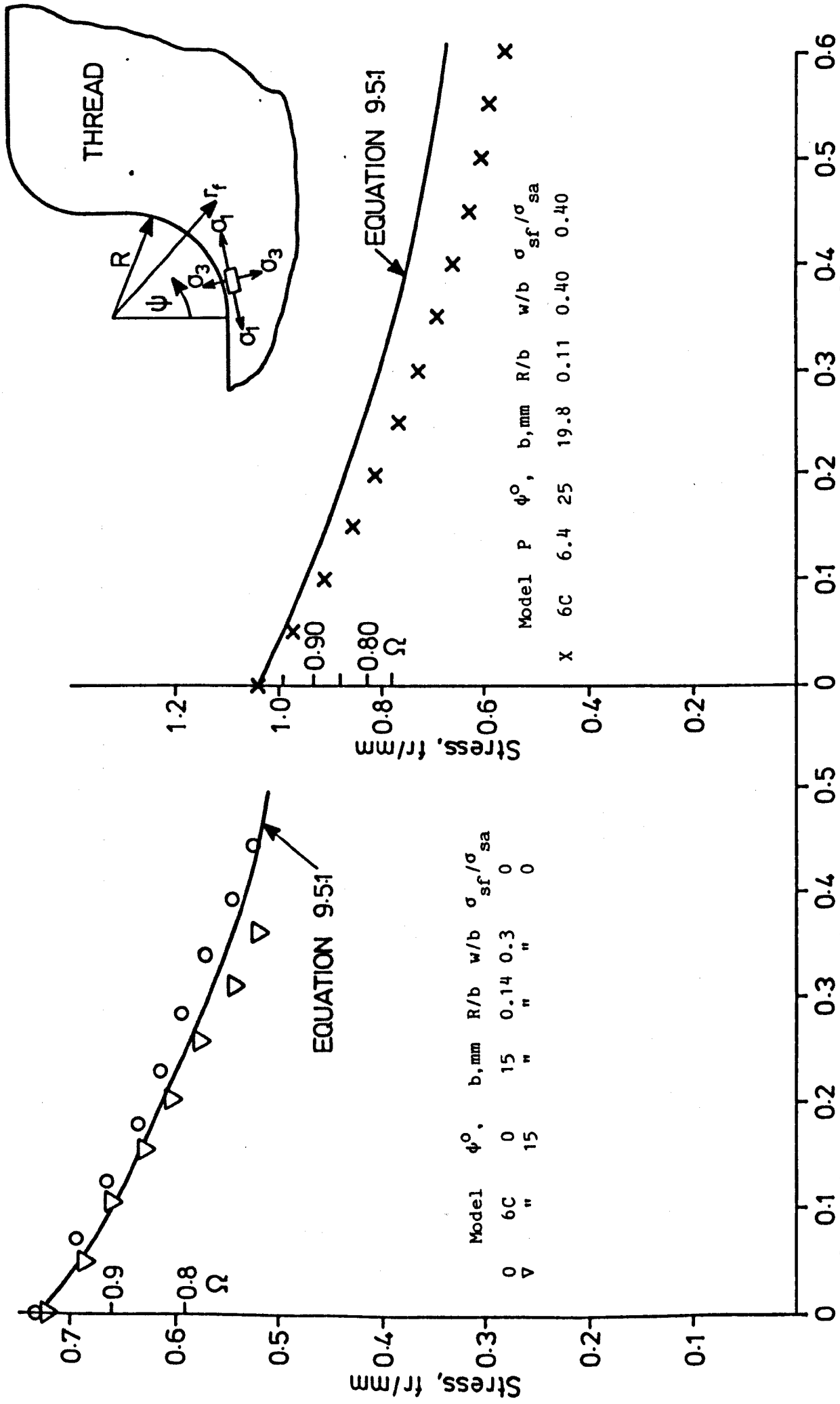

Fig 9.5.1 Photoelastically Measured Sub Surface Stresses In Thread Loaded with Wall Tension Only, Compared with Stresses Predicted by Glinka

Fig 9.5.2 Photoelastically Measured Sub Surface Stresses in a Thread Loaded with Wall Tension and Shear Force, Compared with Stresses Predicted by Glinka

Fig 9.5.3

Distribution of Stress Contours for a Thread Loaded with Wall Tension Only and a Thread Loaded with Wall Tension and Shear Force.

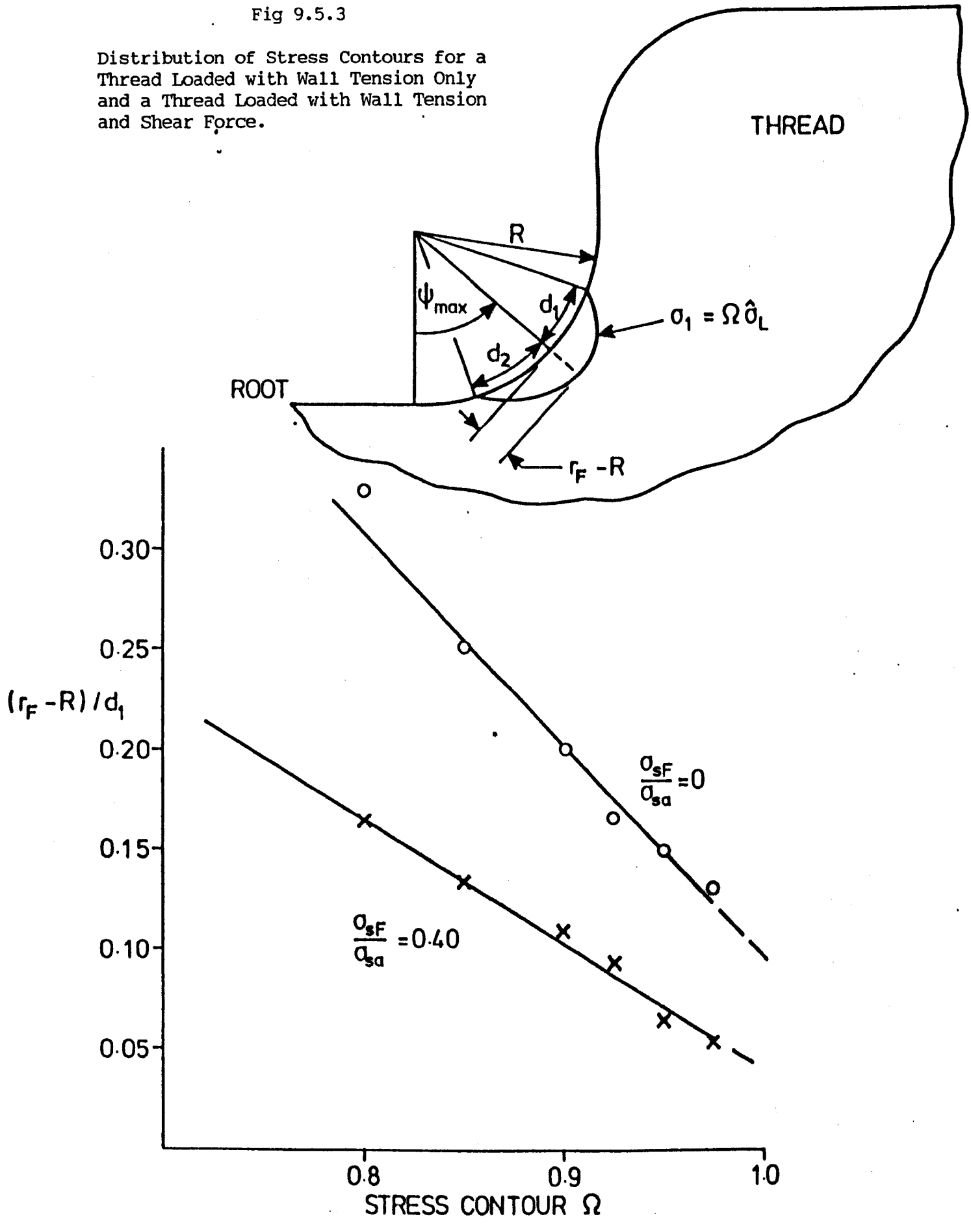

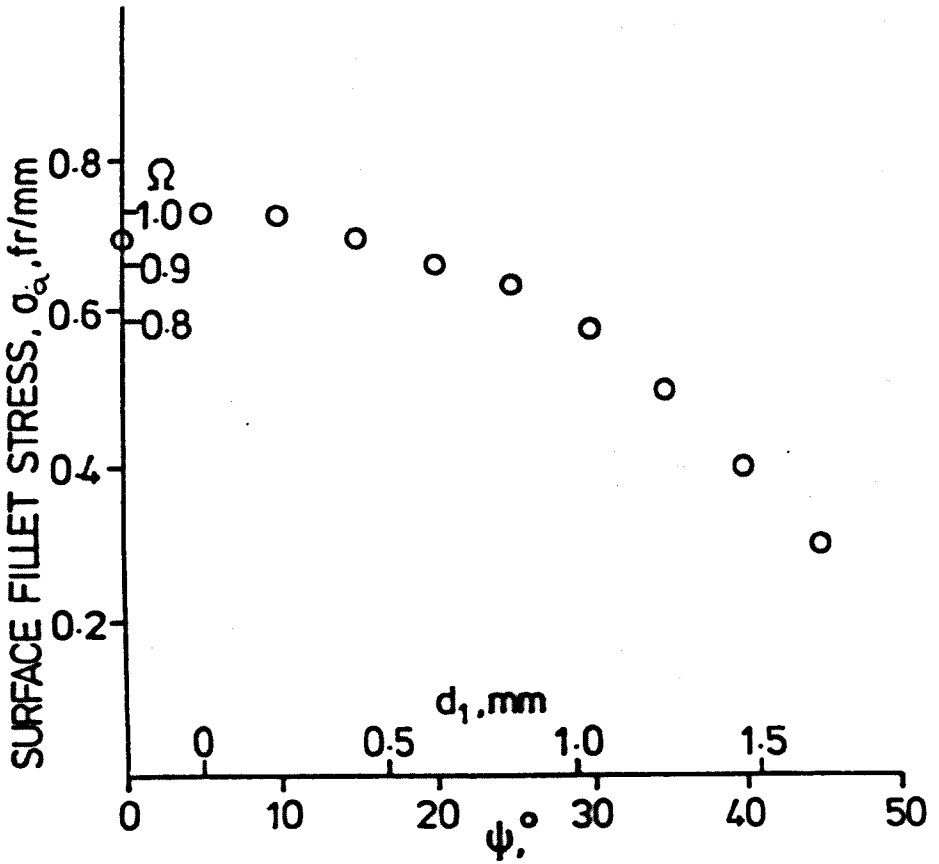

Fig 9.5.4 Distribution of Surface Stress, Measured Photoelastically in a Typical Thread Fillet Loaded With Wall Tension Only

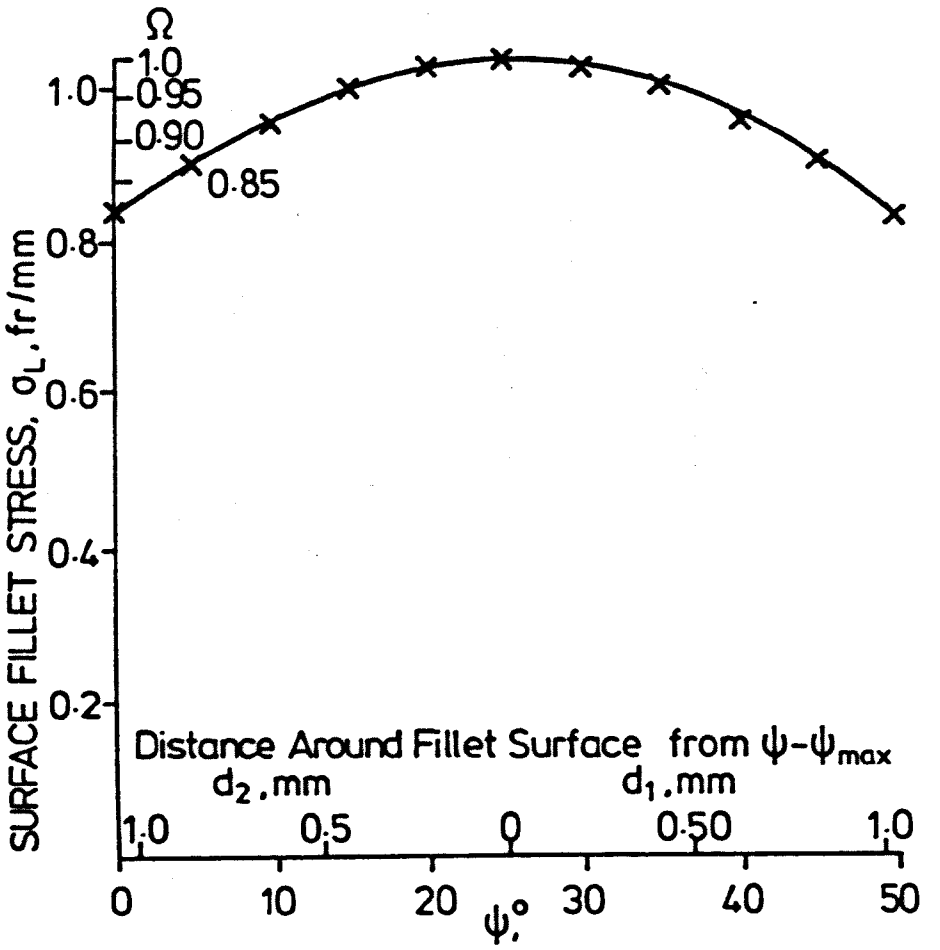

Fig 9.5.5 Distribution of Surface Stress, Measured Photoelastically in a Typical Thread Fillet Loaded with Wall Tension Plus Shear Force

CHAPTER 10

CONCLUSIONS

10.1 Analysis

Fairly simple axisymmetric finite element meshes can be used to model the stress distributions found in the loaded fillets of 3-dimensional Araldite models.

The stresses in thread fillets in the contact region are due to a combination of fillet stresses due to wall tension and fillet stresses due to shear forces applied directly to the thread. The distributions of fillet stresses due to wall tension only around a section of thread are different from those due to shear force only. Empirical parametric equations for the stresses in thread fillets for either wall tension only or shear force loading only have been obtained from axisymmetric Finite Elements. Equations for the distributions of wall tensions and thread shear forces have been obtained from measurements made in 3-dimensional photoelastic models. Using the equations for the fillet stress distributions and the load distributions, the peak fillet stresses have been calculated and compared with those measured photoelastically in 3-dimensional models with different shapes and different loads. The calculated peak fillet stresses generally agree to within $\pm$ 10% of the measured pitch average peak fillet stresses.

10.2 Equations For Loads

The following equations have been obtained from 3-dimensional photoelastic measurements in male and female threaded components with similar shapes. They can be used to calculate the distributions of normalised thread shear force due to the externally applied loads of axial tension only

$$\bar{V}_F = 0.81 + 15(z/L - 0.5)^4 \qquad \ldots\ldots 8.1.3$$

and preload only

$$\bar{V}_Q = 0.58 + 0.65(z/L) - 1.4(0.5 - z/L)^2 \quad \text{for } 0<z/L<0.5 \qquad \ldots\ldots 8.1.14$$

and $$\bar{V}_Q = 0.58 + 0.65(z/L) + 59\,(z/L - 0.5)^5 \quad \text{for } 0.5<z/L<1.0 \qquad \ldots\ldots 8.1.15$$

where the suffices F and Q_o refer to axial tension and preload.

The distribution of shear force V, normalised using the axial tension in a screwed connection loaded with axial tension F and preload Q_o can be found from

$$\bar{V} = \bar{V}_F + \frac{Q_o}{F}\bar{V}_Q$$

where $\bar{V}_F$ is the normalised distribution due to axial tension and $\bar{V}_Q$ is the normalised distribution due to preload.

From the equations for the distributions of shear forces, equations for the distribution of wall forces can be obtained by integrating the shear force equations with respect to the non-dimensional distance along the thread spiral. For the tube models loaded with axial tension only, the full wall tension occurs at z/L = 0

$$\therefore\ W_{tf} = 1 - \int \bar{V}_F\, d\,(z/L) \qquad \ldots\ldots 8.1.8$$

and substituting the equation for $\bar{V}_F$ into equation 8.1.8 gives

$$W_{tf} = 1 - (0.81\,(z/L) + 3\,(z/L - 0.5)^5 + 0.094) \qquad \ldots\ldots 8.1.10$$

For the coupling models loaded with axial tension only, the full wall tension occurs at z/L = 1, hence

$$\therefore \quad W_{cf} = \int \bar{V}_F \, d\,(z/L)$$

hence $W_{cf} = 0.81\,(z/L) + 3(z/L - 0.5)^5 + 0.094$ 8.1.11

where the suffices c and t refer to coupling and tube

Preload puts the tube wall into compression and the coupling wall into tension, therefore

$$W_{tQ} = - \int \bar{V}_Q \, d(z/L) \qquad \text{..... 8.1.16}$$

hence substituting the equation for $\bar{V}_Q$ into equation 8.1.16 gives

$$W_{tQ} = - [0.58(z/L)+0.325(z/L)^2+0.466(0.5-z/L)^3 - 0.0586] \quad \text{... 8.1.17}$$

for $0<z/L<1.0$

and $W_{tQ} = - [0.58(z/L)+0.325(z/L)^2+9.833(z/L-0.5)^6 - 0.0586]$ ... 8.1.19

for $0.5<z/L<0.5$

and

$$W_{cQ} = \int \bar{V}_Q \, d(z/L) \qquad \text{..... 8.1.17}$$

hence $W_{cQ} = - W_{tQ}$

Since the shear forces due to axial tension plus preload can be found so can the wall forces, hence

$$W_t = FW_{tF} + \frac{Q_o}{F} W_{tQ} \qquad \text{.....8.1.20}$$

and

$$W_c = FW_{cF} + \frac{Q_o}{F} W_{cQ} \qquad \text{.....8.1.21}$$

where F and Q_o are the normalised tension and preload

10.3 Equation for Fillet Stresses Due to Wall Tension Only

The stresses in a thread fillet loaded with wall tension only can be characterised by the equation

$$\sigma_a = \sigma_{sa} (C_1 + C_2 \cos 2\phi) \qquad \ldots\ldots 8.2.1$$

where σ_a is the normalised fillet stress, σ_{sa} is the normalised mean wall tensile stress at the section of thread considered, ϕ is the angular position around the thread fillet measured from the blend of fillet and thread root and C_1 and C_2 are non-dimensional coefficients for which empirical parametric equations have been obtained. Equation 8.2.1 is valid from $\phi = 10^\circ$ to the value of ϕ where $\sigma_a \simeq 0$.

The equations for the coefficients C_1 and c_2 which have been obtained using axisymmetric Finite Elements are

$$C_1 = 0.38(w/b-0.05)^{0.45} (R/b)^{-0.56}$$
and
$$C_2 = 1.29 - 0.144\ w/b \qquad \ldots\ldots 8.2.2$$

Equation 8.2.2 is applicable for $0.02<R/b<0.17$ and $0.05<w/b<0.7$

Equation 8.2.3 is applicable for $0.02<R/b<0.17$ and $0.1<w/b<1.0$

The mean wall tensile stress, σ_{sa}, is obtained from the equation for wall force. The equation for the wall stress, normalised by the full tube wall stress is, for the tube

$$\sigma_{sa} = W_t \frac{(D_o - t)t}{(D_o - b)b} \qquad \ldots\ldots 8.1.22$$

and for the coupling

$$\sigma_{sa} = W_c \frac{(D_o - t)t}{(D_i + b)b} \qquad \ldots\ldots 8.1.23$$

where D_o is the tube outside diameter, D_i is the coupling inside diameter, t is the full tube wall thickness and b is the local wall thickness beneath the tube or coupling thread considered.

10.4 Equations for Fillet Stresses Due To Wall Tension Plus Shear Forces

The fillet stresses for a thread loaded with shear force and wall tension σ_L can be obtained from the equation

$$\sigma_L = \sigma_a + \sigma_F \qquad \ldots\ldots 8.2.14$$

where σ_a is found from Equation 8.2.1 and σ_F, the fillet stresses due to shear forces only, can be found from

$$\sigma_F = \sigma_{sF} (C_3 + C_4 \sin 2\phi) \qquad \ldots\ldots 8.2.4$$

where σ_{sf} is the nominal surface bending stress and is calculated from 'beam-on-elastic-foundation' type equations for an axisymmetric bending moment applied near one end of an infinitely long thin tube and C_3 and C_4 are non-dimensional coefficients for which empirical relationships between them and the thread parameters have been obtained.

The equations for C_3 and C_4 are

$$C_3 = 0.311\ (e/b)^{-0.19}(R/b)^{-0.56}(w/b)^{(-0.154(R/b)^{-0.36})} \qquad \ldots 8.2.9$$

and $$C_4 = (w/b)^{-0.25}(R/b)^{(-0.32(w/b)^{-0.43})} \qquad \ldots\ldots 8.2.13$$

for $0.15<w/b<1.0$
$0.02<R/b<0.25$
$0.06<e/b<0.25$
and $e/b>R/b$ and $w/b<2R/b$ are practical limits

set by the thread type and geometry. Equation 8.2.4 does not accurately describe the fillet stress distribution when $e/b > w/b$ i.e. when the thread becomes very deep radially and thin axially.

10.5 Effect of some shape variations on maximum fillet stresses

In Section 9.3 the equation developed in Section 8.1 and 8.2 were used to investigate the effects of parameter changes on peak fillet stresses in the most highly loaded threads of a coupling loaded with preload and tension. It was found that:-

i) maximising the fillet radius for given thread height to the value of R = h/2 will reduce the peak fillet stress.

ii) increasing the thread height to accommodate an increased fillet radius may or may not reduce peak fillet stresses. The effect of increasing R may be outweighed by the reduction in cross-sectional wall area.

iii) increasing the pitch will reduce the peak fillet stresses.

iv) increasing the number of pitches of thread engagement will reduce peak fillet stresses

v) there is likely to be a value of coupling wall thickness b which gives a minimum value of peak fillet stress. The value of b will vary depending on the other parameters.

vi) if the axial length of engagement is limited to a given value, then altering both N and p is likely to give optimum values at which the peak fillet stresses are minimised. These optimum values of N and p will vary as the other thread parameters vary. For the 2 thread shapes examined, one of which had a large R/b ratio and the other a small R/b ratio, the optimum pitch was near the minimum value of p=4R. But, each proposed shape should be examined in detail since large values of $\partial\hat{\sigma}_L/\partial p$ were found near p=4R for the thread with the small radius. It may be wiser to increase the pitch to slightly

greater than the optimum since the gradient $\partial\hat{\sigma}_L/\partial p$ is smaller for $p >$ optimum value of p than for $p <$ optimum value of p.

10.6 Fatigue Considerations

Although the greatest peak fillet stresses were observed in the couplings of connections loaded with preload and tension, Section 9.4 showed that during a fatigue cycle the greatest stress ranges would occur in the fillets of the most highly loaded tube threads. Hence both tubes and couplings should be analysed when doing fatigue life assessments.

References

1. Webster, S. E., Rudd, W. J. and Cook, W. T. 'Review of information on the fatigue properties of tethering systems for Tethered Buoyant Platforms'. BSc report OT-R-8241, 1982.

2. Cuneyt Capanoglu 'TLP Design: Interaction of Naval Architectural & Structural Design considerations' Marine Technology Vol 16. No. 4 Oct. 1979 pp. 343-352.

3. From Chung 'Offshore & Arctic Frontiers-Structures, Ocean Mining' Mech. Eng. May 1985, Pg. 54.

4. 'General Description of Tension Leg Platform Systems', Deep Oil Technology, Long Beach, California, USA 8th Feb 1977.

5. Vam Joints Design and Applications, Vallourec, Paris, 1982.

6. Skillbeck, F. et al, 'Design and Manufacture of Couplings for the Hutton TLP Mooring Systems, Proc. of Offshore Technology Conference, OTC 4946, Houston, Texas 1985.

7. Dutta, D. and Wendler, W., 'Tubular Tendon for a Tension Leg Platform: Material Development and Threaded Connection Design', Proc. of Offshore Technology Conference, OTC 5075, Houston, Texas 1985.

8. Sakakaguchi, I. et al, 'Dynamic Response Analysis and Fatigue Life Prediction of TLP Tension Legs', 5th Int. Sym. on Offshore Mechanics and Artic Engineering, Tokyo, April 1986.

9. Kawashima, H., Morita, Y. and Ishihara, K., 'Stress and Contact Pressure Analysis of Premium Connections by Finite Element Method', 9th E.T.C.E., 1986.

10. Glinka, G. Dover, W.D. and Topp, D.A., 'Fatigue Assessment of Tethers', Int. Conf. on Fatigue and Crack Growth in Offshore Structures, London, April 1986.

11. Dutta, D., Private Communication, October 1986.

12. Crose, J. G., et al, 'Nonlinear Finite Element Analysis of Buttress Threaded Casing Connections'.

13. Fessler, H. and Perla, M., 'Precision Casting of Epoxy-Resin Photoelastic Models', Journal of Strain Analysis, Vol. 8, No. 1, 1973.

14. Fessler, H., Little, W. J. G. and Whitehead, P.S., 'Precision Casting of Epoxy Resin Models using Expendable or Re-usable Moulds', 8th All-Union Conference of Photoelasticity, Tallinn, USSR, 1979.

15. Marino, R. L. and Riley, W. F., 'Optimising Thread-root contours using Photoelastic Methods', Experimental Mechanics, Vol. 4, pp. 1-10, 1964.

16. Kenny, B. and Patterson, E. A., 'Load and Stress Distribution in Screw Threads', Experimental Mechanics, Vol. 25, pp. 208-213, 1985.

17. Fessler, H. and Wang Jiong-Hua, 'Stress analysis of some unsymmetric screwed connections', Journal of Strain Analysis, Vol. 19, No. 2, 1984.

18. Fessler, H., Marston, R.E. and Ollerton, E., 'A Micropolariscope for Automatic Stress Analysis', Journal of Strain Analysis, Vol. 22, No. 1, 1987.

19. Frocht, M. M. and Guernsey, R., 'Studies in Three-Dimensional Photoelasticity - the Application of the Shear-Difference Method to General Space Problems', Proc. 1ST US Nat. Cong. of Appl. Mech., Dec 1952, pp. 301-307.

20. Specification for Threading, Gaging and Thread Inspection of Casing, Tubing and Line Pipe Threads, API Std 5B, 10th Edition, March 1979 (American Petroleum Institute, Washington D.C.).

21. Det Norske Veritus, 'Rules for the Design, Construction and Inspection of Offshore Structures', 1977, Appendix C, Steel Structures.

22. Glinka, G., 'Calculation of Inelastic Notch-Tip Strain-Stress Histories Under Cyclic Loading', Engineering Fracture Mechanics, Vol. 22, No. 5, 1985.

23. Heywood, R. B., 'Designing by Photoelasticity', Chapman and Hall, pp. 231-266, 1952.

24. Neuber, H., 'Kerbspannungslehre', J. Springer, Berlin, 1937; trans. by Navy Dept., David Taylor Model Basin, Washington, D. C., 1945.

25. Sopwith, D. G., 'The Distribution of Load in Screw Threads', Proc. I.Mech.E., Vol. 159, 1948.

26. Heywood, R. B., 'Tensile Fillet Stresses in Loaded Projections', Proc. I. Mech. E, Vol. 159, 1948.

27. Heywood, R. B., 'Stress Analysis of Turbine Blade Fixtures by Photoelastic Methods', external Ph.D. Thesis London University, 1946.

28. Fessler, H. and Jobson, P. K., 'Stresses in a Bottoming Stud Assembly with Chamfers at the Ends of the Threads', Journal of Strain Analysis, Vol. 18, No. 1, 1983.

29. 'Development of a Tubular Steel Tether Systems', BSC Report, S50/78/11/D, Feb. 1979.

30. Ballinger, M. R., et al, 'The Design of a Hard Seal for the Screwed Connection of a Tension Leg Platform', B.Sc. Dissertation, Department of Mechanical Engineering, Nottingham University, 1985.

31. Stanley, P. 'Three-dimensional Photoelastic Stress Analysis Techniques and Applications', Experimentelle Technik der Physik. XVI, 1968.

32. Fessler, H. and Ollerton, E., 'Contact Stresses in Toroids under Radial Loads', British Journal of Applied Physics, Vol. 8, October 1957.

33. PAFEC 75, Data Preparation Manual, PAFEC Ltd., Nottingham, 1978.

34. Marston, R. E., 'An Automatic Micropolariscope: Its Design, Development and Use for Tubular Joint Stress Analysis, Ph.D. Thesis, University of Nottingham, 1985.

35. Edwards, C. D., 'Design and Stress Analysis of Cast Tubular Joints', Ph.D. Thesis, University of Nottingham, 1983.

36. Lyons, G. J. et al, 'Theory and Model Test Data for Tether Forces on Tensioned Buoyant Platforms', Proc. of Offshore Technology Conference, OTC 4643, Houton, Texas 1983.

37. Schijve, J., 'Stress Gradients around Notches', Fatigue of Engineering Materials and Structures, Vol. 3, No. 4, pp 325-338, 1980.

38. Timoshenko, S. 'Theory of Elasticity', 2nd edition, McGraw Hill, pp 78-85, 1951.

39. Roark, R. J. and Young, W. C., 'Formulas for Stress and Strain', 5th Ed., McGraw-Hill, 1975.

Appendix 1 Photoelastic Measurements of Loads in the Tube and Coupling Models

The distributions of threaded surface, unthreaded surface and mean through thickness axial stresses measured in both the tube and coupling undercuts have been plotted against θ in Figures A.1.1 to A.1.8 for Models 1, 3, 5 and 6 loaded with pure tension, Models 7 and 10 loaded with preload only and Models 8 and 9 loaded with tension and preload. For the preloaded Models 7 and 10, no wall stresses were present in the tube undercuts. For Model 2, loaded with eccentric tension, the surface stresses and mean through thickness stresses have been plotted against sin θ in Fig. A.1.9.

From the distributions of mean through thickness tension, the applied loads were calculated, see Section 5.1.

For Models 1 and 3 detailed distributions of undercut stress were measured in the tube models only. For the couplings, only 2 positions were selected and the undercut stresses measured in order to confirm the tube load measurements.

The mean through-thickness stress and standard deviations for each model are presented and discussed in Chapter 7.

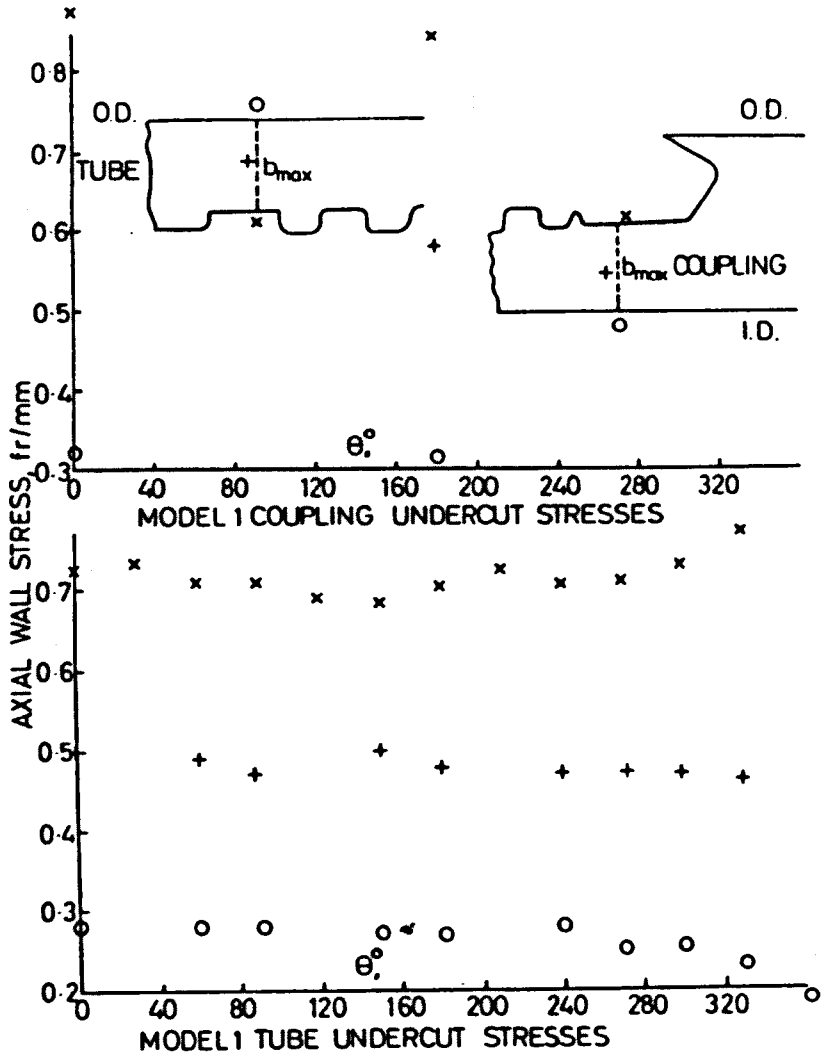

Fig A1.1 Distribution of Axial Stresses in the Undercuts of the Tube and Coupling in Model 1 Loaded with Axial Tension

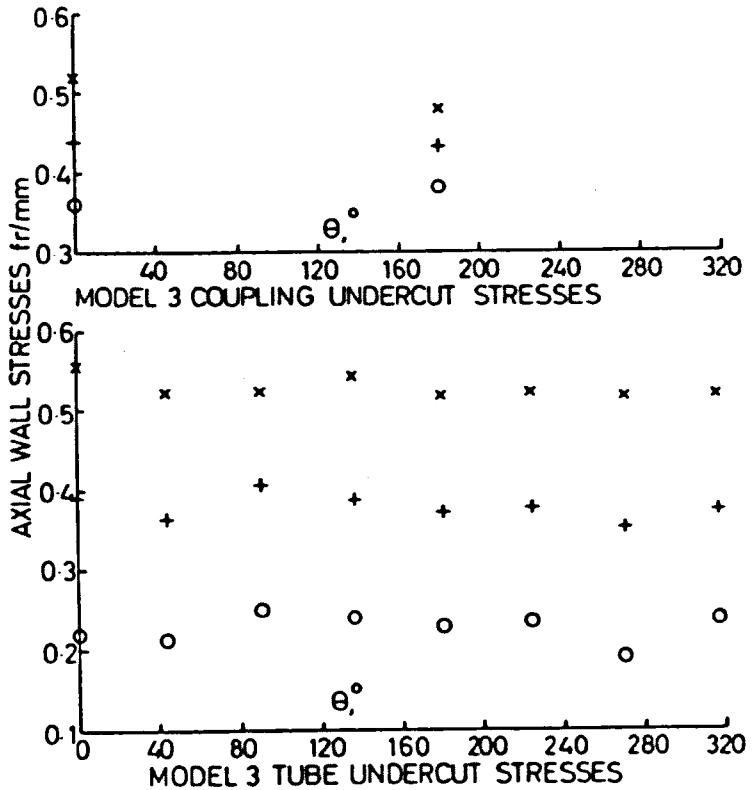

Fig A1.2 Distribution of Axial Stresses in the Undercuts of the Tube and Coupling in Model 3 Loaded with Axial Tension

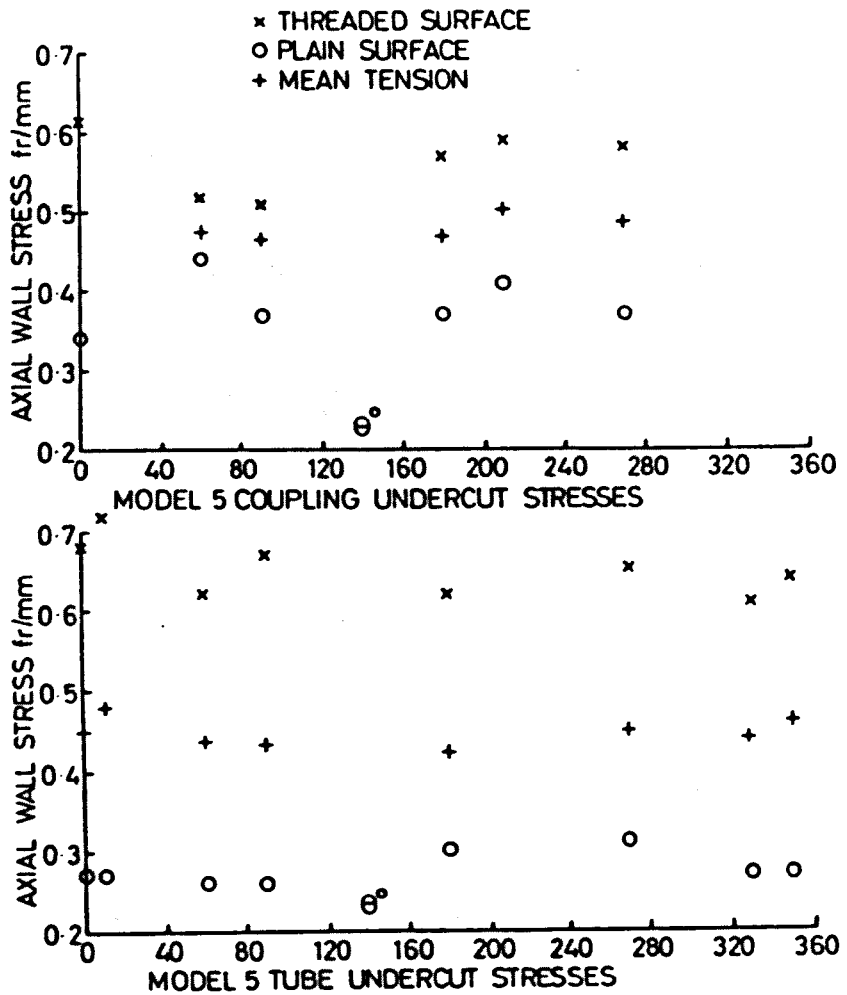

Fig A1.3 Distribution of Axial Stresses in the Undercuts of the Tube and Coupling in Model 5 loaded wiht Axial Tension

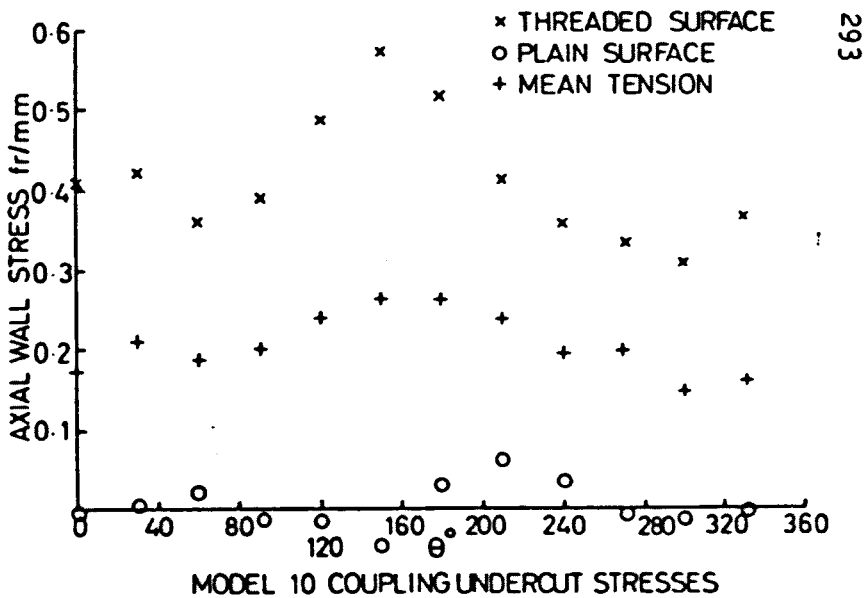

Fig A1.4 Distributions of Axial Stresses in the Undercut of the Coupling of Model 10 Loaded with Preload

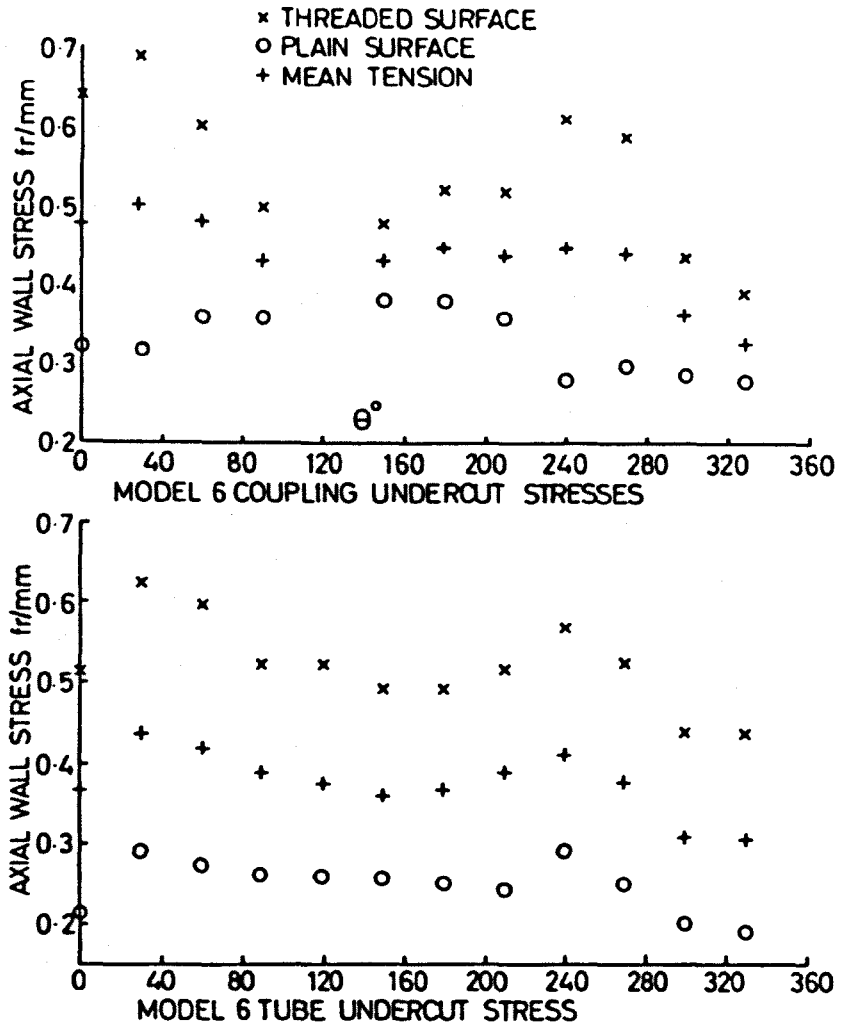

Fig A1.5 Distributions of Axial Stresses in the Undercuts of the Tube and Coupling of Model 6 Loaded with Axial Tension

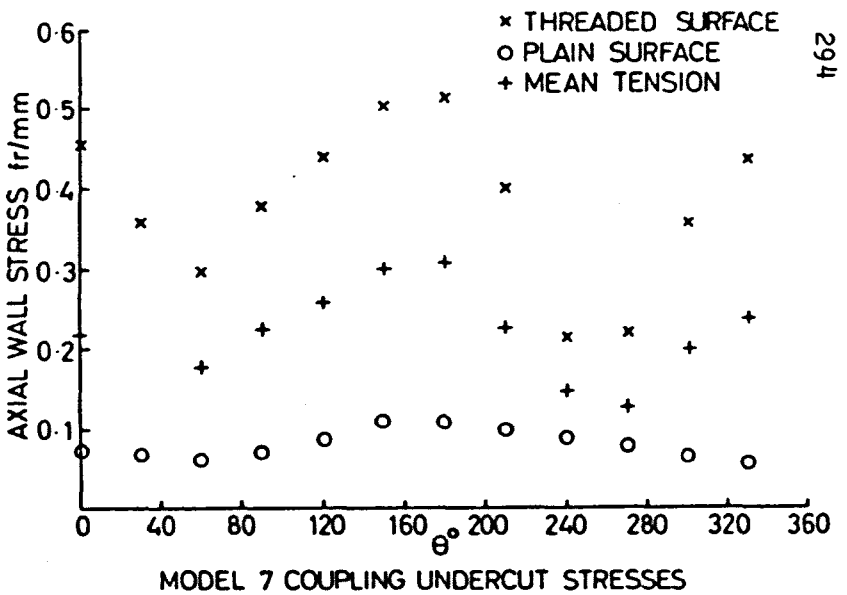

Fig A1.6 Distributions of Axial Stresses in the Undercut of the Coupling of Model 7 Loaded with Preload

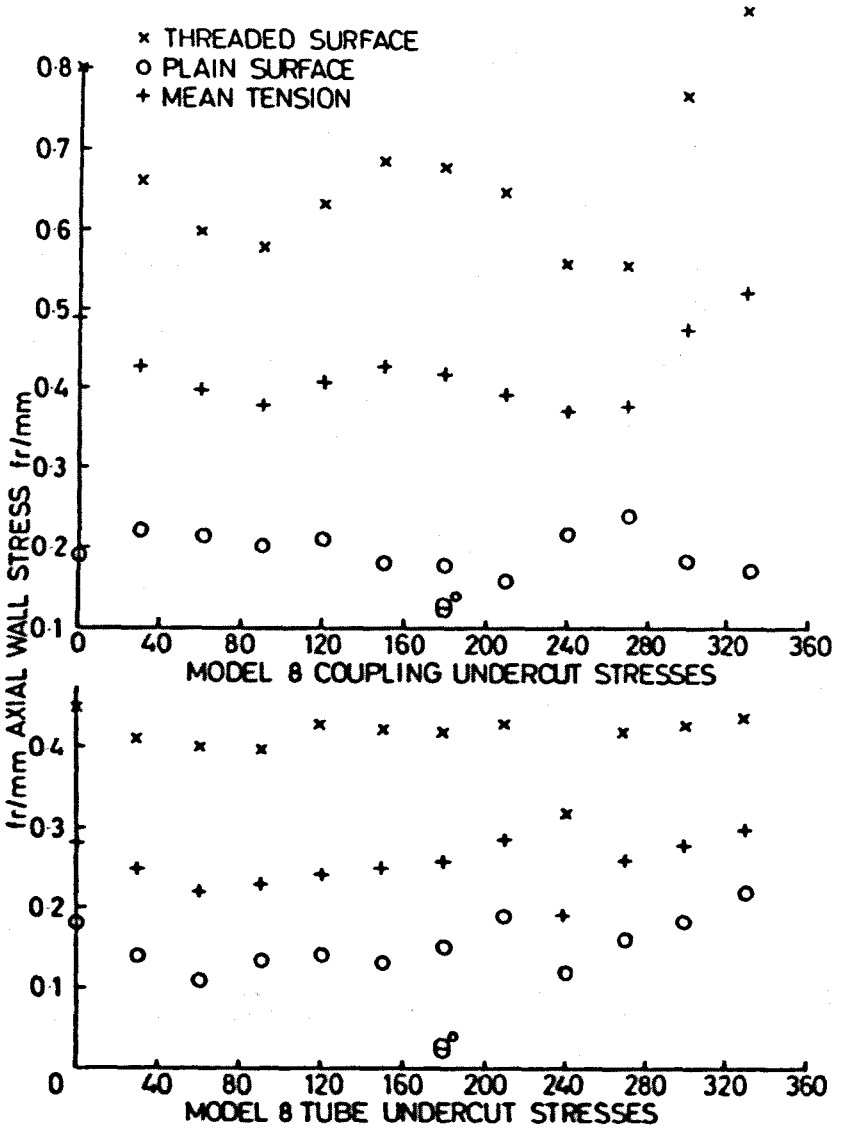

Fig A1.7 Distributions of Axial Stresses in the Undercuts of the Tube and Coupling of Model 8 Loaded with Tension Plus Preload

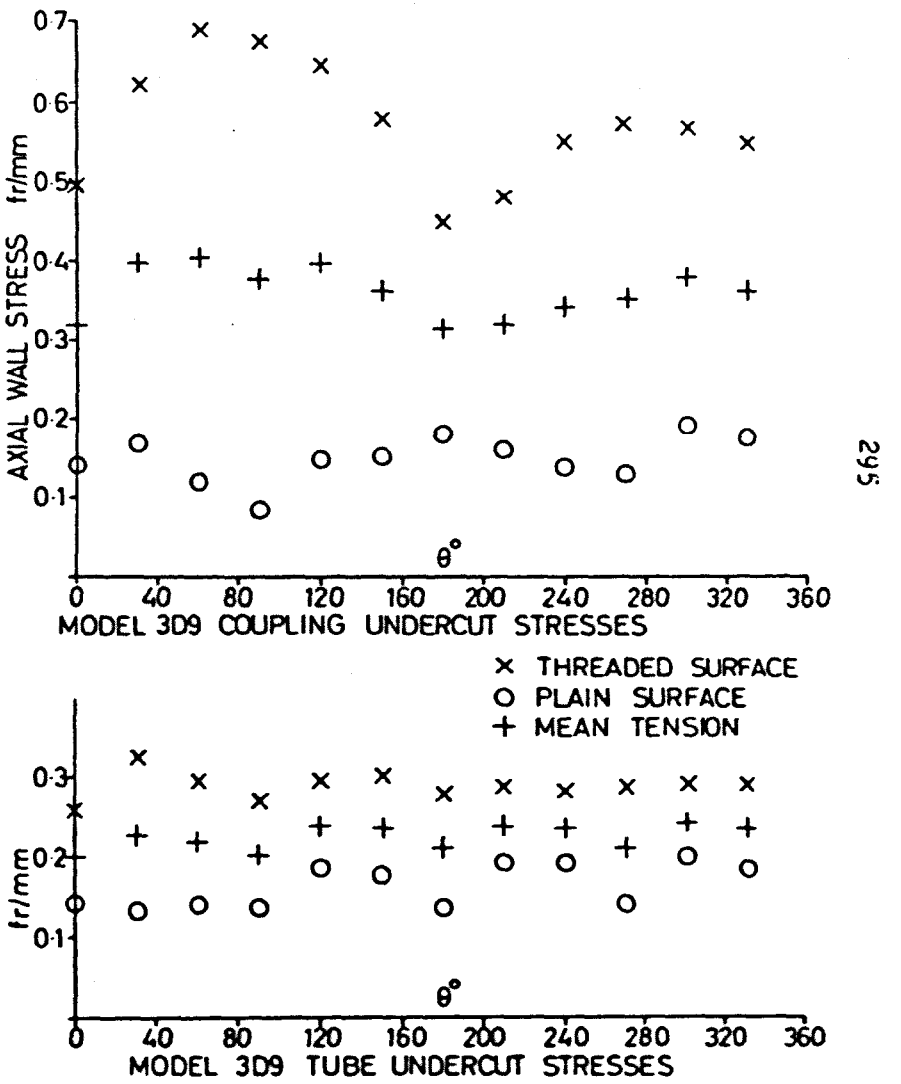

Fig A1.8 Distributions of Axial Stresses in th Undercuts of the Tube and Coupling of Model 9 Loaded with Tension Plus Preload

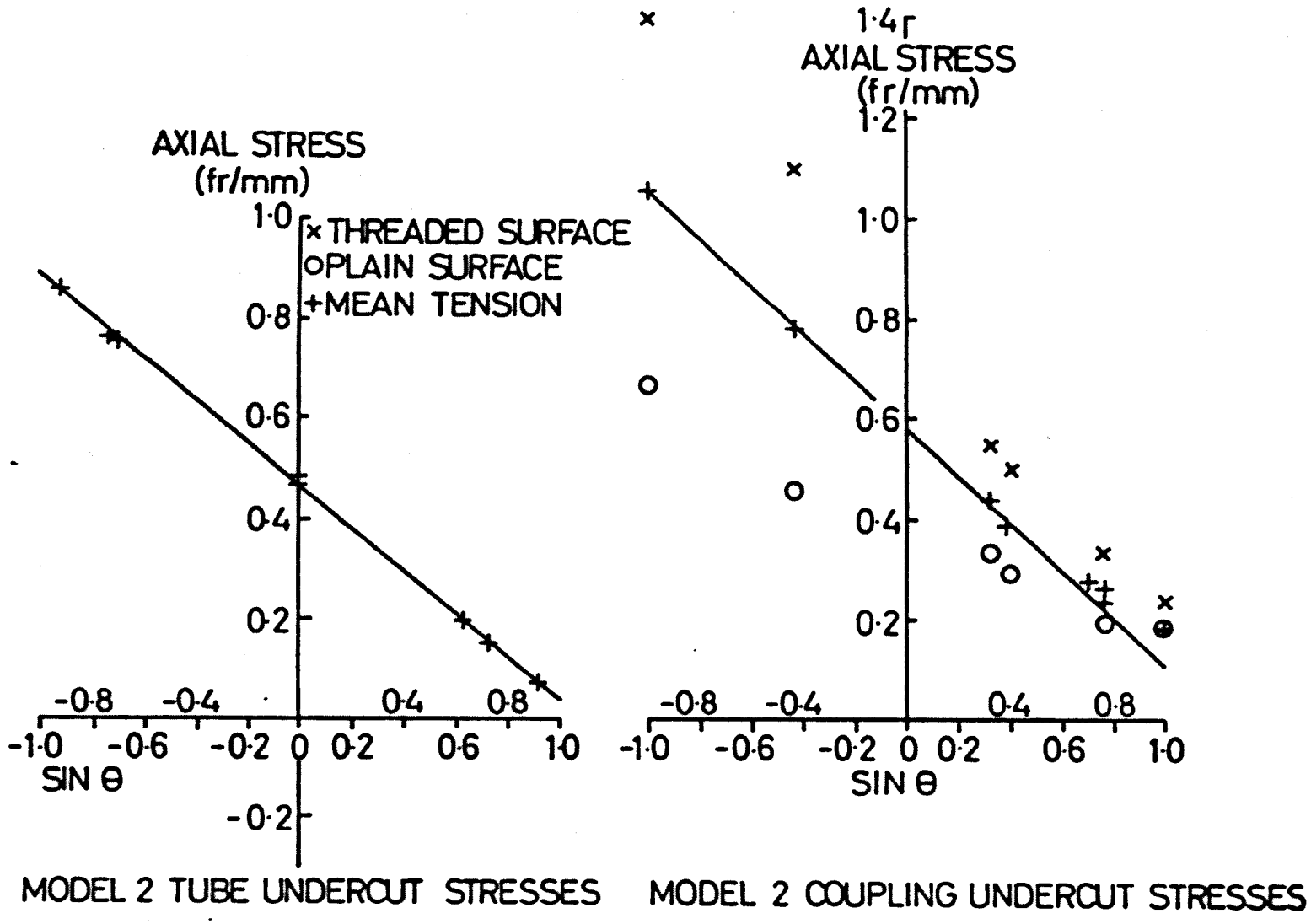

Fig A1.9 Definition of Coordinate System Used and A.M.P. Measured Distributions of Shear Stress τ_{rz} in the Tube Nose of Model 4

Appendix 2 Calculation of Model 4 Preload Using the Frocht Shear Difference Method

Frocht's shear difference method (19) uses the equilibrium equation in cartesian co-ordinates

$$\frac{\partial \sigma_r}{\partial r} + \frac{\partial \tau_{rz}}{\partial z} + \frac{\partial \tau_{r\theta}}{\partial \theta} = 0 \qquad \ldots \text{ A2.1}$$

to determine, along a straight line in the r direction, the changes in σ_r from the known values σ_{ro} at a free boundary. In finite difference form

$$\frac{\partial \tau_{r\theta}}{\partial \theta} = \frac{(\tau_{r\theta})_2 \quad (\tau_{r\theta})_4}{2\Delta\theta} \quad \text{and} \quad \frac{\partial \tau_{rz}}{\partial z} = \frac{(\tau_{rz})_1 \quad (\tau_{rz})_3}{2\Delta z} \qquad \ldots \text{ A2.2}$$

where Δz and $\Delta\theta$ are the spacing between adjacent grid lines, defined in Fig. A.2.1. The optimum spacing is the minimum necessary to obtain significant differences $(\tau_{r\theta})_2 - (\tau_{r\theta})_4$; $\Delta z = \Delta r = 0.3$ mm has been used for the work shown. Slices (containing the r-z plane) have to be >1 mm thick because 0.2 mm is needed between the edge of the sub-slice (containing the r-θ plane) and a line of measurements to account for surface irregularities, malalignment of the grid lines and sufficient time for measurements to be taken before time-edge effect (due to absorption of moisture from the atmosphere) affects the readings.

Tesar's modification (34) was used to determine the shear stress gradients. With material fringe value f, fringe order n and slice thickness s

$$\frac{\partial \tau_{r\theta}}{\partial \theta} = \frac{f}{2} \frac{\partial}{\partial \theta} \left(\frac{n}{s} \sin 2\Phi\right) = \frac{f}{2s} \left(2n \cos 2\Phi \frac{\partial \Phi}{\partial \theta} + \frac{\partial n}{\partial \theta} \sin 2\Phi\right) \qquad \ldots \text{ A2.3}$$

where Φ is the isoclinic angle measured from the r direction to the greater principal stress. In finite difference form, for the lines

defined in Fig. A2.1

$$\frac{\partial \tau_{r\theta}}{\partial \theta} = \frac{f}{4S\Delta\theta}[2n_o\ (\Phi_2 - \Phi_4)\ \cos 2\ \Phi_o + (n_2 - n_4)\ \sin 2\ \Phi_o] \quad \ldots\ A2.4$$

similarly

$$\frac{\partial \tau_{rz}}{\partial z} = \frac{f}{4S\Delta z}[2n_5\ (\Phi_1 - \Phi_3)\ \cos 2\ \Phi_5 + (n_1 - n_3)\ \sin 2\ \Phi_5] \quad \ldots\ A2.5$$

Numerical integration of equation A2.1 from a position where σ_r is known (starting from a free surface) to a point Δr from the surface yields the value of σ_r at that point i.e.

$$\sigma_{ri} = \sigma_{ro} - \Delta r \left(\frac{\partial \tau_{rz}}{\partial z} + \frac{\partial \tau_{r\theta}}{\partial \theta} \right) \qquad \ldots A2.6$$

$\partial \tau_{rz}/\partial_z$ and $\partial \tau_{r\theta}/\partial\theta$ have been found from equations A2.4, A2.5 and from measurements of n and Φ in the r-z and r-θ planes.

The distributions of σ_z and τ_{rz} have been found from measurements in the r-z plane at line 0 from

$$\sigma_z = \sigma_r - \frac{f}{s}\ n_o\ \cos 2\Phi_o \qquad \ldots\ A2.7$$

and

$$\tau_{rz} = \frac{f}{2s}\ n_o\ \sin 2\Phi_o \qquad \ldots\ A2.8$$

and the distributions of σ_θ and $\tau_{r\theta}$ have been found from measurements in the r-θ plane at line 3 from

$$\sigma_\theta = \sigma_r - \frac{f}{2s} n_3\ \cos 2\Phi_3 \qquad \ldots\ A2.9$$

and

$$\tau_{r\theta} = \frac{f}{2s} n_3\ \sin 2\Phi_3 \qquad \ldots\ A2.10$$

Fig. A2.1 and Fig. A2.2 shows the AMP measured shear stresses τ_{rz} and $\tau_{r\theta}$ obtained from the fringe order and isoclinic angle readings in the r-z and r-θ planes of 1 stress separation carried out. Fig. A2.3 and

A2.4 shows the shear stress gradients calculated by equations A2.4 and A2.5 and the values of σ_r obtained from them using equation A2.6. The through thickness distribution of cartesian stresses is shown in Fig. 5.4. For the other plane in which a stress separation was carried out i.e. $\theta=0^{o}$, the distribution of cartesian stresses is shown in Fig. A2.5.

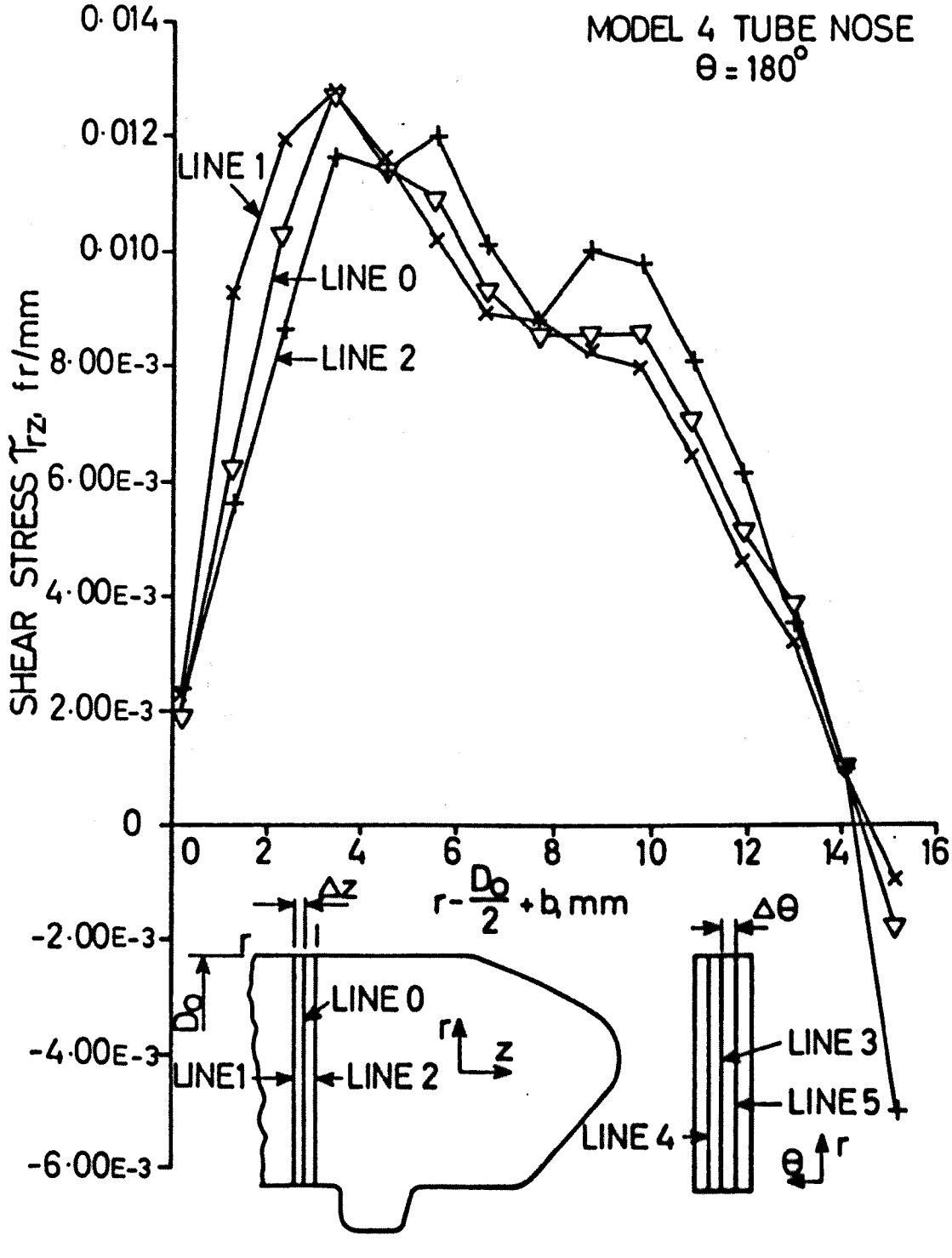

Fig A2.1

Definition of Coordinate System Used and A.M.P. Measured Distributions of Shear Stresses τ_{rz} in the Tube Nose of Model 4

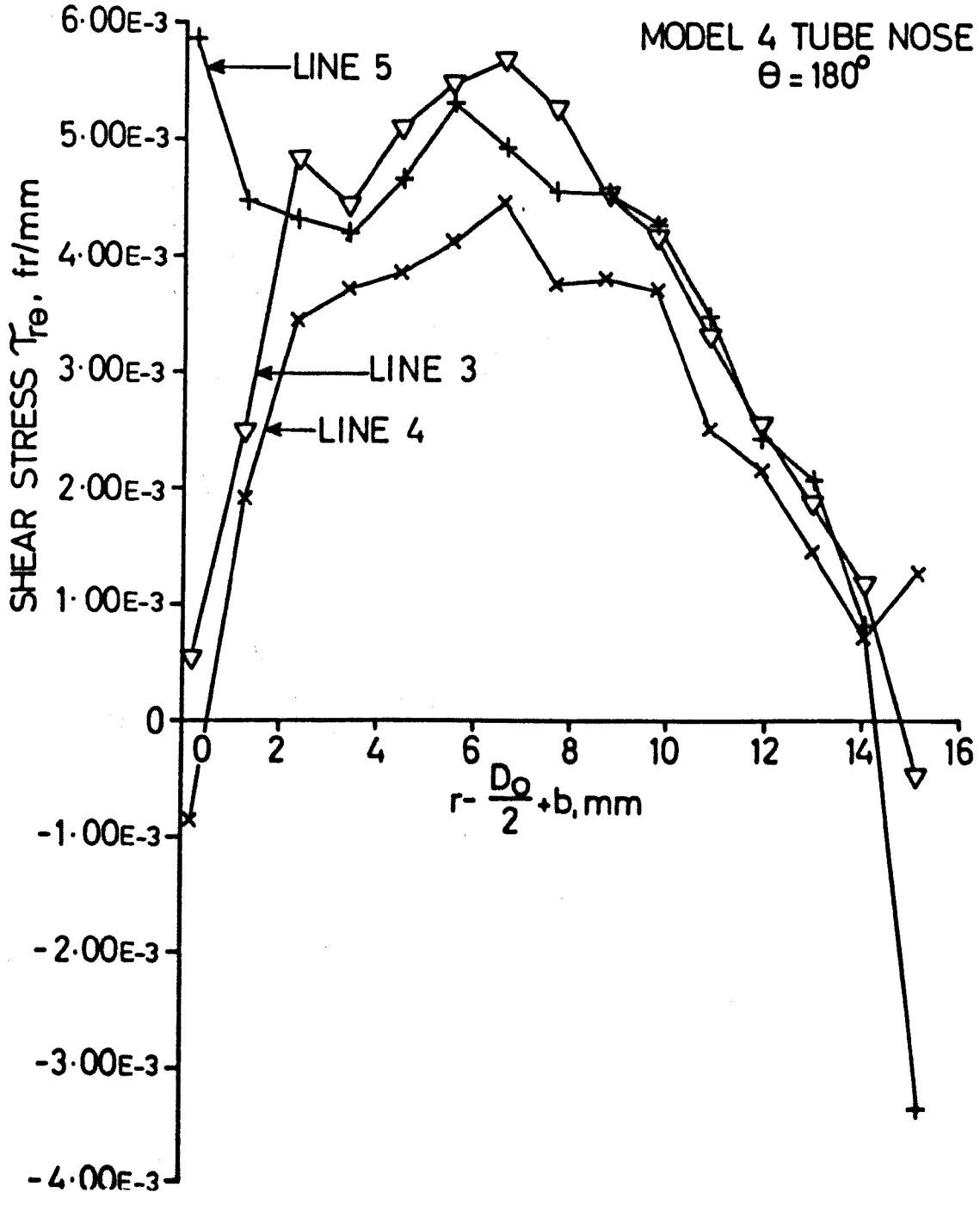

Fig A2.2

Distributions of $\tau_{r\theta}$ Measured Using the A.M.P. in the Tube Nose of Model 4

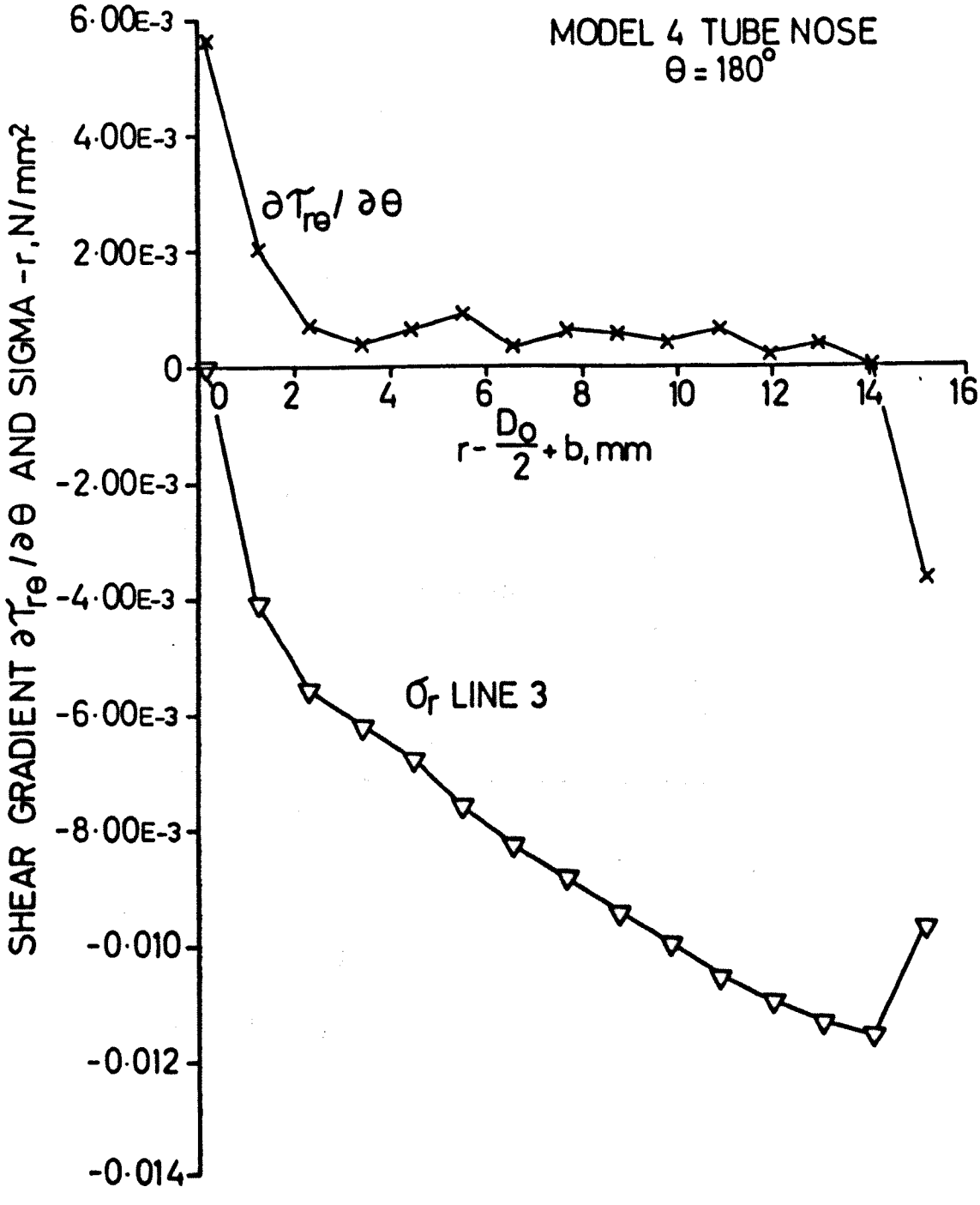

Fig A2.3

Distribution of Shear Stress Gradient $\partial\tau_{r\theta}/\partial\theta$ and σ_r in the Tube Nose of Model 4

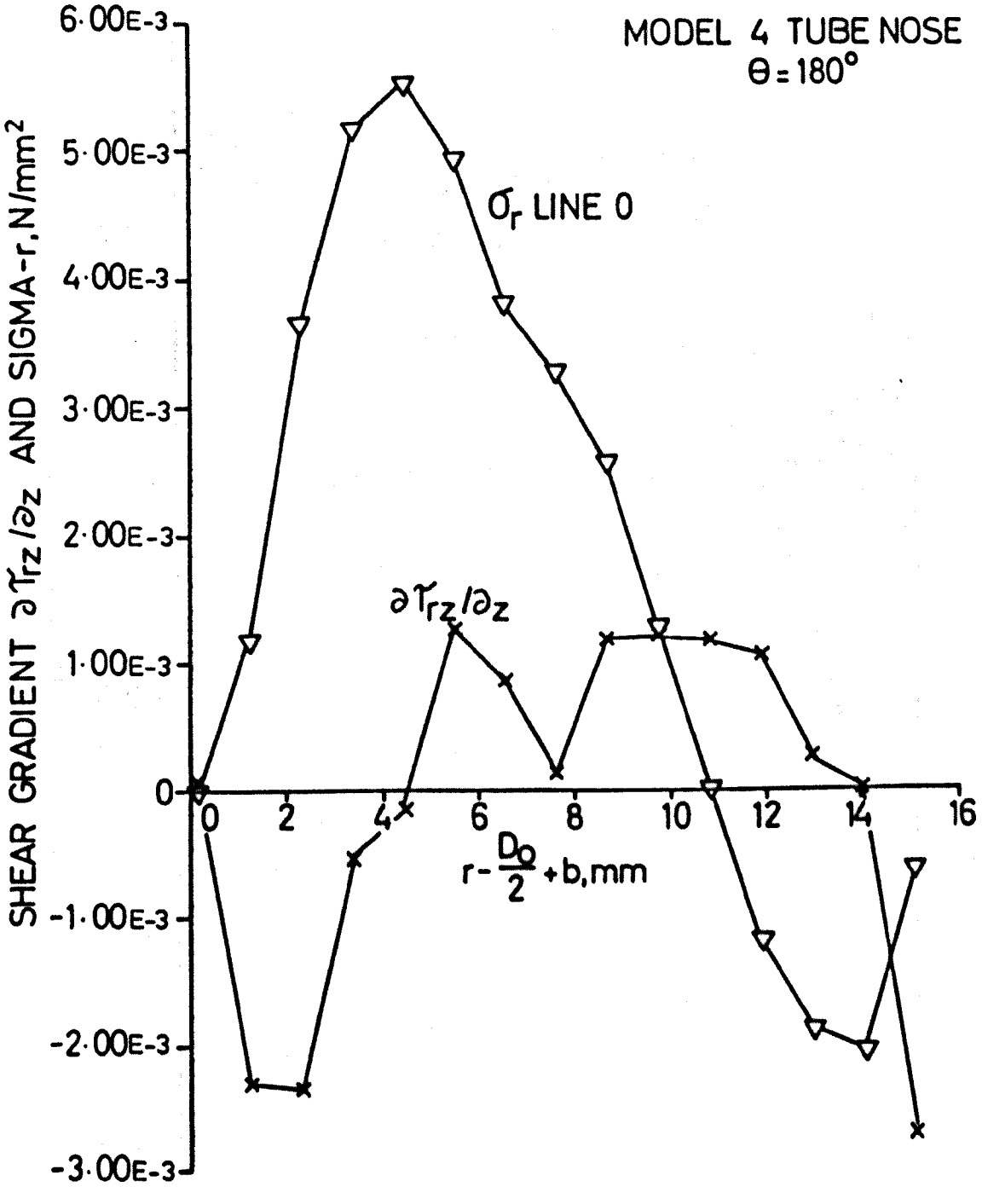

Fig A2.4

Distribution of Shear Stress Gradient $\partial\tau_{rz}/\partial_z$ and σ_r in the Tube Nose of Model 4

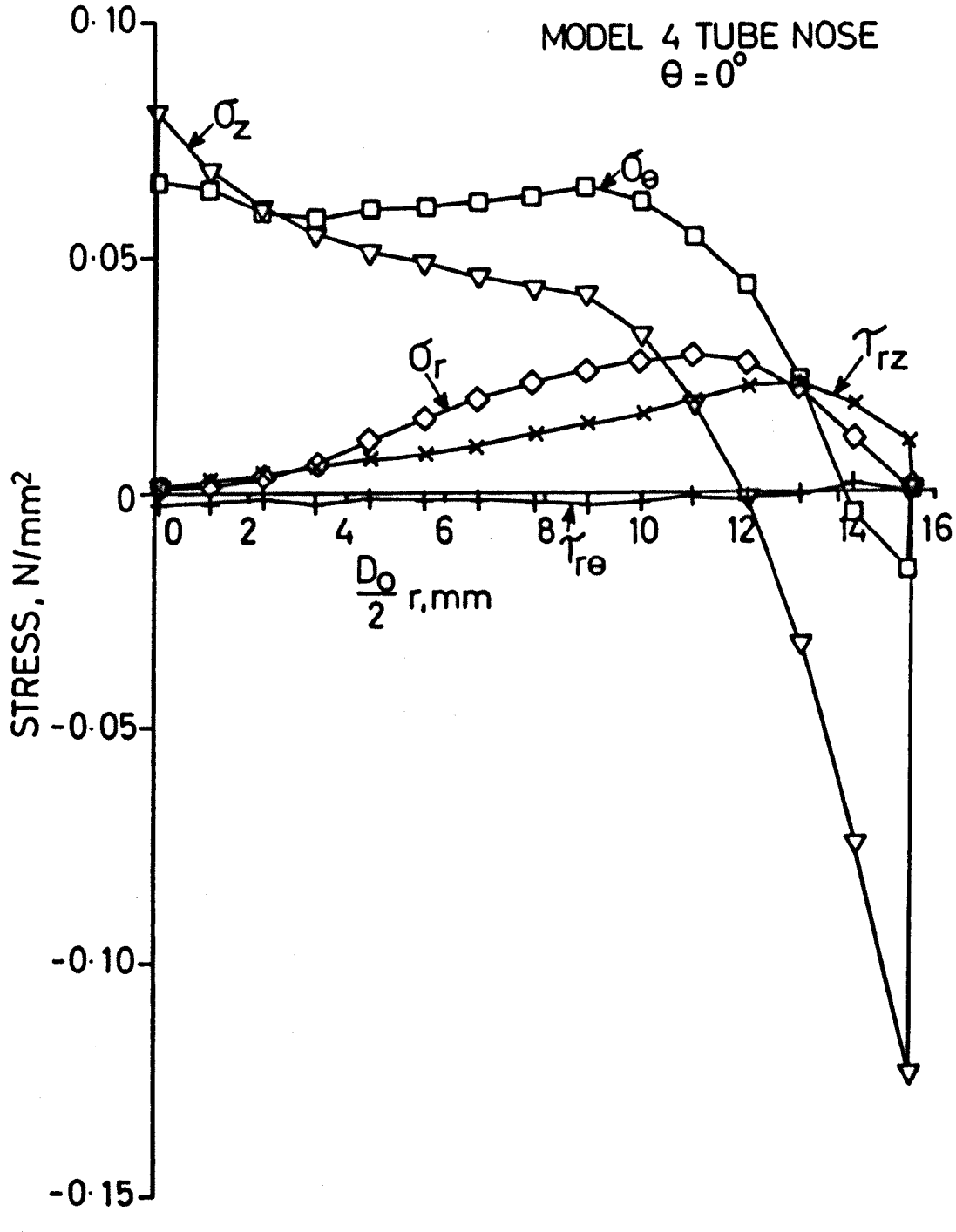

Fig A2.5

Distribution of Cartesian Stresses in the Tube Nose of Model 4

Appendix 3 Explanation of Forces In Seal Region of Model 4

A small preload Q_o was applied to Model 4 which put the tube nose into contact with the coupling seal. When the axial force F was applied, a radial force aF was applied to the coupling seal due to tube model bending and also due to the coupling seal which restrained the tube model's diametral growth due to Poissons ratio effects.

The radial force aF on the seal can be separated into components parallel and perpendicular to the seal i.e. $aF\sin\emptyset$ and $aF\cos\emptyset$, where $\emptyset$ is the seal angle, see Fig. A3.1. The component perpendicular to the seal surface created a frictional force ϕ a F $\cos\emptyset$ parallel to the surface which opposed relative movement at the seal surface and hence separation of the tube nose and coupling seal. Measurements of the total shear forces carried by the thread spiral, and stress separation in the tube nose, have shown that the remaining axial force in the tube nose = 0.14F, see Section 5.1. From Equilibrium of the forces parallel and perpendicular to the seal surface, the value of the coefficient of friction at the seal has been found.

For Forces parallel to the seal

$$\mu\ aF\cos\emptyset = aF\sin\emptyset + 0.14\ F\cos\emptyset \qquad \text{..... A3.1}$$

For forces perpendicular to the seal

$$0.14\ F\sin\emptyset = aF\cos\emptyset \qquad \text{..... A3.2}$$

Substituting $\emptyset = 30^\circ$ into Equation A3.2 gives $\alpha = 0.081$ which when substituted into Equation A3.1 gives the coefficient of friction

$$\mu = 2.3$$

This high value of μ indicates that the lubricant had been expelled from the seal.

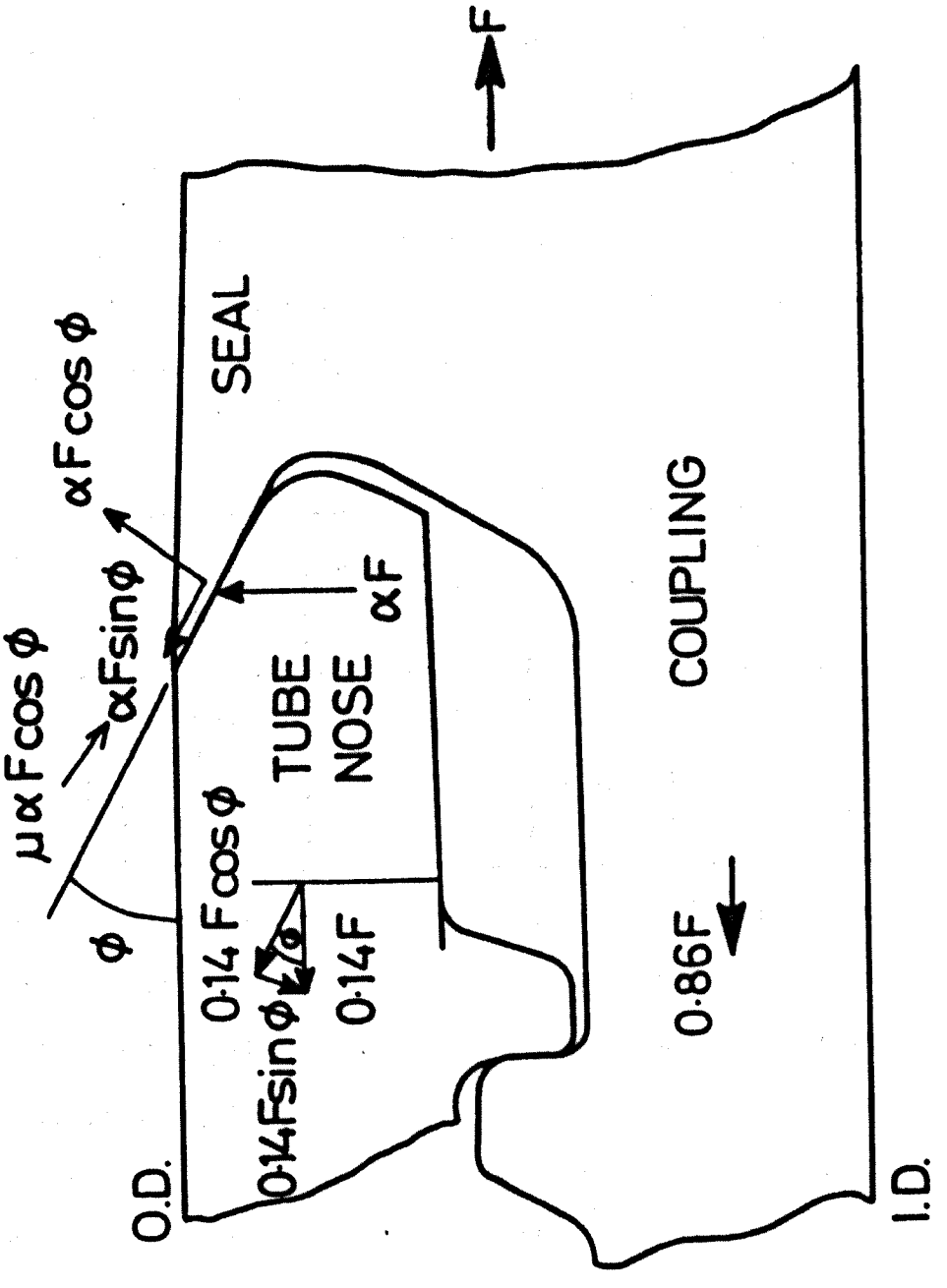

Fig A3.1

Forces in the Seal Region of Model 4

Appendix 4 Typical Distributions of Shear Stress Across the Roots of Threads

As was explained in Section 5.2, the distribution of shear stress τ_{rz} was measured across the root of each thread whose shear force was to be obtained. Due to the large number of measurements of shear forces which were made it is impractical to show all of them but a selection is shown here. They show that the differences in shape of the distributions of τ_{rz} are primarily due to the position in the thread where the measurements were taken. Table A4.1 gives the important information for each shear stress distribution shown.

Table A4.1

FIGURE	MODEL	POSITION OF THREAD z/L	NORMALISED SHEAR FORCE	THREAD RADIUS R, mm	DISTANCE OF MEASUREMENTS FROM THREAD ROOT, mm
A4.1	4TUBE	-0.026	-0.005	1.98	0.55
A4.2	"	0.128	1.07	"	0.70
A4.3	9COUPLING	0.989	3.15	2.38	0.50
A4.4	"	0.500	1.50	"	1.50

Fig A4.1 shows the distribution of τ_{rz} across an unloaded thread in the region of the tube of Model 4 where the normalised wall force $\simeq$ 1.

Fig A4.2 shows a typical distribution of τ_{rz} for a loaded thread. Three regions have been highlighted:-

1) This peak in shear stresses is due to the high stresses in the thread fillet, and the fact that the line of mesurements was inclined at an angle to the free surface,

2) A position where $d\tau_{rz}/dz = 0$, this local maximum is due to the proximity and magnitude of the shear stresses due to the contact region,

3) This local peak in the shear stresses at the unloaded flank surface is due to the proximity of the fillet. Its magnitude is generally less than that of 1) since the surface stresses in this fillet were less than the loaded face fillet. Also due to the cone angle, the position 3) was further around the fillet on the unloaded flank. It can be seen from figures A4.2, A4.3, A4.4 and Fig. 5.5 that the relative magnitudes of the shear stresses at positions 1) 2) and 3) varied with the position in the thread of the line of measurements. As the line of measurements moved up the thread and out of the fillet then the value of the shear stresses at positions 1) and 3) reduced since the angle of inclination between the line of measurements and the free surfaces tended to 90^{o} for the loaded face and 80^{o} for the unloaded face. Also the relative magnitude of the shear stresses at position 2) increased as the position of the line of measurements neared the contact region.

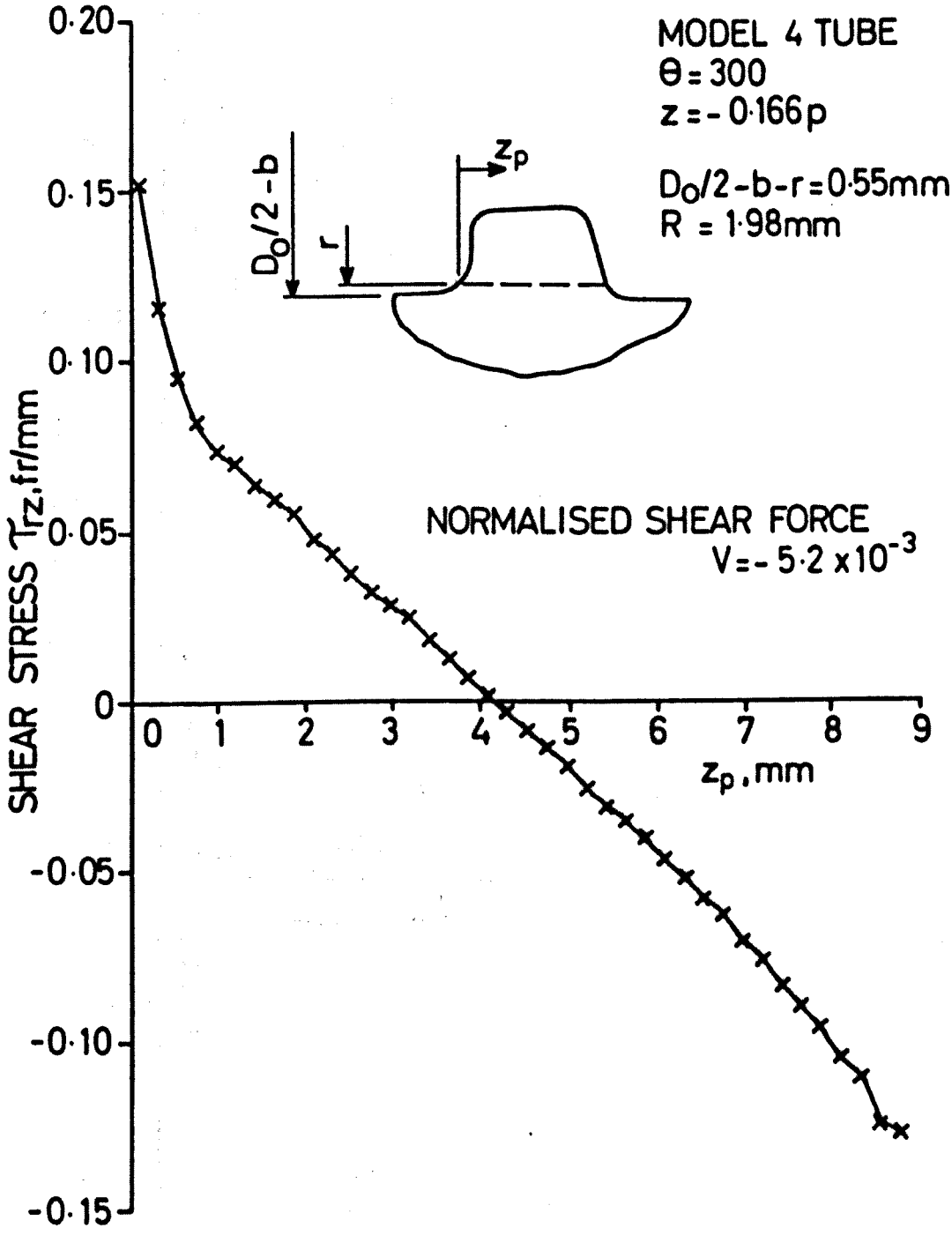

Fig A4.1

Distribution of Shear Stress τ_{rz} Across a Thread Carrying no Shear Force

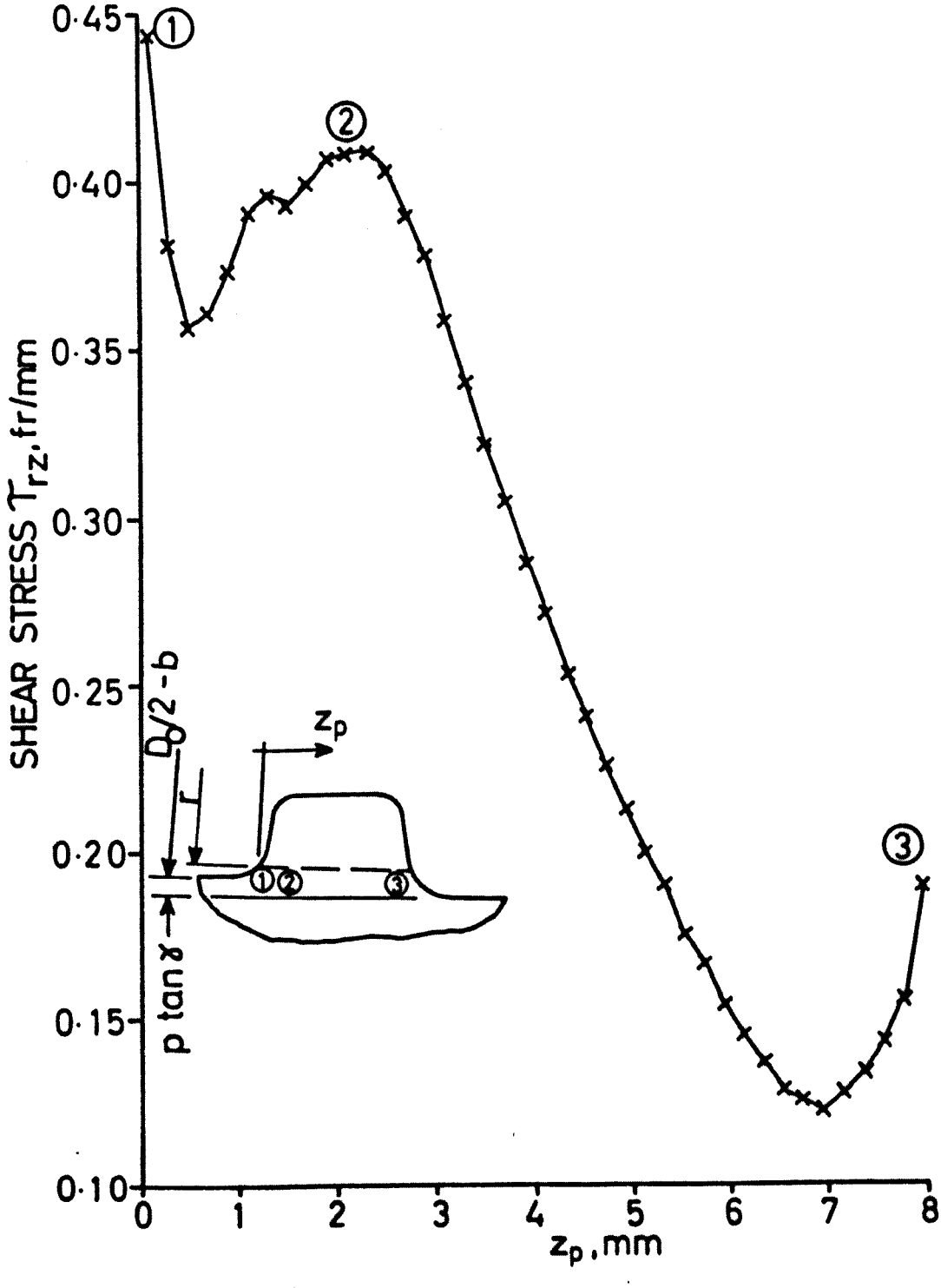

Fig A4.2

Distribution of Shear Stress τ_{rz} Across a Typical Thread Carrying Shear Force and Measured 0.7 mm from the Thread Root

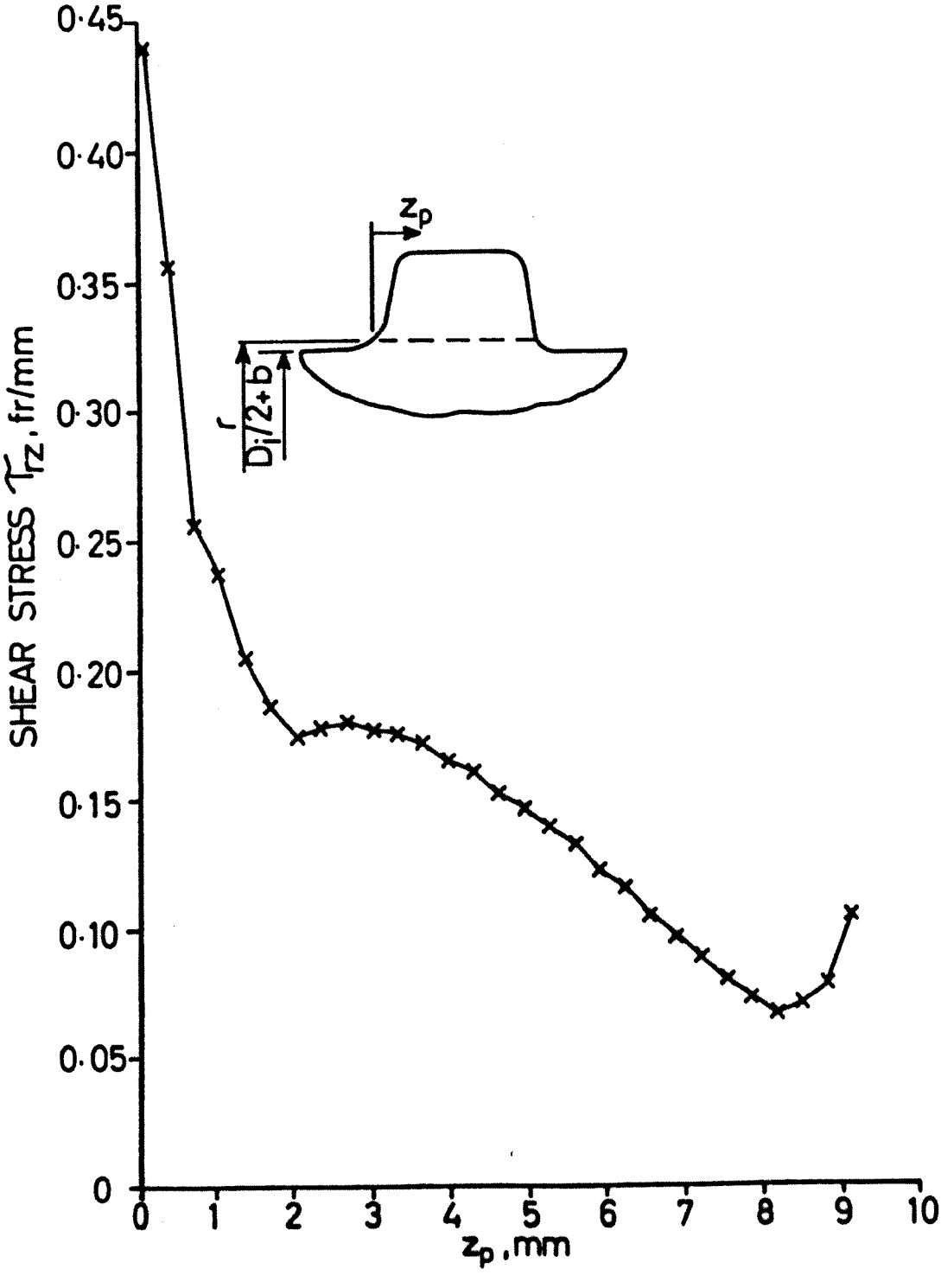

Fig A4.3

Distribution of Shear Stress τ_{rz} Across a Typical Thread Carrying Shear Force and Measured 0.5 mm from the Thread Root

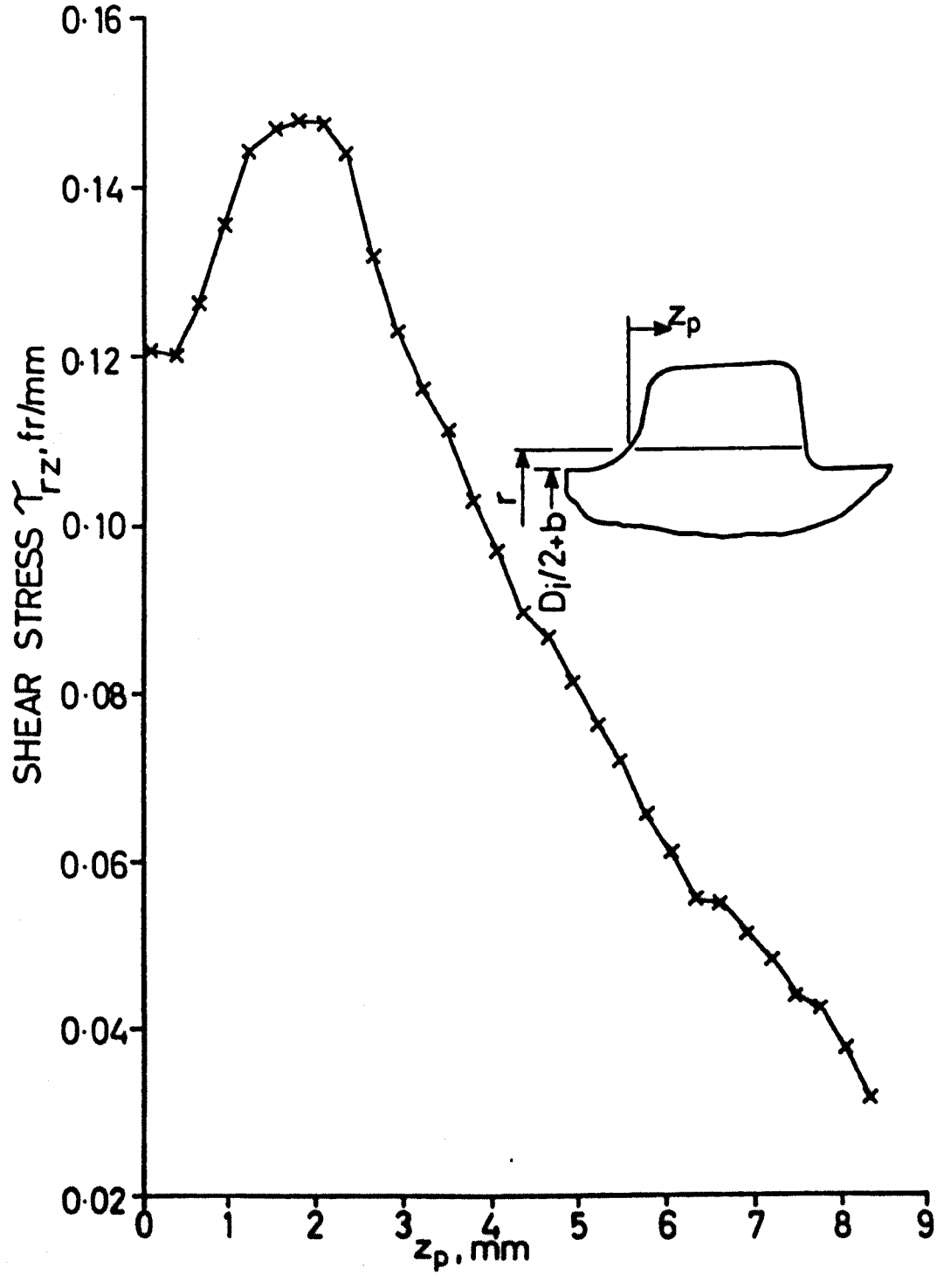

Fig A4.4

Distribution of Shear Stress τ_{rz} Across a Typical Thread Carrying Shear Force and Measured 1.5 mm from the Thread Root

Appendix 5 Kirsch Solution for a Hole in an Infinite Plate

Kirsch (38) developed a mathematical solution for a hole of radius R in an infinite plate under uniform uniaxial tensile stress . It gives the stresses anywhere in the plate as:

$$\sigma_r = \frac{\sigma}{2}\left(1 - \frac{R^2}{r_F^2}\right) - \frac{\sigma}{2}\left(1 - \frac{4R^2}{r_F^2} + \frac{3R^4}{r_F^4}\right) \cos 2\Psi \qquad \text{A5.1}$$

$$\sigma_\Psi = \frac{\sigma}{2}\left(1 + \frac{R^2}{r_F^2}\right) + \frac{\sigma}{2}\left(1 + \frac{3R^4}{r_F^4}\right) \cos 2\Psi \qquad \text{A5.2}$$

$$\tau_{r\Psi} = \frac{\sigma}{2}\left(1 + \frac{2R^2}{r_F^2} - \frac{3R^4}{r_F^4}\right) \sin 2\Psi \qquad \text{A5.3}$$

at $r_F = R$

$\sigma_r = \tau_{r\Psi} = 0$ and

$\sigma_\Psi = \sigma(1 + 2 \cos 2\Psi)$ A5.4

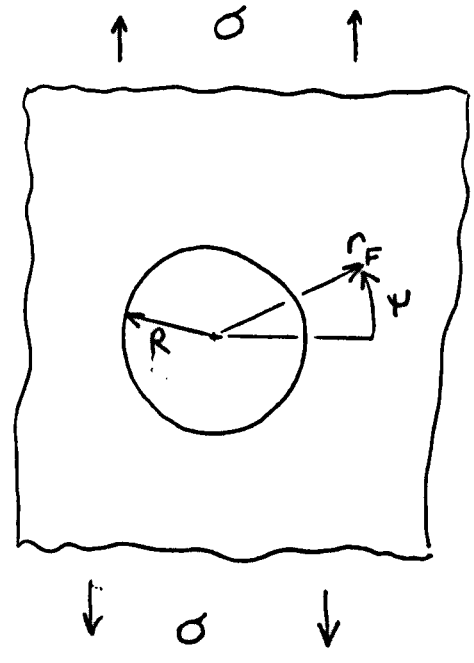

or in terms of the coefficients used to describe the stress distribution around thread fillets

$$\sigma_a = \sigma_{sa}(C_1 + C_2 \cos 2\Psi)$$

where for the case of a hole in an infinite plate $C_1 = 1$ and $C_2 = 2$. Since both w and b are infinite, no information can be obtained about the effects of the parameters R/b and w/b on the coefficients C_1 and C_2 from a hole in an infinite plate.

Appendix 6 Calculations of Nominal Bending Stresses Due to Shear Forces

Roark and Young (39) give formulas for the calculation of forces, moments and displacements for long and short thin-walled cylindrical shells with free ends subjected to axisymmetric loadings. The formulas are based on differential equations similar to those used to obtain formulas for beams-on-elastic-foundations.

The shear forces applied at the threads in the Araldite models and the Finite Element meshes could be considered to produce an axial force V and a moment M_o.

Several assumptions have been made in analysing the threaded connections as a thin walled cylinder loaded axisymmetrically:-

i) the tubes and couplings should have been thin i.e. $(D_o - b)/2b > 10$ for tubes and $(D_i + b)/2b > 10$ for couplings. In fact the ratios varied from 6 for threads near the undercuts of the thicker walled Araldite models to 12 for threads at the thin end of the thinner walled models.

ii) the tubes and couplings were not true cylinders due to the cone angle and the thread spiral. But. the cone angle was small and the stiffening effect of the thread spiral would have been similar to increasing the wall thickness by h/2.

iii) the tubes and couplings acted and reacted independently of each other to the applied loads. In practise this was only partially true. Variations in thread radial clearance show some relative radial movement between the mating halves of the connection but pitch measurements shows the pitch strains to be equal in mating threads.

iv) the ends of the tubes models were not free when loaded with preload,

v.) Araldite model loading was not axisymmetric but Section 8.1 shows that $dV/d\theta$ was small for tension only loading but was larger when preload was included.

The finite element meshes differed from the Araldite threaded connections in several respects, (see Section 6.2) and the only assumptions needed to be made when calculating the nominal bending stresses for the F.E. meshes is to neglect the stiffening effect of the thread-like projection on the tube.

The bending stress can be found from

$$\sigma_{SF} = \frac{6M}{b^2} \qquad \text{..... A6.1}$$

where M is the actual bending moment and is a function of the theoretical bending moment M_o where

$$M_o = V\ (e + b/2) \qquad \text{..... A6.2}$$

$$\therefore\ M = F\ (M_o)$$

$$\text{and}\quad F(M_o) = -r_A 2D\lambda^2 F_3 - \Psi_A D\ F_4 + LT_M \qquad \text{..... A6.3}$$

The constants are given in (39) for various values of λa, where for a coupling model

$$\lambda^4 = \frac{3(1 - \nu^2)}{(D_i + b)^2\ b^2} \qquad \text{..... A6.4}$$

Substituting values of D_i, b and ν into Equation A6.4 gives $\lambda \simeq 0.02\text{mm}^{-1}$. For the lengths of thread considered, a, varied from 10mm to 120mm, hence $\lambda a < 3$.

Hence

$$r_A = \frac{M_o\ A_4}{D\lambda^2} \qquad \text{..... A6.5}$$

$$\Psi_A = \frac{-2M_o A_1}{D\lambda} \qquad \text{..... A6.6}$$

$$LT_M = M_o\ F_{a1} \qquad \text{..... A6.7}$$

Substituting equations A6.5, A6.6 and A6.7 into A6.3 gives

$$F(M_o) = -2M_o(A_4F_3 - A_1F_4 - \frac{F_{a1}}{2}) \qquad \text{.....A6.8}$$

Where

$$A_4 = \tfrac{1}{2}e^{-\lambda a}(\sin\lambda a + \cos\lambda a) \quad \ldots\ldots \text{A6.9}$$

$$F_3 = \sinh\lambda z_M \sin\lambda z_M \quad \ldots\ldots \text{A6.10}$$

$$A_1 = \tfrac{1}{2}e^{-\lambda a}\cos\lambda a \quad \ldots\ldots \text{A6.11}$$

$$F_4 = \cosh\lambda z_M \sin\lambda z_M - \sinh\lambda z_M \cos\lambda z_M \quad \ldots\ldots \text{A6.12}$$

$$F_{a1} = \langle z_M - a\rangle^0 \cosh\lambda\langle z_M - a\rangle \cos\lambda\langle z_M - a\rangle \quad \ldots\ldots \text{A6.13}$$

where the function $\langle z_M - a\rangle^n$ is defined as

$$\langle z_M - a\rangle^n = (z_M - a)^n \text{ if } z_M > a$$

$$\text{and } \langle z_M - a\rangle^n = 0 \qquad \text{if } z_M < a$$

For the thread shape analysed the nominal bending stress was required at the blend of the fillet and thread root, hence

$$z_M = a + R$$

$$\therefore \quad F_{a1} = \cosh\lambda R \cos\lambda R$$

and since $\lambda R \to 0$, $F_{a1} = 1$.

If equations A6.9, A6.10, A6.11, A6.12, A6.13 and $F_{a1} = 1$ are substituted into equation A6.8 it can be shown that since R is small . . .

$$F(M_o) = M_o e^{-\lambda a}\{-\sinh\lambda a + \sin\lambda a\cos\lambda a\ (\cosh\lambda a - \sinh\lambda a) + 1/e^{-\lambda a}\}$$

$$\ldots\ldots \text{A6.14}$$

Equation A6.14 has been used to calculate $F(M_o)$ and M_o can be obtained from measurements of V, e and b from either photoelastically analysed models or finite element meshes. Hence, the nominal bending stress σ_{SF} has been found.

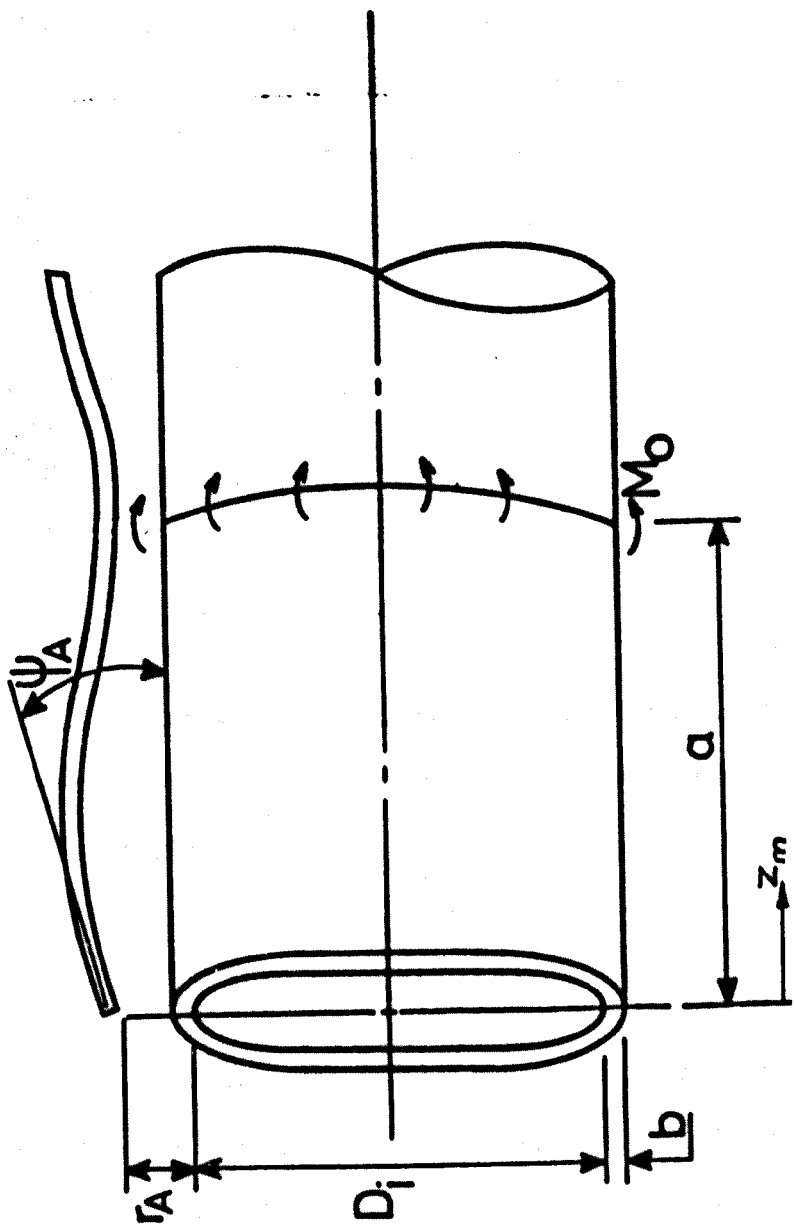

Fig A6.1

Definition of Symbols used in Calculating the Nominal Bending Stresses Due to Shear Forces

Appendix 7 Distribution of Stress Around Fillets Loaded with Wall Tension, Thread Shear Forces and Wall Bending Measured Using Finite Element and Photoelastic Techniques

Examples of the distribution of stress around fillets plotted against cos 2ϕ (for wall tension and wall bending) and against sin 2ϕ (for shear force only) have been presented in earlier chapters. The remaining distributions are presented in this Appendix. From these distributions best fit straight lines have been plotted and the coefficients C_1, C_2, C_3 and C_4 have been found which characterise the straight lines i.e.

$$\sigma_a = \sigma_{sa} (C_1 + C_2 \cos 2\phi)$$

for wall tension loading, and

$$\sigma_F = \sigma_{SF} (C_3 + C_4 \sin 2\phi)$$

for shear force loading

Figures A7.1, A7.2 and A7.3 show plots of normalised fillet stresses plotted against cos 2ϕ for different thread shapes and measured using Finite Element techniques. These threads were loaded with axial tension and the fillet stresses were normalised by the mean axial tensile stress.

Figures A7.4, A7.5 and A7.6 show plots of normalised fillet stresses plotted against cos 2ϕ for different thread shapes and measured using Finite Element techniques. These threads were loaded with wall bending and the fillet stresses were normalised by the tensile stress at the threaded surface of the mesh. This normalising stress was obtained by extrapolating the surface axial stresses to the position of the fillet and ignoring the stress raising effect of the fillet.

Fig A7.7, A7.8, A7.9 and A7.10 shows distribution of normalised surface fillet stress plotted against cos 2ϕ measured using the AMP in the unloaded runouts by different models. Although measurements were generally taken at $\Delta\phi = 2\frac{1}{2}^{o}$ only the measurements at $\Delta\phi = 5^{o}$ have been plotted on these figures for clarity.

Fig A7.11 to A7.15 show distributions of normalised fillet stresses due to shear forces plotted against sin 2ϕ for different thread shapes measured using Finite Element techniques. The distribution of fillet stress due to the wall tension (caused by the shear force) has been subtracted from the combined fillet stress to leave those stresses due to shear forces.

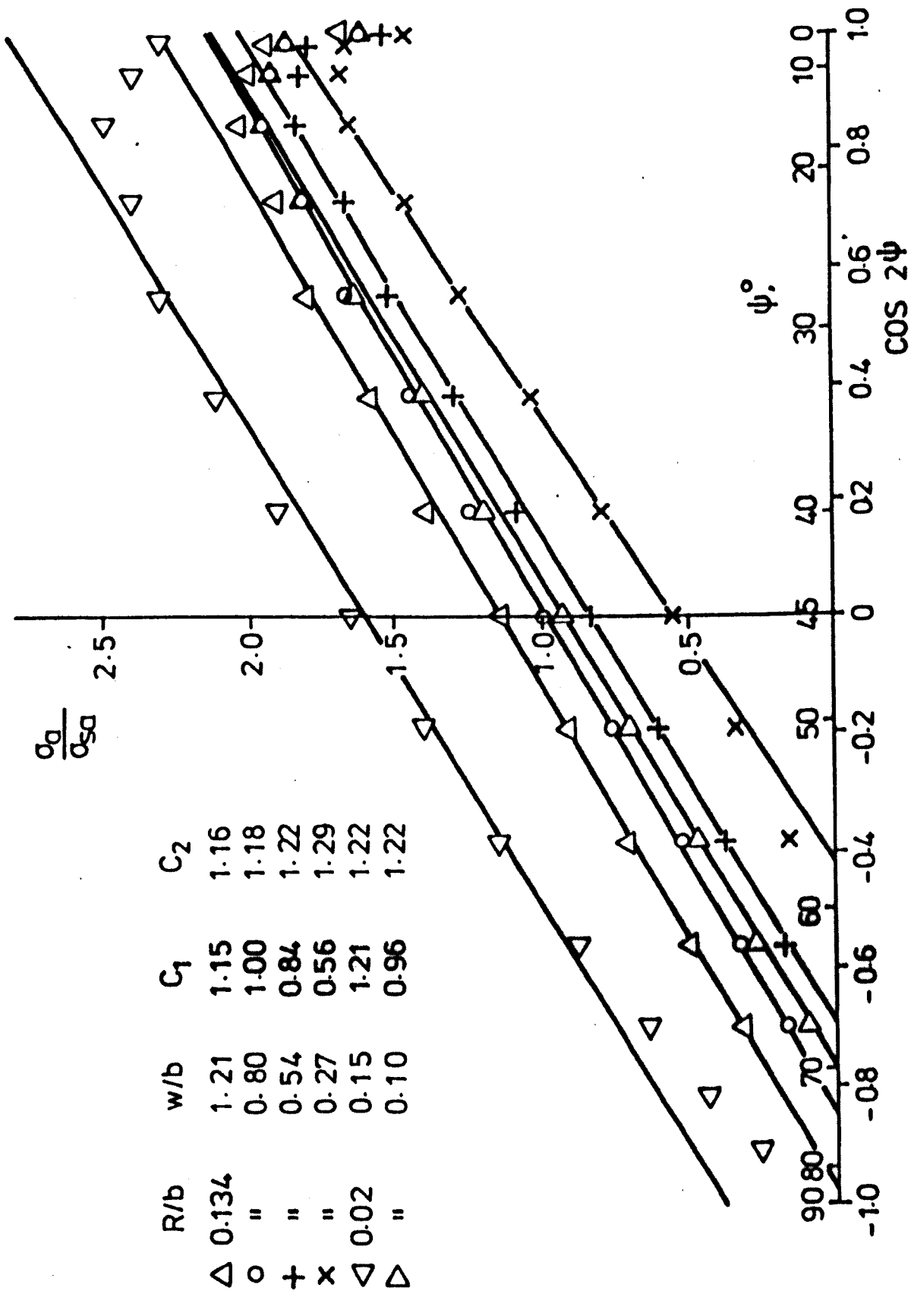

FIG. A7·1 Distributions of Normalised Fillet Stresses due to Wall Tension Plotted Against Cos 2Ψ from Finite Elements

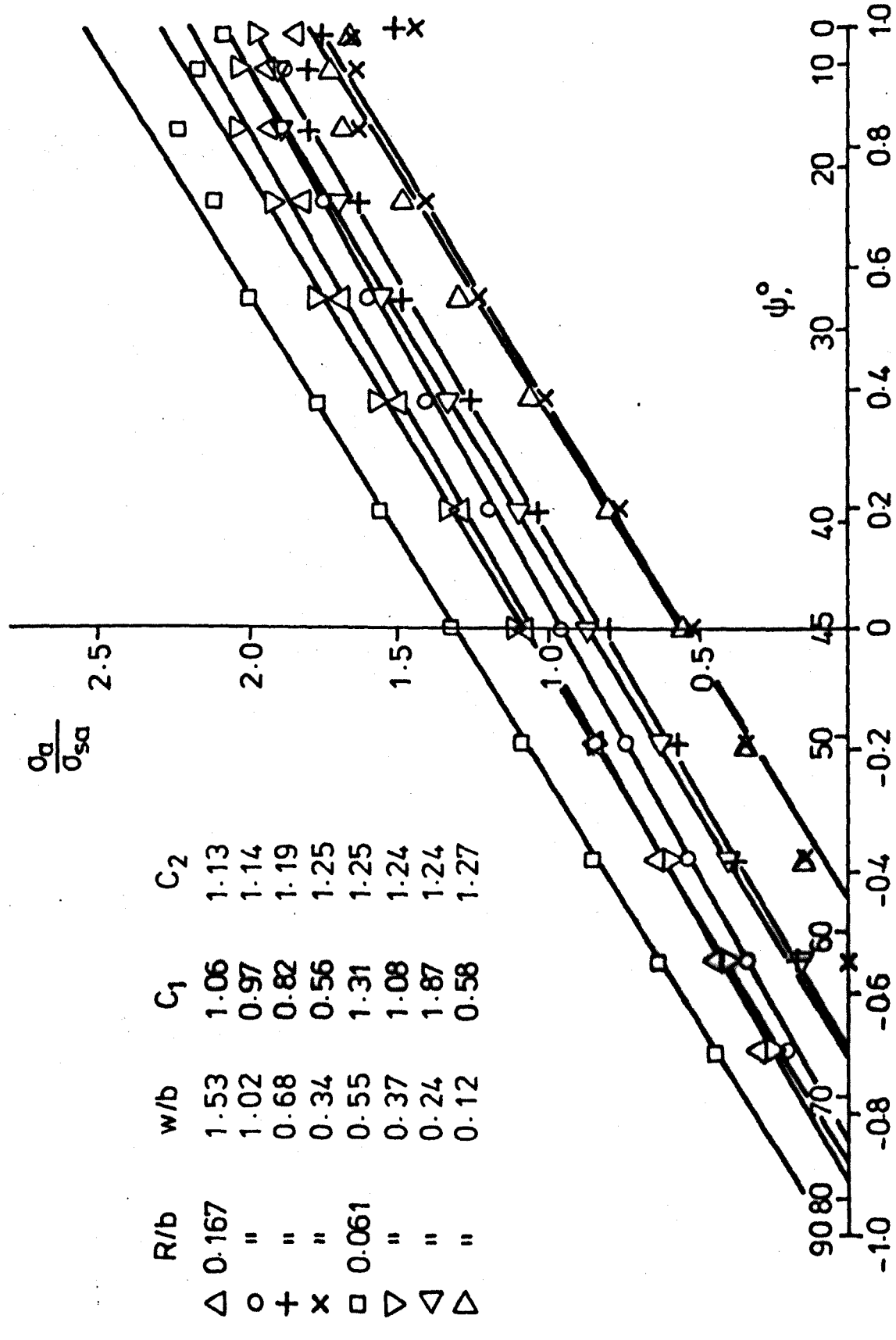

FIG. A7.2 Distributions of Normalised Fillet Stresses due to Wall Tension Plotted Against Cos 2ψ from Finite Elements

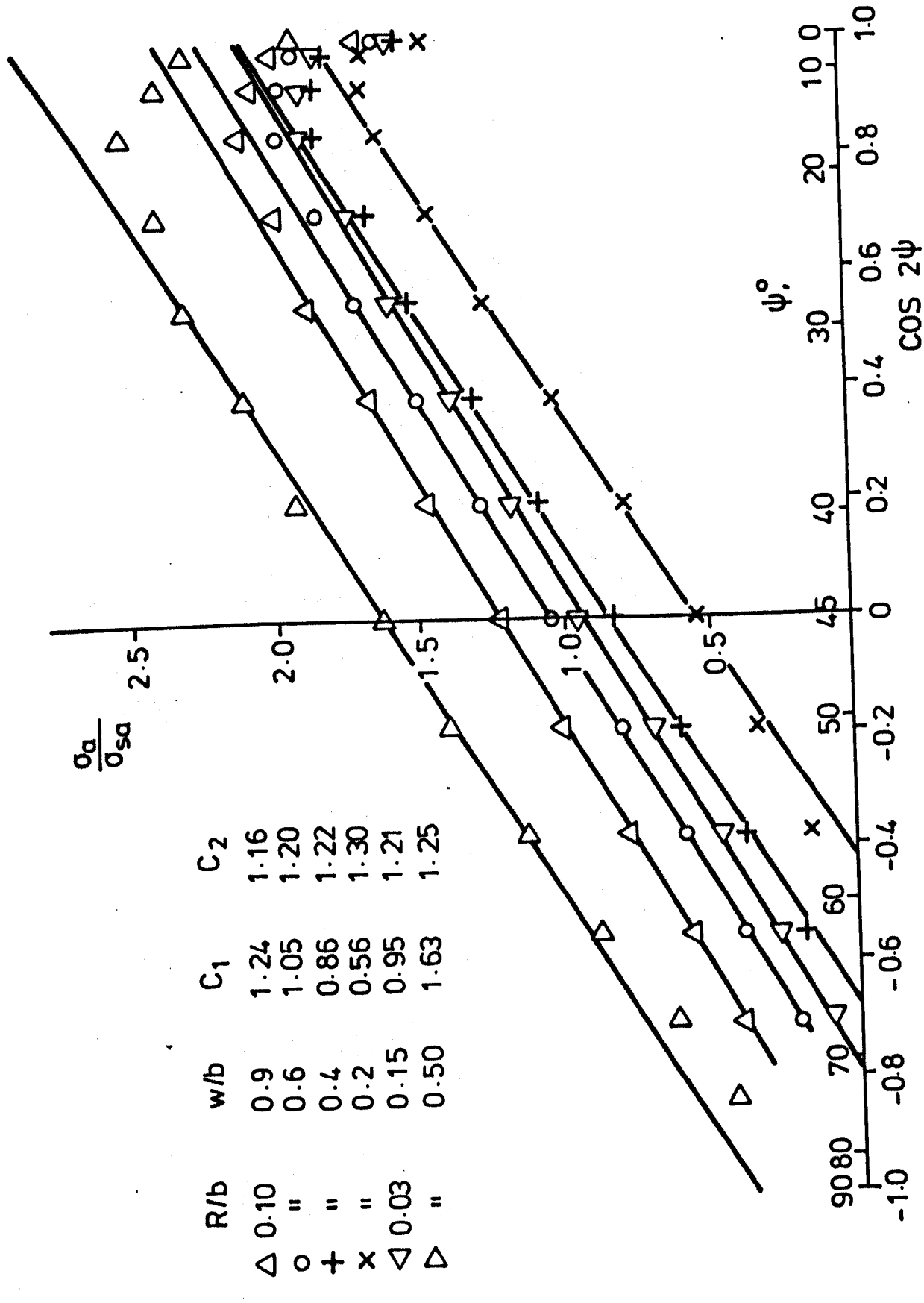

FIG. A7.3 Distributions of Normalised Fillet Stresses due to Wall Tension Plotted Against Cos 2ψ from Finite Elements

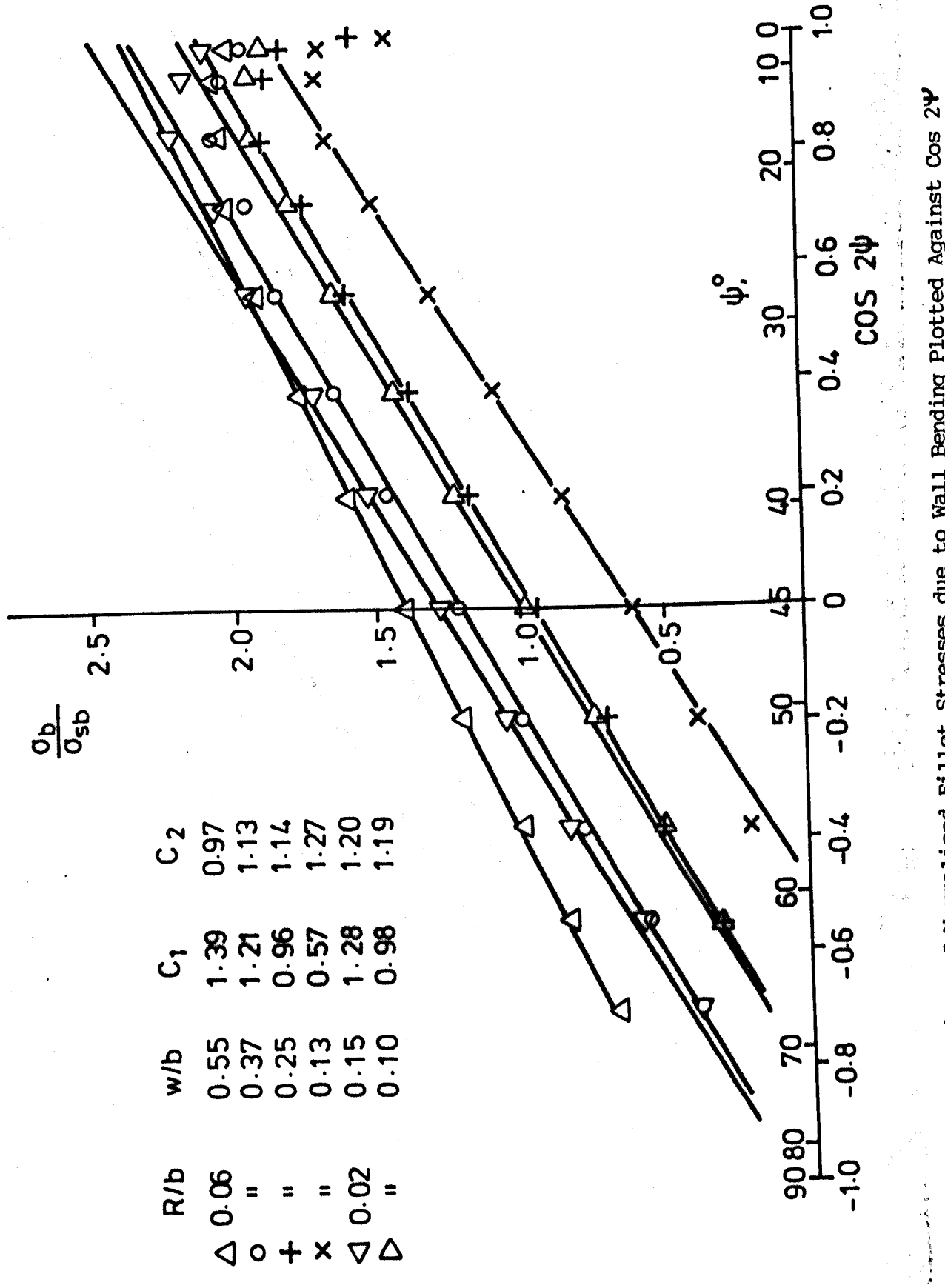

FIG. A7.4 Distributions of Normalised Fillet Stresses due to Wall Bending Plotted Against Cos 2ψ from Finite Elements

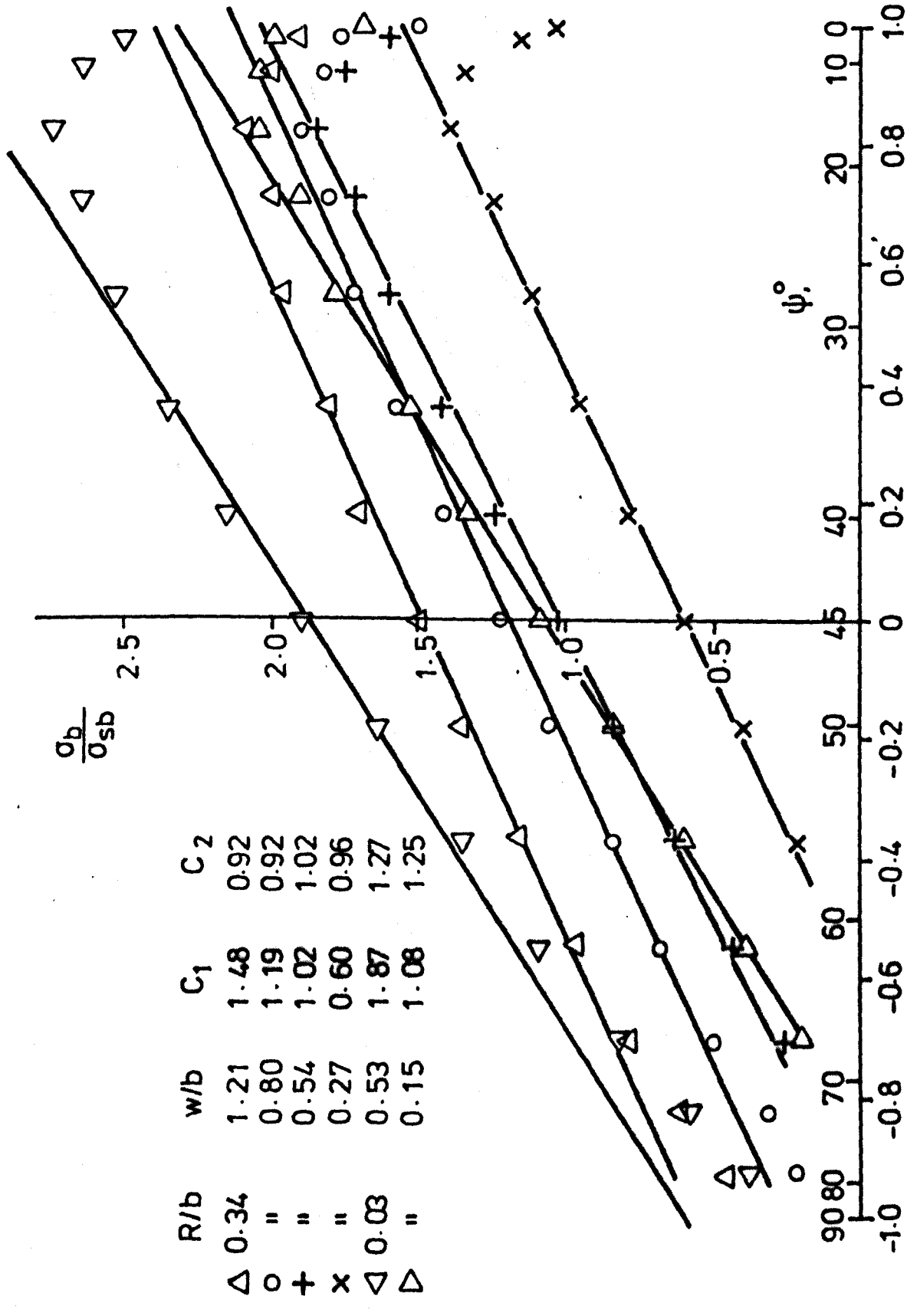

FIG. A7.5 Distributions of Normalised Fillet Stresses due to Wall Bending Plotted Against Cos 2Ψ from Finite Elements

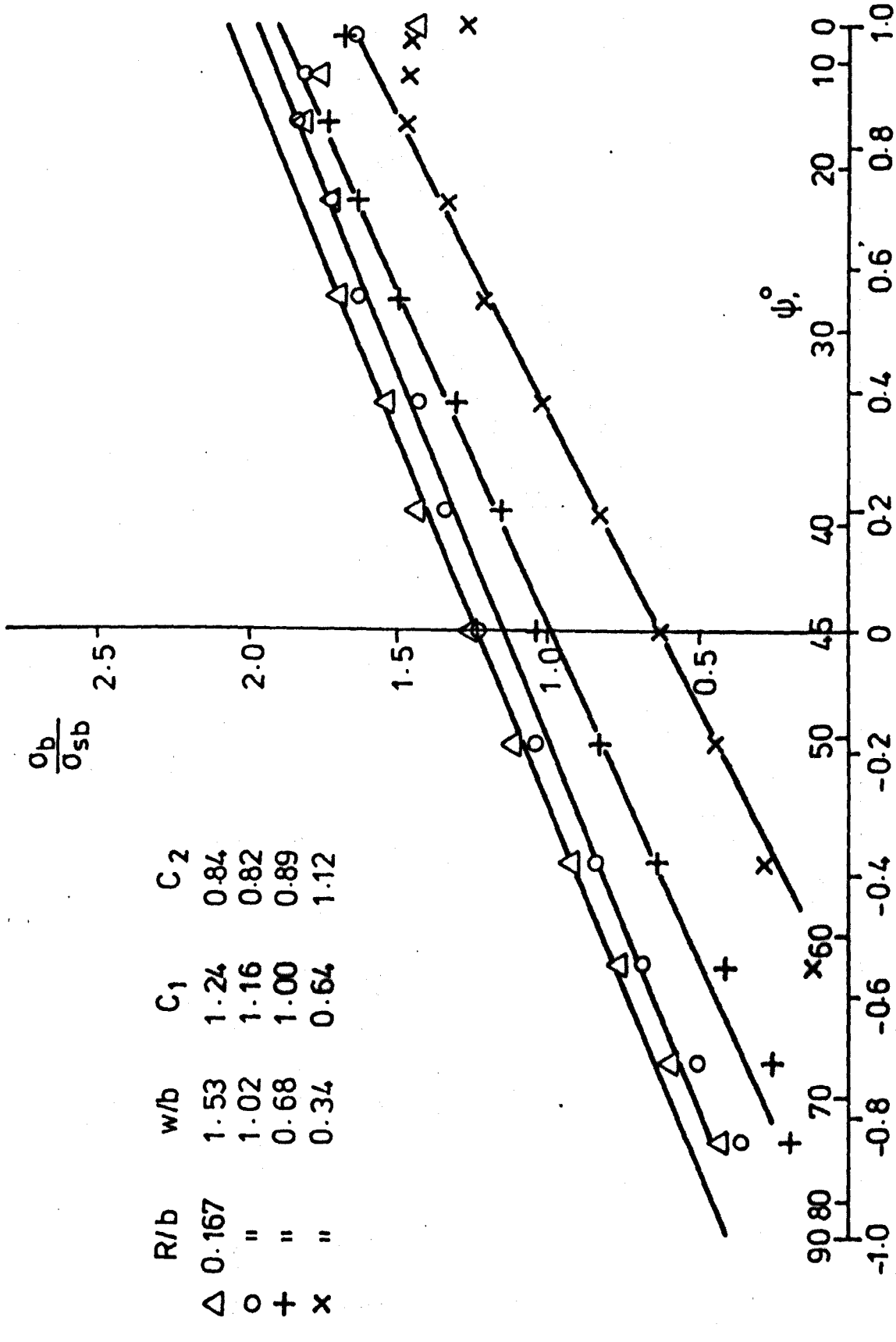

FIG. A7.6 Distributions of Normalised Fillet Stresses due to Wall Bending Plotted Against Cos 2ψ from Finite Elements

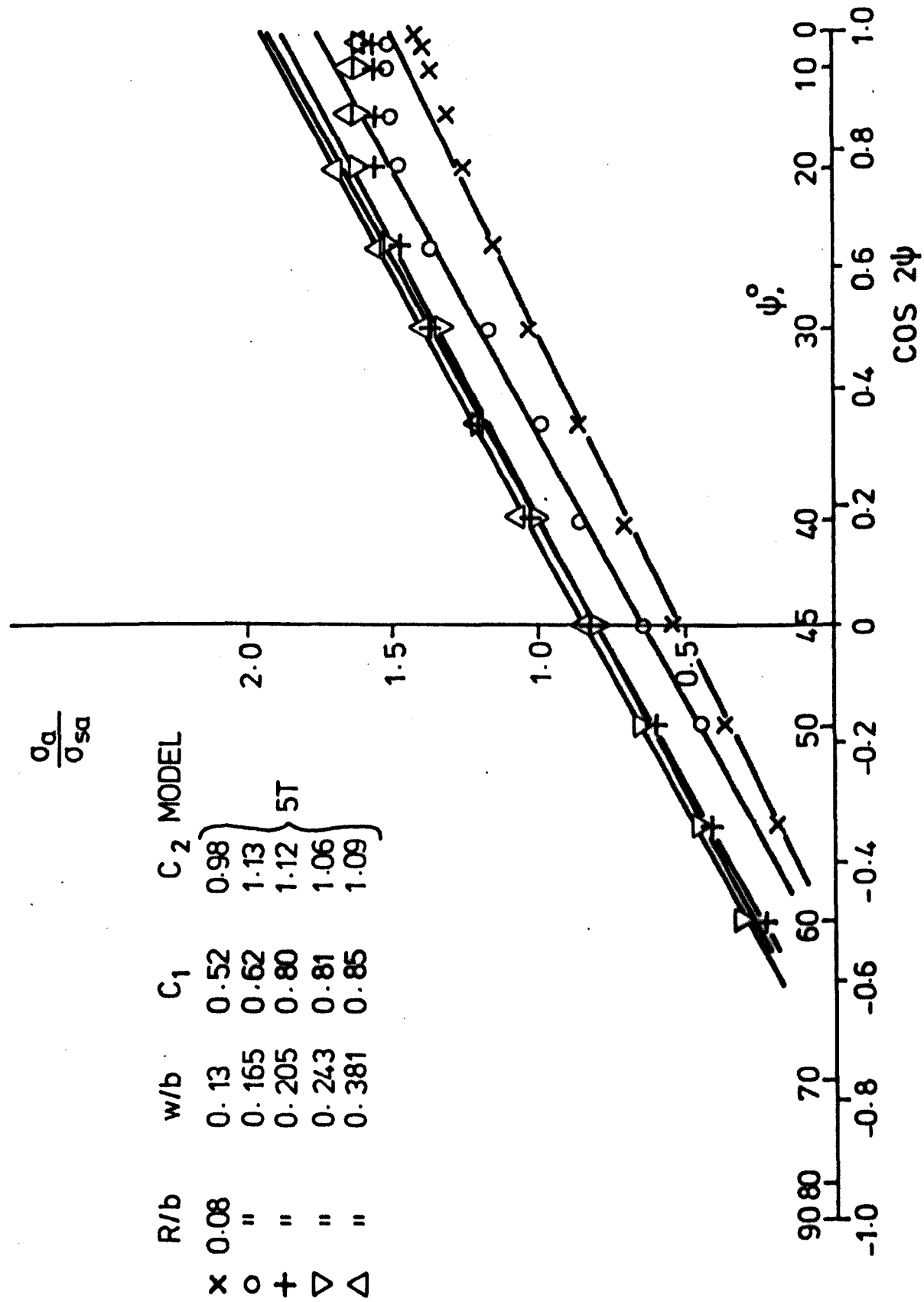

FIG. A7.7 Distributions of Normalised Fillet Stresses due to Wall Tension Plus Wall Bending Plotted against Cos 2ψ - Measured using the AMP

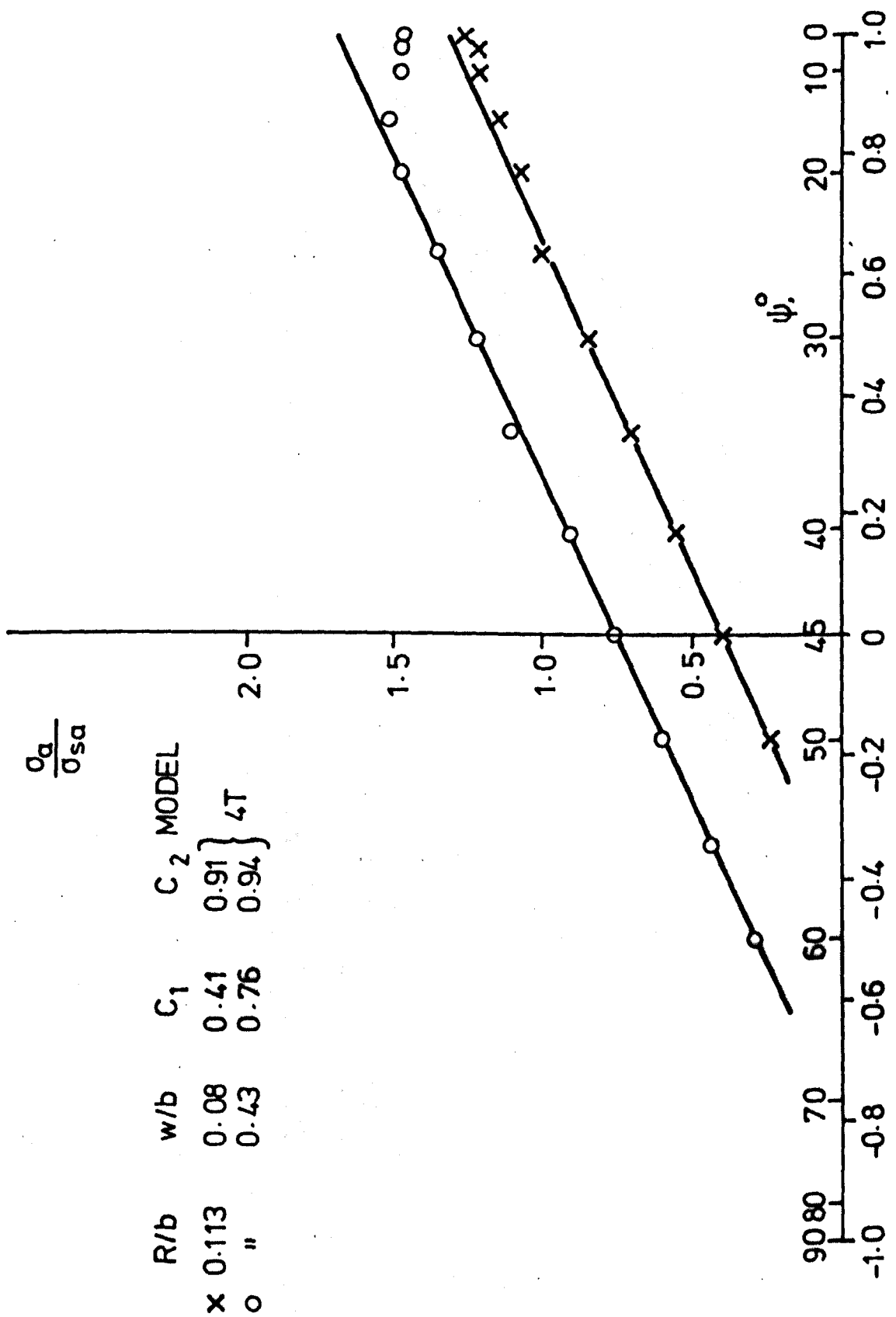

FIG. A7.8 Distributions of Normalised Fillet Stresses due to Wall Tension Plus Wall Bending Plotted Against Cos 2Ψ - Measured using the AMP

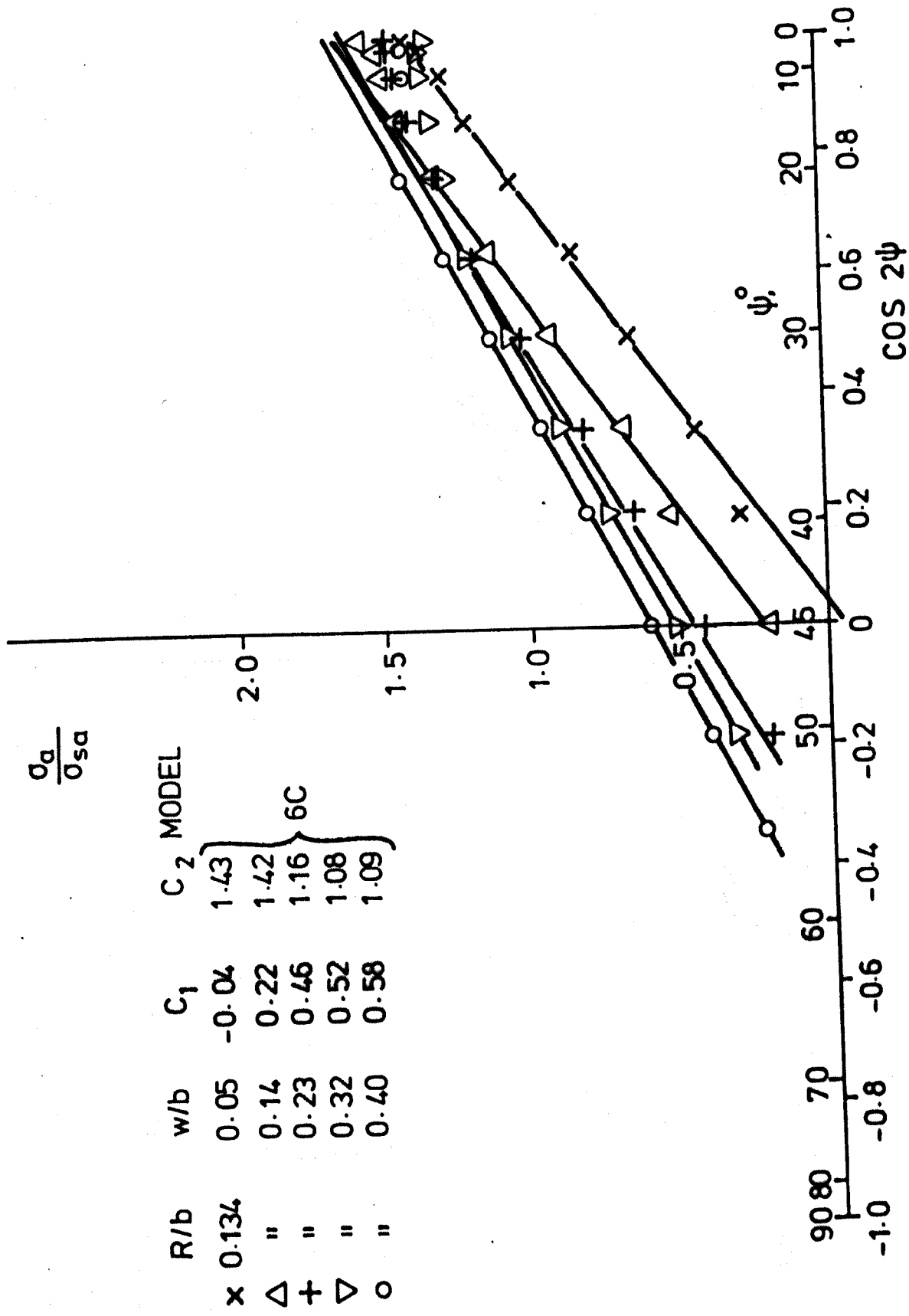

FIG.A7.9 Distributions of Normalised Fillet Stresses due to Wall Tension Plus Wall Bending Plotted Against Cos 2Ψ - Measured Using the AMP

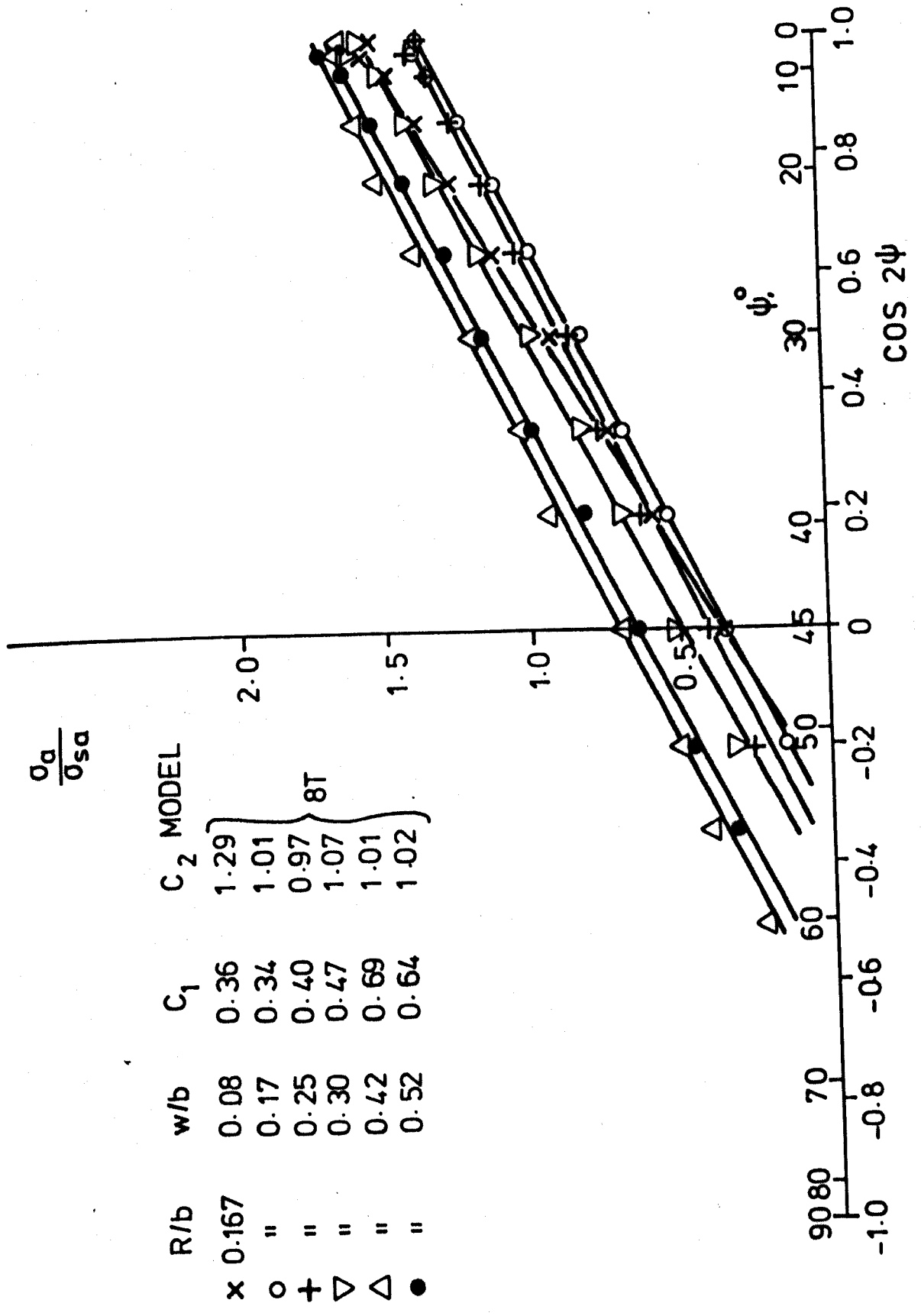

FIG. A7.10 Distributions of Normalised Fillet Stresses due to Wall Tension Plus Wall Bending Plotted against Cos 2Ψ - Measured using the AMP

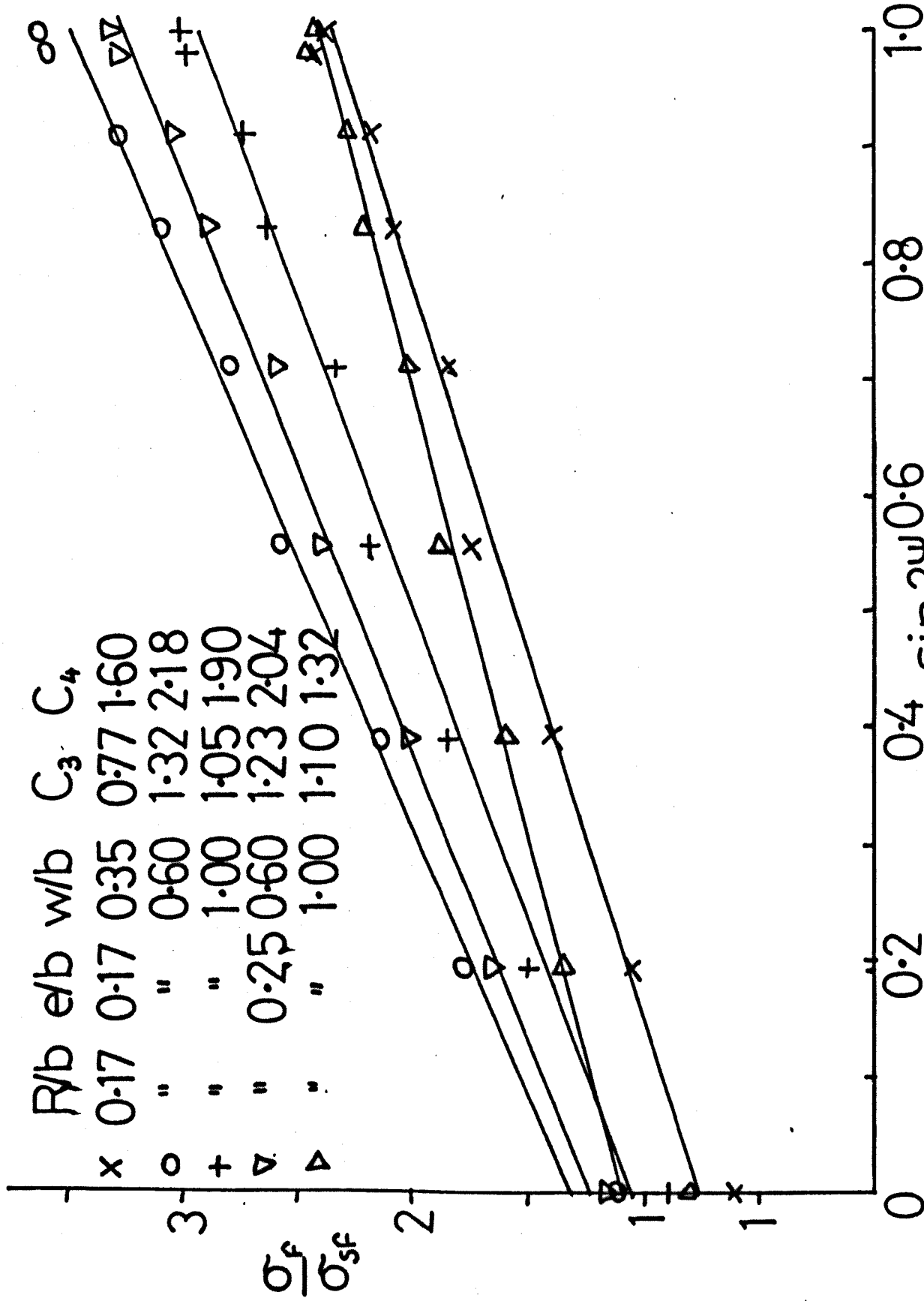

Fig A7.11 Distributions of Normalised Fillet Stresses due to Thread Shear Force Only Plotted Against $\sin 2\psi$ from Finite Elements

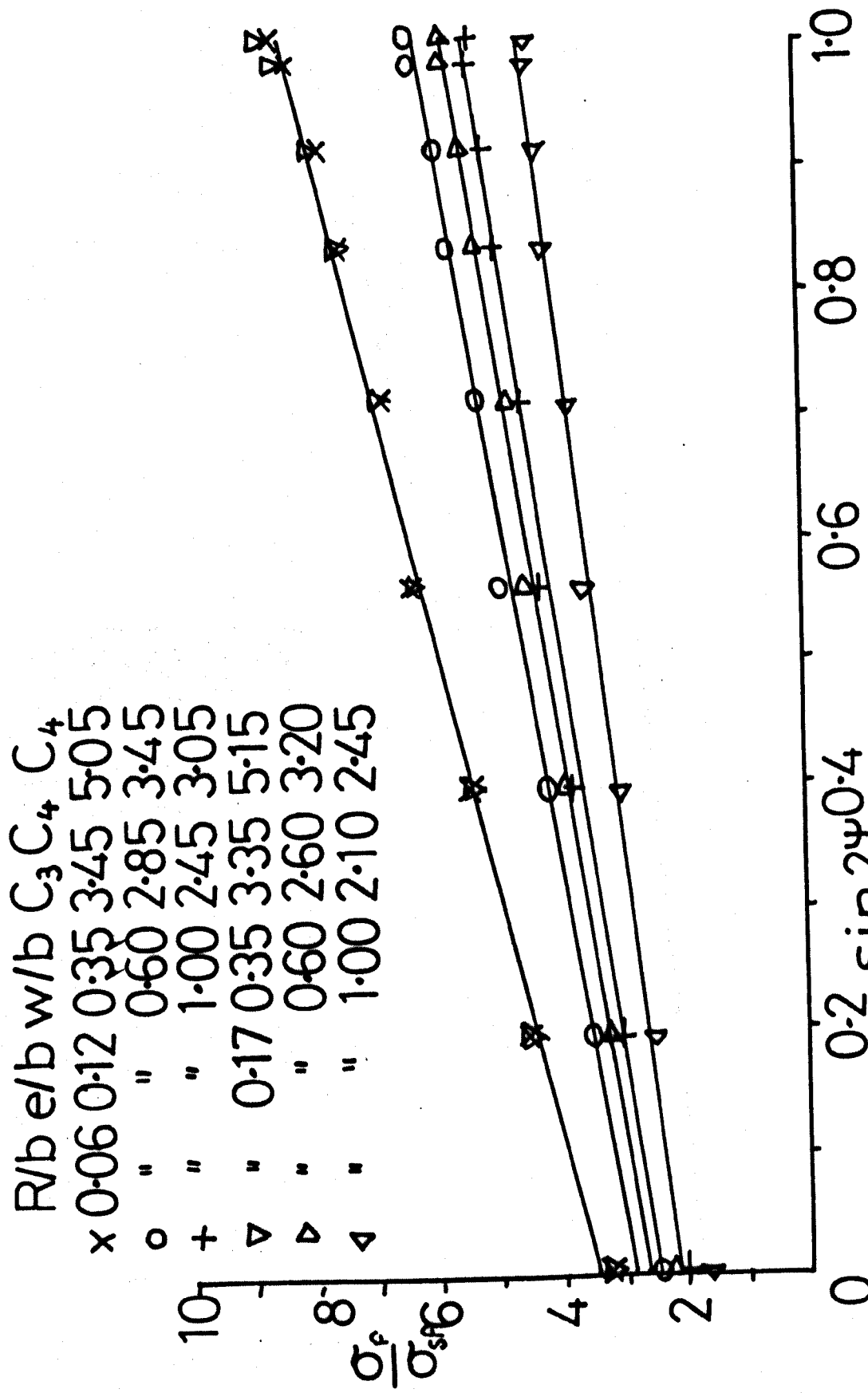

Fig A7.12 Distributions of Normalised Fillet Stresses due to Thread Shear Force Only Plotted Against Sin2Ψ from Finite Elements

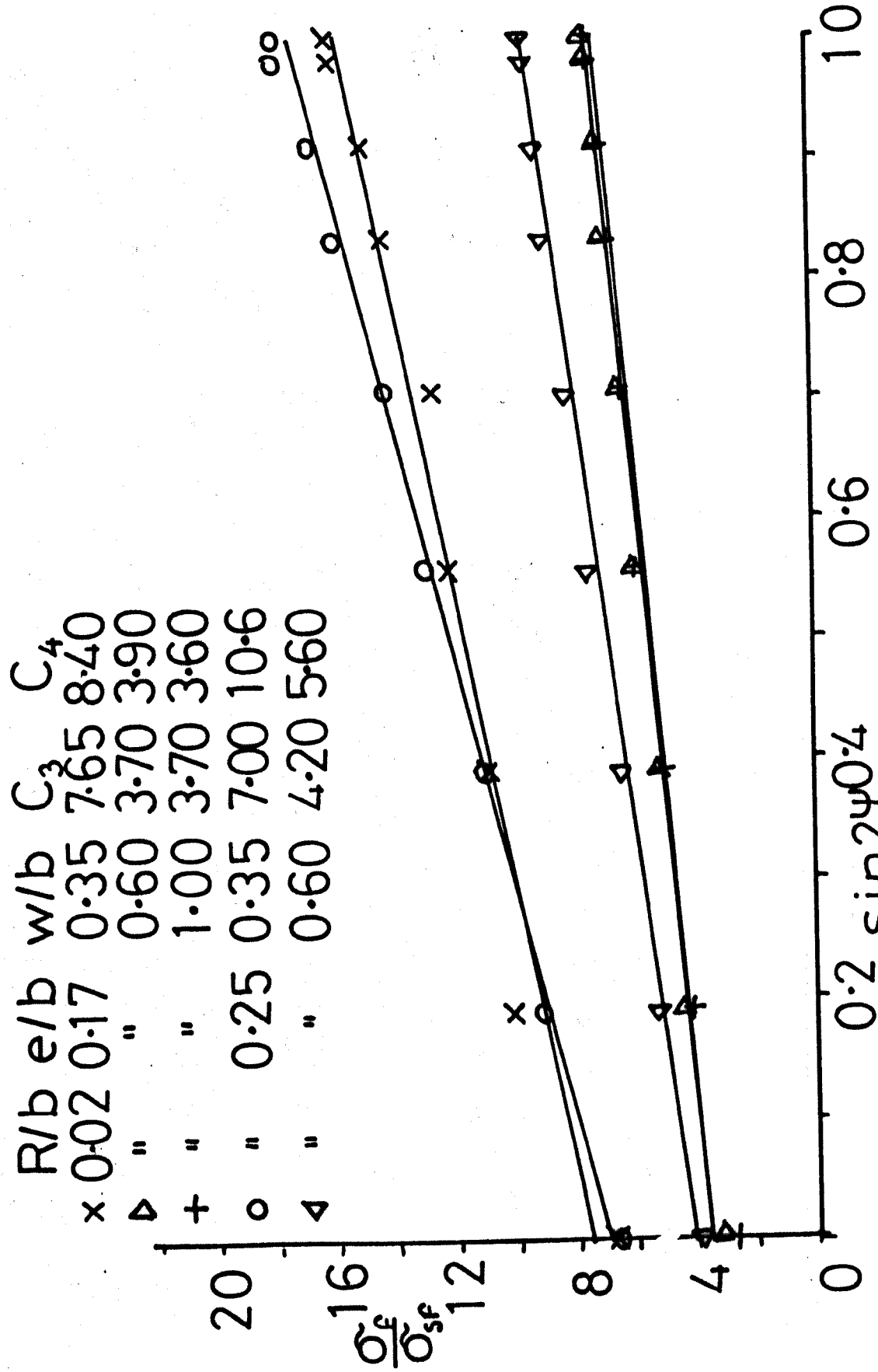

Fig A7.13 Distributions of Normalised Fillet Stresses due to Thread Shear Force Only Plotted Against $\sin 2\psi$ from Finite Elements

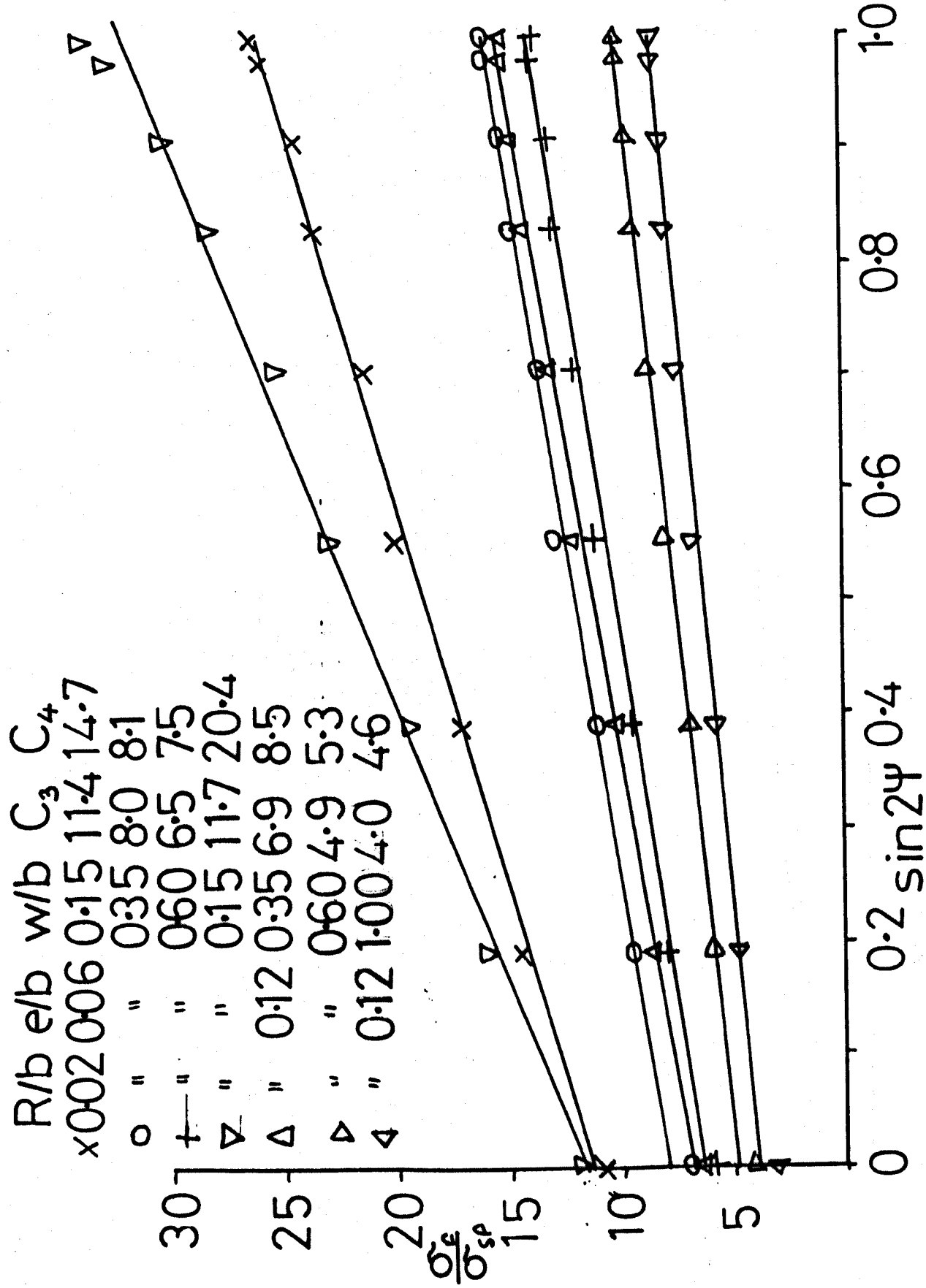

Fig A7.14 Distributions of Normalised Fillet Stresses due to Thread Shear Force Only Plotted Against $\sin 2\psi$ from Finite Elements

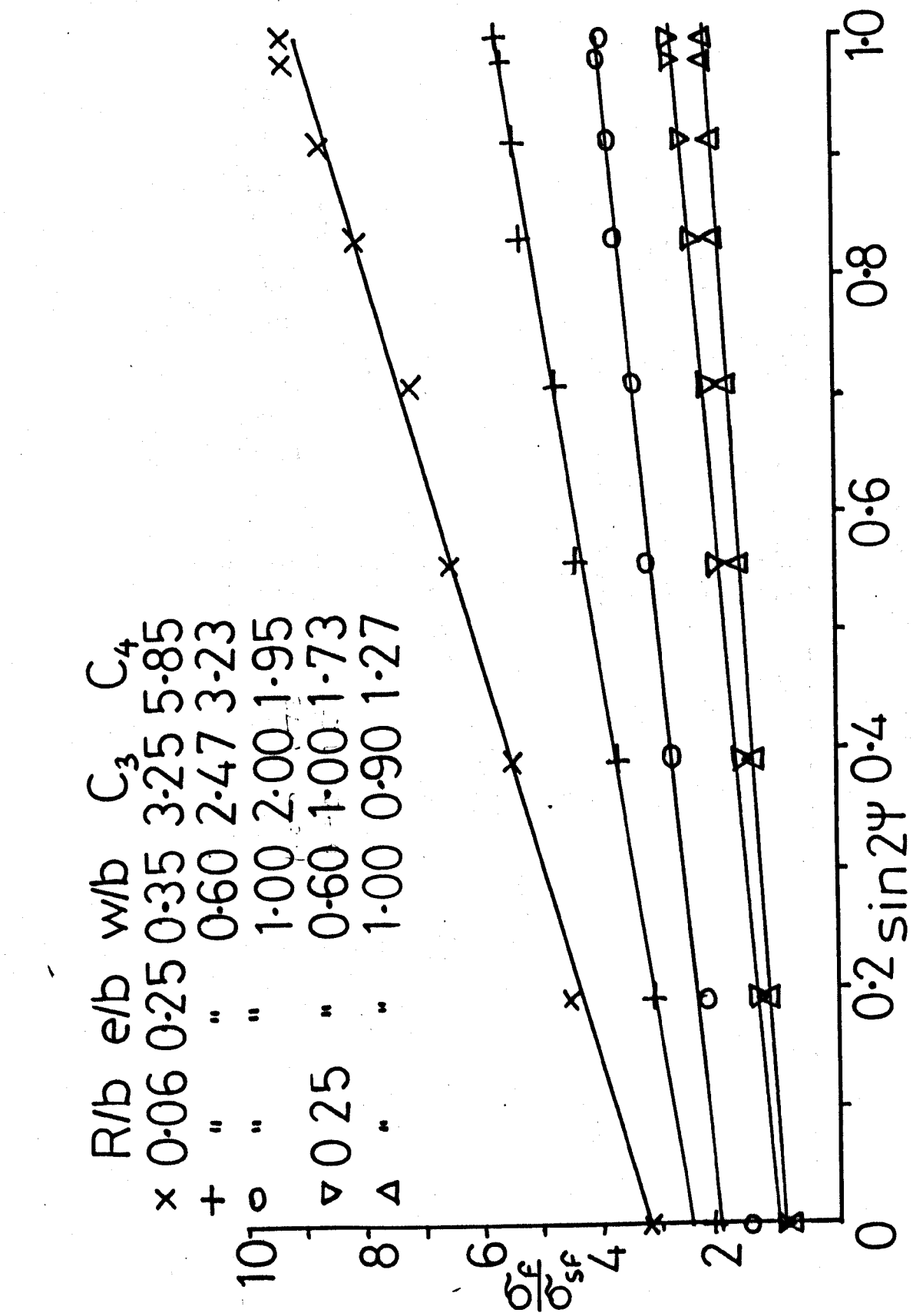

Fig A7.15 Distributions of Normalised Fillet Stresses due to Thread Shear Force Only Plotted Against Sin2Ψ from Finite Elements

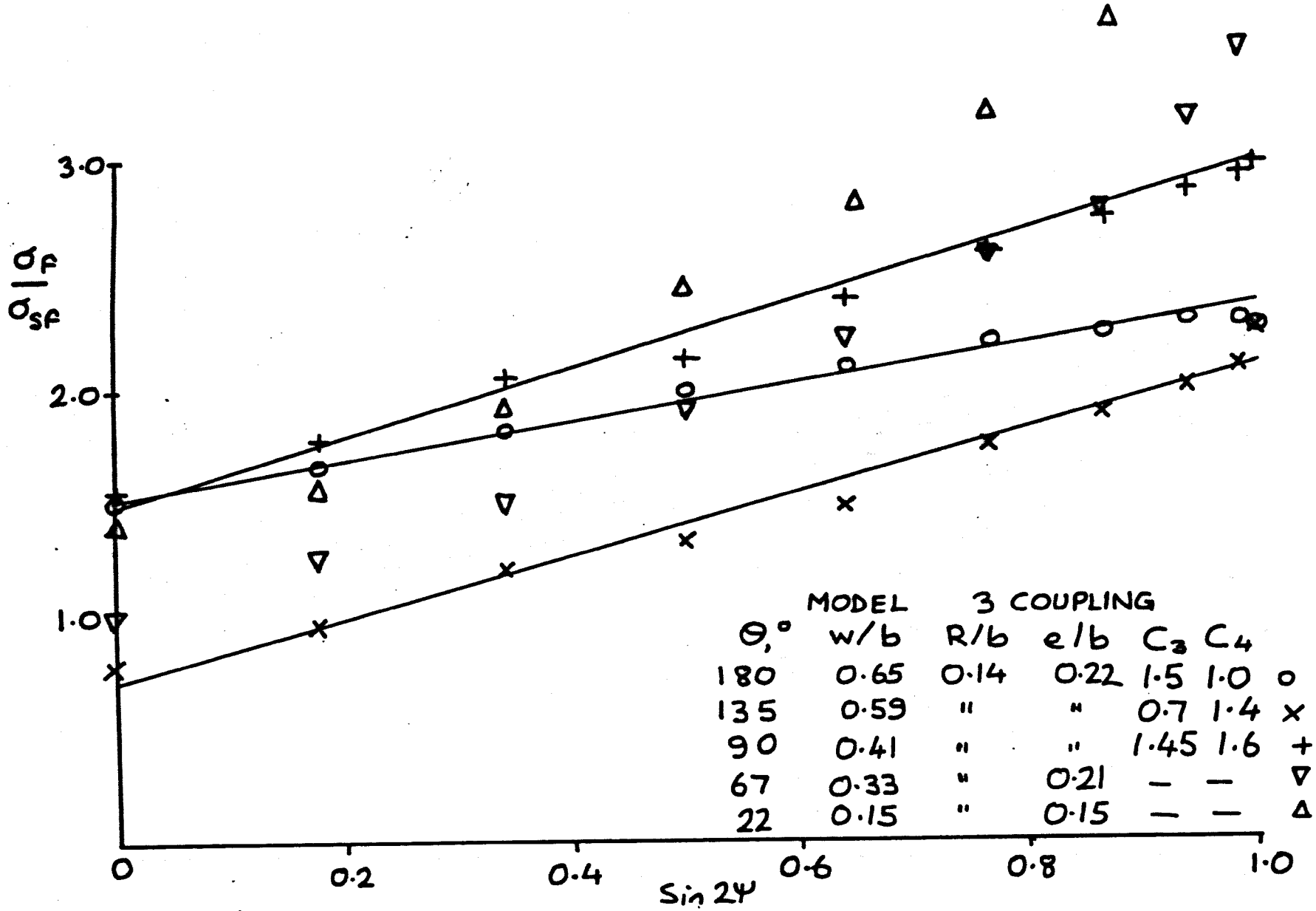

Fig A7.16 Distributions of Normalised Fillet Stresses due to Thread Shear Force Only Plotted Against Sin2Ψ Measured Using the AMP

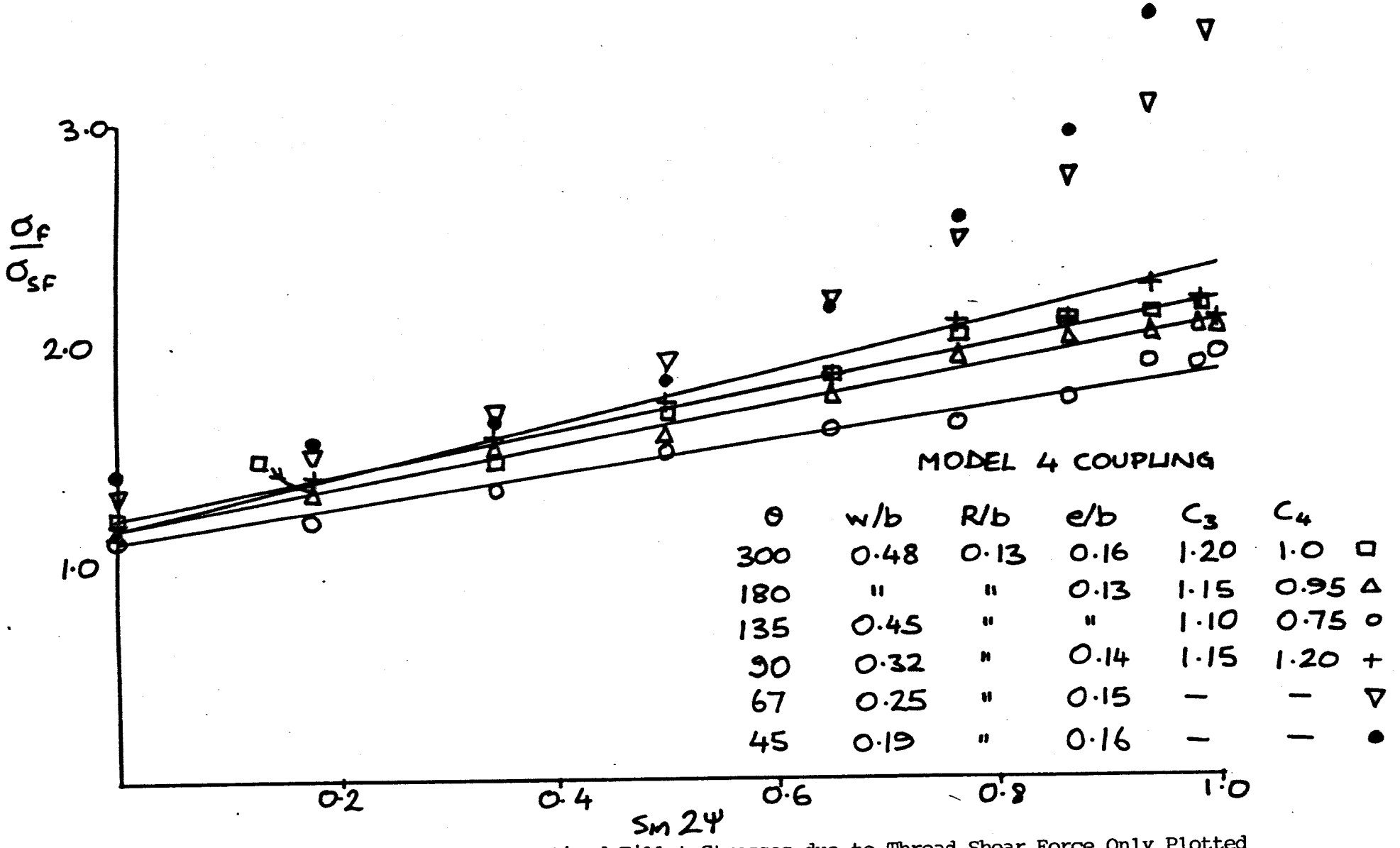

Fig A7.17 Distributions of Normalised Fillet Stresses due to Thread Shear Force Only Plotted Against Sin2Ψ- Measured Using the AMP

Appendix 8 Calculation of Position and Magnitude of Typical Peak Fillet Stress

The position P=6.5 in the coupling of the tension and preloaded Model 9 has been chosen to show the procedure for calculating the position and magnitude of the peak fillet stress in a typically loaded model.

The important parameters obtained from measurements of the model were:-

$z/L = 0.86$, $R/b = 0.126$, $w/b = 0.42$, $e/b = 0.155$, $L/p = 7.5$

$b = 19.08$ mm, $D_M = 211$ mm, $D_i = 176$ mm, $D_o = 260$ mm, $t = 25$ mm

The loading magnitudes were:-

$F = 764$N, $Q = 420$ N

The following steps have been followed:-

i) Calculate the coefficients C_1, C_2, C_3, and C_4 from the equations

$$C_1 = 0.38(w/b-0.05)^{0.45} (R/b)^{-0.56}$$

$$C_2 = 1.29 - 0.144\ w/b$$

$$C_3 = 0.311\ (R/b)^{-0.56}\ (w/b)^{(-0.154(R/b)^{-0.36})}\ (e/b)^{-0.19}$$

$$C_4 = (w/b)^{-0.25}\ (R/b)^{(-0.32(w/b)^{-0.425})}$$

Using the above values of the parameters in the equations

$C_1 = 0.709$

$C_2 = 1.23$

$C_3 = 1.873$

$C_4 = 3.24$

ii) Calculate the magnitude of the normalised shear force $\bar{V}$. Since $z/L>0.5$, the equation for V due to the preload is

$$\bar{V}_Q = 0.58 + 0.65\ (z/L) + 59\ (z/L - 0.5)^5.$$

The equation for V due to the axial tension is

$$\bar{V}_F = 0.81 + 15(z/L - 0.5)^4$$

Combining the two equations and normalising by the applied tension

$$\bar{V} = 0.81 + 15(z/L - 0.5)^4 + \frac{Q}{F}(0.58 + 0.65\,(z/L) + 59\,(z/L - 0.5)^5)$$

substituting the values for z/L, Q and F gives

$$\bar{V} = 1.885$$

iii) Calculate the magnitude of the normalised nominal bending stress σ_{SF} from

$$\sigma_{SF} = \frac{6M\ t(D_o - t)}{b^2\ D_M\ (L/p)}$$

where $M = F(M_o)$

and $M_o = V(e + b/2)$, see Appendix 6

From the above equations and parameters

$$\sigma_{SF} = 0.720$$

iv) Calculate the magnitude of the normalised wall tension W at that section,

where

$$W = W_F + \frac{Q}{F} W_Q$$

and $W_F = 0.81\ (\frac{z}{L}) + 3\ (\frac{z}{L} - 0.5)^5 + 0.094$

and since $z/L > 0.5$

$$W_Q = 0.58\ (z/L) + 0.325\ (z/L)^2 + \frac{59}{6}\ (z/L - 0.5)^6 - 0.0586$$

Hence, $\underline{W = 1.195}$

v) Calculate the magnitude of the mean normalised wall stress, σ_{sa}

where $\sigma_{sa} = W\ \frac{(D_o - t)t}{(D_i + b)b}$

hence, $\sigma_{sa} = 1.886$

vi) Calculate the value of ϕ_{max}, the position of the peak fillet stress from

$$\phi_{max} = 0.5 \tan^{-1}\left(\frac{C_4 \ \sigma_{SF}}{C_2 \ \sigma_{sa}}\right)$$

hence $\phi_{max} = 22.6^{o}$

vii) Calculate the magnitudes of the normalised fillet stress due to the wall tension σ_a and due to the shear force σ_F, at the position $\phi = \phi_{max}$ from

$$\sigma_a = \sigma_{sa} (C_1 + C_2 \cos 2\phi_{max})$$

and

$$\sigma_F = \sigma_{SF} (C_3 + C_4 \sin 2\phi_{max})$$

$\therefore \ \sigma_a = 2.973$ and $\sigma_F = 3.00$

viii) Combine σ_a and σ_F to obtain the peak fillet stress i.e.

$$\hat{\sigma}_L = \sigma_a + \sigma_F$$

$$\hat{\sigma}_L = 5.97$$

Appendix 9 Friction Tests

To determine the coefficient of friction of the loaded faces of mating threads, tests were carried out on the partially assembled (not fully tightened up), cleaned and lubricated threads of Model 7 at the stress freezing temperature. For each test, a small axial tension, F, was applied to ensure contact on the loaded face. Small increments of torque ($0.05N_m$) were applied simultaneously to both torque hangers, see Fig 4.11 until there was relative movement between the models.

The models were left for at least 10 minutes between each application of torque to give the tube model chance to rotate. Tests were carried out at two different screwed up positions, i.e. the axial gap between the tube nose and coupling contact face was varied. Torque was applied in the screwing up direction until relative movement between the models occurred. Marks had been made in the seal regions of both models at the same value of θ to help determine when relative movement had occurred.

The coefficient of friction μ, is related to the torque T_o which overcomes friction by

$$\mu = (T_o \pi D_m - \frac{FD_m}{2}p)/(F\, D_m{}^2 \frac{\pi}{2} + T_o p) \qquad \text{A9.1}$$

where D_m is mean thread diameter = 211mm, p is thread pitch = 15.8 mm μ coefficient of friction, F axial force and T torque needed to overcome friction. Equation A9.1 was used to calculate the values of μ presented in Table A9.1.

TABLE A9.1 Friction Test Results

F(N)	THICKNESS STRAIN ε (%)	AXIAL GAP (mm)	APPLIED TORQUE T_o (Nm)	μ
159	0.09	19	4.36	0.24
257	0.14	19	6.11	0.20
159	0.09	12.5	3.89	0.21
257	0.14	12.5	6.53	0.22